



Atomistic simulation of fatigue in face centred cubic metals

Zhengxuan Fan

► To cite this version:

Zhengxuan Fan. Atomistic simulation of fatigue in face centred cubic metals. Mechanics of materials [physics.class-ph]. Université Paris Saclay (COmUE), 2016. English. NNT : 2016SACLX076 . tel-01526211

HAL Id: tel-01526211

<https://pastel.hal.science/tel-01526211>

Submitted on 22 May 2017

HAL is a multi-disciplinary open access archive for the deposit and dissemination of scientific research documents, whether they are published or not. The documents may come from teaching and research institutions in France or abroad, or from public or private research centers.

L'archive ouverte pluridisciplinaire **HAL**, est destinée au dépôt et à la diffusion de documents scientifiques de niveau recherche, publiés ou non, émanant des établissements d'enseignement et de recherche français ou étrangers, des laboratoires publics ou privés.

NNT : 2016SACLX076

THÈSE DE DOCTORAT
DE L'UNIVERSITÉ PARIS-SACLAY
préparée à l'ÉCOLE POLYTECHNIQUE

ÉCOLE DOCTORALE N° 573

Interfaces — Approches interdisciplinaires : fondements, applications et innovations

Spécialité : **PHYSIQUE**

par
Mme Zhengxuan FAN

**Simulation atomistique de la fatigue dans les métaux
cubiques à faces centrées**

Thèse soutenue à Palaiseau le 18 novembre 2016

Composition du jury :

Mme	Sandrine BROCHARD	Rapporteur
M.	Derek WARNER	Rapporteur
M.	Gilbert HÉNAFF	Président
M.	Haël MUGHRABI	Examineur
M.	Boubakar DIAWARA	Examineur
M.	Maxime SAUZAY	Co-directeur
M.	Olivier HARDOUIN DUPARC	Directeur

NNT : 2016SACLX076

Thesis to be presented to obtain the degree of
DOCTOR OF UNIVERSITÉ PARIS-SACLAY
prepared at the **ÉCOLE POLYTECHNIQUE**

DOCTORAL SCHOOL No. 573

Interfaces — Approches interdisciplinaires : fondements, applications et innovations

Speciality: **PHYSICS**

by
Zhengxuan FAN

**Atomistic simulation of fatigue in face centred cubic
metals**

Thesis defended at Palaiseau 18 November 2016

Thesis committee:

Prof.	Sandrine BROCHARD	Referee
Prof.	Derek WARNER	Referee
Prof.	Gilbert HÉNAFF	President
Prof.	Haël MUGHRABI	Examiner
Prof.	Boubakar DIAWARA	Examiner
Dr.	Maxime SAUZAY	Co-Supervisor
Dr.	Olivier HARDOUIN DUPARC	Supervisor

Remerciements

Je tiens à remercier chaleureusement toutes les personnes qui ont cru en moi et qui m'ont permis d'arriver au bout de cette thèse.

Tout d'abord, je souhaite exprimer ma profonde gratitude à mon directeur de thèse, Monsieur Olivier Hardouin Duparc, pour son accueil, sa gentillesse extraordinaire, le temps passé ensemble et le partage de son expertise au quotidien. Il a dirigé mes travaux avec beaucoup de disponibilité, de patience et des conseils très constructifs. Sa compétence scientifique exceptionnelle et sa rigueur m'ont beaucoup appris. Ils ont été et resteront des moteurs de mon travail de chercheuse.

Je tiens à remercier vivement mon co-directeur de thèse, Monsieur Maxime Sauzay pour la confiance qu'il m'a accordée en acceptant ma candidature, pour ses multiples conseils et pour sa direction de mes travaux de recherche même pendant la période où il était malade. Je lui suis reconnaissante de m'avoir fait bénéficier tout au long de ce travail de l'étendue exceptionnelle de ses connaissances ainsi que de sa rigueur intellectuelle.

Je désire aussi remercier mes rapporteurs Mme Sandrine Brochard et M. Derek Warner, pour le temps qu'ils ont accordé à la lecture de mon manuscrit de thèse, l'élaboration de leurs rapports, et pour toutes leurs corrections, suggestions et remarques.

J'exprime mes remerciements à l'ensemble des membres de jury :

- M. Gilbert Hénaf, pour sa participation en qualité de président.
- M. Haël Mughrabi, pour ses multiples conseils ainsi que pour l'intérêt qu'il a manifesté par rapport à mes travaux et toutes les corrections et suggestions qu'il a apportées à mon manuscrit.
- M. Boubakar Diawara, pour son support sur le potentiel ReaxFF et de nombreuses discussions à l'Ecole Chimie ParisTech.

Je remercie aussi M. Kees Van Der Beek, directeur du laboratoire LSI, Mme Nathalie VAST, responsable du groupe TSM, ainsi que Mme Michèle Raynaud et Mme Jelena Sjakste. Merci de m'avoir accueillie et de m'avoir permis de travailler dans d'aussi bonnes conditions. Je remercie aussi bien sûr l'ensemble du LSI pour son accueil.

Un grand merci à tous les membres du laboratoire LC2M pour leur accueil, leur soutien, leur partage de connaissance et les discussions enrichissantes. Votre aide m'a permis de surmonter les difficultés que j'ai pu rencontrer.

Je remercie M. Andrea Cucca et M. Louis Ziolk, ingénieurs informaticiens des laboratoires LSI à l'École polytechnique et LC2M au CEA Saclay, pour leur aide au niveau informatique, leur gentillesse et leur disponibilité.

Je remercie Mmes Sylvie Michèle, Cathy Vidal, Isabelle Taquin, Nathalie Palayan, et Marylène Raclot pour leur aide administrative indispensable.

J'exprime ma gratitude à Mme Sylvie Lartigue, pour son intérêt pour mes travaux et son aide pour l'analyse des dislocations.

Je n'oublie évidemment pas mes amis et camarades doctorants/post-doc du LSI et LC2M: Liang, Gaston, Maxime (Maksim), Antoine, Giuliana, Oleksandr, Mariya, Sabuhi, Sky, Houng, Hai-Yan, Ikbal, William, Irina, Benjamin, Marcos, Peppe, Deniz, Seonyong, Liang, Jérôme, Marios, Marie, Diogot, Elric, Bertrand, Xiangjun, Yiting, Fatima et Jia. J'ai partagé avec eux tous les moments de doute et de plaisir, leur soutien fut indispensable pour ces trois années de thèse.

Je remercie aussi bien sûr l' IDEX et le CEA qui ont financé ma bourse de thèse, l'Ecole polytechnique et particulièrement les laboratoires LSI et LLR pour les moyens de calculs mis à ma disposition.

A titre plus personnel, je remercie mes parents pour leur soutien. C'est avec plaisir qu'à mon tour je leur dévoile le fruit de mes efforts. Enfin, je remercie mon mari, Jigang, pour son soutien quotidien, sa confiance et ses encouragements. Sans lui, tout ce travail n'aurait pas la même saveur pour moi.

Résumé

La fatigue induite par chargements cycliques est un mode d'endommagement majeur des métaux et alliages. Elle se caractérise par des effets environnementaux importants et elle n'est toujours pas bien comprise.

L'endommagement de fatigue s'amorce souvent par la surface, par l'accumulation de marches irréversibles créées par les dislocations. Dans ce travail, l'évolution de ces marches de surface et l'initiation des nano-fissures sont analysées à l'échelle atomique par dynamique moléculaire en environnement inerte d'abord et aussi en environnement oxygène. La propagation des nano-fissures sous chargement cyclique est également simulée en environnement inerte.

Les simulations permettent de suivre et d'analyser l'évolution des premières marches créées en surface jusqu'à leur accumulation, c'est-à-dire du premier cycle jusqu'à plusieurs cycles de chargement. Les matériaux étudiés sont de type métallique cubique à faces centrées : aluminium, cuivre, nickel et argent. Des potentiels de type EAM (embedded atom model) sont appliqués pour les simulations en environnement inerte (sous vide). Des potentiels ReaxFF (reactive force field) et COMB (charge optimized many body) sont utilisés pour les simulations sous environnement oxygène. Ces potentiels donnent de bonnes estimations de nombreuses propriétés physiques des matériaux étudiés.

La création et l'évolution des marches en surface sont d'abord analysées sous environnement inerte. Des dislocations coin avec un vecteur de Burgers standard $\mathbf{b} = a \langle 110 \rangle / 2$ sont insérées dans le volume. Elles glissent sous chargement et émergent en surface en y créant des marches. On observe alors un phénomène de reconstruction qui rend ces marches reconstruites irréversibles sous chargement inverse. Trois types de mécanismes de reconstruction sont identifiés. La reconstruction quasi-instantanée se produit à toutes les températures, elle se fait en quelques picosecondes et diminue fortement l'énergie des marches. Pour la reconstruction assistée par vibrations thermiques l'agitation des atomes en surface leur permet de surmonter des barrières énergétiques locales et d'atteindre des configurations d'énergies plus faibles. Le troisième mécanisme est la reconstruction assistée par la diffusion d'adatoms en surface, il n'a lieu qu'à des températures assez élevées qui permettent l'apparition spontanée d'adatoms.

L'irréversibilité de ces marches est ensuite analysée. Elles restent irréversibles pour toutes les amplitudes de chargement caractéristiques des essais expérimentaux, sauf en cas d'arrivée de dislocations de signe opposé sur un plan de glissement atomique directement voisin. Avec l'arrivée de dislocations de signes opposés sur des plans non voisins, l'irréversibilité s'accumule cycle par cycle et on constate alors dans la simulation l'apparition en surface de nano entailles dont la profondeur augmente peu à peu.

Le facteur d'irréversibilité p est estimé en couplant des modèles de la littérature basés sur des mécanismes de volume (le modèle de Differt, Essmann, Gösele et Mughrabi en 1981 et le modèle de Lépinoux et Kubin en 1986) et nos simulations en surface. On trouve un facteur d'irréversibilité compris entre 0,4 et 0,7. Ces valeurs sont supérieures aux estimations qui ne tiennent compte que des mécanismes de volume et elles se rapprochent de la valeur de 0,8 mesurée en microscopie à force atomique par Weidner et Sauzay en 2011.

Des simulations similaires sont ensuite effectuées sous environnement oxygène en utilisant des potentiels ReaxFF et COMB3 pour le nickel et pour le cuivre afin d'évaluer l'influence de l'oxygène sur l'irréversibilité des marches créées en surface. On simule d'abord les premiers stades d'oxydation de surfaces de nickel et de cuivre pour étudier les mécanismes d'oxydation à l'échelle atomique et pour constater que les résultats de ces mécanismes sont en accord avec ce qui est connu au niveau des observations expérimentales.

Les molécules d'oxygène adsorbées sur la surface du nickel se dissocient en atomes d'oxygène qui pénètrent ensuite dans le métal sur une petite profondeur. Certains atomes de nickel diffusent vers l'extérieur, ce qui entraîne une croissance externe et l'initiation de petits îlots bidimensionnel de NiO, de stœchiométrie 1:1 (type plan (100) du NiO 3d cubique).

Les mécanismes d'oxydation en surface du cuivre sont différents de ceux du nickel. L'oxygène est principalement chimisorbé à l'état moléculaire. Les molécules O₂ chimisorbées se dissocient rarement, même à relativement haute température (600 K). Aucun germe d'oxyde cuivreux ou cuivrique n'est observé pendant les premiers stades d'oxydation et il n'y a qu'une très faible pénétration d'oxygène dans le cuivre. Il est intéressant de noter que le potentiel COMB3 prédit la formation en surface d'une couche amorphe tandis qu'avec ReaxFF les atomes de cuivre gardent essentiellement leur environnement cubique à faces centrées.

Pour les premiers stades d'oxydation aux températures que nous avons considérées dans nos simulations, à savoir 300 K et 600 K, l'oxygène n'augmente pas l'irréversibilité des

marches en surface et les surfaces simulées évoluent de la même manière qu'en environnement inerte. L'environnement oxygène n'a pas d'effet significatif sur la reconstruction des marches en surface et n'empêche pas le glissement des dislocations vers la surface. Ces résultats sont en accord avec les observations expérimentales selon lesquelles le relief de fatigue en surface des bandes de glissement persistantes est le même sous environnement inerte et sous air. Donc, sur la base de nos simulations, le facteur d'irréversibilité doit être le même sous environnement inerte et sous environnement oxygène en se limitant au cas de la formation de très fines couches de métal oxydé. Des nano-entailles peuvent de la même manière être initiées sous chargement cyclique.

Des simulations ont également été effectuées sur la propagation des fissures sous environnement inerte. Si plusieurs systèmes de glissement peuvent être activés à la pointe de fissure, nous avons constaté que les fissures se propagent (grandissent) sous chargement cyclique. Cela est dû au fait que de nombreux verrous de dislocations se forment lors de l'interaction entre les dislocations glissant dans des systèmes différents. Ces verrous bloquent la réversibilité de glissement des dislocations sous chargement inverse et la pointe de fissure croît au chargement suivant. Le cas d'une boîte $\{[100], [010], [001]\}$ avec une fissure parallèle à un plan (100) est exemplaire de ce point de vue. À l'inverse, aucune propagation évidente n'est observée pour une boîte $\{[-131], [714], [11-2]\}$ avec une fissure orientée le long d'un plan (111) avec seulement deux systèmes de glissement activés en chargement en mode mixte. Ces simulations montrent donc l'effet de l'orientation qui affecte directement le nombre de systèmes de glissement activés et joue ainsi un rôle dans le mécanisme de propagation de la fissure. L'émoussement (blunting) de la pointe de fissure est observé dans les deux boîtes sous tension.

Un autre mécanisme de propagation observé dans les simulations de films très minces (sans condition périodique) est la propagation par coalescence entre la pointe de fissure et des nano-vides qui sont nucléés immédiatement devant elle.

Le chargement contrôlé par force ou par déplacement, l'épaisseur de l'échantillon, l'application des conditions aux limites périodiques, l'orientation de l'échantillon et la température affectent le mécanisme et la vitesse de propagation des fissures. La vitesse de propagation des fissures à l'échelle nanométrique peut être grossièrement estimée de l'ordre de l'angström par cycle à 300 K dans la boîte $\{[100], [010], [001]\}$ avec une fissure parallèle à un plan (100), mais ce travail indique aussi que bien d'autres simulations sont encore à faire.

Table of Contents

CHAPTER 1.	INTRODUCTION	1
1.1	Industrial context.....	1
1.2	Basic concepts of fracture mechanics and fatigue	3
1.2.1	Ductile and fragile fracture.....	3
1.2.2	A brief history of fatigue	4
1.2.3	Fatigue S-N curve and endurance limit.....	5
1.2.4	Fatigue loading and fracture modes.....	7
1.2.5	The stress intensity factor K	8
1.3	Fatigue crack initiation and propagation	10
1.3.1	Different stages of crack initiation and propagation.....	10
1.3.2	The fatigue propagation rate da/dN	12
1.4	Dislocations.....	13
1.4.1	General presentation of edge and screw dislocations and their motions	13
1.4.2	More details about dislocations in fcc metals	15
1.4.3	Image forces	20
1.5	Computer simulations	21
CHAPTER 2.	SURFACE STEP IRREVERSIBILITY & CRACK INITIATION IN INERT ENVIRONMENT .	25
2.1	Literature review on experimental observations and irreversibility models	26
2.2	Simulation system and methods.....	32
2.3	Surface slip reconstruction and slip irreversibility during one full loading cycle	37
2.3.1	Slip reconstruction during one half-loading cycle	37
2.3.2	Surface slip irreversibility during one full cycle without additional dislocations	44
2.3.3	Surface slip irreversibility during one full cycle with opposite sign dislocations	47
2.4	Slip irreversibility and micro-notch initiation during cyclic loading	48
2.5	Discussions	53
2.6	Conclusions	56
2.7	Section appendix.....	57
CHAPTER 3.	SURFACE STEP IRREVERSIBILITY & CRACK INITIATION IN OXYGEN ENVIRONMENT .	59
3.1	Literature study.....	60
3.1.1	Some definitions	60
3.1.2	Oxidation on nickel / air interface.	60
3.1.3	Oxidation on Copper / air interface.....	63
3.1.4	Environmental effects on the surface slip irreversibility	66
3.2	Computational simulations	67
3.3	Oxidation on nickel surfaces	69
3.3.1	Ni and NiO physical properties	69
3.3.2	Oxidation of the nickel {111} surface	70
3.3.3	Oxidation of the nickel {100} surface	76
3.3.4	Discussions about the oxidation of the Ni (111) and (100) surfaces	79
3.4	Irreversibility of nickel surface steps in oxygen environment	80
3.5	Copper surface oxidation using both COMB3 and ReaxFF.	88
3.5.1	Copper surface oxidation using COMB3 potential	89
3.5.2	Copper surface oxidation using ReaxFF.....	91
3.5.3	Comparison between copper surface oxidation using COMB3 and ReaxFF	92
3.5.4	Comparison between copper and nickel (-131) surface oxidation.....	93

3.6 Irreversibility of copper surface steps in oxygen environment.	94
3.6.1 Slip irreversibility and notch formation using the COMB3 potential	94
3.6.2 Slip irreversibility and notch formation using the ReaxFF potential	97
3.7 Chapter conclusions and discussions	98
CHAPTER 4. CRACK PROPAGATION IN INERT ENVIRONMENT	100
4.1 Literature review on experimental studies about crack propagation	101
4.1.1 General introduction of crack propagation in inert and in air environment.....	101
4.1.2 Crack growth rate and initial stage of crack propagation	102
4.1.3 Crack propagation models	105
4.1.4 Role of gas partial pressure and temperature on fatigue life	107
4.1.5 Fatigue crack closure	109
4.1.6 Hysteresis loop	110
4.1.7 Evaluation of the fatigue crack propagation rate	111
4.1.8 Discussions about experimental studies	112
4.2 Literature review on computer simulations	113
4.2.1 Crack propagation mechanisms	113
4.2.2 Nano-structural small crack propagation rate	114
4.2.3 Limitations and advantages of computer simulations	115
4.3 Simulation systems	117
4.4 Force controlled loading and displacement controlled loading	119
4.5 Specimen thickness effect and boundary conditions	122
4.5.1 Thickness effect under periodic boundary conditions	122
4.5.2 Emission of non standard dislocations induced by periodic boundary conditions .	124
4.5.3 Thickness effect without boundary conditions (Nano thin foil)	128
4.5.4 Section conclusions	129
4.6 Crack propagation mechanisms	130
4.6.1 Crack propagation in the (100) box	130
4.6.2 Crack propagation in the (714) box	132
4.7 Temperature effect on the crack propagation	136
4.8 Comments about the influence of the crack plane orientation on the crack propagation rate	136
4.9 Chapter conclusions and discussions	138
CHAPTER 5. SUMMARY, CONCLUSIONS, AND PERSPECTIVES	140
References	144
Appendix	154
Publications	156

CHAPTER 1.

INTRODUCTION

1.1 Industrial context

Besides corrosion, from which it may be dependent, fatigue of metals and alloys is a well-known problem because it is estimated that 80% of metal fractures are caused by fatigue [Cotterell 2010; Suresh 1998; François et al. 2013]. Fatigue of metals is of concern for all metallic structures which are subjected to cyclic stresses as in transportations (railways, trains, airplanes, cars, bicycles) and for machines in industrial plants. In the field of nuclear reactor components, fatigue is also one of the most severe aging factors. The effective management of fatigue is important for the continued safe and reliable operation of plant components during present, long-term and next-generation operations.

The pressurized water reactors (PWRs) constitute a large majority of nuclear power plants in France. In a typical design concept of a commercial PWR, as shown in Fig.I.1, the core inside the reactor vessel produces heat. Pressurized water in the primary coolant loop carries the heat to the steam generator. Inside the steam generator, heat from the primary coolant loop vaporizes the water in a secondary loop, steam is produced. The steamline directs the steam to the main turbine, causing it to turn the turbine generator, which produces electricity.

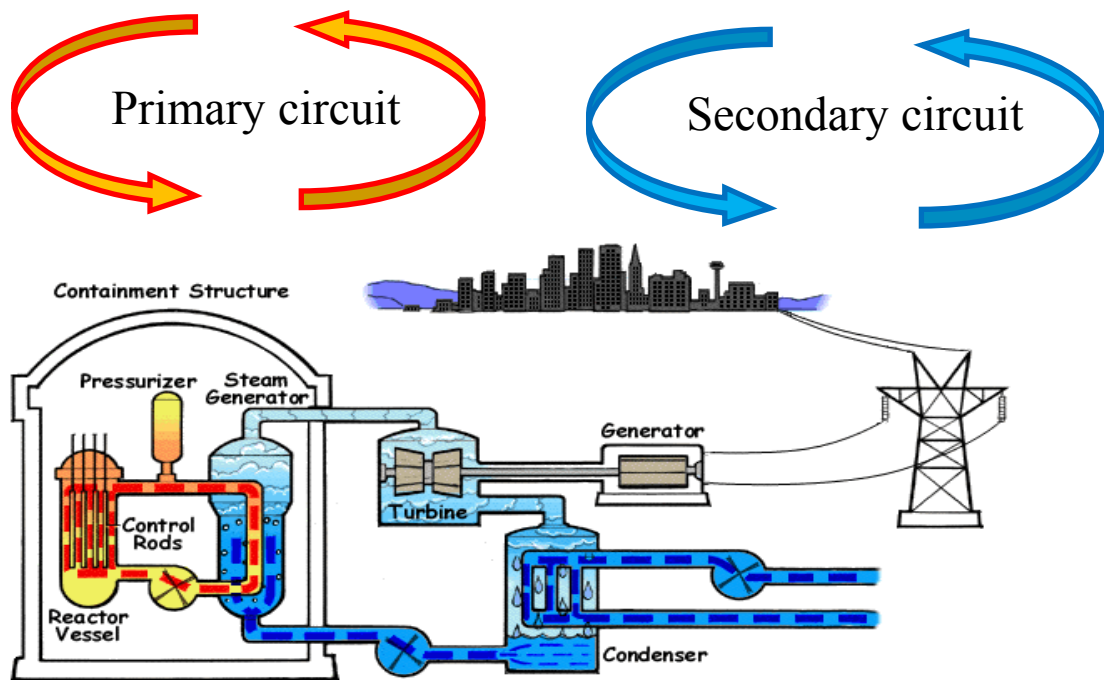


Fig .I.1 pressurized water reactor in a nuclear power plant

For this type of nuclear reactor, fatigue damage may be detrimental in the secondary loop. The origin of this fatigue could be thermal fluctuations, vibrations, or due to the stop and restarting operations. Materials of the steam generator and pipes in the secondary loop are made in fcc (face centred cubic) structure austenitic stainless steels or nickel-based alloys. A fair understanding of the fatigue mechanisms of these alloys could help to better predict the lifetime of those components.

The objective of this Ph.D. work is to analyse the mechanisms of mechanical fatigue, crack initiation and propagation in fcc metals, in order to have a better understanding of the surface relief evolution, the crack initiation and propagation, in inert environment and in oxygen environment.

In the first chapter, the background concerning fracture and fatigue, dislocations, crack initiation, and computer simulations are delivered.

In the second chapter, mechanisms of surface evolution are investigated at the atomic level in inert environment.

In the third chapter, we focus on the oxygen effect on the surface relief evolution.

In the fourth chapter, simulations are carried out on crack propagation mechanisms in inert environment.

Conclusions and perspectives are given in the last chapter.

1.2 Basic concepts of fracture mechanics and fatigue

Fracture is the separation of an object or material into two or more pieces under the action of stress, at temperatures below the melting point. Two main steps in failure analysis are the identification of the failure mode and the identification of failure mechanisms. The failure mode describes the way in which the failure happens, such as ductile and brittle fracture under monotonous loading, fatigue, creep, thermal shock or relaxation, radiation damage etc. Failure mechanism is the actual physical defect or event that causes the failure mode to occur. For example, physical, chemical, mechanical or other processes that lead to failure are called failure mechanisms.

The two typical mechanical failure modes, viz. ductile and brittle fractures, are defined depending on the ability to undergo plastic deformation before fracture.

1.2.1 Ductile and fragile fracture

In ductile fracture, extensive plastic deformation takes place ahead of a crack. The cracks propagate slowly and a large amount of energy is absorbed before fracture. The crack is 'stable': it usually does not extend unless an increased stress is applied. A rough surface is left behind the crack (Fig.I.2). This type of fracture takes place in most metals, except at very low temperatures. Many ductile metals, especially materials with high purity, can sustain very large strains, up to 50–100% or even more, before fracture under favourable loading environmental conditions.

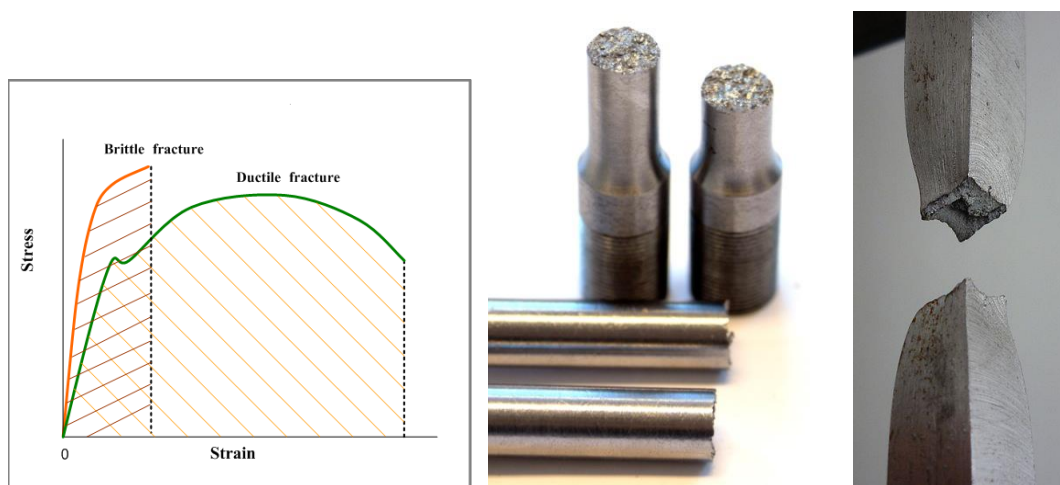


Fig.I.2 Left: Stress-strain curves for brittle and ductile fractures. The shaded area shows the absorbed energy. Middle: brittle fracture surfaces. Right: ductile fracture of a specimen by necking.

In brittle fracture, relatively low plastic deformation takes place and little energy is absorbed before fracture (Fig.I.2). The fracture can occur by cleavage (breaking of atomic bonds along specific crystallographic planes) in crystalline materials. The crack is ‘unstable’ and propagates rapidly without increase in applied stress. This type of fracture usually takes place in metals at very low temperatures, ceramics and glasses.

The materials in which ductile fracture dominates are called ductile materials. Similarly, brittle materials are the ones that are subjected to brittle fracture. As temperature decreases, a ductile material can become brittle (ductile-to-brittle transition) and vice-versa. Fcc metals remain ductile down to very low temperatures with respect to room temperature. Alloying usually increases the ductile-to-brittle transition temperature. Ceramics are brittle at room temperature and may become ductile only at very high temperature and under high pressure, although there are exceptions to this rule. The ductile-to-brittle transition can be measured by impact testing: the impact energy needed for fracture drops suddenly over a relatively narrow temperature range which is the temperature of the ductile-to-brittle transition.

In this work, ductile fcc metals are investigated, at different temperatures.

1.2.2 A brief history of fatigue

Fatigue is a fracture mode. As understood by materials scientists, it is a process in which damage accumulates due to the cyclic application of loads that may be well below the yield point. As a simple example, we are not able to break a simple clip by applying a constant force by hand, but if we apply a repetitive force back and forth, sooner or later the clip will break. Fatigue has been a problem since the earliest days of industrial revolution. The first study of metal fatigue was conducted by a German mining engineer, Wilhelm August Julius Albert (1787-1846), who performed cyclic loading tests on iron mine-hoist chains around 1829. Since then, significant progress has been made in the study of fatigue [Cotterell 2010; Suresh 1998; Krupp 2007; Schijve 2009; François et al. 2013]. The first detailed researches into fatigue were initiated after the 1842 Versailles-Paris railway accident at Meudon-Bellevue, which killed between 52 and 200 people [Smith 1990]. An early explanation for fatigue was the ‘crystallization theory’, which postulated that the cause of fatigue failure in materials resulted from microstructural crystallization. This explanation which now sounds very odd to us was due to the very fine and smooth appearance of fatigue cracks. It remained

unchallenged for several decades until the work of [Ewing and Humfrey 1903] showed the development of slip bands and subsequent fatigue cracks in polycrystalline materials (see Fig .I.3). With the invention of electron microscopes, considerable progress has been made in developing a detailed understanding of substructural and microstructural changes induced by cyclic loadings.

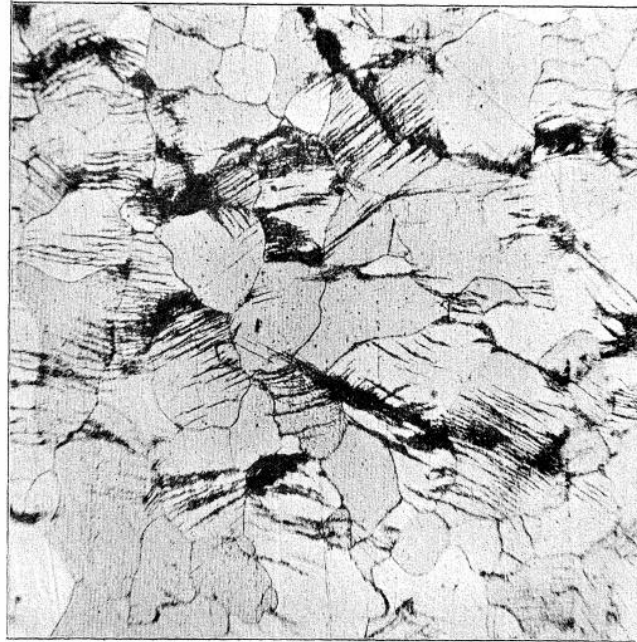


Fig.I.3. Development of slip bands and appearance of fatigue cracks in Swedish iron after 60,000 reversals of a stress of 14.3 tons per sq. inch. From [Ewing and Humfrey 1903].

1.2.3 Fatigue S-N curve and endurance limit

Before microstructural evolution under fatigue was investigated, empirical means of quantifying the fatigue process had been developed. An important concept, associated to the name of August Wöhler (1819-1914), is the S-N diagram (Fig.I.4, left image), for which a constant cyclic stress amplitude S is repetitively applied to a specimen until it fails, after a number N of loading cycles. The fatigue life diagram can also be presented in the form of a Manson-Coffin plot by transforming the stress amplitude to plastic strain amplitude (Sam Manson, 1953, and Louis Coffin, Jr., 1954, independently). The ‘S(N)’ value flattens out towards a value traditionally called fatigue limit or endurance limit σ_e . For applied stresses below that limit, failure is assumed to never occur. Now, ‘never’ can never be never. Traditional S-N curves were established for a lifetime of about 10^6 cycles. One now knows

that for much higher number of cycles, metals are eventually found to fail for some S values which are lower than σ_e . [Bathias and Paris 2005] and [Mughrabi 2006] proposed that fatigue life diagrams may exhibit a second lower fatigue limit in the form of so-called step-wise or duplex or, more generally, multi-stage fatigue life diagrams. This regime for higher loading cycles is usually called high-cycle fatigue (HCF), and for number of cycles in excess of 10^8 , the regime is usually called very high cycle fatigue (VHCF) or, alternatively, gigacycle or ultrahigh-cycle fatigue. Such a diagram which is valid for ductile materials without inclusion is shown in Fig.I.4, right image. The stage II corresponds to the conventional fatigue limit, the stage IV is the fatigue limit for VHCF regime; stage III is the transition from stage II to stage IV. However, the existence of stage IV still needs further experimental confirmations.

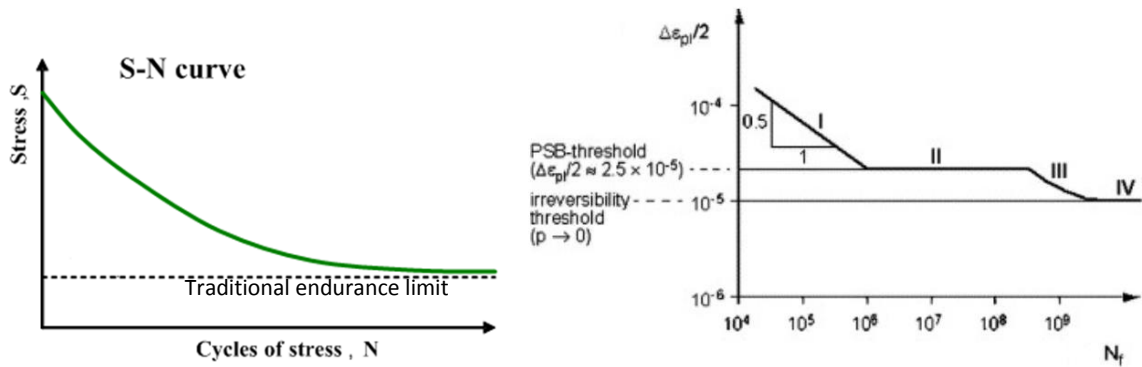


Fig.I.4. Left: Typical fatigue S-N curve with the conventional fatigue limit.

Right: a Manson-Coffin fatigue curve with the conventional fatigue limit (stage II) and a VHCF regime fatigue limit (stage IV). Numerical values apply to copper. From [Mughrabi 1999; Mughrabi 2006]. Further details about PSB or irreversibility are mentioned in the cited articles and in the section 2.1.

For some materials such as ferrous alloys and titanium alloys, a distinct fatigue limit exists. For some other materials such as some aluminium alloys, no endurance limit seems to exist and engineers deduce from the planned lifetime of the structure the compatible load accounting for the S-N curve.

During fatigue tests, a large scattering of lifetime is observed [Stanzl-Tschegg and Schönbauer 2007; Stanzl-Tschegg and Schönbauer 2010; Phung et al. 2014] which makes prediction very difficult (see Fig.I.5). Several explanations to this scatter are possible: the nature of each specimen, orientation of grains, existence of inclusions, misalignment of the loading axis from one specimen to the other one, etc. An investigation into the microstructural

mechanisms is important in order to better predict lifetime and help to improve our understanding of fatigue damage, whence this work.

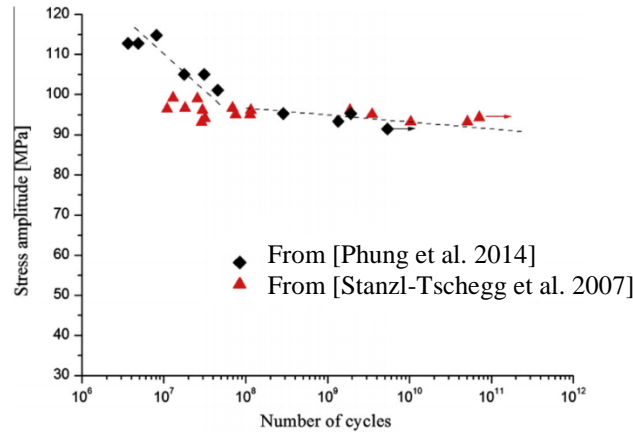


Fig.I.5. S-N curve of polycrystalline pure copper obtained from ultrasonic fatigue tests at 20 kHz, showing scattering of lifetime during experimental fatigue tests. From [Phung et al. 2014].

1.2.4 Fatigue loading and fracture modes

The tension-compression loading is the most applied loading in fatigue tests. This kind of loading can be characterized by several parameters such as σ_{\min} , σ_{\max} , the mean stress, σ_m , and the variation $\Delta\sigma$, as shown in Fig. I.6. The stress ratio R or R_σ , is the ratio between the lowest and highest stresses: $R_\sigma = \sigma_{\min}/\sigma_{\max}$. A fully reversed so-called ‘alternated loading’ corresponds to $R_\sigma = -1$. A so called ‘repeated loading’ correspond to $R_\sigma = 0$. Cyclic loading with $R_\sigma = 0.1$ is often used in aircraft component testing and corresponds to a tension-tension cycle in which $\sigma_{\min} = 0.1\sigma_{\max}$. This is also used for thin specimen to avoid buckling during compression.

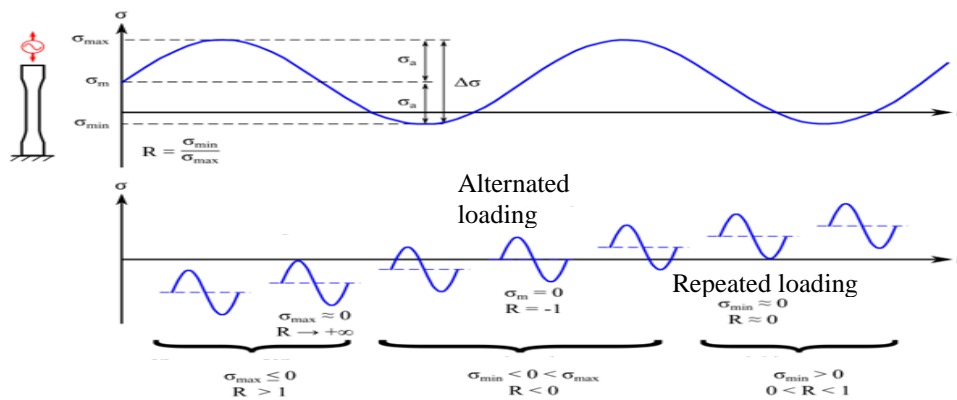


Fig.I.6. Definition of cyclic stress loading (top) and of different types of fatigue stress loadings (bottom).

Two essential stages play a role during fatigue: crack initiation and crack propagation. There are three basic separation modes corresponding to different slip displacements.

Mode I is the tensile opening mode in which the crack lips separate in a direction normal to the crack plane.

Mode II is the in-plane sliding mode in which the crack lips are mutually sheared in a direction normal to the crack front.

Mode III is the tearing or anti-plane shear mode in which the crack lips are sheared parallelly to the crack front.

Crack initiation takes place first; it is followed by propagation which finally may lead to fracture. The manner through which the crack propagates through the material gives great insight into the mode of fracture. The crack lip displacements in modes II and III find an analogy to the motion of edge dislocations and screw dislocations, respectively. The basic background of dislocations will be presented in Section I.4.

Mode I and mixed mode I+II displacements will be studied in chapter IV.

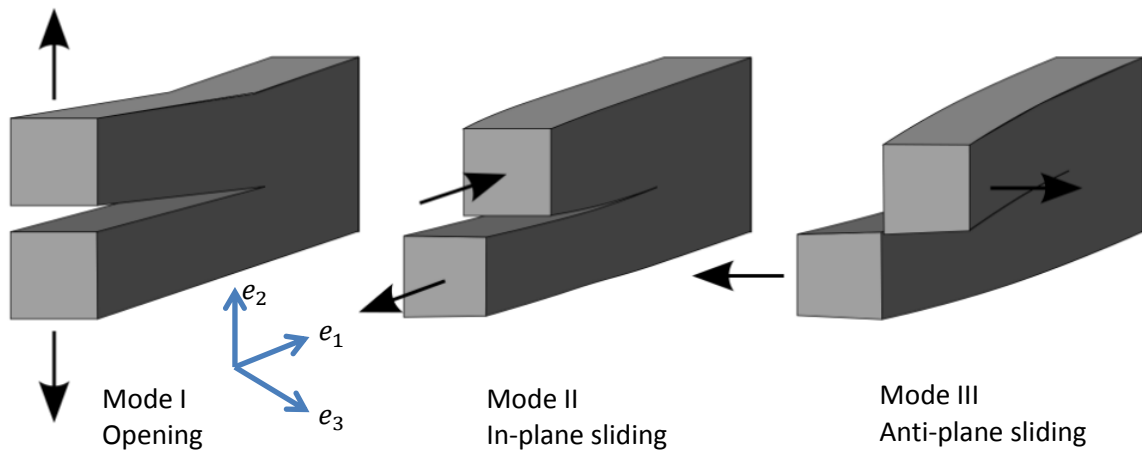


Fig. I.7 Fracture crack separation modes

1.2.5 The stress intensity factor K

The stress intensity factor, K , allows a quantitative evaluation of the stress state near the crack tip caused by a remote load or residual stresses, based on the assumption of linear elastic fracture mechanics. The magnitude of K depends on the sample geometry, the size and location of the crack, and the magnitude and the modal distribution of loads on the material. An extensive background concerning the stress intensity factor theory is delivered in the “stress intensity handbook” [Murakami 1987], where numerous formulae providing K values

are given according to different geometries, cracks and loads (see appendix). The stress intensity factor can be described using the general formula:

$$K_i = \sigma_i \beta_i \sqrt{\pi a}$$

where the β_i factor is used to relate geometrical and loading features to the stress intensity factors. σ_i is the value of the remote stress and a is one-half of the crack length. $K_i = K_I, K_{II}, K_{III}$ and $\sigma_i = \sigma_{22}, \sigma_{12}, \sigma_{23}$ depending on mode I, mode II and mode III loading, respectively.

Different subscripts are used to designate the stress intensity factor for the three different fracture modes. The stress intensity factor for mode I is denoted as K_I which applies to the crack opening mode. The mode II stress intensity factor, K_{II} , applies to the crack sliding mode. The mode III stress intensity factor, K_{III} , applies to the tearing mode. Mode I and II lead to plane strain field within a thick body, plane stress field in a thin plate. Mode III is anti-planar; it is the simplest as the displacement has one component only everywhere. This is similar to a screw dislocation. Note that mode II is similar to the glide of an edge dislocation and mode I to its climb.

Using this stress intensity factor related to a far-field loading, the close-field stress field can be calculated in an arbitrary body with an arbitrary crack under an arbitrary loading. At a position (r, θ) ahead of the crack tip (polar coordinates, see Fig. I.8), the tensor stress field in an isotropic linear elastic solid can be developed as:

$$\sigma_{ij}(r, \theta) = \frac{K}{\sqrt{2\pi r}} f_{ij}(\theta) + \text{other terms}$$

where the function $f_{ij}(\theta)$ varies with the load and geometry, $\sigma_{ii}(r, \theta)$ is denoted as $\sigma_i(r, \theta)$ and $\sigma_{ij}(r, \theta)$ is denoted as $\tau_{ij}(r, \theta)$. Other terms should be considered for a full description of the stress field. Among these other terms, a very important one is the so-called T stress term [Irwin 1958].

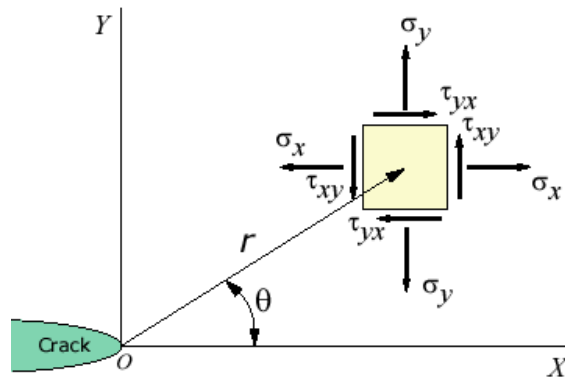


Fig. I.8 Close-field stress tensor at a point of polar coordinates (r, θ) ahead of the crack tip

The toughness, K_{IC} , describes the ability of a material to absorb energy and plastically deform without fracturing. It is defined as the material resistance to fracture when stressed. If the K_{IC} value is exceeded, fracture will occur.

This stress intensity concept is based on the use of linear elastic stress analysis. Plastic deformation typically occurs at high stresses and the linear elastic solution is no longer applicable close to the crack tip. However, if the crack-tip plastic zone is small, it can be assumed that the stress distribution near the crack but outside the small plastic zone is still given by the above relationship.

1.3 Fatigue crack initiation and propagation

1.3.1 Different stages of crack initiation and propagation

It is generally agreed that in ductile metals, fatigue damage usually occurs at the surface and then propagates into the bulk. Fatigue failure proceeds in three distinct stages:

- Stage I: Crack initiation usually starts at surface discontinuity such as a notch, which acts as a stress riser. In the absence of initial surface defects, crack initiation may occur due to the formation of persistent slip bands which are described in Chapter II. The initial crack propagates parallel to the slip band planes which are $\{111\}$ planes. The crack propagation rate during stage I is very low [Sauzay and Liu 2014]. During a tension-compression test, cracks are parallel to planes oriented at $\pm 45^\circ$ with respect to the principal stress direction as illustrated schematically in Figure I.9. The crack propagates that way until it is decelerated by a microstructural barrier, such as a grain boundary or an inclusion, which cannot accommodate easily the initial crack growth direction.

- Stage II: As the stress intensity factor K increases as a consequence of crack growth even at the same peak and stress amplitude, activation of several slip systems occurs close to the crack tip, initiating stage II. An important characteristic of stage II is the presence of surface ripples known as “striations,” (Fig.I.10) which are visible with the help of a scanning electron microscope. Not all engineering materials exhibit striations. They are clearly observed in pure metals and many ductile alloys such as aluminium. The most accepted mechanism for the formation of striations on the fatigue fracture surface of ductile metals is

the successive blunting and re-sharpening of the crack tip which will be described and discussed in Chapter IV.

- Stage III: Finally, stage III is related to unstable crack growth when K_{\max} approaches K_{IC} , the fatigue cracks become so long that the remaining cross sections can no longer bear the applied load. Sudden failure occurs, often by necking.

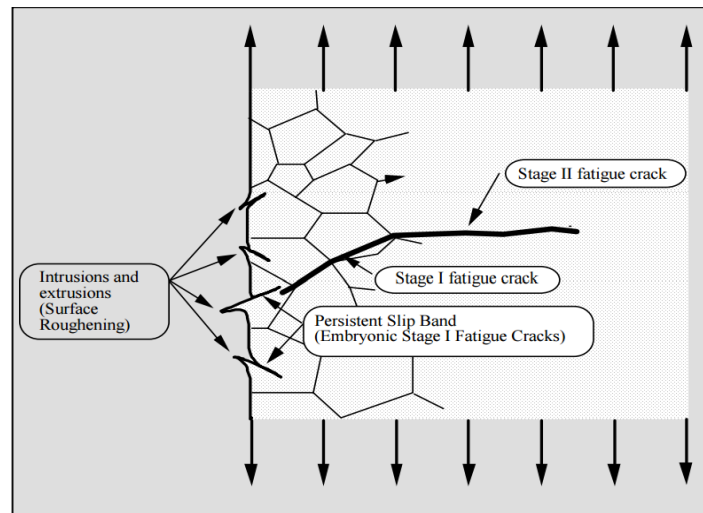


Fig. I.9. Definition of Stage I initiation and stage II propagation

Macroscopically, the fatigue fracture surface can be divided into two distinct regions, as shown by Fig. I.10. The first region corresponds to the stable fatigue crack growth. The other region corresponds to the final fracture and presents an irregular aspect. In this region, the fracture can be either brittle or ductile, depending on the mechanical properties of the material, dimensions, temperature and loading conditions.

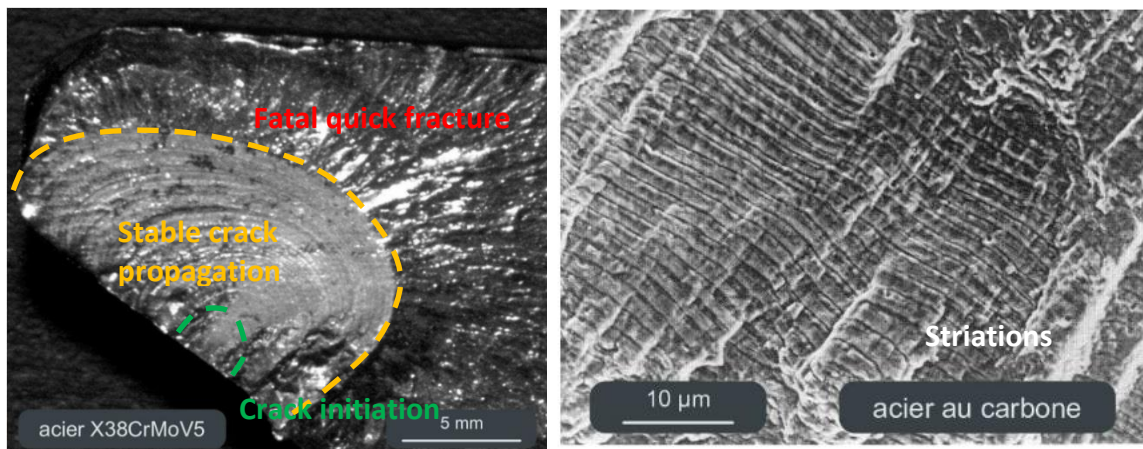


Fig. I.10. Left: a fracture surface of a steel showing the three stages of crack initiation, stable propagation, and final propagation. Right: striations during stable propagation. From [Lours 2016]

Microscopically, the mechanisms of cyclic plasticity are based on the glide of dislocations and its irreversibility. Over a number of cycles, intrusions and extrusions are generated at the free surface which leads to gradual roughening of the surface [Essmann et al. 1981; Differt et al. 1986; Polák and Sauzay 2009]. These intrusions and extrusions are sites of stress concentrations at which micro cracks can be produced. The required background in dislocation concepts are delivered in section 1.4.

1.3.2 The fatigue propagation rate da/dN

The rate of fatigue crack propagation is determined by subjecting fatigue cracked specimens to constant-amplitude (ΔK) cyclic loading. The crack growth rate da/dN is usually correlated with the cyclic variation in the stress intensity factor: $da/dN = C (\Delta K)^m$ where $\Delta K = K_{\max} - K_{\min}$, is the stress intensity factor range during the cycle, and C and m are parameters that depend the material, environment, frequency, temperature and stress ratio. This is known as the “Paris law” (Paul C. Paris, [Paris et al. 1961; Paris and Erdogan 1963]) and leads to plots similar to the one shown in Fig. I.11.

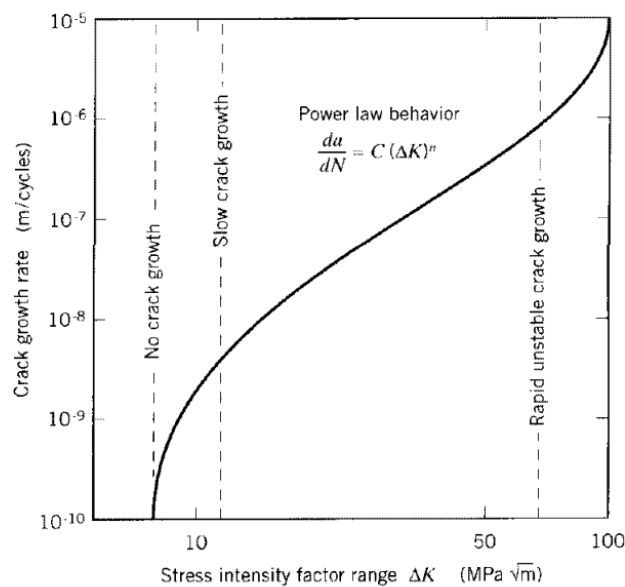


Fig. I.11. The Paris Law for fatigue crack growth rate of long cracks

1.4 Dislocations

In materials science, by definition, a dislocation is a crystallographic line defect within a crystal structure. On top of the elements recalled in the following sections, the reader is referred to the following books on dislocations: [Read 1953; Fisher et al. Eds. 1957; Cottrell 1964; Friedel 1963; Weertman and Weertman 1964; Hull and Bacon 2011; Nabarro 1967; Hirth and Lothe 1992].

1.4.1 General presentation of edge and screw dislocations and their motions

There are two basic types of dislocations: edge dislocations and screw dislocations. Mixed dislocations are intermediate between these. Dislocations can be perfect, defined with respect to the crystalline lattice or partial. This notion will be illustrated later on, with Figures I.14 and I.15.

An edge dislocation is a defect where an extra half-plane (see Fig.I.12) or several extra-planes (see Fig.I.15) of atoms is introduced mid-way through the crystal. The crystalline lattice distortion is serious where the extra half plane ends. This corresponds to what is called the dislocation line (line CD in Fig.1.12(a)) or dislocation core (cylinder of small, arbitrary radius surrounding the CD line). The atoms outside the dislocation core are only elastically disturbed. An important definition of a dislocation is given in terms of its Burgers circuit. A Burgers circuit in a crystal containing a dislocation is an atom-to-atom path which forms a closed loop path as illustrated in Fig.1.12(b). If the same atom-to-atom sequence is made in a perfect crystal without dislocation, the circuit does not close Fig.1.12(c). This means that the first circuit, Fig.1.12(b), encloses a dislocation. The vector required to complete the circuit in the perfect crystal Fig.1.12(c), is called the Burgers vector of the dislocation. For an edge dislocation, the Burgers vector is normal to the line of the dislocation.

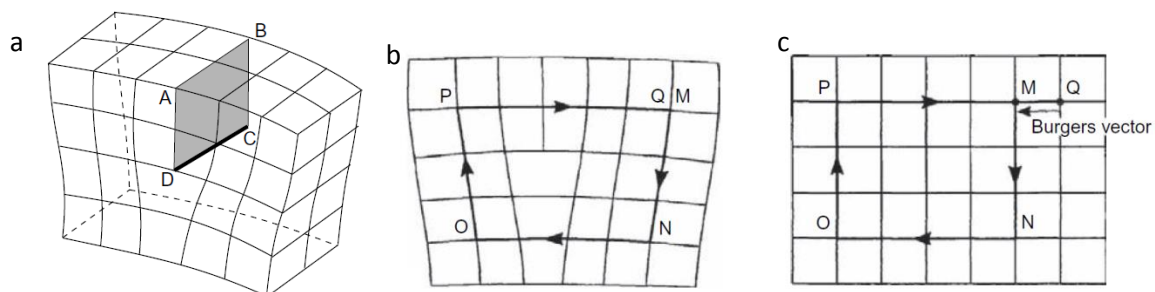


Fig. I.12 An edge dislocation (a) and the Burgers circuit (b and c). From Hull and Bacon (2011)

When a large enough shear stress is applied from one side of the crystal structure, the edge dislocation glides: the ‘extra plane’ passes through planes of atoms, breaking and producing new bonds (see Fig.I.13), until it reaches a free surface (Fig.I.13) or another extended defect. A surface step is created when the dislocation comes out of a free surface. In the first part of this work, edge dislocations will be produced by inserting extra half planes and calculating the elastic displacements of the atoms nearby. The dislocation will be driven to the free surface under a small shear stress or because of the attractive image force. This point will be explained in details later on in this chapter. We call a ‘slip system’ the ensemble of Burgers vector, dislocation line and the slip plane.

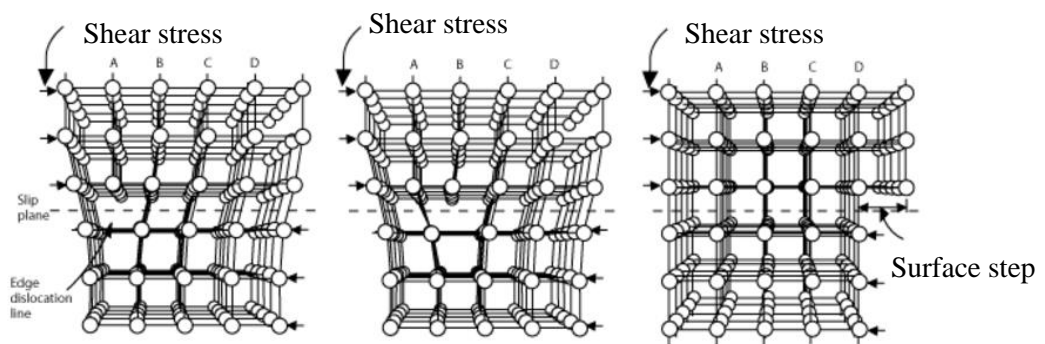


Fig. I.13. Glide of an edge dislocation and the creation of a surface step

A screw dislocation is much harder to visualize. Imagine cutting a crystal along a half-plane and slipping one-half across the other by a lattice vector, the halves fitting back together without leaving a defect except for the line defining the half plane and its surrounding core (Fig.I.14). For a screw dislocation, the Burgers vector is parallel to the line of dislocation. We refer the reader to classical textbooks for more illustrations and details. A screw dislocation in an otherwise perfect but finite crystal implies the existence of two semi-extended surface steps which will further extend if the screw dislocation moves.

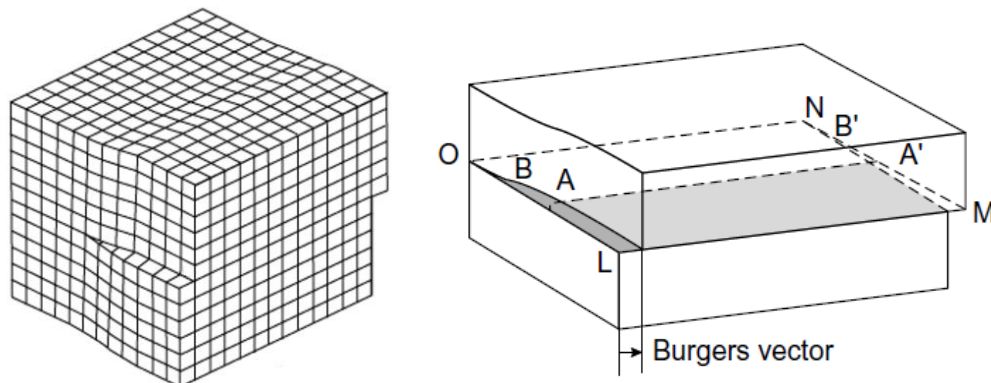


Fig. I.14. A screw dislocation, with the creation of two surface steps. The AA' line glides and reaches the BB' position.

1.4.2 More details about dislocations in fcc metals

Our work focus on fcc metals, therefore the following focuses on dislocations in fcc structures. We use the conventional cubic crystallographic referential system, usually normalising the cubic lattice parameter to 1. In fcc crystals, the smallest Burgers vector \mathbf{b} for perfect dislocations are $\frac{1}{2} \langle 110 \rangle$. The atomic $\{110\}$ planes are perpendicular to $\langle 110 \rangle$ and have a two-fold stacking sequence ABAB. The ‘extra half-plane’ for such an edge dislocation thus actually consists of two (110) atomic half planes in the ABAB sequence as shown in Fig.I.15. The dislocation core is located in a close-packed (111) type plane which is the glide plane. Dislocations glide in a (111) type close-packed plane and rarely in other planes. In reality, the two extra (110) planes do not stay immediately adjacent to each other. The dislocation separates into two dislocations which are called ‘partial dislocations’ and can be associated to shorter, partial, Burgers vectors. The original dislocation with a $\frac{1}{2} \langle 110 \rangle$ Burgers vector is called a perfect dislocation. The most important partial dislocations observed in face centred cubic metals are the so-called Shockley partials (Heidenreich and Shockley). An example of decomposition into two Shockley partials is:

$$\frac{1}{2} [110] = \frac{1}{6} [211] + \frac{1}{6} [12\bar{1}]$$

Because the elastic energy of a dislocation is proportional to b^2 , this decomposition can be considered energetically favourable (Frank’s rule, an approximate rule):

$$(b_{perfect})^2 > (b_{partial1})^2 + (b_{partial2})^2 \quad : \quad \frac{1}{2} > \frac{1}{3}$$

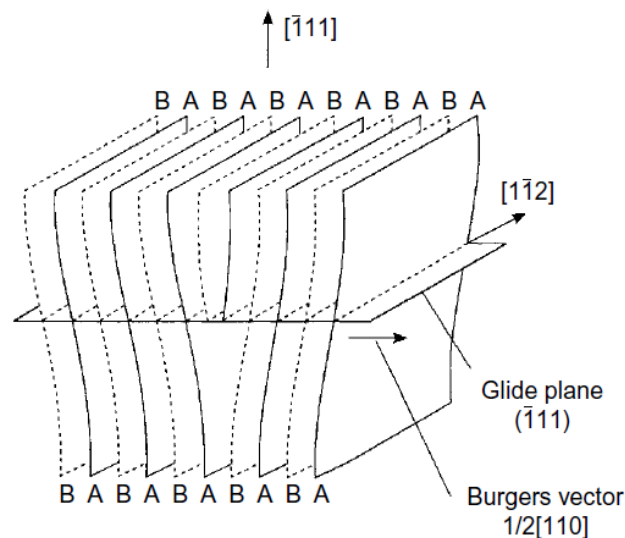


Fig. I.15 Edge dislocation with two additional half planes in fcc metals. [Seeger 1957]

Shockley partials are ‘glissile’ because the partials can glide on the considered slip plane. There are also some ‘sessile’, i.e. non glissile partials in fcc metals such as Frank partials, Hirth partials and stair-rods.

In my simulations, perfect dislocations are produced by carefully introducing two extra half planes of atoms in the metal. More precisely, a pre-adapted elastic displacement field is firstly applied to all atoms of the crystal with respect to a chosen origin, Burgers vector and line orientation. Only then are two extra atomic half planes inserted in the ‘void’ created by elastic displacement field (see Fig. I.16).

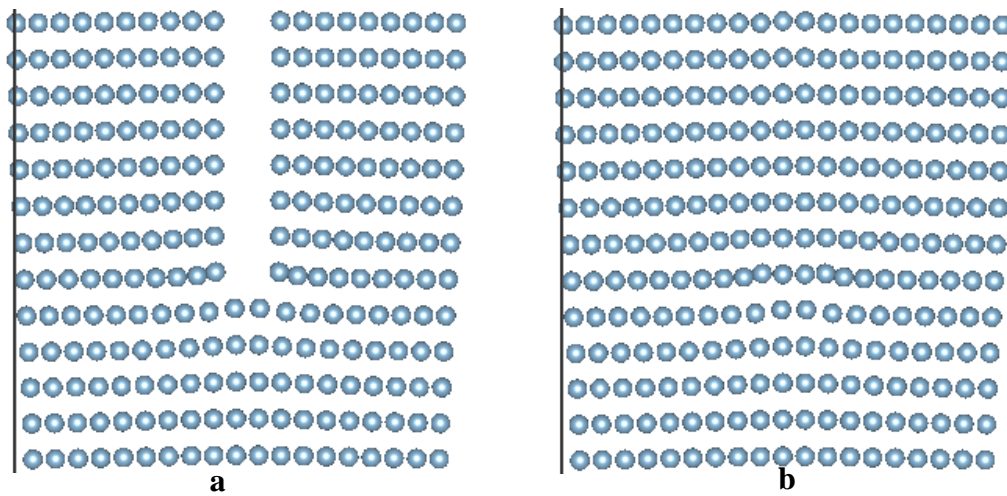


Fig. I.16. Insertion of an edge dislocation.

Left: crystal subjected to the pre-adapted elastic displacement field.

Right: introduction of an edge dislocation composed of two half planes.

The displacement field (u_x u_y) is taken from the isotropic elastic theory, derived from the stress field induced by one edge dislocation in an infinite body [Hirth and Lothe 1992]. Fig.I.17 shows a well-known representation of the stress field surrounding an edge dislocation. On the left half (a) of the picture, the stresses plotted on the elementary cube are shown around the dislocation. Since there is no stress component in the direction perpendicular to Fig.I.17, a two-dimensional representation is sufficient. On the right half (b), contours of stress isovalues are plotted for the normal component and the shear components of the stress tensor.

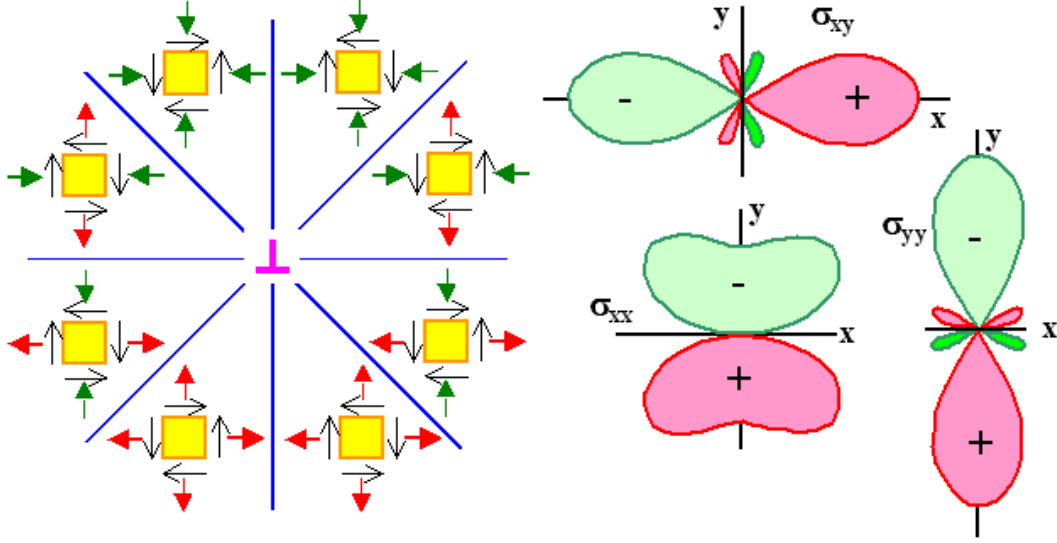


Fig.I.17 Stress field around an edge dislocation in an infinite body.

By integrating the elastic strain field, the displacement field in x direction is given below:

$$u_x = \frac{b}{2\pi} \left[\tan^{-1} \frac{y}{x} + \frac{xy}{2(1-\nu)(x^2+y^2)} \right] + C$$

The constant of integration is determined by the condition that $u_x \rightarrow 0$ as $y \rightarrow -\infty$, so

$$\begin{cases} u_x = \frac{b}{2\pi} \left[\tan^{-1} \frac{y}{x} + \frac{xy}{2(1-\nu)(x^2+y^2)} - \frac{\pi}{2} \right] & \text{if } x < 0 \\ u_x = \frac{b}{2\pi} \left[\tan^{-1} \frac{y}{x} + \frac{xy}{2(1-\nu)(x^2+y^2)} + \frac{\pi}{2} \right] & \text{if } x > 0 \end{cases}$$

Similarly, the displacement along the y direction is given below:

$$u_y = -\frac{b}{2\pi} \left[\frac{1-2\nu}{4(1-\nu)} \ln(x^2+y^2) + \frac{x^2-y^2}{4(1-\nu)(x^2+y^2)} \right]$$

Our equations about the x direction displacement are different from the ones given in Hirth and Lothe's book (both first and second editions).

During the molecular dynamics simulation, the atoms relax their positions through their mutual interactions. The solutions obtained in an infinite body are used to set the initial positions of the atoms. After time relaxation, the elastic displacement field in the finite box of interest is obtained. Similarly, the ν value used in the analytical solution corresponds to an isotropic elasticity value. But, the solution accounting for anisotropic cubic elasticity is obtained after relax. Further details are given in section I.5.

Once a perfect dislocation (made of two additional half-planes) is properly inserted, it dissociates into two Shockley partials during the molecular dynamics relaxation, confirming that the total energy of the two Shockley partials is lower than that the perfect one as previously mentioned, based on Frank's rule. Between these two partials, a ribbon of stacking-fault is formed (Fig. I.18) which corresponds to a local staking fault between (111) atomic planes. This fault is called the intrinsic stacking fault in fcc metals. These interruptions carry a certain stacking-fault energy. The width of the stacking fault ribbon is a consequence of the balance between the 'repulsive force' between two partial dislocations on the one hand and the attractive force due to the surface tension of the stacking fault ribbon on the other hand. There is thus an equilibrium distance between the two partials which is related to the intrinsic stacking-fault energy value (SFE, or ISFE). As the SFE is high the dissociation is impeded, and the distance between the two partials is small. On the contrary, as the SFE is low, the distance between the two partials is large. Table 1 gives the {111} SFE of the fcc metals that we analyse in this work.

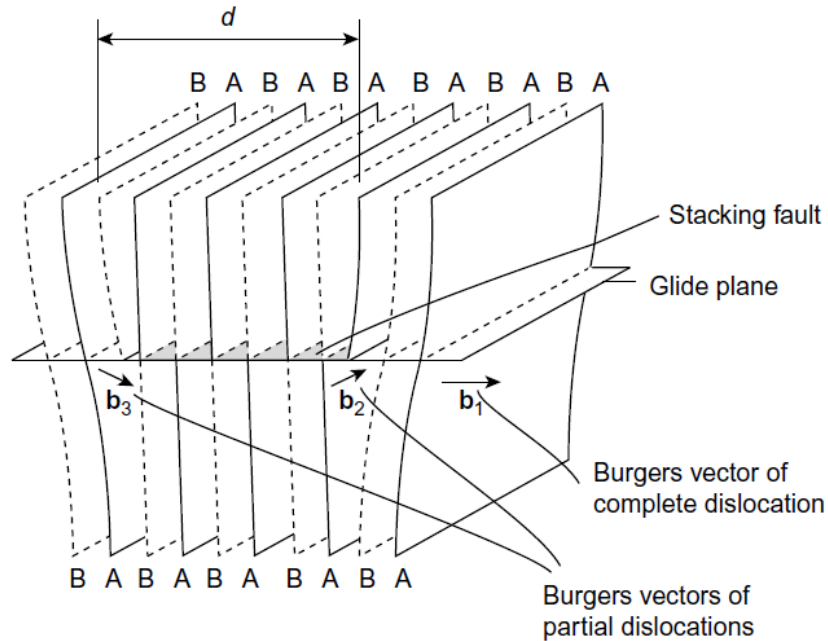


Fig. I.18 Dissociation of a b_1 perfect edge dislocation into two Shockley partials of Burgers vectors b_2 and b_3 separated by a ribbon of stacking fault (Seeger's picture 1957, p 252).

material	Ag	Ni	Cu	Al
SFE (mJ m^{-2})	15-21 ¹	120	44-78 ¹	143-200 ¹
b (10^{-10} m)	2.889	2.492	2.556	2.915
μ (GPa)	42.9	111.3	48	25.5
μb (mJ m^{-2})	12.4	27.7	12.3	7.4
SFE normalized	1.21-1.69	4.33	3.58-6.34	19.32-27.03

Table I.1: Stacking fault energies of different fcc metals. In the last line of the table, the SFE is normalized by μb (normalized SFE = SFE/ μb) to facilitate the comparison between different materials (see [Seeger 1955]). b is the Burgers vector length and μ is the experimental value of isotropic shear modulus for poly-crystals without texture. ¹ [Bernstein and Tadmor 2004], ² [Murr 1975].

In fcc metals, the densest planes are the $\{111\}$ planes which are thus the most favourable slip planes for dislocations. For a non-dissociated $1/2[\bar{1}01]$ screw dislocation slipping in a (111) plane under a given shear stress, it may happen that at a given time or location, a local change in stress direction let that screw dislocation slip in a $(1\bar{1}1)$ plane once that plane also contains the $1/2[\bar{1}01]$ Burgers vector and line screw direction. This phenomenon is called cross-slip. If the screw dislocation is relatively rapidly set back to a (111) plane, this is naturally called a double cross-slip event. Multiple cross-slips produce wavy trajectories for the screw dislocations and wavy slip lines. As illustrated in Fig. I.19, the (111) and $(1\bar{1}1)$ planes both contain the $[\bar{1}01]$ vector, so that the screw dislocation can switch from the (111) plane to the $(1\bar{1}1)$ plane. Fig. I.19(d) shows a double cross-slip. If the screw dislocation is dissociated, its partials are no longer pure screw dislocations and cross-slip is less easy, all the less if the partials are separated by a large ribbon-fault. Nevertheless, partial dislocations are always less separated for a screw dislocation than for an edge dislocation, by a factor of about 2 [Read 1953]. Cross-slip may be locally assisted by local constrictions due to the encounter of a barrier provided by a non glissile dislocation or an impenetrable obstacle (Seeger-Escaig-Friedel mechanism). Pure fcc metals with a low SFE (or SFE / (μb)) are thus less prone to cross-slip than metals with a high SFE. The latter are called ‘wavy’ materials, the former are called ‘planar’ materials [McEvily and Johnston 1967]. Aluminium, copper and nickel, are wavy materials. Let us note that for alloys the low SFE/(μb) criterion does not work in cases of short range order, see [Clément 1984].

In wavy materials, annihilation of dislocations is favoured by cross slip. This will of course induce a high irreversibility of dislocation motions. The concept of irreversibility is defined and used in details in chapter II.

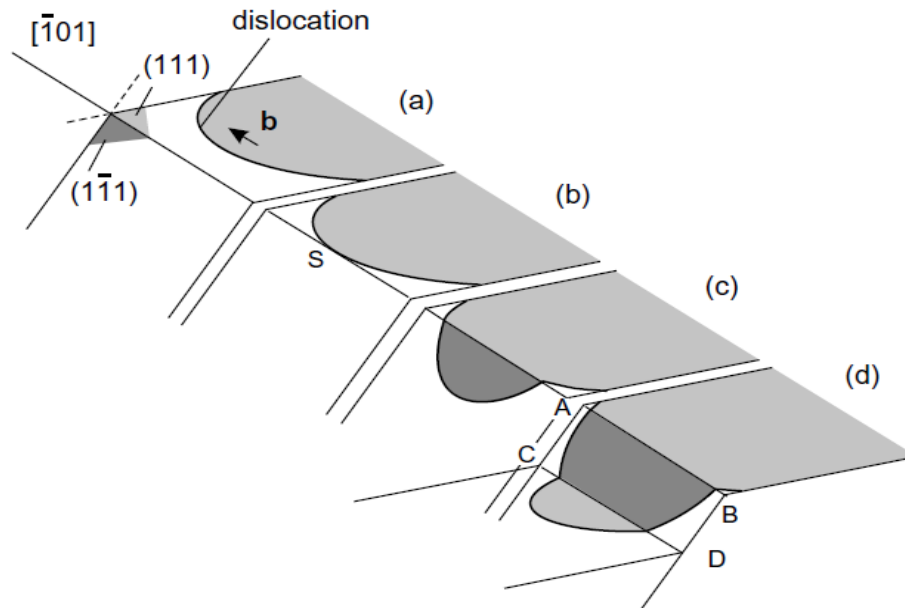


Fig. I.19. Illustration of a cross-slip (a,b,c) and a double cross-slip (d). From [Hull and Bacon 2011].

1.4.3 Image forces

Once a dislocation is close to a free surface, it can be attracted to the surface by the so called image force whose origin is explained below.

The elastic energy of a dislocation is the elastic energy associated to the elastic displacement field caused by the dislocation around itself. Beyond the free surface, where there are no atoms, there is no elastic displacement field, hence no elastic energy. Thus, the closer a dislocation is to a free surface, the smaller the elastic energy it causes in that direction. This corresponds to an attractive force towards the free surface. One can show that this force is equivalent to the force which would be exerted on the dislocation by an image dislocation with respect to the surface plane, hence the expression ‘image force.’ This image trick allows for analytical calculations in very simple cases, e.g. for an edge dislocation whose line is parallel to the surface plane. Unfortunately, however, it is not helpful for more complex geometries (beyond those considered by Jens Lothe in [Indenbom 1992]). It remains that a dislocation is attracted by a free surface. In my simulations, I sometimes intentionally put dislocations near a free surface, so that the emergence of dislocations on the surface can be observed spontaneously without applying any stress to the system.

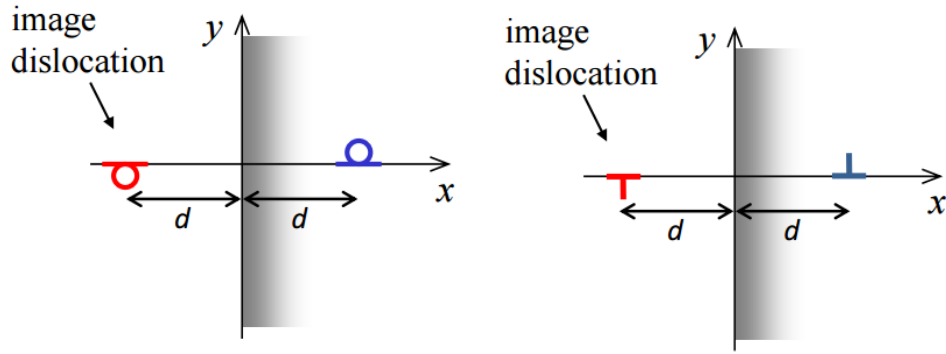


Fig. I.20. Image dislocation of a screw (left) and an edge (right) dislocation near a free crystalline surface.

1.5 Computer simulations

Computer simulation is widely used to model atom behaviour in crystals and provide information not easily accessible by experimental investigation. In this study, Molecular Dynamics (MD) simulations are carried out which allow us to follow the trajectories of atoms in real time. Basic literature on the subject includes: Allen and Tildesley 1987 and 1989, Frenkel and Smit 1996, Ciccotti, Frenkel and McDonald, 1987, Meyer and Pontikis 1991, Kirchner, Kubin and Pontikis 1995. Both homemade programs (from my PhD supervisor O. Hardouin Duparc) and the Large-scale Atomic/Molecular Massively Parallel Simulator (LAMMPS) [<http://Lammps.sandia.gov>] software are used. MD simulations with LAMMPS allow simulating atomic system up to a hundred nano-meters in size during times up to several nanoseconds (Fig. I.21).

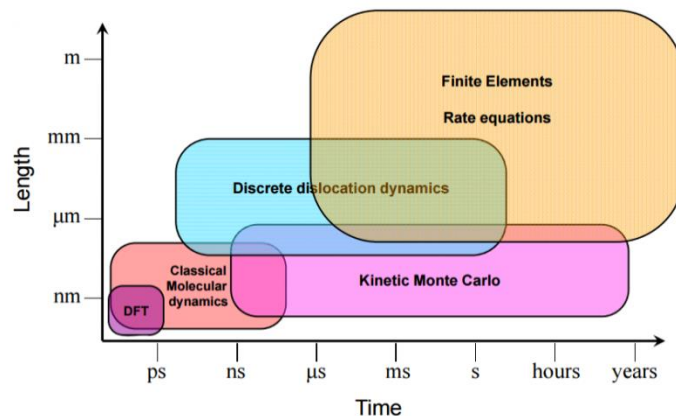


Fig. I.21 Different simulation scales and methods.

The potential energy of the model system and the forces between the atoms are computed from interatomic potentials. As forces are usually deduced from interatomic potentials, ‘Force Field’ is mainly another name for ‘interatomic potential’ (except for ab initio modelling). Such potentials for austenitic steels and nickel based alloys are still in development in 2016. Thus only pure fcc metals are investigated in this work for which reliable interatomic potentials exist. The work of [Bernard et al. 1987] shows that the mechanisms of fatigue damage under a large number of cycles in austenitic steels are rather similar with the copper ones because of the common crystallographic structure. Therefore, investigations with pure fcc metals can be useful and necessary to ensure a better understanding of mechanisms at atomic level. Furthermore, many measurement and observation results are available for copper and nickel whose fatigue mechanisms have been widely studied. These will help us to compare our simulation results with experimental data. Finally, the behaviours of both a low stacking fault energy metal, silver, and a high SFE metal, aluminium, are investigated too. The SFE of austenitic stainless steels is about 20-30 mJ/m², between the silver and copper values.

Reliable interatomic potentials are available for the four fcc materials investigated in this work: aluminium, copper, nickel and silver. The interatomic potentials mostly used for simulations in inert environment are so called Embedded Atom Model (EAM) potentials. Their empirical parameters are adjusted for prediction of material parameters such as cohesive energy, elastic constants, phonon spectra, point defect energies, surface energies and stacking fault energies, as close as possible to measured values or values derived from ab initio calculations. Some smaller scale ab-initio (DFT) simulations have thus been carried out to compare with values estimated by EAM potentials. I used the Vienna Ab initio Software Program (VASP) for these calculations, based on the density functional theory (DFT). Reference books give the required background [Martin 2008; Thijssen 1999; Thijssen 2013]. All the potentials I used give rather good estimations of the physical parameters of the investigated fcc metals. For the simulations carried out in oxygen environment, in order to simulate the chemical reactions of the oxygen molecules with the metals, such as their dissociation into oxygen atoms, I used Reactive Force Fields (ReaxFF) such as those developed by van Duin and co-workers. I also used the COMB (Charge-Optimized-Many-Body) potential which is another force field that allows the simulation of interactions between metal and oxygen.

It should be noticed that the potentials I used also reproduce accurately the unstable stacking fault energy of the metals. The unstable stacking fault energy is an influent parameter linked to the energy barrier for partial dislocation nucleation. The potentials are therefore able to reflect both dislocation nucleation and interaction phenomena. That is required for answering the irreversibility of surface slips and the crack tip behaviour. More details about EAM potentials are given in chapter 2 and some details about ReaxFF and COMB potentials are given in chapter 3.

In molecular dynamics, at a given instant of time t , the acceleration of every atom is calculated from the total force on it due to its neighbours using Newton's second law (force = mass times acceleration, $f(t)=m\gamma(t)$). The computer codes use this equation to predict the evolutions of the positions of all atoms with time. With a finite time difference algorithm such as the Verlet algorithm: $x(t + \delta t) = 2x(t) - x(t - \delta t) + \frac{f(t)}{m} \delta t^2 + o(\delta t^4)$, where δt is the molecular dynamics finite difference time-step. To maintain numerical stability and convergence, the time step δt is typically of the order of one femtosecond.

In some applications, one just wants to find the ground state atom coordinates of a system, for example, minimize the total energy to the nearest energy minimum, this is called molecular statics. In molecular statics, the kinetic energy of the atoms is scaled down to zero, and the system achieves equilibrium as the potential energy is minimized. In our simulations, we do this once an edge dislocation is inserted and the displacement field is pre-calculated and applied (see I.4.2). This process helps to relax the dislocation configuration and to make sure that all atoms are in lower energy positions before running molecular dynamics.

The typical time-step of MD simulation is from one to several femtoseconds, the number of time-steps that can be accomplished within a reasonable computer time during a PhD work for systems containing several hundreds of thousands of atoms is typically in the range 10^5 to 10^7 . As a consequence, the total simulated time is limited to the order of nanoseconds. This has consequences on the strain rates that we apply: their orders of magnitudes are much higher than the strain rates experimentally applied. Yet, extrapolations which are possible for some simulations show that the results are still valid until the order of second. In our largest simulation box, almost 2,000,000 atoms are simulated. Periodic boundary conditions are applied for most simulations. Sometimes, however, in order to allow the oblique glide along

some of the slip systems, periodic boundary conditions are relieved. In this case, some thin foil artefacts could be introduced but these artefacts can correspond to nano thin foils. Otherwise, one has artefacts due to the use of periodic boundary conditions, which do not exist in most of materials. Further assessments will be developed in chapter 4.

The OVITO [<https://ovito.org/>] software is applied in the post-processing of LAMMPS outputs. OVITO is a visualization and analysis tool which can detect point defects, dislocations, different crystallographic structures, stacking faults, etc.

CHAPTER 2.

SURFACE STEP IRREVERSIBILITY & CRACK INITIATION IN INERT ENVIRONMENT

In the first part of this PhD work, surface slip irreversibility is analysed in inert environment. In ductile metals, fatigue damage generally starts at free surfaces. Experiments demonstrate that removing the surface roughness by electro-polishing leads to an increase in total fatigue life [Suresh 1998]. Since the classical work on the fracture of metals under alternated stress by [Ewing and Humfrey 1903], when dislocations were not known for crystals, it is now accepted that the initiation of fatigue cracks at free surfaces often arises from the accumulation of unreversed slip steps. Cyclic micro-plasticity based on the glide of dislocations is one of the mechanisms responsible for the fatigue phenomena in single phase fcc metals and alloys. Irreversibility mechanisms appear to be crucial to understand fatigue microcrack initiation and propagation. Glide irreversibility can be characterized by the fraction p of irreversible plastic slip per cycle compared to the total plastic slip ($p = \gamma_{plirr} / \gamma_{pl}$) [Woods 1973; Mughrabi et al. 1979]. This slip irreversibility p amounts to zero if slip is entirely reversible, and it reaches one if slip is entirely irreversible. Hence, $0 \leq p \leq 1$. Qualitatively, short and long fatigue lives can be expected to be related to large and small values of the glide irreversibility p respectively. Experimental studies of p are usually carried out by direct measurements on surfaces. Analytical models in the literature usually estimate p based on dislocation motions in the bulk and neglect surface mechanisms. A precise description of the surface irreversibility is certainly necessary. The aim of this work is to evaluate random surface step irreversibility by atomistic analyses of surface step evolution mechanisms in order to ameliorate the bulk irreversibility models by explicitly taking into account the mechanisms of surface steps.

2.1 Literature review on experimental observations and irreversibility models

It is generally accepted that fatigue crack initiation occurs at sites of stress concentration caused by the surface relief evolution of emerging persistent slip bands (PSBs). [Cheng and Laird 1981] further found that, in copper, fatal cracks preferentially form at the PSBs with the largest local strain. The occurrence of fatigue-induced slip bands was noted for the first time in 1903 by Ewing and Humfrey. Fifty years later, [Thompson et al. 1956] showed that the slip bands are persistent in the sense that they always re-appear at the same places after repolishing-recycling sequences. These slip bands are thus called ‘persistent slip bands’ (PSBs). Since then, many efforts in the field have been dedicated to the study of the PSBs in the bulk. Studies were first mainly performed on copper crystals [Watt et al. 1968; Basinski et al. 1969; Winter 1973; Finney and Laird 1975; Finney and Laird 1982; Basinski et al. 1983], and also, more recently, nickel single and polycrystals [Mecke and Blochwitz 1982; Hollmann et al. 2000; Weidner et al. 2006; Weidner et al. 2008; Holste 2004]. When the cyclic loading amplitude is under the PSB slip threshold, the microscopic structure contains relatively few dislocations and is rather homogeneous (Fig. II.1a). When the deformation approaches the PSB threshold, instability of the microstructure induces the formation of PSBs (Fig. II.1b) which have the so-called ‘ladder structure’ [Winter 1973; Mughrabi et al. 1979]. There are plenty of edge dislocations in the dark “walls” whereas the screw dislocations glide in the ‘channels’ between the walls. Edge dislocations glide from one wall to the next one.

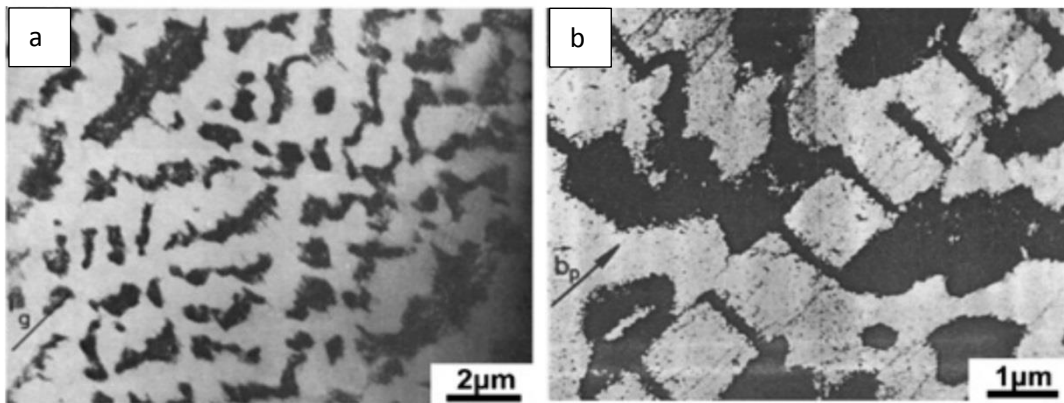


Fig. II.1 Microstructure evolution under cyclic loading in copper. a) load under the PSB slip threshold, b) load higher than PSB threshold, ladder structure of PSB. Image (a) is from [Woods 1973] and image (b) is from [Mughrabi et al. 1979] (also see fig.1 of [Winter 1973]).

The threshold amplitude for the formation of PSBs has been related in the past to the existence of a true fatigue limit [Mughrabi and Wang 1981; Mughrabi et al. 1991; Laird 1976]. In polycrystals, it has also been clarified that these thresholds represent only the condition for initiation of stage I shear micro-cracks but do not necessarily fulfill the conditions for subsequent propagation of these cracks [Mughrabi et al. 1991; Mughrabi and Stanzl-Tschegg 2007; Stanzl-Tschegg and Schönbauer 2007]. Hence, according to these studies, the true fatigue limit actually lies somewhere above the thresholds for PSB formation.

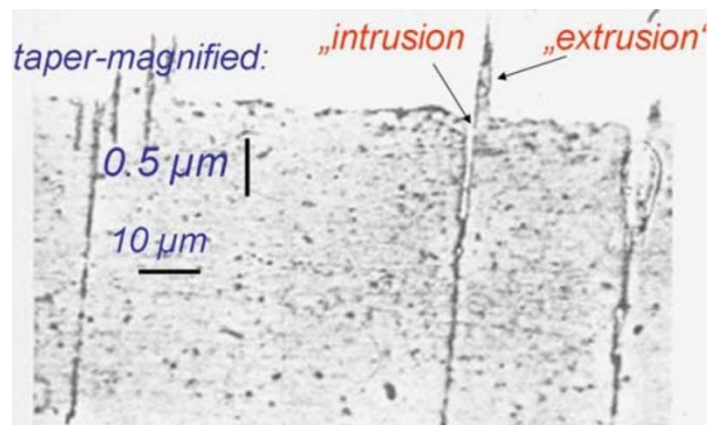


Fig. II.2. Example of optical micrograph of taper section of fatigued copper polycrystal, showing “notches and peaks” forming at the head of a slip band [Wood 1958].

In the early studies, [Wood 1958] showed with the ‘taper sectioning’ technique that the specimen surface roughens rapidly within the PSB’s, thus indicating that a considerable fraction of the cyclic slip in the PSB’s must be irreversible. Wood observed that cracks initiate in the notch-peak surface geometry formed by to-and-fro displacement. [May 1960] formulated the idea of the crack initiation as a consequence of random irreversible slip events. The experimental studies carried out by [Hull 1957] and by [Cottrell and Hull 1957] on copper single and poly crystals showed that the surface relief also developed at very low temperature down to 4.2K, indicating that the evolution of the surface relief could be a pure mechanical mechanism. Numerous models [Cottrell and Hull 1957; Mott 1958; Kennedy 1963; Watt et al. 1968; Woods 1973; Mughrabi et al. 1979; Essmann et al. 1981; Essmann 1982; Differt et al. 1986; Mughrabi 2009; Mughrabi 2010] have been proposed to interpret experimental observations.

A well-known model which describes the evolution of the surface roughness for fcc metals has been developed by Essmann, Gösele, Mughrabi and Differt (EGM or EGDM model)

[Essmann et al. 1981; Essmann 1982; Differt et al. 1986; Mughrabi 2009; Mughrabi 2010]. This model is divided into two parts which are presently introduced.

Part I of this model (EGM I) estimates the surface extrusion growth from the vacancy production induced by cyclic plasticity and possible diffusion. It is based on the cyclic saturation of vacancy concentration, which means a balance between vacancy production and annihilation. [Essmann and Mughrabi 1979; Essmann et al. 1981] showed that in copper fatigued at room temperature, two screw dislocations of opposite signs that, encounter each other will annihilate spontaneously by cross-slip, if the distance between their glide planes is smaller than the so-called screw annihilation distance $y_s \approx 50$ nm. Opposite sign edge dislocations will also annihilate when their glide planes are spaced closer than a corresponding edge annihilation distance y_e estimated to be around 1.6 nm. Rows of vacancies are produced because of this annihilation between dislocations, and the PSB area is subjected to a free dilatation as shown in Fig. II.3b. [Polák 1987; Polák 2003] has developed a related model enhancing the role of atomic diffusion and an analytical solution of coupled diffusion-plasticity has been proposed by [Polák and Sauzay 2006]. At high temperature, the vacancies diffuse towards the PSB-matrix boundaries allowing dynamic extrusion to occur, which induces an intrusion in the matrix at the boundaries of PSB (Fig. II. 3b). This mechanism can thus explain the production of both intrusions and extrusions in the PSB area. Note that intrusions may be due to vacancy agglomeration [Polák 1987; Polák 2003] and/or crack initiation [Sauzay and Liu 2014].

Part II of this model (EGM II, or DEM) first calculates the surface irreversibility factor from the mechanism of annihilation of screw and edge dislocations in the bulk of the PSBs. It then obtains numerically the random surface roughness evolution as a function of that irreversibility factor [Differt et al. 1986] (Fig. II. 3c). In copper at room temperature, a value of p about 0.6 is first found considering only screw dislocations. That value is halved when taking into account the correlation between forward and backward displacement introduced by edge dislocations deposited in the walls of the PSB, which leads to a p about 0.3.

Considering only edge dislocations, based on the model provided by [Differt et al. 1986] (see their eq.(5), also see eq.(7) in [Mughrabi 2009]), the irreversibility factor would be much smaller (<0.1), because edge dislocations do not cross slip, so that their spontaneous annihilation distance y_e is much smaller than y_s , e.g. 1.6 versus 50 nm, see previous paragraph.

Note that the total irreversibility factor of about 0.3 from the EGM model is obtained by considering 80% of screw slips and 20% of edge slips in copper PSBs at room temperature. A different estimation about the fraction of edge and screw slips are given by [Lépinoux and Kubin 1986] who estimated that the fraction of screw slips is about 50% (0.5 ± 0.15). We shall call their model the LK model.

The irreversibility factor p helps us to predict the surface relief evolution. The roughness of the surface (\bar{w}) in EGM part II is defined as mean value of the difference between the largest positive and negative displacements parallel to the effective slip vector. A equation between (\bar{w}) and the number of loading cycles (N) is given by $\bar{w}/b = f(4Np_{\text{PSB}}/\gamma_{\text{pl,PSB}}h/b)^{1/2}$, with h the thickness of a PSB (see [Differt et al. 1986], Eq.[7]).

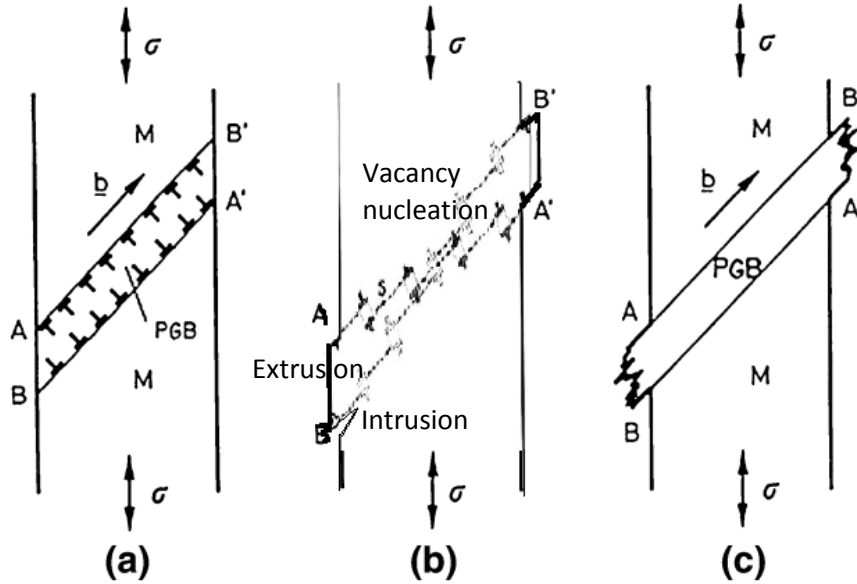


Fig. II.3. —Schematic illustration of evolution of surface relief at an emerging PSB according to the EGM/EGDM model (part I and part II), from [Mughrabi 1984]: (a) interfacial dislocations accumulate at PSB-matrix interfaces, (b) rapid formation of static extrusions by emergence of interfacial dislocations (EGM I), and (c) gradual roughening of surface of extrusions by random slip in the PSB (DEM II or EGM II).

The EGM/EGDM model only considers bulk mechanisms and do not account for surface step production and annihilation as evaluating the p value. That value is estimated under a certain number of assumptions. A more precise description of the evolution of the surface relief using slip surface irreversibility is therefore desirable.

With the development of technology, atomic force microscopy (AFM) now allows a direct evaluation of the slip irreversibility factor by the observation of individual surface steps. Different types of reversibility/irreversibility behaviours have been recently observed and schematically illustrated by [Weidner et al. 2008; Weidner et al. 2011] on well-polished polycrystalline nickel specimen surfaces with a pre-deformation up to 30,000 cycles corresponding to 60% of lifetime (Fig. II.4 and Fig. II.4). In Fig. II.4, the surface evolution is shown at the surface of an individual grain at different breakpoints in the vacuum chamber of the SEM. In that figure, P5 corresponds to the initial zero plastic deformation state. From P5, the material undergoes a loading and an unloading and the plastic deformation goes back to zero at P11. Even if the plastic strain is on average returned to zero in P11, the surface observed in P11 is different from that observed in P5. These observations illustrate the irreversibility of plastic slip at the microscopic scale. On average, the plastic irreversibility may be very low at the average grain scale. But it is high at the PSB/atomistic plane scale. Three different types of irreversibility are defined in Fig. II.5.

Type A: Complete Reversibility. The slip step which occurred during the half-cycle in tension disappears completely during the following half-cycle in compression.

Type B: Partial Irreversibility. The slip during the half-cycle in compression is partially irreversible. That means the plastic slip amplitude and/or the thickness of the activated zone is different during the half-cycle in tension and the half cycle in compression.

Type C: Complete Irreversibility. The slip during the half-cycle in compression takes place at another place within the PSB. Consequently, at another location, a second slip step occurs at the surface in the slip direction induced by the compression loading.

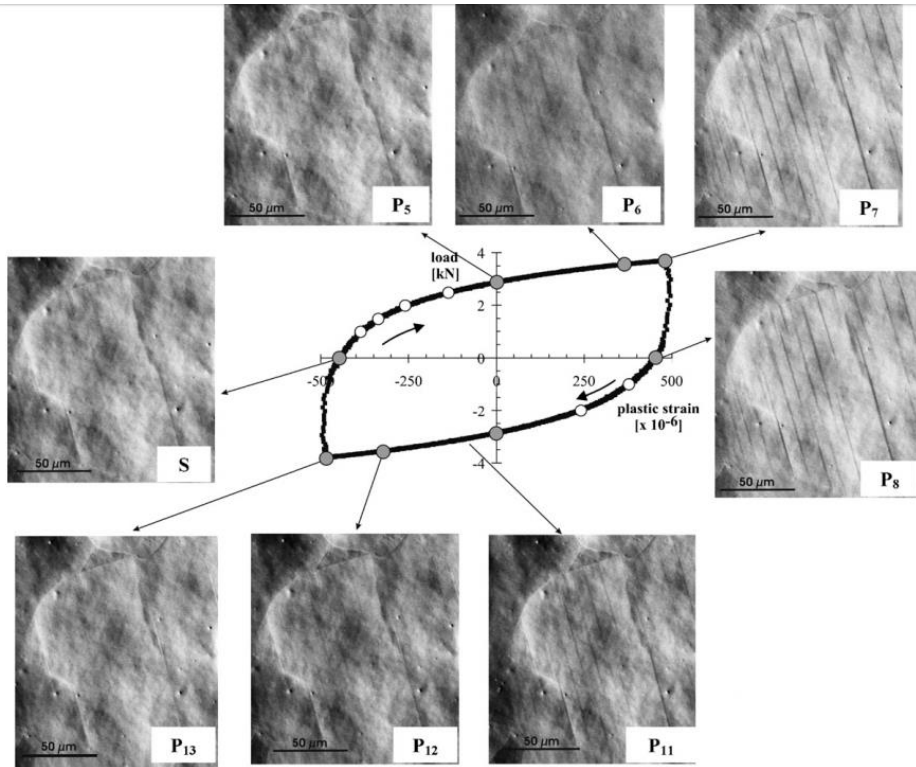


Fig. II.4. Development of slip steps on the polished surface of an individual grain during one loading cycle. From [Weidner et al. 2008].

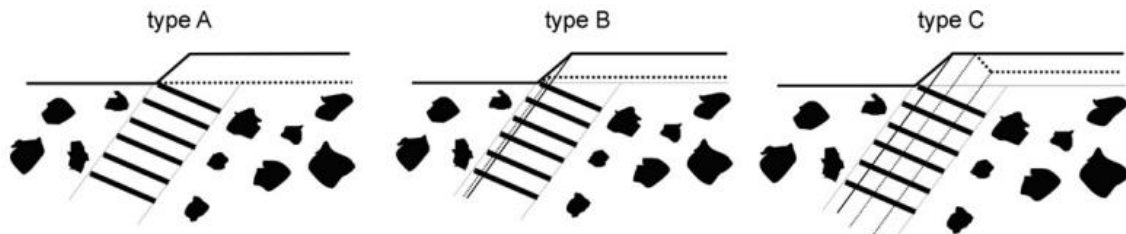


Fig. II.5. Three types of reversibility/irreversibility of slip during one full loading cycle (solid lines correspond to slip step after one half-cycle in tension, dotted lines correspond to slip step after the half-cycle in compression). Type A is completely reversible, type B is partially irreversible and type C is fully irreversible. From [Weidner et al. 2008].

By this direct measurement, the irreversibility factor in one cycle was found to be as high as 0.8 in nickel at room temperature [Weidner et al. 2011]. The limit of this experimental measurement, however, is that it provides no detail about how irreversibility occurred. Atomistic simulation is required to give a more precise description of the surface slip irreversibility mechanisms. The influence of the metal and temperature may be investigated as well.

The aim of this work is to evaluate random surface step irreversibility by molecular dynamics atomistic analyses of surface step evolution mechanisms in order to complete the EG(D)M (part II) model by explicitly taking into account the mechanics of surface steps. Edge dislocations are inserted in the bulk. They then glide to free surfaces and create surface steps. The atom movements are followed from the very first steps created at a free surface until their accumulation, and from the very first cycle to several cycles, in order to capture details about the reversible or irreversible atomic mechanisms from the very beginning. Simulations are carried out on different systems with single sign dislocations or opposite sign dislocations. They are analysed in details in sections 3 to 6. The step reconstruction phenomenon is first investigated. The irreversibility of a single surface step, the influence of opposite sign dislocations on the irreversibility and cyclic irreversibility with opposite sign dislocations are then analysed in sections 4, 5 and 6, respectively. These calculations and discussions have been partially published in [Fan et al. 2016].

As surface ‘roughening’ and micro-notch production-evolution can occur in pure materials in vacuum or in an inert environment at temperatures down to 4.2 K [McCammon and Rosenberg 1957], simulations are firstly carried out in inert environment at different temperatures. [Finney and Laird 1975], [Wang and Mughrabi 1984], [Witmer et al. 1987], [Basinski and Basinski 1992] and other authors (see [Basinski and Basinski 1992]) observed that the development of PSB surface relief is the same for fatigue in inert environment as in air. Our computations in O₂ environment detailed in chapter 3 will allow us to discuss environmental effects on relief formation with reference to experimental observations.

2.2 Simulation system and methods

Molecular dynamics (MD) simulations using semi-phenomenological potentials are carried out. Three fcc ductile metals, aluminium, copper and silver, are analysed at different temperatures. For MD simulations, the choice of the potential affects the reliability of the results; we therefore use different potentials for each metal. All the potentials are n -body embedded atom model like potentials which give fairly correct estimations of different physical properties such as elastic constants, stacking fault energies, free surface energies and thermal expansions. Most of the calculations are carried out with the [Aslanides and Pontikis

1998] potential for aluminium, and the [Hardouin Duparc et al. 2005] potentials for copper (Cu-HD) and silver. The Al-AP potential includes a term which takes into account the Friedel oscillations which are important in aluminium. These potentials are integrated within an OHD classical MD code [Hardouin Duparc et al. 2005]. Other potentials are used via the LAMMPS code, a ‘Jacobsen potential’ for aluminium [Jacobsen et al. 1987], Mishin et al. potential for copper [Mishin et al. 2001], and the Foiles et al. potentials for copper and silver [Foiles et al. 1986], in order to warrant the generality of our results. Some relevant properties obtained with these potentials are listed in Table II.1. The melting temperatures T_m of the different potentials, as well as the solid thermal expansions at room temperature have been estimated via *NPT* (isobaric, isothermal, with pressure $P=0$) simulations. As these potentials dependent T_m are not too far from the experimental T_m , and as we shall perform simulations at quite distinct temperatures, viz. almost zero K (‘4 K’), very low temperature (‘77 K’), room temperature (‘300 K’), and relatively higher or lower temperatures (viz. 200 or 400 K), we shall indicate our simulated temperatures T numerically in Kelvins rather than in reduced units (T/T_m).

The most important dislocations in fcc metals are the $\mathbf{b}=a\langle 110 \rangle/2$ edge dislocations (\mathbf{b} : Burgers vector, a the cubic lattice parameter, we use the conventional cubic crystallographic frame), because they have the smallest Burgers vector ($b=a/\sqrt{2}$), thus the smallest energy, and correspond to twelve ($\{111\}, \langle 110 \rangle$) glide systems. The model system is schematically shown in Fig. II.6. The crystallographic orientations of the three axes are x: $[-131]$, y: $[714]$ and z: $[11-2]$. The (111) slip plane is perpendicular to the x-y plane and the $[1-10]$ slip direction belongs to the x-y plane. Contraction-dilation (compression/extension) will be along the y: $[714]$ direction. This choice of orientations has several advantages: it corresponds to a large Schmid factor value equal to 0.445 (i.e. $\sim 90\%$ of the maximum Schmid value), and it makes the slip plane and the surface steps easy to visualize. The slip plane intersects the vertical free surfaces with an angle of $58.5^\circ/121.5^\circ$. Surface steps schematically shown in Fig. 9 at the vertical free surfaces are due to the getting out of dislocations. The typical dimensions of the simulated box in x, y and z are 77 (-131), 446 (714) and 24 ($11-2$) atomic planes, roughly corresponding to 9.3, 11 and 2 nm for aluminium for example. There are nearly 12,500 atoms in the box. Periodic boundary condition is used along the z-direction with a length period which is temperature adapted to take into account the thermal expansion and keep the z-pressure essentially equal to zero. The initial length along y is also thermally adapted. Upper and lower horizontal boundaries are monitored to initially apply a uniform extension or contraction in the y direction. These upper and lower monitored walls are typically 3 Å thick

(0.3 nm, which roughly corresponds to twelve (714) ‘atomic planes’, although these planes are not physically separated atomic planes as the (111) atomic planes are). Simulations occasionally performed with larger systems showed that the dimensions indicated are large enough to have a negligible influence on the presented results. The {113} surface has a lower atomic density than the {110} surface, viz. ~ 1.206 and ~ 1.414 (at/ a^2) respectively (the most compact {111} surface has ~ 2.309 (at/ a^2)). Yet these atomic densities are purely bidimensional and neglect the depth dimension. Atoms at a {113} surface actually have 7 first neighbours, 10 neighbours up to the second ones and 24 up to the third neighbours, very similarly to the case of atoms at a {110} surface, 7, 11 and 25 respectively, to be compared to the 12, 18 and 42 figures for bulk atoms. This probably explains why the {113} and {110} surfaces have very similar energies (Table II.1). The temperature of the Burton-Cabrera-Frank roughening transition (believed to be a Kosterlitz-Thouless like transition) is, for large systems, about $0.5T_m$ for the {113} surface and $0.75T_m$ for the {110} surface [Salanon et al. 1988]. The formation of Frenkel defects with adatoms free for surface diffusion may occur before, during long enough MD runs.

Table II.1: Some physical characteristics of aluminium, copper and silver, as reproduced by the potentials used in this work, versus experimental or ab initio values. Lattice parameter a_0 at 0K, linear thermal expansion coefficient at room temperature α , melting temperature T_m . The potential melting temperatures have been estimated with zero pressure MD or Monte Carlo Metropolis simulations. Elastic constants C_{11} , C_{12} and C_{44} , shear anisotropy ratio $A = C_{44}/C'$ (with $C' = (C_{11}-C_{12})/2$), stacking-fault energies, intrinsic γ_i and unstable γ_{us} , (corresponding to a $\langle 112 \rangle/10$ rigid displacement between two rigid blocks). $\gamma(111)$, $\gamma(110)$ and $\gamma(113)$ are the $\{111\}$, $\{110\}$ and $\{113\}$ surface energies respectively. The ab initio values for the surface energies have been calculated with the density functional theory VASPTM code [Kresse and Furthmüller 1996] using the GGA-PBE exchange and correlation functional within the PAW method with 3, 11 and 11 explicit valence electrons for Al, Cu and Ag respectively. Units: a_0 is in Angströms (1 Å=0.1 nm); α is times $10^{-5}K^{-1}$; The elastic constants are in GPa. The γ values are in mJ/m². T_m is in Kelvins.

	Al-AP	Al-J	Al	Cu-HD	Cu-M	Cu-F	Cu	Ag-HD	Ag-F	Ag
a_0	4.022	3.99	4.05 ¹	3.615	3.615	3.615	3.61 ⁵	4.0862	4.09	4.08 ¹
α	2.3		2.4 ²	1.4	≈ 1.6		1.6 ⁴	2.0		1.8
T_m	~ 850	~ 1050	933.3	~ 1400	~ 1300	~ 1250	1358	~ 1200	~ 1400	1235
C_{11}	116.5	76*	106.8 ³	168.8	169.9	167	166.1 ⁶	128.2	129	124 ¹
C_{12}	60.9	30*	60.4 ³	128.3	122.6	124	119.9 ⁶	98.3	91	93.7 ¹
C_{44}	29.7	28*	28.3 ³	63.4	76.2	76	75.6 ⁶	42.9	57	46.1 ¹
A	1.07	1.22	1.22 ³	3.13	3.22	3.53	3.27 ⁶	2.87	3.00	3.04
γ_i	148		176 \pm 33 ⁴	42	44		61 \pm 17 ⁴	10		$\sim 18 \pm 3$ ⁴
γ_{us}	168		199 \pm 25 ⁴	147	158		184 \pm 26 ⁴	103		190 ⁴
$\gamma(111)$	769.9		726.2	937			1280	533.9		727
$\gamma(110)$	861.8		1048.9	1123.5			1548.7	658.5		874
$\gamma(113)$	859.5		951	1118.5			1540.7	652.6		863.9

Al-AP: [Aslanides and Pontikis 1998]; Al-J=Al-Jacobsen [Jacobsen et al. 1987]; Cu-HD, Ag-HD: [Hardouin Duparc et al. 2005]; Cu-M: Cu-Mishin [Mishin et al. 2001]; Cu-F, Ag-F: Cu-Foiles, Ag-Foiles [Foiles et al. 1986].

* The elastic constants for the Jacobsen potential implemented in LAMMPS are extrapolated from the phonon curves published in [Jacobsen et al. 1987].

¹[Kittel 2005] ²[van Lancker 1967] ³[Thomas 1968] ⁴[Bernstein and Tadmor 2004] ⁵[Foiles et al. 1986] ⁶[Hiki and Granato 1966]

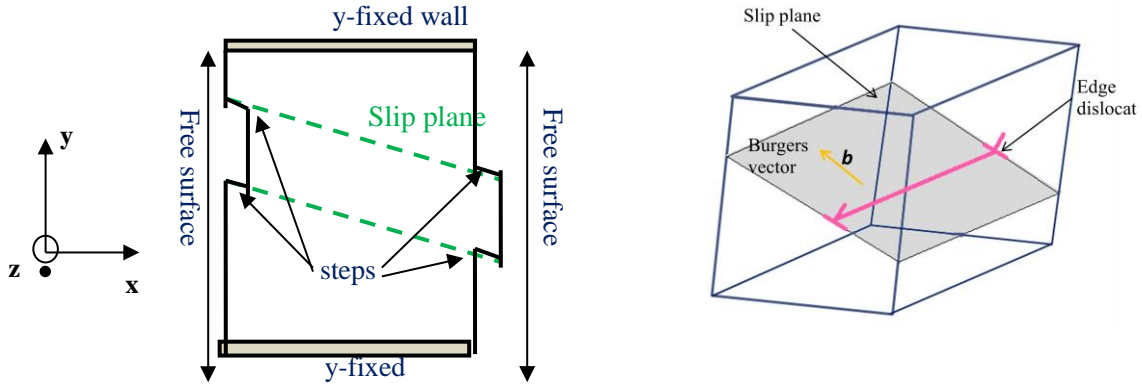


Fig.II.6. Schematic diagram for the system used in this work. Left: x-y plane view with free surface steps and y-fixed walls. The axes are x: $[-131]$, y: $[714]$, z: $[11-2]$, in the conventional crystallographic cubic frame. Right: 3D view showing a (111) glide plane with an edge dislocation of Burgers vector $\mathbf{b} = a_0[1-10]/2$. The system is z-periodic.

The typical time step used in the simulations with the Verlet algorithm is equal to 1 fs, small enough to ensure its stability. Temperatures are initially introduced through random initial velocity Maxwell-Boltzmann distributions and are later maintained using the Nosé-Hoover thermostat. Both linear and angular momenta are initially set to zero so that the system neither translates nor rotates during the simulations.

Surface relief evolutions are analysed depending on the number of applied cycles. MD cyclic loadings are performed by sudden homogeneous elongation or compression along the y direction followed by long relaxations (Fig. II.7).

The strain rates are in the order of $10^7 - 10^8 \text{ s}^{-1}$, typical in similar MD simulations [Zhu et al. 2008, Brochard et al. 2010]. Although this sounds more like in the explosive Crussard-Hugoniot ranges than in the usual fatigue test ranges which are below 1 s^{-1} , it should be noted that our MD moves are truly homogeneous strain moves, and not localized push moves as experimentally performed. Thus, a sudden 1% strain on a 100 \AA y-large sample for example does not correspond to a 1 \AA move of some atoms with respect to the other being kept fixed, but to a 1% strain of all interatomic distances in y. We have also performed pushing tests, moving one wall, the other being kept fixed. These moves require more care but do not change the response of the sample.

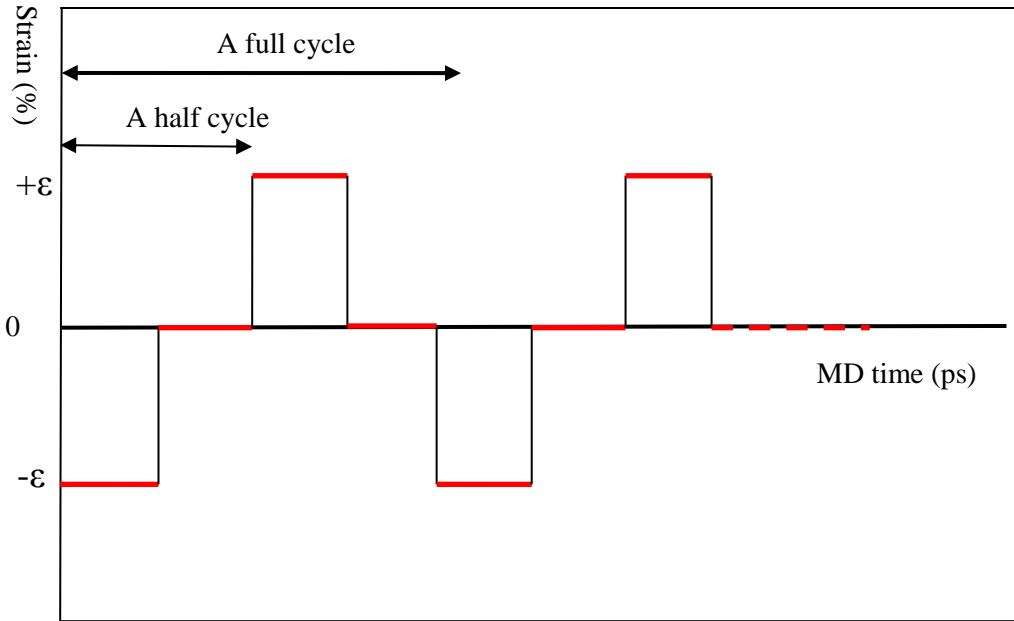


Fig.II.7. Schematic diagram for MD cyclic loading.

2.3 Surface slip reconstruction and slip irreversibility during one full loading cycle

2.3.1 Slip reconstruction during one half-loading cycle

We start with a first half-loading cycle. Before applying loading, a perfect $a[1-10]/2$ edge dislocation is inserted in the bulk by introducing two atomic semi-planes in the simulation box (Fig. II.8a) and the other atoms are displaced according to the usual isotropic elastic formulae. The system is then relaxed and the dislocation dissociates into two Shockley partials. The two partials can glide to the left free surface under a small tension, or to the right free surface under compression. The order of magnitude of the resolved stress needed for the glide of such an edge dislocation is of the order of one MPa for fcc metals (see [Brochard et al. 2010] and [Shin and Carter 2013], with a broad range of magnitude on the experimental side). When this dislocation comes out of the surface, a step of two atomic layers corresponding to a height of the Burgers vector appears on the surface (Fig. II.8b). We shall call it a “ $1b$ ”height surface step.

The exit of the dislocation at a free surface is not the end of a surface step creation: most surface steps are not stable and changes of surface profiles are observed after the dislocation escape. The case of a $1b$ dislocation in aluminium at a simulation temperature of 300 K is presently taken as an example and analysed in details. The dislocation is inserted near the right surface. When it glides out of the surface, a concave shaped surface step, with an acute

angle with the free surface is created. The geometry of this surface step changes afterwards. Some atoms on the surface step ‘fall’ down to the lower surface. More precisely, as illustrated by arrows in Figs II.8c and II.8d, the atoms of the column position M will move to N and the concave form of the surface step thus turns into a convex geometry.

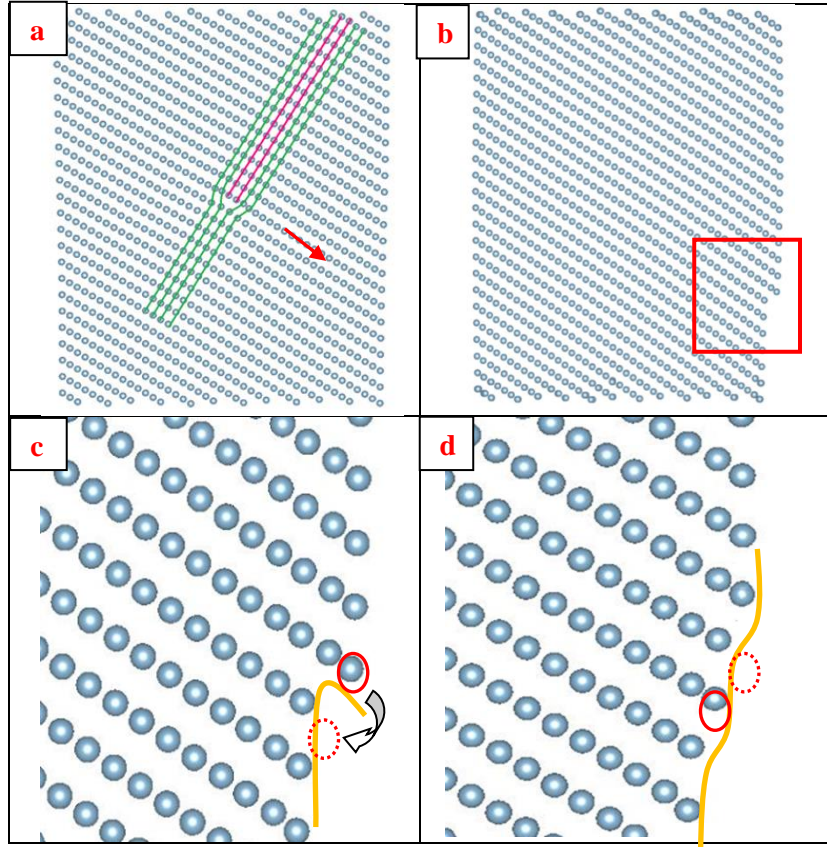


Fig. II.8. Formation and evolution of a simple, $1b$, concave surface step at room temperature in Al. a: A perfect $1b$ dislocation is inserted in the system. b: After dissociation and gliding to the right surface, a concave surface step is created (framed). c to d: Mechanism of reconstruction of that surface step, c: before (it corresponds to Fig. 8b enlarged), d: after. The profile goes from concave (exaggerated) to convex. See text for details. The MD configurations have been quenched for the sake of clarity.

By doing this move, the step atoms get more neighbours, optimize their cohesive energies and thus minimize the surface step energy. Table II.2 shows the cumulated numbers of the 1st, 2nd and 3rd nearest neighbours for the atoms of some surface steps before and after a reconstruction; atoms have more neighbours after the reconstruction. These moves occur gradually and actually result from collective movement of atoms which are further analysed in the Appendix.

Table II. 2. Number of neighbour atoms for different steps before and after reconstruction (see Fig.II.9) compared with the total number of neighbours that an atom of a corresponding perfect surface. The cumulated numbers of 1st, 2nd and 3rd neighbours in the bulk of a perfect fcc structure are respectively 12, 18 and 42. All steps are (111) like. The x, y, z axes for the straight step are [111], [1-10] and [11-2].

Geometry	Concave 1 <i>b</i> step		Convex 1 <i>b</i> step		Perfect surface	Straight 1 <i>b</i> step		Perfect surface
	before	after	before	after		before	After	
1st neighbours	5	6	6	6	7	5	6	7
1st+2nd n.	7	9	8	9	10	8	9	11
1st+2nd+3rd n.	19	23	20	22	24	19	23	25
Surface type	(-131)					(1-10)		

Tests have been carried out by increasing the thickness of the box in the z-direction. Increasing the number of z-layers has no influence on the results presented here.

Different “1*b*” surface steps with different intersection angles between the initial step and the surface are created by dislocation glide in order to compare the reconstruction mechanisms (Fig. II.9). Atoms at a convex step have more neighbours than atoms at the tip of a concave one (see Table II.2). The driving force for the reconstruction at a convex step is thus smaller than the one at a concave step. A convex step is therefore more difficult to reconstruct. For example, the reconstruction at 400 K in aluminium of a 58.5° concave angle step needs only some tens of picoseconds, but the reconstruction for a 121.5° convex step in the same material at the same temperature takes about one nanosecond or more.

Some other examples of reconstructions are given for surface steps with different sizes. Pictures in Fig. II.10 show the reconstructed configurations in aluminium at 300 K for 1*b*, 2*b* and 3*b* large concave surface steps for which 1*b* dislocations have been glide-driven to the surface one by one. These steps reconstruct rapidly during the emergence of dislocations on the surface. The model configurations without reconstruction are given so as to appreciate the real reconstructed configurations. A convex surface geometry is preferred because it allows the increase of neighbours per atom, and so decreases the step energy.

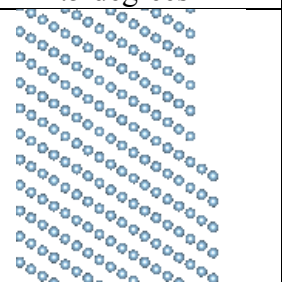
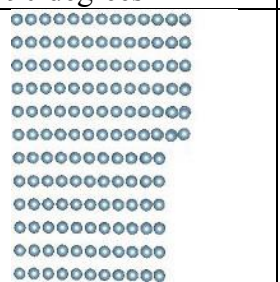
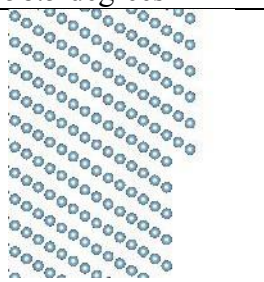
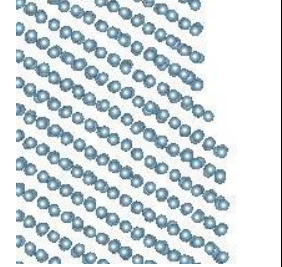
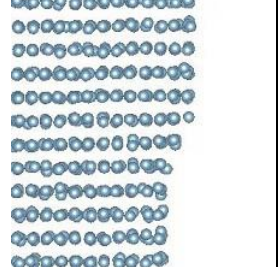
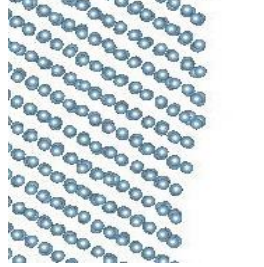
angle	121.5 degrees	90 degrees	58.5 degrees
Before reconstruction			
After reconstruction			

Fig.II.9. Configurations before and after 20 ns of MD relaxation at 300 K in Al for a “1*b*” (two layers) step with different intersection angles with the surface. The mechanisms are the same in Cu and in Ag. The x, y, z axes for the straight step are [111], [1-10] and [11-2].

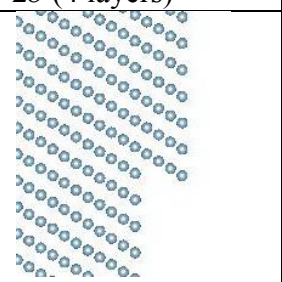
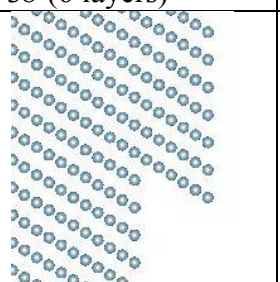
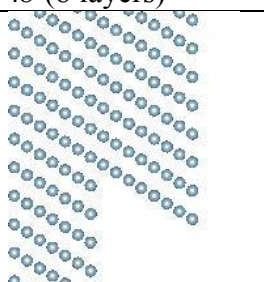
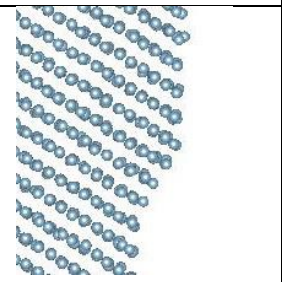
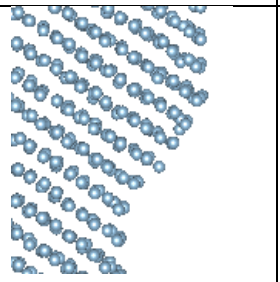
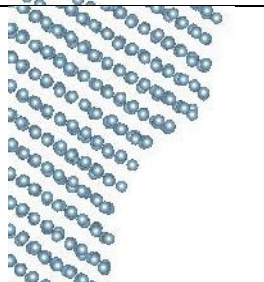
	2 <i>b</i> (4 layers)	3 <i>b</i> (6 layers)	4 <i>b</i> (8 layers)
Without Reconstruction			
With reconstruction			

Fig.II.10. Model configurations without reconstruction and reconstructed configurations corresponding to the emergence of dislocation at the free surface at 300 K in Al for 2*b*, 3*b* and 4*b* concave surface steps. The mechanisms are same in Cu and in Ag.

Three different types of mechanisms can be identified for the reconstruction:

- Quasi-instantaneous reconstruction
- Thermal vibration assisted reconstruction
- Surface diffusion assisted reconstruction

The ‘quasi-instantaneous reconstruction’ occurs at any temperature and effectively decreases the step energy. It takes place when the path to be followed by some edge atoms to get more neighbours and thus optimize their cohesive energies is straightforward. One can say that the local ‘energy gradient’ is large. Very low energy vibrations, if any, are sufficient to let the atoms go down the gradient slope (Fig. II.11A). This is what we observe for a “ $2b$ ” (4 layer large) concave surface step at such a low temperature as 4 K. The reconstruction takes place instantaneously once a “ $2b$ ” surface step has appeared on the surface. The reconstruction time of this quasi-instantaneous step is nearly independent of temperatures. It takes 1.5 ps for this $2b$ concave step.

When it gets less easy for step atoms to optimize the global cohesive energy because of the step geometry, thermal vibrations are necessary to let the atoms of the surface step overcome some energy barrier and achieve lower energy configurations. This mechanism is clearly temperature dependent and we call it ‘thermal vibration assisted reconstruction’. The higher the temperature, the faster the reconstruction. It allows a surface step to reconstruct further than the reconstruction due to the ‘quasi-instantaneous’ mechanism at higher temperature.

The ‘surface diffusion assisted reconstruction’ mechanism means that surface atomic diffusion plays a role in the reconstruction. For any general surface, there is a range of temperature above which there is a non negligible probability that some atoms may become adatoms and diffuse at the surface. In the case of our $\{113\}$ surface, this probably starts to occur at the time scale of our MD simulations (nanosecond) at roughly $T_m/2$. These wandering adatoms may either get back to their initial place, or reach another surface vacancy or reach a hollow position at a non completely reconstructed surface step and fill it to further minimize the surface step energy.

several times because of the ‘thermal vibration activated reconstruction’ and ‘diffusion activated reconstruction’. The step at 400 K is more reconstructed than at 4 K (Fig. II.12).

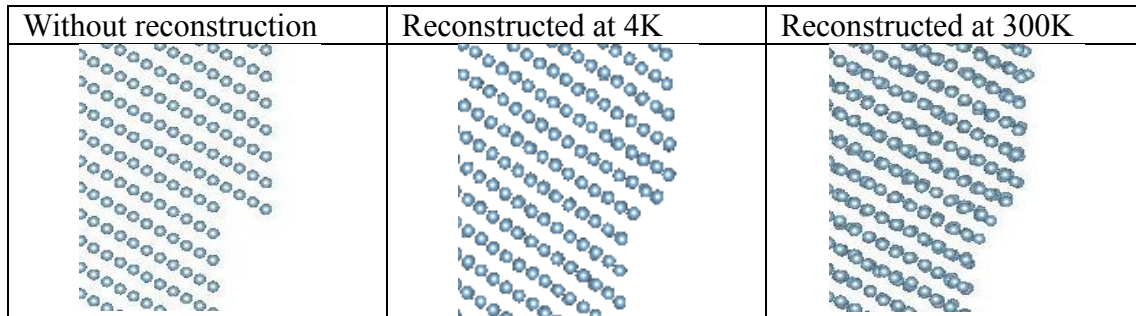


Fig. II.12. Reconstruction of a “2b” surface step at 4 K (middle) and 300 K (right), the configuration at 300 K is more reconstructed.

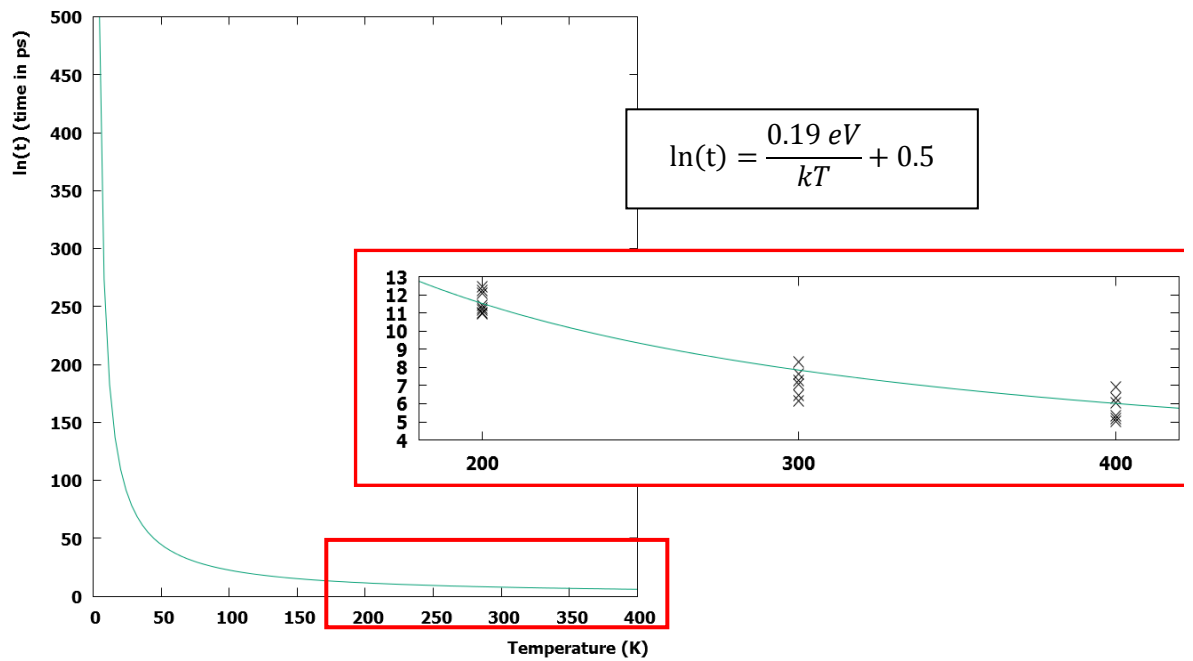


Fig. II.13. A deduced temperature-reconstruction time Arrhenius like curve for a two layers concave surface step in copper (potential of Mishin et al.). k is the Boltzmann constant. The extrapolated reconstruction time at low temperature (77 K) is several seconds, which is tremendously large compared to the reconstruction time at room temperature (~2 ns).

Temperature	77 K	200 K	300 K	400 K
Reconstruction time	4.48 s	120 ns	1.8 ns	0.4 ns

A 1b height concave step is taken as another example. For this step, no ‘quasi-instantaneous reconstruction’ seems to occur. A simulation at 20 K shows that at this temperature, no reconstruction occurs and atoms simply vibrate around their positions. At 200 K, ‘thermal vibration activated reconstruction’ takes place and the step is reconstructed (Fig. II.11B). But as the ‘thermal activated reconstruction’ is temperature dependent, at very

low temperature, it seems nearly impossible or it takes dramatically long time. We tried to deduce the reconstruction time at 77 K which is about the highest temperature for liquid nitrogen and is widely used in experiments. By extrapolating with an Arrhenius like equation the curve towards lower temperatures from the reconstruction times at 200 K, 300 K and 400 K obtained from eight MD simulations for each temperature (Fig. II.13), it is found that the reconstruction at 77 K can take several seconds. Such a step thus would not be reconstructed at 77 K in real experiments for which cycle loading times last from 10^{-4} to one second.

The energy drawn in Fig. II.11 is the sum of the cohesive energies of the moving atoms during the reconstruction. The other atoms just vibrate around their original positions. Calculations also including some of these other atoms showed that the energy variations during the reconstruction are not affected.

To sum up, the reconstruction is a mechanism which decreases the surface step energy induced by the appearance of a surface defect; it can be “quasi instantaneous” but it may also need thermal activation to be complete. At room temperature and above, almost all steps reconstruct via different mechanisms. But at lower temperatures, there are steps which may not reconstruct. These tests have been carried out in Al, Cu and Ag. Similar mechanisms have been observed in the three metals.

2.3.2 Surface slip irreversibility during one full cycle without additional dislocations

The surface step reconstruction has a strong influence on the surface step irreversibility. The reversibility of a simplest single surface step in aluminium is analysed during the following opposite sign half-cycle loading. The system is firstly elongated or compressed with 1% increment every 10,000 MD steps up to a deformation of 5%. From then on, 0.1% increments are used (corresponding to a strain rate of 10^8 s^{-1}) until reversibility is obtained (or not).

The behaviour of both reconstructed and non-reconstructed steps is studied. Firstly, tests are performed on two different non-reconstructed steps, a concave one and a convex one, at 77 K which is a low temperature at which reconstruction cannot occur. Both steps are reversible and can slip back into the material. But a tensile strain of 4% is required in order to

make the concave step disappear corresponding to a critical resolved shear stress (CRSS) of 1.2 GPa and a contraction strain of 5.2% is necessary for the convex step, corresponding to a resolved shear stress of 1.8 GPa. These CRSS leading to step annihilation are much higher than the stress applied during experimental cyclic loadings which are from several to hundreds of MPa [Mughrabi 2010]. Thus, in practice, these steps are irreversible because the experimentally applied stresses never reach these critical values in usual cyclic fatigue tests.

Tests are also performed on both concave and convex reconstructed steps and it is found that they are fully or partially irreversible. A tensile test is performed on a “1b” concave step at 300 K. After a tensile strain of 7% corresponding to a resolved shear stress of 2.15 GPa, other plastic irreversible deformations occur somewhere else in the material, but the reconstructed step does not change. One can thus conclude that it is irreversible at least up to a tensile strain of 7%. Contraction tests are also performed on “1b” reconstructed convex steps previously obtained by 20 ns relaxations at 300 K. Contrary to the case of a concave reconstructed step, a convex reconstructed step under compression is reversible but only partially (Fig. II.14): it leaves behind a surface defect induced by the reconstruction. The contraction needed to achieve the (partial) reversibility is 6.4%, corresponding to a CRSS of 2.2 GPa. All results are listed in Table II.3 for the sake of clarity.

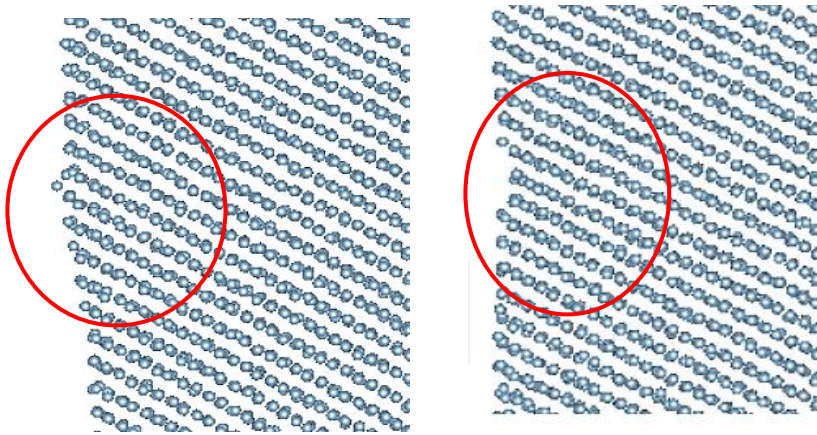


Fig.II.14. Configurations before (left) and after (right) a compression test of a box containing a convex surface step at 300 K in aluminium. The step is partially irreversible.

Table II.3. Reversibility of different surface steps during the opposite half cycle.

	1 <i>b</i> concave step under elongation		1 <i>b</i> convex step under compression	
State after the first half cycle	Non-reconstructed	reconstructed	Non-reconstructed	reconstructed
Temperature	77 K	300 K	77 K	300 K
Critical axial strain	~4%	>7%	~5.2%	~6.4%
Critical shear stress	~1.2 GPa	>2.15 GPa	~1.6 GPa	~2 GPa
Reversibility	reversible	irreversible	reversible	Partially reversible

The erase of more complex surface steps should be even more difficult than for simple 1*b* surface steps.

These results can be compared to the results already obtained by [Brochard et al. 2010]. Having found that a surface step is a preferential site for the nucleation of dislocations, they carried out a tensile test on a box with an artificially built {111} surface two layer step and found that dislocations begin to nucleate from the free surface at an elongation of 6.2%, corresponding in their case to a CRSS of ~2 GPa at 300 K in aluminium. In our study, using the same atomistic potential, the surface step is naturally created by the glide of dislocations towards the surface, so that the nucleation of the same dislocation from this naturally created step corresponds to the simple annihilation of the step. We can thus compare our CRSS under reverse loading leading to surface step reversibility to Brochard et al.'s values. These values are indeed very similar, 1.8 vs. 2 GPa.

How should one transfer this value to experimental cases? As mentioned at the end of section 2.2, our strain rate is many orders of magnitude larger than experimental ones. [Zhu et al. 2008] showed that passing from strain rates typical of MD simulations to experimental ones only decreases the nucleation stress by half at room temperature [Stoltze et al. 1988]. [Brochard et al. 2010] additionally showed that the CRSS also depends on step height. Yet, even after this type of correction, these CRSS values remain in the same order of magnitude which means that they are much larger than experimentally applied ones.

To sum up this section, we found that annihilation of a surface step is possible but quite difficult for a non-reconstructed step. Reconstructions can induce strong irreversibility. But as the stress applied during cycling is much lower than the critical shear stress for annihilation,

all the surface steps are irreversible ($p=1$) in the experimental conditions, at least as long as we ignore the influence of the other dislocations.

2.3.3 Surface slip irreversibility during one full cycle with opposite sign dislocations

The influence of the glide of an opposite sign dislocation on a step previously built during a first half-cycle is presently studied. Let us assume that there is a dislocation source which successively creates, during a loading and an opposite sign loading, two edge dislocations of opposite signs, with dislocation cores located in two adjacent atomic slip planes. The first dislocation generates a surface step which evolves alone until the arrival of the second, opposite sign, dislocation. In the simulation, the opposite sign dislocation is inserted by using the same method as for the first dislocation (see section 2.3.1) after a relaxation of the first surface step. The subsequent evolution will depend on the state of the step when the opposite sign dislocation arrives close to the free surface. We basically distinguish two cases. (i) If the step is still in the non-reconstructed state, as it may happen at very low temperature, it will be erased by the new dislocation almost instantaneously. This is true for all geometries of non-reconstructed steps. (ii) If the step is already in a reconstructed state, as it will happen at temperatures above 100 K, the new dislocation cannot erase it and there is a remaining surface hole defect (Fig. II.15). At 400 K, the ‘surface diffusion activated reconstruction’ will subsequently take place and diffusing surface atoms eventually fill the small hole of the surface. The step is finally completely erased (Fig. II.15, right).

As atomic diffusion depends on temperature, the test in Fig. II.15 has been performed at 400 K rather than 300 K in order to speed up the last mechanism in our simulations, within the nano-second order. During experimental cycling tests at room temperature, as cycles are in the order of the second, reconstructed steps are very likely to be reversible (annihilated) thanks to the opposite-sign dislocations. At low temperatures, there is virtually no surface diffusion, a reconstructed step is irreversible and there will be a permanent surface step after one cycle.

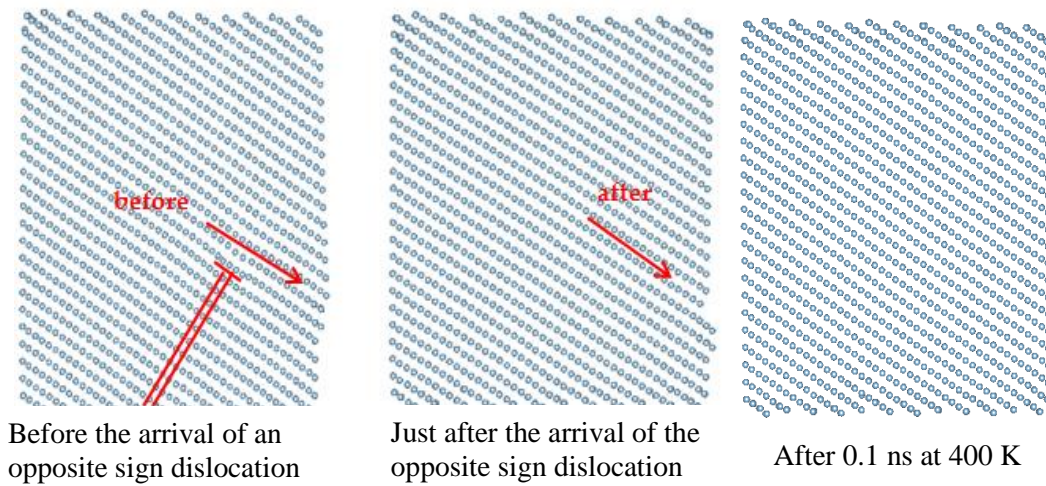


Fig.II.15. Evolution of the surface relief after arrival of an opposite-sign dislocation at 400 K in aluminium. It is located in the direct neighbour atomic plane.

To sum up this section, after the arrival of an opposite sign dislocation located at a direct neighbour plane, non-reconstructed steps which exist at low temperatures are reversible ($p=0$) and reconstructed steps are reversible ($p=0$) at room temperature and above. At intermediately low temperatures (around 100-200K) where reconstruction can take place but diffusion is almost inactive, new opposite sign dislocations cannot totally erase the surface step and a permanent surface defect is left behind. For some larger surface steps ($2b$ large surface step for example) which reconstruct even at 4K, they can only be erased at higher temperatures by surface diffusion.

2.4 Slip irreversibility and micro-notch initiation during cyclic loading

Cyclic loading is now performed on different simulation systems at different temperatures in aluminium. The system is first strained at -0.2% and relaxed during 40,000 MD time steps (40 ps) keeping that strain level, thus corresponding to a strain rate of 10^7s^{-1} . The strain is then set back to 0%, with another 40,000 time steps of MD relaxation, followed by an elongation to a strain level of +0.2%, again relaxed, and the system is finally brought back to 0% strain. A full cycle loading is hence performed and will be repeated several times (Fig. II.7 in section 2.2). Dislocations are inserted one by one. A $1b$ dislocation is inserted just before the first compression. Contraction is then applied and the dislocation glides to the right surface. After 20,000 MD steps, a second dislocation of the same sign is inserted keeping the strain level

constant and the system evolves during another 20,000 MD steps. The second dislocation also goes to the right surface. Two opposite sign dislocations are inserted using the same method during the following half-cycle, just before and during the elongation, so that they glide to the same surface. This choice facilitates the observation of various mechanisms in different simulation systems at different temperatures.

Several simulations systems are presented in Fig. II.16: opposite sign dislocations can be inserted in neighbour gliding planes, but it is also possible that there are one or several planes between these planes.

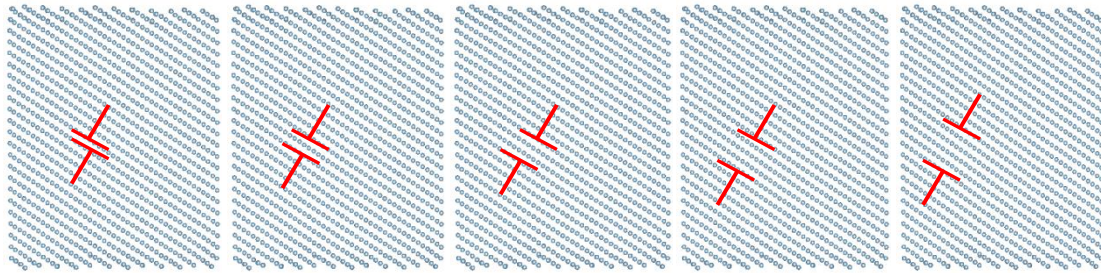


Fig.II.16. Different systems with respectively 0, 1, 2, 3, 4 atomic planes between opposite sign dislocations

Low temperature tests are carried out at 77 K, where atomic vibrations are small and atomic diffusion negligible. The reconstruction mechanism activated by surface diffusion will rarely take place, and the vibration activated mechanism is difficult. Only the quasi-instantaneous reconstruction can occur easily.

Let us first start with the case when opposite sign dislocations are inserted in neighbour planes. The first inserted dislocation comes out at the right surface and a surface step appears (Fig. II.17A) which does not reconstruct easily at 77 K. Then the second dislocation comes out and the surface step reconstructs almost immediately within 1 ps (Fig. II.17B). The system strain is then set back to 0% and an opposite-sign dislocation is inserted, which moves towards the same surface because of the elongation. A relief evolution is observed. The height of the step is decreased to $1b$ with a reconstructed geometry (Fig. II.17C). A second opposite-sign dislocation is inserted while keeping the strain level constant and it moves towards the same surface. The surface step is again partially erased but a surface defect remains and does not evolve during the following MD relaxation time (Fig. II.17D). The strain is set back to zero and a full loading cycle is thus finished. A second loading cycle is started when inserting a dislocation whose sign is the same as the first one, the surface relief returns to its previous (Fig. II.17C) geometry once this dislocation comes out of the surface. A second dislocation is

inserted and the surface geometry reverses back to its B shape (Fig. II.17B). During the second half of the second cycle, another two opposite sign dislocations come out at the same surface and at the end of the second cycle, the surface geometry is the same as at the end of the first cycle (Fig. II.17D). The cycle is repeated another three times and the relief evolution is observed to be stationary. Therefore, one can conclude that at 77 K, when the opposite sign dislocations are in neighbour planes, there is a partial irreversibility after one cycle due to the reconstruction phenomena and there is no more complementary irreversibility during the following cycles.

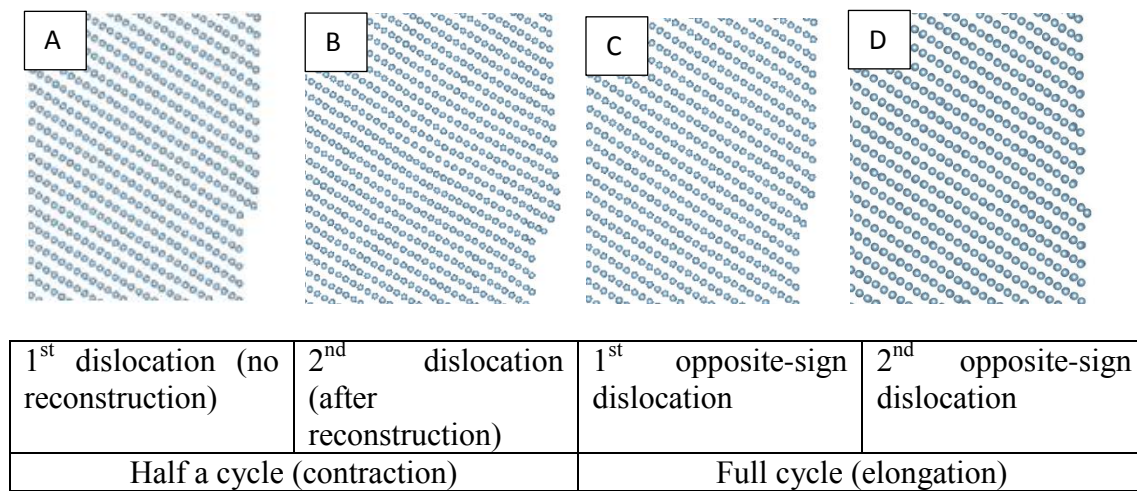


Fig.II.17. Evolution of a $2b$ large surface step during cyclic loading at 77 K in aluminium. The evolution becomes stationary after the first loading cycle.

It is possible of course that opposite sign dislocations do not appear at immediate neighbouring planes. Simulations are thus carried out for cases where there is one, two, three or four atomic planes between the planes of insertion of the opposite sign dislocations (see Fig.II.16). Two dislocations come out of the surface every half-cycle as described above. They have respectively a concave and a convex intersection angle with the free vertical surface. At 77 K, a concave step will reconstruct but a convex one is stable. The reconstruction mechanism for the concave step is firstly the quasi-instantaneous one, and, the thermal vibration assisted mechanism can also take place.

It is found that when the opposite sign dislocations are not in immediate neighbouring planes, a micro-notch is initiated and grows deeper cycle by cycle, as shown in Figs. II.18.

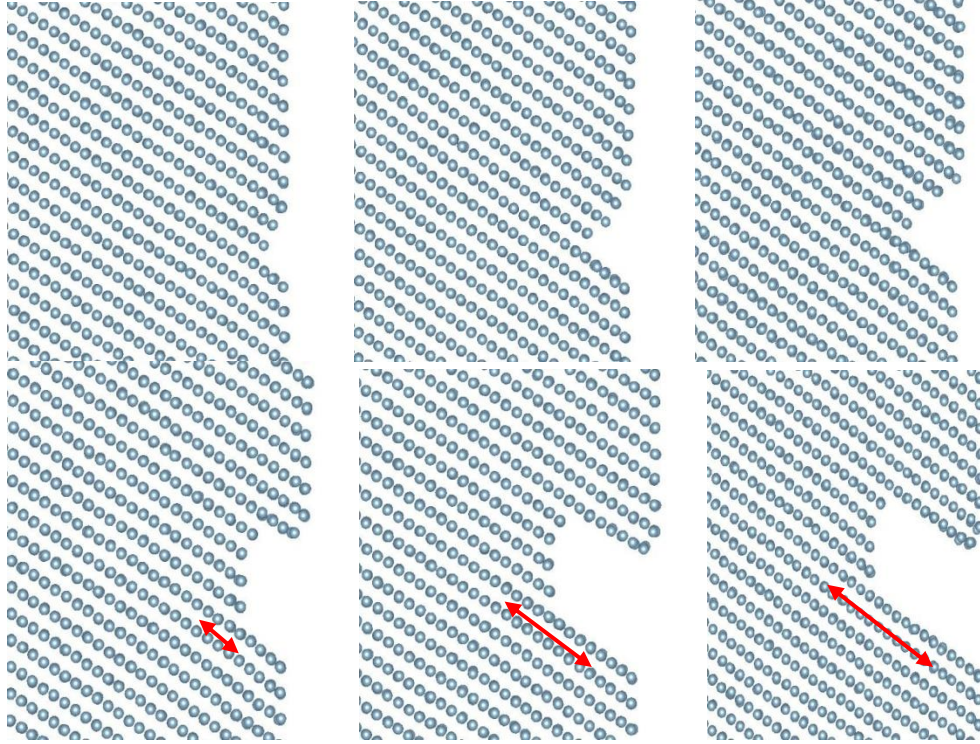


Fig.II.18. Surface configurations after one, two and three loading cycles for two different systems where there is respectively 1 (top) and 4 (bottom) planes between opposite sign dislocations. Red arrows show crack depth. (Al, 77 K).

At 77 K, the reconstruction of the concave step does not extend beyond the second neighbouring (111) atomic plane. Thus, when there are three or more atomic planes between the concave and the convex plane steps, the evolution of these two steps are independent.

The depth of a micro-notch is defined as the longest distance between the surface and the crack tip measured along the Burgers vector. For the cases where there are more than two (111) atomic planes between the gliding planes of opposite sign dislocations, reconstructions of these two steps are independent, the depth of the micro-notch is the height of the convex non-reconstructed step, because reconstruction decreases the step height, and the depth of the reconstructed side is shallower. Thus, when there is more than two atomic planes distance between opposite sign dislocations, the notch-crack depth is $2b$, $4b$ and $6b$ large after one, two and three cycles respectively. When there is less than three planes between opposite sign dislocations, reconstructions decrease notch-crack depth (cf. Table II.4). Final configurations can of course be slightly different if we change the random Maxwell-Boltzmann velocity distribution at the beginning.

Tests are carried out at higher temperatures, viz. 400 K, in order to speed up the thermally activated mechanisms. For the case where the opposite sign dislocations are in immediate neighbour planes, the starting mechanisms are the same as at 77 K, but the surface defect that was left at the end of a full cycle at 77 K can be now erased by the diffusion assisted reconstruction: adatoms appear on the surface diffuse and fill the step hole defect. The step created is reversible. For systems where there is one or more planes between inserted dislocations, surface steps are naturally further reconstructed at 400 K than at 4 K. Yet, micro-notches still appear, with step heights only slightly reduced as shown in Fig. II.19 and Table II.4. Initiation of micro-notch is thus revealed and the mechanism is general for different step geometries. This micro-notch may grow afterwards during cyclic loading with different mechanisms described by [Horstemeyer et al. 2010] and [Baker and Warner 2014]. MD simulations for crack propagation will be carried out using continuous boundary conditions provided by finite element computations [Bennett and McDowell 2003; Ferrie and Sauzay 2009].

Table II. 4. Evolution of the notch depth during 3 cycles for different geometries at 77 K and 400 K.

Distance cycles	0 plane	1 plane	2 planes	3 planes	4 planes
1 cycle 77K	$1b$	$1b$	$1.5b$	$2b$	$2b$
2 cycles 77K	$1b$	$2b$	$3.5b$	$4b$	$4b$
3 cycles 77K	$1b$	$2.5b$	$5.5b$	$6b$	$6b$
1 cycle 400K	0	$0.5b$	$1b$	$1.5b$	$1.5b$
2 cycles 400K	0	$1b$	$2b$	$2.5b$	$3b$
2 cycles 400K	0	$1.5b$	$2.5b$	$4b$	$5b$

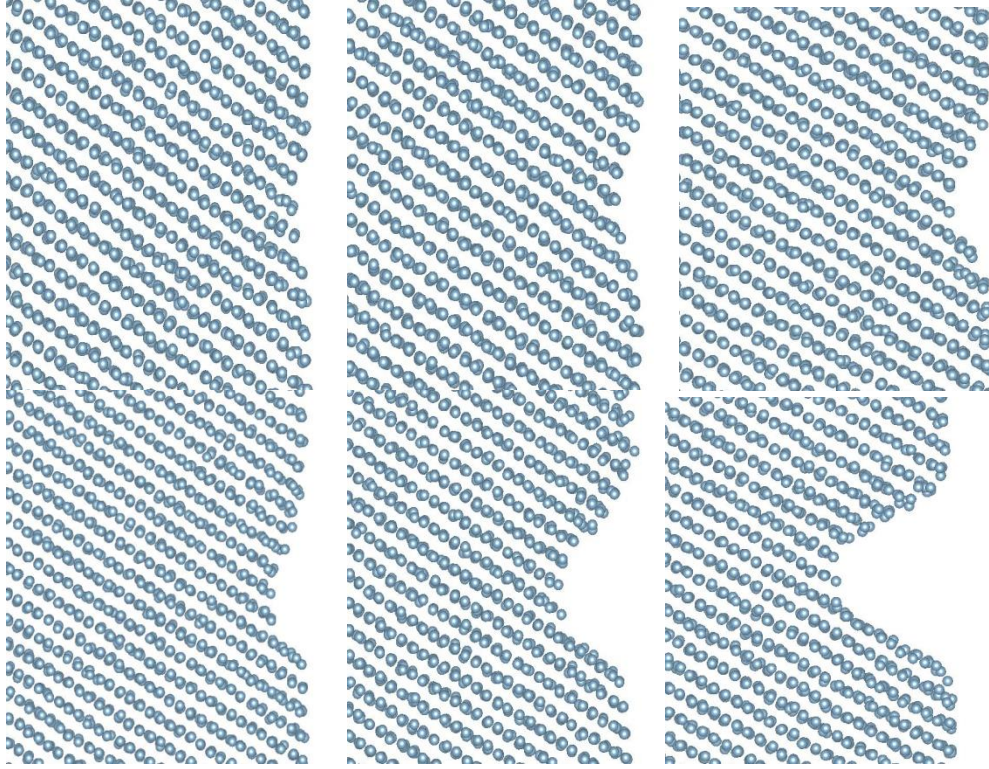


Fig.II.19. Surface configurations after three loading cycles for two different systems where there is respectively 1 (top) and 4 (bottom) planes between opposite sign dislocations. (Al, 400 K).

2.5 Discussions

The atomistic simulations carried out in this work show a strong irreversibility of surface slips. One can propose a tentative coupling of our surface irreversibility computations and bulk calculations. Both the EGM model and the LK model (see the literature review section 2.1) are considered.

The total irreversibility factor p can be calculated using a weighted rule of mixture considering both edge and screw slip irreversibility factors:

$$p = C_e p_{\text{edge}} + C_s p_{\text{screw}}$$

C_e and C_s correspond to the percentages of edge and screw slips contributing to p , with $C_e = 1 - C_s$. p_{edge} and p_{screw} are the irreversibility factors due to pure edge and screw slips, respectively. Taking into account both bulk and surface mechanisms, one has $p_{\text{edge}} = p_{\text{edge}}(\text{bulk mechanisms}) + p_{\text{edge}}(\text{surface mechanisms})$, and similarly for p_{screw} .

For edge dislocation slips, the irreversibility factor predicted by the DEGM and LK bulk models should be very small since the annihilation distance between edges dislocations are

quite small. The estimation of $p_{\text{edge}}(\text{surface mechanisms})$, considering surface mechanisms is based on our simulations. We observed that a surface step is reversible only when an opposite sign dislocation carrying out the same Burgers vector amplitude glides in a direct neighbour plane. A simple irreversibility calculation taking this neighbourhood effect into account can be proposed: let us assume that a persistent slip band (PSB) lamella corresponds to a stack of N planes, and that during one half cycle n dislocations glide to that surface zone in a random way and create n steps. During a subsequent opposite half cycle, n opposite sign dislocations glide to the same surface zone. n and N are linked by the value of the plastic shear strain per cycle $\Delta\gamma_{\text{pl}} = nb/Nd$ with d being the interplanar (111) distance ($d=a/\sqrt{3}$, vs. $b=a/\sqrt{2}$) and Nd varies from $0.4 \mu\text{m}$ to $1 \mu\text{m}$ in copper at room temperature [Basinski and Basinski 1992]. The plastic slip amplitude $\Delta\gamma_{\text{pl}}$ is experimentally found to be of the order of one percent [Differt et al. 1986; Mughrabi 2009]. If the material is ‘wavy’, with double cross-slips (see section 1.4.2), the opposite sign dislocations during the opposite half loading cycle will glide to the surface in a random way quite independent of the first n dislocations. Using statistical combinatorics, a rough estimation of the surface slip irreversibility after one full cycle is thus $p_{\text{edge}}(\text{surface mechanisms}) \approx C_{N-n}^n / C_N^n$, which gives a value between 0.5 and 0.75 for the case mentioned above in copper. Knowing that the irreversibility factor estimated via bulk mechanisms considering edge dislocations alone is estimated to be very small (see section 2.1, page 28), the value of p_{edge} considering both surface and bulk mechanisms can still be considered to be between around 0.5 and 0.75.

Contrary to edge dislocations which disappear as such when they emerge at a surface (one no longer has extra atomic planes in a bulk environment), screw dislocations always exists when they glide along surface where they create surface steps. A screw dislocation can thus be easily slip back under reverse loading, even in case of reconstruction, because the surface step energy may be decreased by slipping back of a screw dislocation. This means that surface steps created by screw dislocations are highly reversible ($p_{\text{screw}}(\text{surface mechanisms}) \approx 0$) when there is no cross-slip. In wavy materials where cross-slip can occur easily, a screw dislocation can be easily annihilated by an opposite sign dislocations (by cross slip) [Mughrabi 2009]. The irreversibility caused by this annihilation mechanism in the bulk is 0.3 in copper at room temperature following EGM II [Differt et al. 1986] (see section 2.1, page 28). A larger value of 0.7 is found following the LK model, with similar considerations about the annihilation of screw dislocations by cross slips and correlated movements of edge dislocations, but with a

more complex model. As the complementary irreversibility due to surface mechanisms is very small, the value of p_{screw} considering both surface and bulk mechanisms can still be considered to be about 0.3 (EGM) or 0.7 (LK).

Concerning planar materials where cross slip is difficult, bulk annihilation of screw dislocations should be rare. This may decrease the irreversibility. Much lower irreversibility factors have been found in planar materials (see tables 1 in [Mughrabi 2009] and [Mughrabi 2010]). Further simulations need to be carried out and compared with experimental results. In particular, additional MD computations should allow to check the behaviour of surface steps induced by screw dislocation glide.

The total irreversibility is calculated using the mixture rule ($p = C_e p_{\text{edge}} + C_s p_{\text{screw}}$). For the sake of clarity, different irreversibility factors are listed in Table II.5.

It is found that our coupled total irreversibility factors considering surface mechanisms are larger than the values estimated by the EGM II bulk model or the related Lépinoux and Kubin model.

Table II.5. Synoptic table of the irreversibility factor calculations, from bulk models and from our MD computations. C_e and C_s are the fractions of slip carried out by the edge and screw dislocations respectively. The total weighted irreversibility factor p is $p = C_e p_{\text{edge}} + C_s p_{\text{screw}}$.

	$C_e = 20\%, C_s = 80\%$ [Differt et al. 1986]			$C_e = C_s = 50\%$ [Lépinoux and Kubin 1986]		
	Bulk (EGMII)	Surf. (MD)	Bulk+Surf. (EGM + MD)	Bulk (L&K86)	Surf. (MD)	Bulk+Surf. (L&K86 + MD)
p_{edge}	very small	0.5 - 0.75	0.5 - 0.75	very small	0.5 - 0.75	0.5 - 0.75
p_{screw}	0.3	0	0.3	0.7	0	0.7
Total p	0.25	0.1 - 0.15	0.35 - 0.4	0.35	0.25 - 0.375	0.6 - 0.725

Similar calculations have been carried out for nickel using our irreversibility model considering both bulk and surface mechanisms. Similar values of p are found as those in copper. These values are close to the AFM experimental measurement [Weidner et al. 2011].

The roughness of the surface (\bar{w}) (see section 2.1) will have to be calculated using the surface irreversibility factor estimated in this study and be compared to the value estimated by

the EGM II model. Calculations of micro-notch initiation or crack propagation can also be envisaged. The adsorption of oxygen and water molecules may trigger irreversibility phenomena. The environmental effect on surface slip irreversibility will be analysed in the next chapter.

2.6 Conclusions

Molecular dynamics simulations have been carried out to study the mechanical behaviour of cyclic surface steps at the atomic level in order to understand the surface relief evolution mechanisms under cyclic loading and to evaluate the surface step irreversibility factor in three fcc metals, Al, Cu, and Ag. We focused on the $a\langle 110 \rangle/2$ edge dislocations generating or removing surface steps because they are prevalent dislocations in elementary fcc metals. A surface step reconstruction phenomenon including three mechanisms is observed which increases the irreversibility level. Without opposite sign dislocations, all the surface steps are irreversible at the stress magnitudes usually considered in fatigue laboratories. Surface steps are only reversible when opposite sign dislocations located in the close atomic plane to the previous dislocations glide towards the free surface during the following half-cycle. When there is some distance between the planes of insertion of opposite sign dislocations, a micro-notch initiates cycle by cycle.

These atomic level simulations reveal an irreversibility fraction between 0.4 and 0.7 in copper at room temperature coupling both bulk and surface mechanisms. The value of p in nickel should be similar to that in copper which is larger than the value estimated by the EGM II model or related models. Our estimated values are closer to the value measured by AFM, 0.8 [Weidner et al. 2011].

2.7 Section appendix

Collective reconstructive movements of atoms

Reconstructions at surface steps occur gradually and result from more or less collective movements of atoms. For the reconstruction of the $1b$ concave surface step presented in Fig. II.8, for instance, the atoms in the outer column do not move simultaneously towards the surface. Instead, they ‘fall down’ in a rather random way one by one to the surface (from column M to column N), as shown in the quenched and tilted snapshots in Fig.II.A1. Their “drop” is naturally assisted by the vibrations of the neighbouring atoms. For some other surface steps, reconstruction is not as simple but implies a multi-step collective movement of the atoms. A $1b$ large convex surface step is shown in Fig.II.A2. A follow up of the atomic motions reveals that the atoms of column A do not drop from A to C. Instead, atoms from column B go to C and are replaced by A atoms. The A atoms initially undergo an inward force towards B. The A atoms thus push atoms from column B towards C and take their place. A similar mechanism occurs with a $2b$ large concave step (Fig.II.A2). The atoms of the column at the point of the surface step push the lower plane atoms to drop towards the surface and the reconstruction occurs due to this complex collective movement.

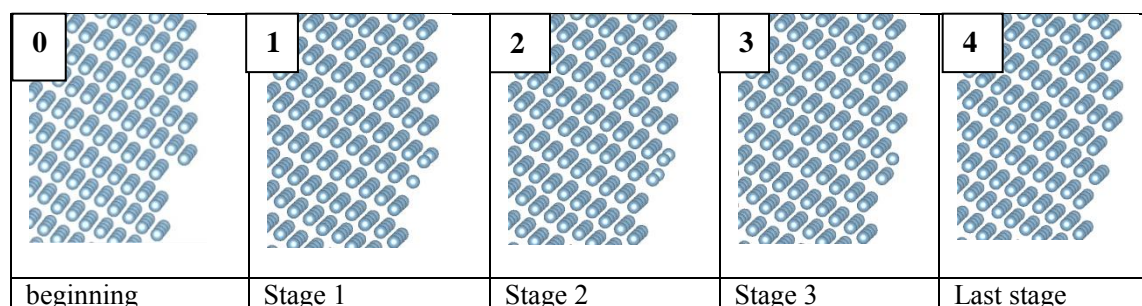


Fig.II.A1. Successive snapshots, quenched and tilted, of the reconstruction described in Fig. 3 (in aluminium at 300 K), showing that the drops of atoms from column M to column N occur one by one.

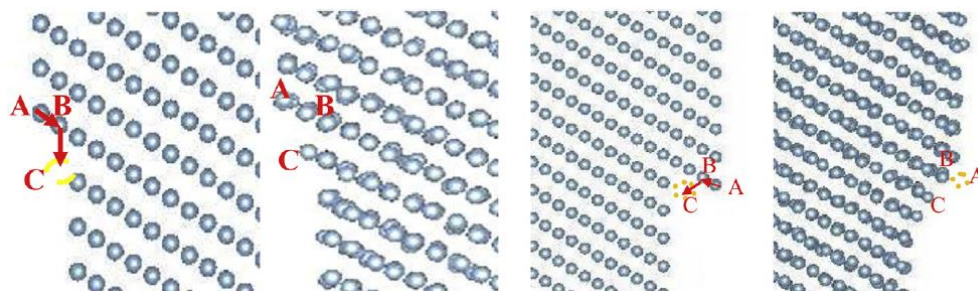


Fig.II.A2. Collective movements of atoms for the reconstruction of a $1b$ convex step and a $2b$ concave surface step.

CHAPTER 3.

SURFACE STEP IRREVERSIBILITY & CRACK INITIATION IN OXYGEN ENVIRONMENT

In air environment, a thin oxide film can easily form at the metal/air interface and may have some effect on the surface evolution and the dislocation emergence. In the second part of this Ph.D. work, simulations similar to the ones carried out in the previous chapter are done on copper and nickel in oxygen environment in order to check if oxygen changes the behaviour of surface step reconstruction, the emergence of dislocations and the nucleation of surface micro-notches. For aluminium, water molecules have a dominant effect on the fatigue crack propagation. Neither aluminium nor water effects will be considered in this chapter. There are many experimental studies of oxide formation on nickel and copper which have already been published. Our simulations on the first stages of oxidation will be tentatively compared to these experimental studies.

Even though an investigation of oxidation is not the main purpose of this study, it is important to make sure that our simulation results concerning first stages oxide layer formation on metal surfaces are realistic and comparable to experimental observations. Oxygen/metal interactions and oxide layer formations are first analysed in relationship with experimental observations. Dislocations will then be inserted and surface slip irreversibility will be studied as in the previous chapter, but now in oxygen environment.

3.1 Literature study

3.1.1 Some definitions

Different observed oxidation mechanisms for nickel and copper are reviewed in this section. Several definitions are firstly clarified:

- Adsorption is defined as the adhesion of atoms or molecules from a gas to a surface. This process creates a film of the adsorbate *on the surface* of the adsorbent. Chemisorption and physisorption are two kinds of adsorption.
 - Chemisorption is a kind of adsorption which involves a chemical reaction between the surface and the adsorbate. New chemical bonds are generated at the adsorbant surface.
 - Physisorption leaves the chemical species of the adsorbate and surface chemically intact.
- Absorption: The atoms or molecules from the gas penetrate into the bulk of the (metallic) solid. In the case of molecules, they are normally first decomposed and their atoms are absorbed by the solid.

Recall of some pressure units: $1 \text{ Pa} = 1 \text{ N/m}^2$ is the pressure unit in the metric system (SI: *Système International*, international but for Myanmar, Liberia, and the USA). Several other pressure units are found in the literature: $1 \text{ bar} = 10^5 \text{ Pa}$, $1 \text{ Atm} = 101,325 \text{ Pa}$, $1 \text{ Torr} = 133.332 \text{ Pa}$ (exact value now accepted by definition, so that 1 mm of mercury (1mm Hg) $\sim 1 \text{ Torr}$), $1 \text{ psi} \sim 6894.757 \text{ Pa}$, ...

3.1.2 Oxidation on nickel / air interface.

Based on experimental investigations reported in early studies (see for instance [Fehlner and Mott 1970; Holloway and Hudson 1974; Rhodin and Adams 1974; Smeenk et al. 1980; Holloway 1981] three reaction regimes can be identified during nickel oxidation:

- The first regime is when oxygen exposure is below 20L (where L is the Langmuir unit: the exposure during one second to a gas pressure of 10^{-6} Torr . Hence $1 \text{ L} = 10^{-6} \text{ Torr s} \sim 1.33 \cdot 10^{-4} \text{ Pa s}$). It is associated with very rapid dissociative chemisorption leading to two dimensional structures based on the initial crystallography of nickel surface, with oxygen coverage of approximately 0.5 monolayer (1 monolayer = one oxygen per (hkl)-surface unit cell) for (100) and (111) surface.

- The second regime corresponds to the epitaxial nucleation of ‘NiO’ islands and lateral growth of these islands until coalescence over the nickel surface, with a thickness of about two atomic layers.
- The oxide film then thickens over times of hours or days at atmospheric pressures. This is the third reaction regime: a final slow thickening of a true NiO structure at the expense of the nickel substrate.

It has been shown by many studies that the interaction between oxygen and a ‘clean’ nickel surface begins with chemisorption and incorporation of oxygen atoms [Quinn and Roberts 1964; Delchar et al. 1967; Holloway and Hudson 1974]. [Delchar et al. 1967] found that the chemisorption stage is extremely short compared with the subsequent growth of the oxide layer. The atomistic details of the initial incorporation of atoms into the metal cannot be captured experimentally. Yet one knows that the distance between the metal layers at the surface can be expanded a little because of oxygen atoms. [Van der Veen et al. 1979] have shown that while the (110) nickel surface is contracted by 4% when clean, it is expanded by 1% with chemisorbed oxygen. [Oed et al. 1989] also found that the spacing between nickel (100) first substrate layer and second substrate layer is expanded by nearly 6% after adsorption of oxygen atoms. Experiments about the initial stages of oxidation are now usually performed at very low pressure (5×10^{-9} Torr for example) and most studies in the literature are on nickel (100) (111) and (110) surfaces. Simulations on the (111) and (100) nickel surface have been carried out in this work in order to compare with existing experimental results.

During the chemisorption, the oxygen chemisorbed atoms on (100) and (111) surfaces are firstly arranged in a (2×2) superstructure (the two dimensional crystallographical vocabulary is from [Wood 1964]), then $c(2 \times 2)$ and $(\sqrt{3} \times \sqrt{3})R30^\circ$ superstructures may form on (100) and (111) surfaces, respectively (see Fig. III.1 and Fig. III.2). The (2×2) means that the chemisorbed oxygen atoms are arranged in a superstructure that has dimensions that are twice those of the substrate unit mesh in two directions. For this reason, this superstructure is referred to as the (111) (2×2) superstructure or (001) (2×2) superstructure. Similarly, for a $(\sqrt{3} \times \sqrt{3})R30^\circ$, the two dimensions of the oxygen mesh are $\sqrt{3}$ times the corresponding sides of the substrate unit mesh and this oxygen mesh is rotated 30° with respect to the orientation of the substrate unit mesh, this superstructure is referred to as the (111) $(\sqrt{3} \times \sqrt{3})R30^\circ$ superstructure. Let us note that the first observation of a nickel (111) (2×2) oxygen superstructure was actually done by [Davisson and Germer 1927], in their pioneering paper

which founded electron diffraction. They found that on (111) nickel surfaces, in presence of adsorbed gas, a beam was observed which "could be accounted for as radiation scattered by a layer of gas atoms of the same structure and orientation as the nickel atoms, but of twice the scale factor." This is what is now known as the Ni (111) (2×2)-O superstructure.

The (100) (2×2) superstructure is also called (100) p(2×2) superstructure for the (100) surface. As it can easily be seen in Fig III.2, p stands for primitive (primitive (2×2) square) and c stands for centred (centred (2×2) square). The p(2×2) superstructure corresponds to a quarter of a monolayer coverage of oxygen atoms and the c(2×2) superstructure to a half a monolayer of oxygen.

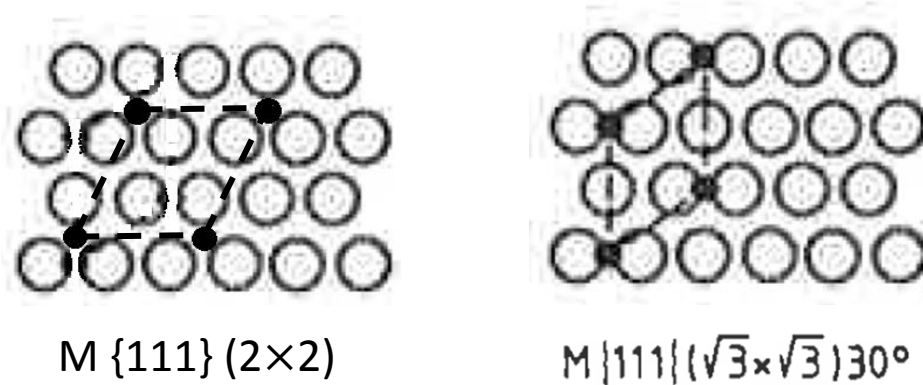


Fig. III.1 Sketch of a (111) (2×2) superstructure and a (111) ($\sqrt{3} \times \sqrt{3}$)R30° superstructure. Right image from [Lüth 2014]. For further details, see [Lüth 2014].

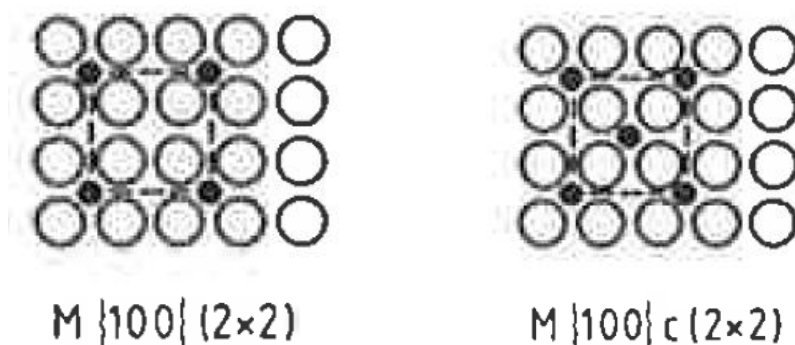


Fig. III.2 Sketches of a (100) (2×2) superstructure and a (001) c(2×2) superstructure. Image from [Lüth 2014]. For further details, see [Lüth 2014].

When oxygen interacts with a “clean” metal surface, a chemisorbed layer can form; Increasing the oxygen two dimensional (2d) coverage over a certain 2d density induces strong repulsive dipole forces so that the incorporation of cations into the adlayer become favourable to maintain a low access energy [Quinn and Roberts 1964]. Such a rearrangement within the surface adlayer is, therefore, the precursor of oxidation [Quinn and Roberts 1964]. This is the

second regime which corresponds to the epitaxial NiO nucleation of about two atomic layers thick. A well-known model for that nucleation is the ‘island model’, which describes the oxide formation as nucleation of islands and union between them [Holloway 1980]. Crystallographic oxide layers will then grow, very slowly, during hours and days: this is the last regime of the oxidation. A study carried out by [Cathcart et al. 1969] of the structural details of thin oxide films formed on the (100), (111), (110), and (311) surfaces of nickel shows that the oxide thickness produced were between 25 and 500 Å thick when oxidation temperatures ranged from 400° to 600°C. The oxidation mechanism could vary according to the metal surface structure, temperature and pressure. A lot of studies have been published using different experimental methods but will not be presented here.

3.1.3 Oxidation on Copper / air interface.

The copper oxidation will also be presented according to the three possible regimes: rapid chemisorption, oxide nucleation and epitaxy, and the final slow growth of the true oxide.

At the initial chemisorption stages of copper oxidation, both chemisorbed molecular O₂ and chemisorbed atom O are detected in the temperature range between 100 and 300 K [Spitzer and Lüth 1982]. Oxygen dissociation is observed by [Sueyoshi et al. 1996] and by [Wiame et al. 2007]. Wiame et al. found that oxygen molecules can be chemisorbed dissociatively on the Cu (111) surface with an initial sticking probability of $\sim 10^{-3}$ (at 300 K), for oxygen exposures lower than 10^5 L. At variance with the case of nickel for which no chemisorbed oxygen molecules are detected experimentally, chemisorbed states of oxygen are detected in copper. [Lou et al. 1994] found in their theoretical ab-initio (DFT) study the presence of two stable chemisorbed states of oxygen molecules on copper clusters and the absence of such states on nickel clusters. This is consistent with experimental findings. The adsorption of oxygen on copper can induce a small surface atom rearrangement on the (111) surface, and an obvious surface reconstruction at surface steps [Wiame et al. 2007].

During the second regime, epitaxial growth of copper oxide begins. Whereas only one type of bulk nickel oxide is known to exist, namely NiO (even if there are controversial claims of observation of Ni₂O), there are two main oxides for copper: cuprous oxide, Cu₂O, and cupric oxide, CuO (not to mention the rare paramelaconite Cu₄O₃ mineral). Bulk Cu₂O is cubic, space group *Pn3m*, Pearson symbol *cP12*. Bulk CuO is monoclinic, space group *C2/c*. According to the Ellingham-Richardson diagram (see note below), the oxidation of copper into Cu₂O should start for gas oxygen pressures (pO₂) above $\sim 10^{-51}$ Atm at room temperature

and be in thermodynamical favourable competition with the formation of CuO for pressures above $\sim 10^{-49}$ Atm. The early stages of oxide formation on copper will depend on the crystallographic nature of the copper surface, see for instance Lawless and Gwathmey 1956 (mentioned below). The first X-ray investigations of Cu₂O grown upon Cu actually started in the 1930's: Thompson in 1930, Mehl, McCandles and Rhines in 1934 and 1937, Preston and Bircumshaw in 1935, Brueck in 1936 and Thiessen and co-workers in 1937. It was found that if copper is oxidized at oxygen pressures below the equilibrium pressure for the formation of CuO, a uniform film of Cu₂O is formed, its rate of growth obeying the quadratic law (the thickness grows linearly with \sqrt{t} , this law is also known as the parabolic law) except for the very early stages of the oxidation [Jost 1960]. Rhodin concluded in 1950 that the celebrated Cabrera-Mott theory works for thicknesses in the range of 5-50 Å (as measurement under 5 Å was not accessible) and temperature between 78 to 300 K. [Gulbransen and McMillan 1952] found that Cu₂O is the essential oxide in the surface layer for oxidations in the temperature range of 200° to 400°C, with CuO forming during longer oxidation times at 400° and 500°C. These observations show that at temperatures of 200° to 500°C the cuprous ion diffuses through the Cu₂O structure. [Lawless and Gwathmey 1956] studied (001), (011), (111), (113), (112), (012), (122) and (133) surfaces, at 170° and 450°C, at pressures from 0.8 mm Hg to one Atm. They observed film thicknesses between 250 and 5000 Å. Both Cu₂O and CuO are formed above certain minimum thicknesses, the values of which depend on the Cu surface and on temperature. [Ertl 1967] found that there is a great difference in the reactivity of the different surfaces.

A familiar epitaxy is between Cu (100) and Cu₂O (111) surfaces. When oxygen is electrochemically deposited on the copper surface (100), Cu₂O forms a film with the (111) orientation. The resulting interface is atomically sharp and suspected to be semi-coherent. For surfaces other than (100), there would probably not be easy relations between Cu₂O and Cu. In natural oxidation in atmospheric condition, epitaxy will probably not occur as nicely as in the case of (100) electrochemical deposition. Another epitaxy orientation relationship has been proposed by [Menzel 1949], between Cu (113) and Cu₂O (110). (I have not had time to check it in my M.D. simulations.

Note on the Ellingham diagram, with the Richardson P_{O_2} axis.

As explained in many good textbooks of thermodynamics of materials (e.g. Lesoult 2010, in French, also see wiki), an Ellingham diagram shows the temperature and pressure

P_{H_2}/P_{H_2O}
 P_{CO}/P_{CO_2}
 Ω 0 température [°C] 500 1000 1500 2000
 1/10⁸ 1/10⁷ 1/10⁶ 1/10⁵ 1/10⁴ 1/10³ 1/10² 1/10¹ 1/10⁰ 1/10⁻¹ 1/10⁻² 1/10⁻³ 1/10⁻⁴ 1/10⁻⁵ 1/10⁻⁶ 1/10⁻⁷ 1/10⁻⁸ 1/10⁻⁹ 1/10⁻¹⁰ 1/10⁻¹¹ 1/10⁻¹² 1/10⁻¹³ 1/10⁻¹⁴ 1/10⁻¹⁵ 1/10⁻¹⁶ 1/10⁻¹⁷ 1/10⁻¹⁸ 1/10⁻¹⁹ 1/10⁻²⁰ 1/10⁻²¹ 1/10⁻²² 1/10⁻²³ 1/10⁻²⁴

cette droite n'est valable que pour des composés stoechiométriques.

2Cu + O₂ → 2CuO
 2Fe + O₂ → Fe₂O₃
 2Al + O₂ → Al₂O₃
 2Mg + O₂ → 2MgO
 2Zn + O₂ → 2ZnO
 2Na + O₂ → Na₂O
 2K + O₂ → 2K₂O
 2Ca + O₂ → 2CaO
 2Ba + O₂ → 2BaO
 2Sr + O₂ → 2SrO
 2Pb + O₂ → 2PbO
 2Sn + O₂ → 2SnO
 2Ni + O₂ → 2NiO
 2Co + O₂ → 2CoO
 2Mn + O₂ → 2MnO
 2V + O₂ → 2V₂O₅
 2Cr + O₂ → 2Cr₂O₃
 2Ti + O₂ → 2TiO₂
 2Zr + O₂ → 2ZrO₂
 2Hf + O₂ → 2HfO₂
 2Nb + O₂ → 2Nb₂O₅
 2Ta + O₂ → 2Ta₂O₅
 2W + O₂ → 2WO₃
 2Mo + O₂ → 2MoO₃
 2U + O₂ → 2UO₂
 2Th + O₂ → 2ThO₂
 2Ce + O₂ → 2CeO₂
 2La + O₂ → 2La₂O₃
 2Y + O₂ → 2Y₂O₃
 2Sc + O₂ → 2Sc₂O₃
 2In + O₂ → 2In₂O₃
 2Ga + O₂ → 2Ga₂O₃
 2Ge + O₂ → 2GeO₂
 2As + O₂ → 2As₂O₃
 2Sb + O₂ → 2Sb₂O₃
 2Bi + O₂ → 2Bi₂O₃
 2Pb + O₂ → 2PbO
 2Sn + O₂ → 2SnO
 2Ni + O₂ → 2NiO
 2Co + O₂ → 2CoO
 2Mn + O₂ → 2MnO
 2V + O₂ → 2V₂O₅
 2Cr + O₂ → 2Cr₂O₃
 2Ti + O₂ → 2TiO₂
 2Zr + O₂ → 2ZrO₂
 2Hf + O₂ → 2HfO₂
 2Nb + O₂ → 2Nb₂O₅
 2Ta + O₂ → 2Ta₂O₅
 2W + O₂ → 2WO₃
 2Mo + O₂ → 2MoO₃
 2U + O₂ → 2UO₂
 2Th + O₂ → 2ThO₂
 2Ce + O₂ → 2CeO₂
 2La + O₂ → 2La₂O₃
 2Y + O₂ → 2Y₂O₃
 2Sc + O₂ → 2Sc₂O₃
 2In + O₂ → 2In₂O₃
 2Ga + O₂ → 2Ga₂O₃
 2Ge + O₂ → 2GeO₂
 2As + O₂ → 2As₂O₃
 2Sb + O₂ → 2Sb₂O₃
 2Bi + O₂ → 2Bi₂O₃
 2Pb + O₂ → 2PbO
 2Sn + O₂ → 2SnO
 2Ni + O₂ → 2NiO
 2Co + O₂ → 2CoO
 2Mn + O₂ → 2MnO
 2V + O₂ → 2V₂O₅
 2Cr + O₂ → 2Cr₂O₃
 2Ti + O₂ → 2TiO₂
 2Zr + O₂ → 2ZrO₂
 2Hf + O₂ → 2HfO₂
 2Nb + O₂ → 2Nb₂O₅
 2Ta + O₂ → 2Ta₂O₅
 2W + O₂ → 2WO₃
 2Mo + O₂ → 2MoO₃
 2U + O₂ → 2UO₂
 2Th + O₂ → 2ThO₂
 2Ce + O₂ → 2CeO₂
 2La + O₂ → 2La₂O₃
 2Y + O₂ → 2Y₂O₃
 2Sc + O₂ → 2Sc₂O₃
 2In + O₂ → 2In₂O₃
 2Ga + O₂ → 2Ga₂O₃
 2Ge + O₂ → 2GeO₂
 2As + O₂ → 2As₂O₃
 2Sb + O₂ → 2Sb₂O₃
 2Bi + O₂ → 2Bi₂O₃
 2Pb + O₂ → 2PbO
 2Sn + O₂ → 2SnO
 2Ni + O₂ → 2NiO
 2Co + O₂ → 2CoO
 2Mn + O₂ → 2MnO
 2V + O₂ → 2V₂O₅
 2Cr + O₂ → 2Cr₂O₃
 2Ti + O₂ → 2TiO₂
 2Zr + O₂ → 2ZrO₂
 2Hf + O₂ → 2HfO₂
 2Nb + O₂ → 2Nb₂O₅
 2Ta + O₂ → 2Ta₂O₅
 2W + O₂ → 2WO₃
 2Mo + O₂ → 2MoO₃
 2U + O₂ → 2UO₂
 2Th + O₂ → 2ThO₂
 2Ce + O₂ → 2CeO₂
 2La + O₂ → 2La₂O₃
 2Y + O₂ → 2Y₂O₃
 2Sc + O₂ → 2Sc₂O₃
 2In + O₂ → 2In₂O₃
 2Ga + O₂ → 2Ga₂O₃
 2Ge + O₂ → 2GeO₂
 2As + O₂ → 2As₂O₃
 2Sb + O₂ → 2Sb₂O₃
 2Bi + O₂ → 2Bi₂O₃
 2Pb + O₂ → 2PbO
 2Sn + O₂

65

3.1.4 Environmental effects on the surface slip irreversibility

In air environment, a thin oxide film can be easily formed at the metal/air interface and could be the cause of the loss of fatigue resistance. Different mechanisms have been proposed in literature and reviewed by [Petit et al. 2003].

From the chemical point of view, as reactions with oxygen is supposed to be the dominant environmental effect, [Thompson et al. 1956] suggested that there is a strong interaction between oxygen atoms and highly strained material. High oxygen concentration would build up in slip bands, due to the presence of plasticity-induced vacancies and this would in turn lead to micro-crack initiation as illustrated in Fig III.4(a). [Shen et al. 1966] suggested that the presence of a deep oxide film on the surface could strengthen the surface and impede the vanishing of dislocations on the surface (creation of surface steps). As a consequence, dislocations would accumulate near the surface, induce pile-up stress field which trigger the formation of micro-cracks, as shown in Fig.III.4(b).

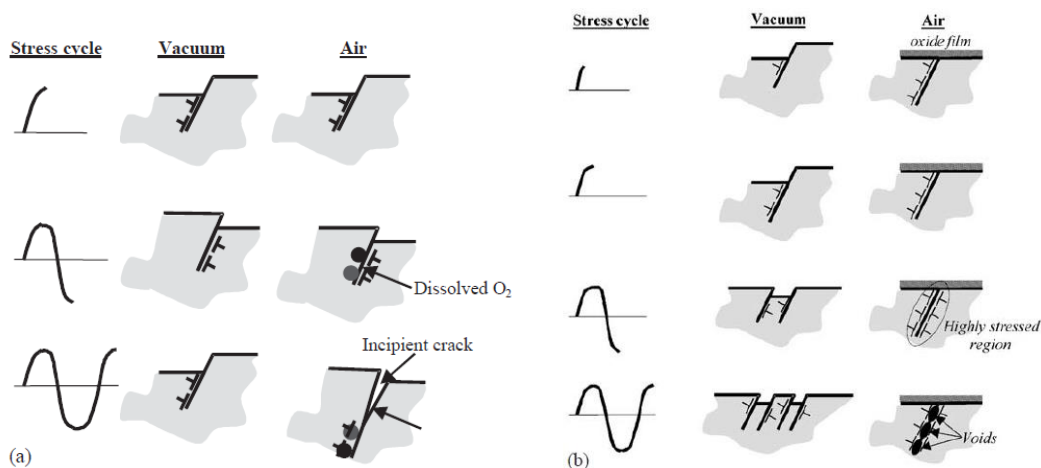


Fig.III.4. (a) Model for oxygen and slip band interaction in crack initiation (after [Thompson et al. 1956]; [Laird and Duquette 1971]; and (b) model of void initiation under oxide films (after [Shen et al. 1966]; [Laird and Duquette 1971]).

On the mechanical side, a proposed mechanism was based on the idea that the development of a surface film in air would constitute a source of irreversibility in cyclic deformation which prevents surface step re-welding during the compression part of the cycle. Re-welding of the surface steps in vacuum can be regarded as a mechanistic process to account for the longer fatigue lives. However, the relevance of the mechanism has been ruled out by several investigators such as [Laird and Smith 1963] and [Martin 1965]. These investigators believe that it is the crack growth, but not the crack initiation, which is delayed in the absence of atmosphere. It has also been noted by several workers [Thompson et al. 1956; Greenfield 1971; Finney and Laird 1975; Wang et al. 1984; Basinski and Basinski

1989; Witmer et al. 1987] that the development of PSB surface relief is the same for fatigue in inert environment as in air.

3.2 Computational simulations

Computer simulations are carried out in this work in order to study the surface oxidation, the surface step evolution and the micro notch formation in oxygen environment. In this section, a brief description is given for the simulation method we use. Molecular dynamics simulation are carried out using ReaxFF (Reactive Force Field) and/or COMB3 (Charge-Optimized Many-Body potential, style three) force fields within the LAMMPS code (Sandia Corporation, 2003, already introduced in section I.5). These potentials differ from the EAM type force fields which are employed to simulate pure metals in inert environment. Let us first mention that from a computational point of view, the ReaxFF and COMB force fields (potentials and forces, in MD) are much more time and memory consuming than the EAM potentials.

These two potential models, applied here, were developed to simulate interactions between different elements, viz. nickel and oxygen or copper and oxygen. In the bond order concept, these are two major potential families: the first family is the “pairs+3bodies+etc” family with possible ‘embedding functions’ which contains SW, F-S, EAM, MEAM and ReaxFF type potentials; the second is the “modulated pairs” family which contains Pettifor, Abel, Tersoff, REBO and COMB potentials. According to [Iwasaki 2004], one can say that these two families are mathematically equivalent.

Self-consistent charge equilibration is a scheme by which each atom can dynamically and autonomously determines its charge according to its local environment based on the principle of electronegativity equalization (EE). Based on this principle, there is an electronegativity equalization method (EEM) developed by Mortier, Gosh and Shankar in 1986, and an electronegativity equilibration (QEq) method developed by Rappe and Goddard III in 1991 which involves iterative charge equilibration. The ReaxFF type potentials uses EEM and the COMB type potentials uses QEq coupled with Tersoff potentials. The ReaxFF approach has been developed by Adri van Duin et al. (see ReaxFF, van Duin’s homepage, and [Senftle et al. 2016]). In the following work, ReaxFF sets developed for nickel and copper with oxygen are used. There are two styles of COMB potentials that I will use in the simulations of copper

with oxygen, COMB and COMB3, developed by [Shan et al. 2010] and [Liang et al. 2013], respectively with Simon Phillpot and Susan Sinnott. The subtle differences between COMB and COMB3 will not be developed here; we refer the interested readers to [Liang et al. 2013].

When we will study surface oxidation, one may raise the question that in these classical molecular dynamics potentials, the quantum tunnelling of electrons invoked in the Cabrera-Mott theory (for small thicknesses and relatively low temperatures, but up to 300K) is not explicitly treated. Yet, as for the role of directed electronic orbitals for nickel for example, one can say that the phenomenological potentials take into account these instantaneous quantum effects in an implicit and phenomenological way. The instantaneous quantum tunnelling phenomenon does not need to be described explicitly. One can say that it is implicitly adequately taken into account if these potentials of self-consistent charge equilibration scheme correctly describe the results of chemical reactions, oxidations, and picosecond time-scale evolution.

3.3 Oxidation on nickel surfaces

3.3.1 Ni and NiO physical properties

MD simulations are first carried out with ReaxFF to study the oxidation of nickel (111) and (100) surfaces. Different physical properties of Ni and NiO estimated by ReaxFF are compared with experimental and some ab-initio studies in Table III.1. Checking the thermal expansion of nickel, I found a linear thermal coefficient of $4.16 \cdot 10^{-5} \text{ K}^{-1}$ at room temperature (the measured value is $1.3 \cdot 10^{-5} \text{ K}^{-1}$) and a melting temperature between 1950 and 2000K (experimental melting temperature of 1728K). Checking the intrinsic stacking fault energy, I found a strongly negative value when it should be slightly positive ($\sim 120 \text{ mJ/m}^2$, cf. Table I.1).

		a	c_{11}	c_{12}	c_{44}	c'	B
Ni	ReaxFF	3.61	217.5	151.2	151.28	33.15	173.3
	Exptal (RT)	3.52	250.8	150.2	123.5	50.3	183.7
NiO	ReaxFF	4.28	308	-17.52		162.76	91
	H-F	4.26	399	127	115	136	214
	LSDA+U	4.19	396.7	74.7	86	161	182
	Exptal 71 0K	4.168	211	121	109	45	145
	Exptal 71 RT	4.177	224	94	109	65	137
	Exptal 72 RT	4.18	270	125	105	72.5	173
	Exptal 91 RT		345	139	40	103	205

Table III.1. Lattice parameter a (in Å) and stiffness elastic constants (in GPa) of Ni and NiO. The two cubic shear elastic constants are c_{44} and c' with $c' = (c_{11} - c_{12})/2$. The isotropic incompressibility is measured by the bulk modulus $B = (c_{11} + 2c_{12})/3$. ReaxFF values are taken from Assowe Dabar's PhD work 2012. NiO Exptal 71: [Du Plessis et al. 1971], NiO Exptal 72: [Uchida and Saito 1972], NiO exptal 91: [Wang et al. 1991], as weighted average values from four sets of values showing some dispersion. NiO H-F (Hartree-Fock): [Towler et al. 1994], NiO LSDA+U: [Dudarev et al. 1998]. The Ni and NiO ReaxFF needs to be improved in the future.

Experimentally, NiO is a little less stiff than its metallic Ni counterpart, which is probably due to the orientational d bounding in nickel. But the difference between NiO and Ni is not drastic. Neither Hartree-Fock [Towler et al. 1994] nor DFT [Dudarev et al. 1998] appear to predict good elastic moduli (B , c_{44} and c'). Within ReaxFF, NiO has a much stiffer c' shear constant than Ni (five times larger) but a much lower incompressibility B (almost twice smaller). So one cannot say it is absolutely stiffer or softer. When the surface of Ni is only slightly oxidised, it thus seems there is no strong reason to expect a strong behaviour difference with respect to surface step reconstruction at ambient temperature. True nickel is ferromagnetic until its Curie temperature which is 627K. Oxygen diatomic molecules have a magnetic moment. Yet, these magnetic interactions are negligible with respect to the chemical

interactions. NiO is a system with strongly correlated electrons, which forces theoreticians to introduce a completely empirical parameter in their ab initio density functional theory (DFT) scheme, viz. the famous +U Hubbard term, giving rise to various models such as LSDA+U, LDA+U, GGA+U, see [Dudarev et al. 2010, Yu et al. 2011].

True NiO is rhombohedral below its Néel temperature (523K) with an almost fcc structure ($\alpha_R = 60.4^\circ$ at room temperature). An NiO unit cell structure is presented in its cubic approximation in Fig. III.5.

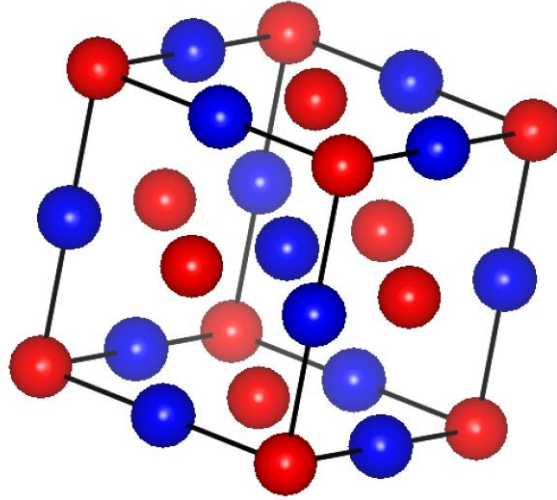


Fig. III.5. NiO structure shown as cubic. Drawn with the VESTA software. No perspective. Nickel atoms are in red, oxygen atoms are in blue, with the same size. The structure is fcc with a motif (an atomic basis) of two atoms per node: one Ni and one O separated by a $[0.5,0.0,0]$ vector. The conventional cubic cell contains 8 full atoms, hence the Pearson $cF8$ symbol (cubic, Face (centred), 8 atoms). The $\{100\}$ atomic planes are stoichiometric. The $\{111\}$ atomic planes are either nickel or oxygen planes.

3.3.2 Oxidation of the nickel $\{111\}$ surface

Nickel $\{111\}$ surface oxidation is first analysed and will be compared to other studies. The simulation box configuration is presented in the following image (Fig. III.6). The X, Y and Z axes are oriented according to $[1-10]$, $[111]$ and $[11-2]$ directions, respectively. The lattice periodicities in these three directions are $a_x = a_0/\sqrt{2}$, $a_y = a_0\sqrt{3}$, $a_z = a_0\sqrt{3/2}$. The dimensions of the nickel crystallite are $14a_x \times 4a_y \times 14a_z$ which equals to $35.74 \times 25.01 \times 61.9 \text{ \AA}^3$ with 4704 atoms ($a_0 = 3.61 \text{ \AA}$, taken from ReaxFF). Periodic boundary conditions

are applied to all directions, but a vacuum space 122 Å large is introduced in the Y direction, which will be filled with oxygen molecules. The nickel Y surface ((111) surface) will be in direct contact with oxygen molecules. 1190 oxygen diatomic molecules (O_2) are introduced in that vacuum space. They are initially put at regularly spaced positions but they rapidly disorder during MD simulation. They fill the space and start to get in contact with the (111) nickel surface after about 3 ps, see Fig. III.6. Simulations are carried out at 300K and 600K. The same interaction mechanism, to be described below, is found between oxygen and nickel surface at these two temperatures. Oxygen atoms simply penetrate deeper into nickel at higher temperature or higher pressure. The temperature and pressure effects will be discussed in details later. We consider the simulations carried out at 600K as an example to describe oxygen-nickel interaction mechanisms.

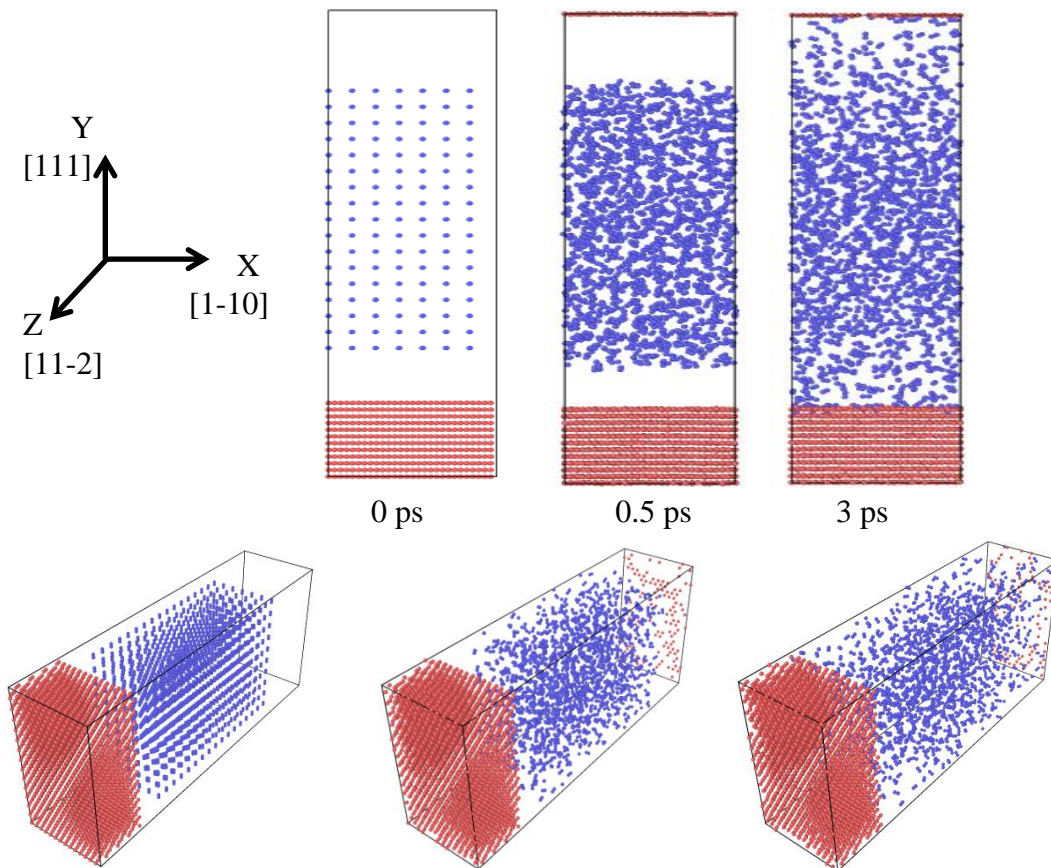


Fig. III.6. The simulation system at 0 ps, 0.5 ps and 3 ps, at 300K, with three projected views along the Z direction and three perspective views. The red dots are the nickel atoms and the blue dots are the oxygen atoms. Periodic boundary conditions are applied in all three directions.

The temperature and oxygen pressure are kept constant during the simulation. Both nickel and oxygen are maintained at a temperature of about 600K. An offensively gross estimation of the oxygen gas pressure, using the perfect gas equation, gives a value of about 0.6 kbars. At the beginning of the simulation, oxygen molecules are placed quite far away from the nickel surfaces (17 Å from the topmost surface and 25 Å from the bottommost surface) so that the oxygen molecules have time to relax and transfer into a random distribution in space before reaching the metal surfaces. The equations of motion are integrated with a time step of 1fs, so that the oxygen molecules only reach the nickel surfaces after about 3000 time steps of MD equilibration. The initial velocities of system are chosen from a Maxwell-Boltzmann distribution corresponding to the required temperature.

Once an oxygen molecule gets on the nickel surface, it dissociates into two oxygen atoms very rapidly, typically within 5 femtoseconds. No stable state of chemisorbed oxygen molecule on the (111) nickel surface is observed, in agreement with ab-initio and experimental observations mentioned in the previous 3.1 section. The number of dissociated chemisorbed oxygen atom increases very fast during the first 10 ps. Then the interaction rate decreases gradually. The adsorption rate depends on the number of particles striking the surface per second and on the so-called ‘sticking coefficient’, which is the probability that an impinging particle actually sticks to the substrate at a location without previously adsorbed oxygen. With the augmentation of the number of absorbed oxygen, the sticking coefficient decreases, and one can see oxygen molecules bouncing back.

Adsorption becomes very difficult once the oxygen coverage reaches nearly 0.35 monolayer, which suggests a (111) ($\sqrt{3} \times \sqrt{3}$)R30° superstructure. By following the dynamic process, we observed that adsorbed oxygen atoms have the tendency to put themselves into ($\sqrt{3} \times \sqrt{3}$)R30° superstructures: some regular areas can be easily identified as shown in Fig. III.7, after 56 ps for instance. This superstructure becomes more and more regular during the simulation. Let us note that I did not observe the (111) (2×2) superstructure at the beginning of the oxidation dynamics, most certainly because our pressure and temperature conditions do not allow this superstructure to develop.

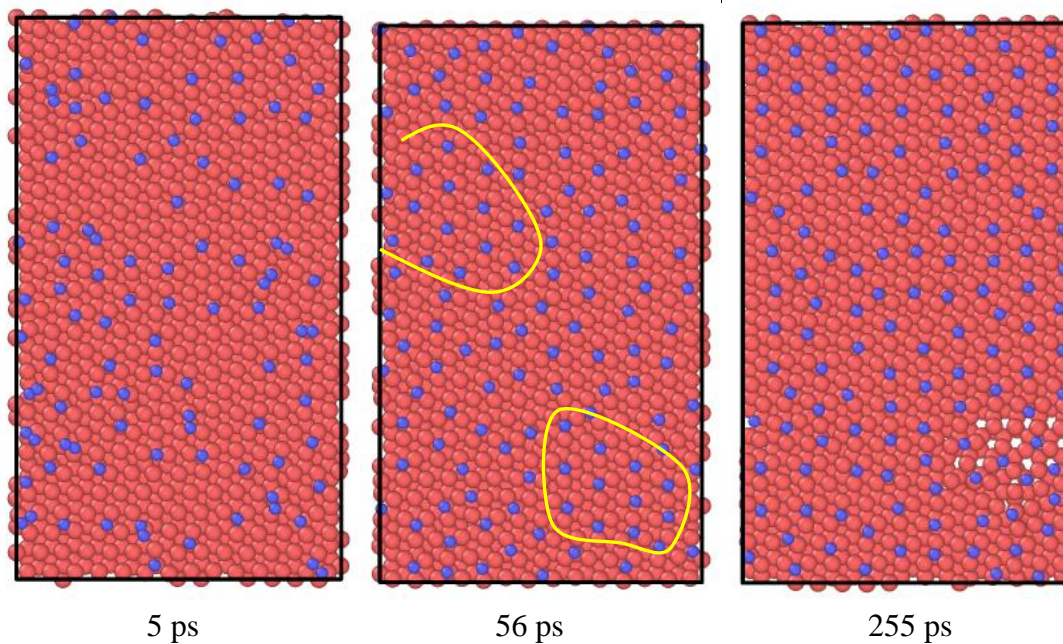


Fig. III.7. Surface oxide structure observed at 5 ps, 56 ps and 255 ps. $(\sqrt{3} \times \sqrt{3})R30^\circ$ structures can be identified at 56 ps and become more regular at 255 ps. Three and only three (111) nickel layers are presented to take into account the (111) ABC stacking. As some nickel atoms have diffused outwards at 255 ps, there are some holes in the third snapshot.

An relatively correct $(\sqrt{3} \times \sqrt{3})R30^\circ$ superstructure observed at time 56 ps is enlarged in Fig. III.8. Blue atoms are oxygen atoms. The light red and the yellow atoms are the topmost nickel atoms. The nickel atoms on the layer below are in dark red and the third layer atoms are in purple. I coloured some topmost nickel atoms in yellow in order to better show the superstructure. In this snapshot, the oxygens are more or less in interstitial sites over the topmost nickel atoms.

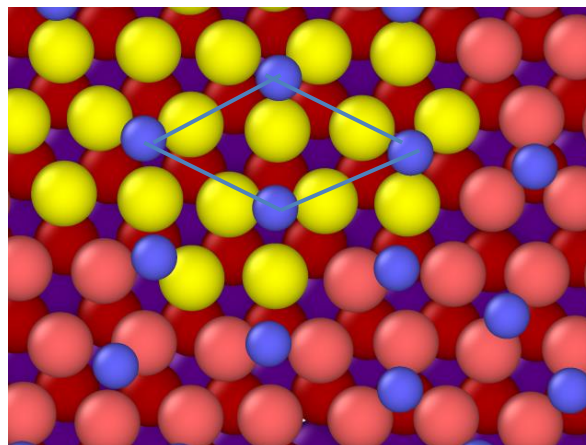


Fig. III.8 An enlarged observed Ni (111) $(\sqrt{3} \times \sqrt{3})R30^\circ$ superstructure as observed at time 56 ps. Oxygen atoms are more or less in interstitial sites, as expected (compare with Lüth's text book).

Oxygen atoms can penetrate into the bulk together with adsorption. Some nickel atoms can diffuse outwards, which induces an additional external growth (see Fig. III.9). According

to the Cabrera-Mott model, for a thin oxide film (less than 3 nm), electrons tunnel from a metal to an adsorbed oxygen atom through an oxide film in order to equalize the electrochemical potential. This creates an electric field across the oxide film, which in turn allows metal ion transport to the top surface and anions inward transport through interstitial sites.

The absorbed oxygen atoms are located between nickel (111) layers. At 600K and 600 bars, oxygen atoms penetrate between the first two layers (nearly 5 Å) easily and rapidly. The penetration then becomes slower. After 2ns, some oxygen atoms have penetrated four atomic layers (nearly 1 nm). All the absorbed atoms are at interstitial sites between (111) planes and there is no obvious change in the nickel substrate except that some nickel atoms also diffuse outwards, after 0.25 ns. An external layer thus forms on the top of the topmost Ni layer (upper part of the nickel crystal), and below the lowest nickel layer (lower part of the nickel crystal), in the Y direction, since we have two free nickel surfaces, see Fig. III.9. The structure of this external layer is presented in Fig. III.10.

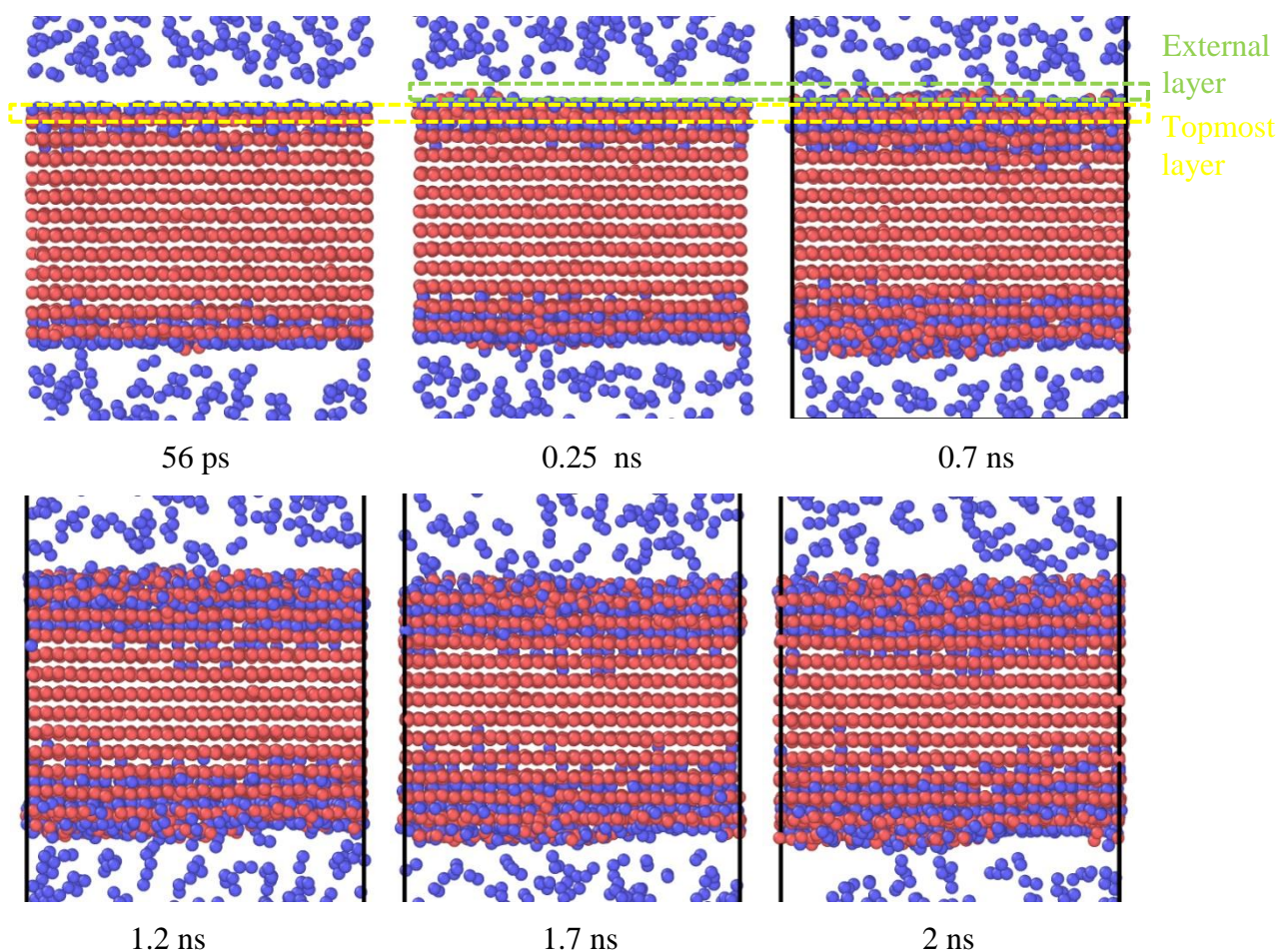


Fig. III.9 Time evolution of Ni (111) surface oxidation until 2 ns.

This external diffusion of nickel atoms produces point defects (vacancies) in the original topmost layer (meaning the topmost layer of the upper part of the nickel crystal and/or the bottom most layer of the lower part of the nickel crystal) and can disturb a little the nickel structure of that layer. The nickel structure of the sub surface layer is not disturbed. The nickel atoms on the new, external atom layer, are intermixed with oxygen atoms and the smallest distance between the nickel atoms is found to be nearly 3 Å, which is larger than the 2.55 Å in the nickel fcc substrate. This distance of nearly 3 Å is the smallest distance between nickel atoms in a perfect cubic NiO structure at 600K (with a cubic lattice parameter nearly equal to 4.2 Å). This clearly suggests the nucleation of monolayer islands of pre-NiO structure as can be seen in Fig. III.10. As we unfortunately could not carry out MD simulations on times longer than 2 ns with our 7084 atoms using ReaxFF (4704 Ni + 2380 O), we only observed the chemisorption regime and the beginning of the 2d stage corresponding to NiO island nucleation at the free surface.

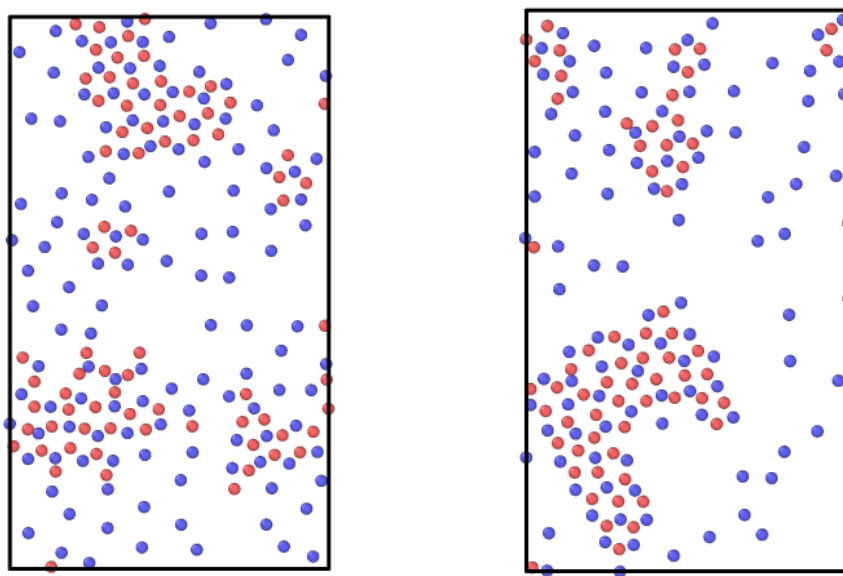


Fig. III.10 Structures of the highest and the lowest external layers with quasi NiO bi-dimensional germs after 2 ns at 600K.

To evaluate the distribution of nickel and oxygen atoms in function of their position in Y, the nickel and oxygen densities are now plotted along the Y direction, see Fig. III.11 with the same colour code, the red curve corresponds to nickel atoms and the blue curve to oxygen atoms. The small ‘peaks’ at each end corresponds to the atoms on the two external layers. There are nearly the same numbers of Ni and O on the external layers, which corresponds to the 1:1 stoichiometry of a (100) plane of NiO.

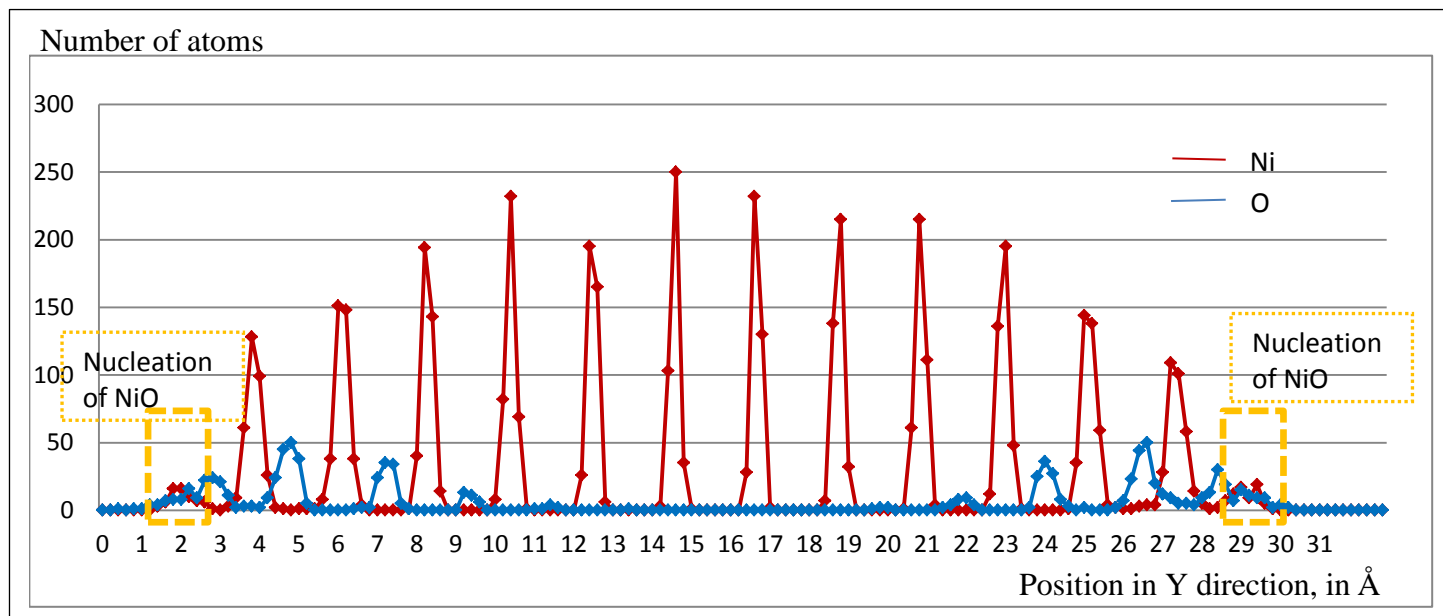


Fig. III.11. Distribution of nickel and oxygen atoms along the Y ([111]) direction, in Å, at 600K. In order to draw this atom distribution, the simulation box is cut by slices of 0.2 Å in the Y direction. The number of atom is counted in every slice and presented by diamond symbols. The symbols are intentionally linked to clearly ‘show’ the atom layers. Every ‘peak’ corresponds to an atom layer. There are twelve initial nickel layers and two external layers corresponding to NiO nucleation.

3.3.3 Oxidation of the nickel {100} surface

Similar simulations have been carried out with nickel {100} surface. The X, Y and Z axes are oriented according to [100], [010] and [001] directions, respectively. The dimensions of the nickel substrate are $50.54 \times 21.66 \times 50.54 \text{ Å}^3$ ($14a_0 \times 6a_0 \times 14a_0$) with a total of 4704 nickel atoms. Periodic boundary conditions are applied to X, Y and Z directions, with a vacuum space of 125 Å in the Y direction. 1440 oxygen molecules are introduced in that vacuum space, as shown in Fig. III.12. As in the previous case, oxygen molecules are initially put in regular positions but rapidly disorder. They fill the space almost immediately and get in random contact with the two (010) surfaces. Both 300K and 600K temperatures are tested and same interaction mechanisms are observed as previously for (111) surface. We also choose to describe the simulations carried out at 600K for the sake of comparison. The temperature and oxygen pressure are kept constant during the simulation. The pressure is again nearly 600 bars.

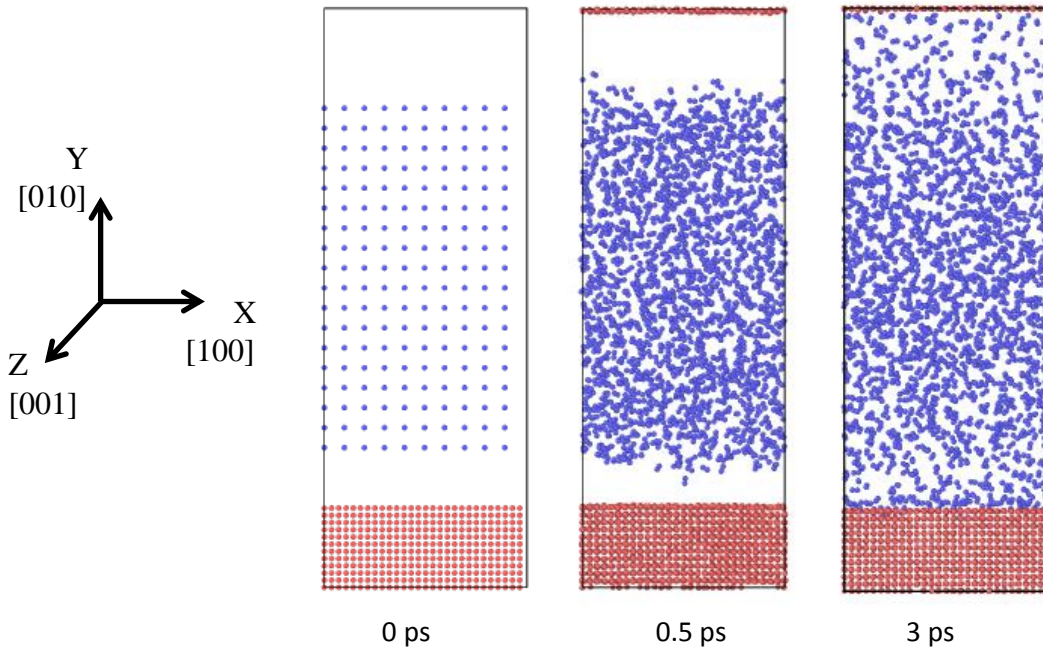


Fig. III.12. The simulation system at 0 ps, 0.5 ps and 3 ps, with three views along the Z direction. Red dots are nickel atoms and blue dots are oxygen atoms. Periodic boundary conditions are applied in all three directions.

Dissociative chemisorption takes place very rapidly and a (100) $c(2 \times 2)$ superstructure, corresponding to a surface oxygen coverage of 50%, is observed, at least locally, and becomes more and more regular, see Fig. III.13. No (100) $p(2 \times 2)$ superstructure corresponding to a surface oxygen coverage of 25% (see section 3.1.1) has been observed at the beginning of the oxidation dynamics, most certainly because our pressure and temperature conditions do not allow this superstructure to develop.

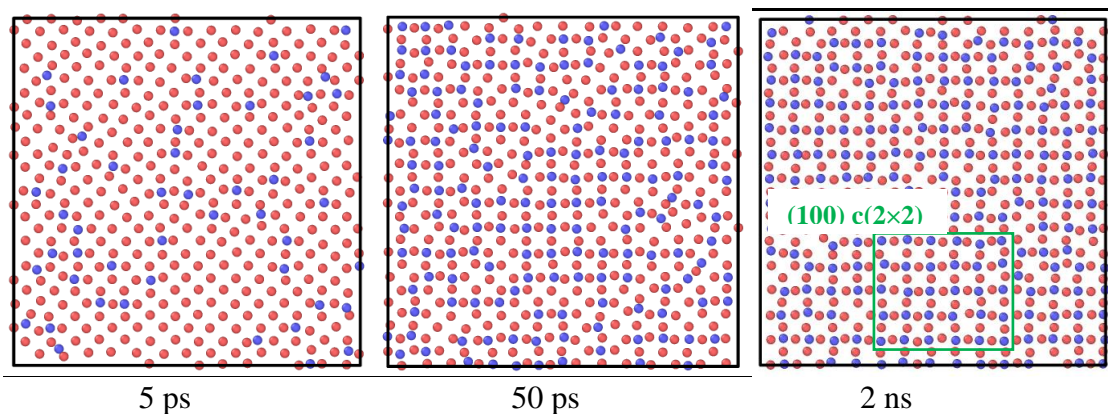


Fig. III.13. Surface oxide superstructure during the oxidation at 5 ps, 50 ps and 2 ns. (010) $c(2 \times 2)$ superstructures progressively appear, at least locally: an example of this structure can be seen in the green rectangle in the 2 ns snapshot. Only the topmost nickel layer is presented. Oxygen atoms are on the top of the nickel atoms.

A side view of nickel (010) surface oxidation is presented in Fig. III.14. Oxygen atoms penetrate until the fourth layer (corresponding to a depth of 5.4 Å), after 1 ns. No further penetration is observed between 1 and 2 nanoseconds. Contrary to the Ni {111} surface case, oxygen atoms absorbed in the bulk are in the same (010) planes as the nickel atoms, but those adsorbed on the topmost layer are above the nickel plane. Another difference between this {010} surface oxidation and the {111} surface oxidation is that only a few nickel atoms have diffused outwards and no NiO small island has formed as an external layer (Fig. III.14).

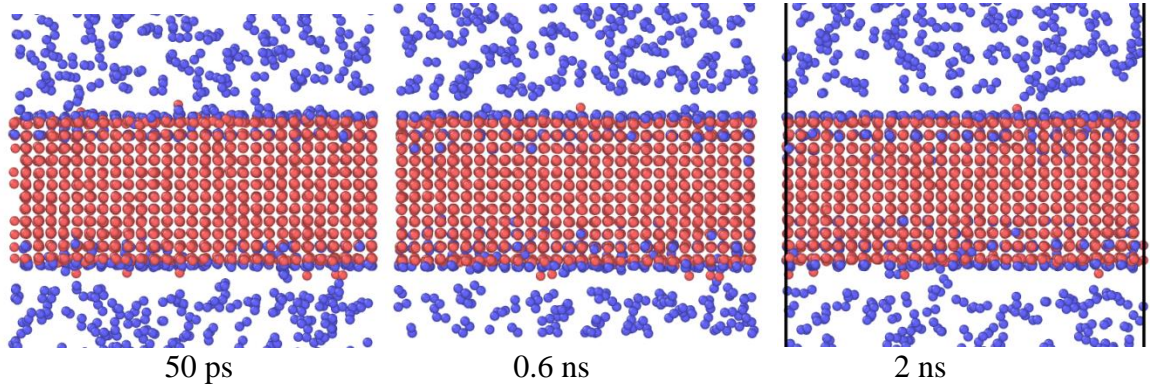


Fig. III.14 Time evolution of Ni (010) surface oxidation until 2 ns

The number of atoms depending on their position in Y is plotted in Fig. III.15. the red curve corresponds to nickel atoms and the blue curve to oxygen atoms. No external growth has taken place in this case. The topmost nickel layer has a high oxygen coverage which is nearly 0.55.

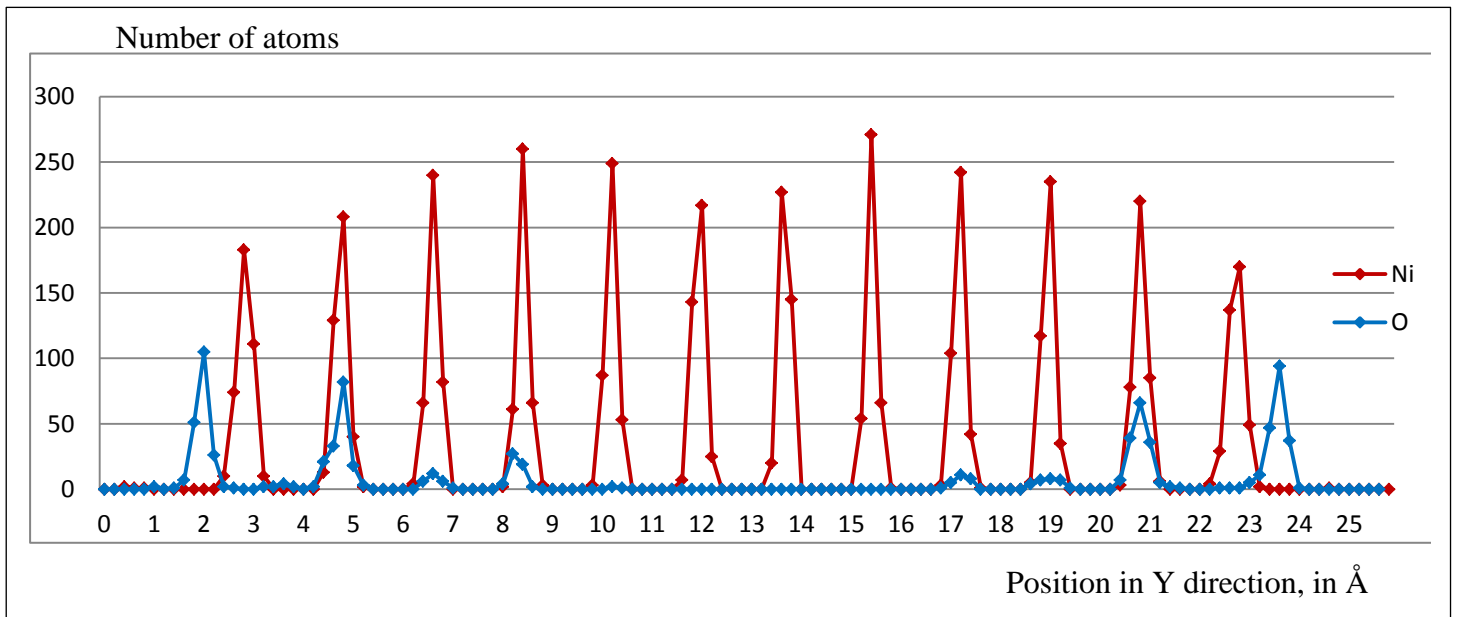


Fig. III.15 Distribution of nickel and oxygen atoms along the Y direction by slices 0.2 Å thick for the (100) surface system. Red and blue ‘peaks’ represent nickel and oxygen layers, respectively. There are 12 nickel layers.

3.3.4 Discussions about the oxidation of the Ni (111) and (100) surfaces

One can confirm that oxidation kinetics is dependent on the crystallographic orientation of the metallic surface, a fact which is experimentally well known since a pretty long time, for copper and nickel for instance.

In our simulations the thickness of the oxide layer of a Ni(111) is about 1 nm after 2ns, but only 0.5 nm for a Ni(100) after the same period of time for the same temperature and pressure conditions, in agreement with [Muñoz-Márquez et al. 2004] who found that the rate of increase in the oxide film thickness on Ni(111) is more rapid than on Ni (100). The difference in the oxidation kinetics for the various surfaces is tentatively attributed by Muñoz-Márquez et al. to the anisotropy in the ionic diffusion through the growing oxide layer. Furthermore, after 2 ns in our simulation, there are already NiO nucleation on the (111) surface together with an external growth. For the (100) surface, only a few atoms diffused outwards and NiO is not nucleated. [Liu et al. 1982] performed studies at temperatures up to 300°C using Auger electron spectroscopy. They found that the initial, essentially isotropic chemisorption phase is followed by oxidation which is highly anisotropic with the {111} surface oxidising most rapidly and the {100} surface most slowly. They suggested that the associated ease of oxide nucleation on the (111) surface relative to {100} is related not to differences in the size of critical nuclei on the surfaces, but to the relative lack of structural blocking of adsorption produced by the chemisorbed layer on {111} compared to {100}.

For both (111) and (100) surface, high coverage superstructures seem more stable at 600K and high pressure. Low oxygen coverage superstructures are not observed in both cases. Once the stable coverage is accomplished, oxidation rate drop down.

Similar results have been found at 300K with the same simulation boxes. At 300K, interaction between oxygen and nickel occurs more slowly and oxide layer thickness is thinner at the end of the 2 ns than at 600K. We have to note that for a simulation at 300K, not only the temperature is lower, but also the pressure is decreased because the pressure depends on the oxygen molecules temperature.

I also found that chemisorbed oxygen atoms are not in the same plane as nickel atoms on the (100) surface but are in the same plane in bulk (100) planes (see Fig. III.15). Conversely, nickel and oxygen atoms are in the same plane on (111) surfaces, but in different planes in bulk (111) planes (Fig. III.11).

To conclude, oxygen chemisorption is observed with different superstructures on (100) and (111) surfaces and the beginning of the NiO nucleation is observed on the (111) surface. These results are in overall agreement with experimental results discussed in section 3.1. Therefore, we can say that this ReaxFF model gives a fairly good estimation of the first stages of nickel oxidation. It can be applied to the (113) surface to study the reversibility of nickel surface steps in oxygen environment.

3.4 Irreversibility of nickel surface steps in oxygen environment

Similar simulations as in Chapter 2 will be repeated in oxygen environment in order to analyse the oxygen effect on the surface roughness and surface step reversibility. Before the execution of simulations with oxygen, tests are carried out in inert environment with ReaxFF to check that it gives the same mechanisms in inert environment as EAM type potentials do. I found that it similarly gives rise to dislocation motions towards the surface and surface step reconstructions.

The simulation system in oxygen environment is the same as in the previous chapter except for the presence of oxygen molecules. The X, Y and Z axes are oriented along [-131], [714], and [11-2], respectively. Vacuum spaces are created along X and Y (and bulk periodicity only applies on Z). So the right and left free surfaces are (-131) surfaces. Oxygen molecules are introduced in the void space of the simulation box as usual, see Fig. III.17 initial configuration. Simulations have been carried out at both 300K and 600K. The oxygen pressure turns out to be nearly 450 bars at 600K.

Simulations are first carried out between bulk nickel substrate and oxygen at 600K, during 2ns, to form oxide layers on the two (-131) surfaces. A temperature of 600K is chosen in order to accelerate the interaction rate. The system will then be cooled down to 300K, which corresponds to room temperature (RT), and we will insert dislocations and analyse surface step irreversibility at RT. An obvious limitation of MD simulation is that only the first stages of oxidation (chemisorption and first NiO embryo nucleation) can be simulated. Yet it is possible that during an experimental fatigue test, only the first oxidation stages have the time to be performed during cyclic loading. To be able to compare our simulations with experimental studies about the first stages of oxidation and fatigue tests, the exposure of nickel to oxygen is calculated on nickel (111) surface for instance. A table is given below (see table III.2). In our simulation, with a pressure of nearly 10^8 Pa during 2ns, the exposure is nearly 1500 L (Langmuir). For a VHCF of frequency of 10,000 Hz at natural atmospheric

conditions (hence a partial oxygen pressure of 0.2 Atm), the exposure is 15,000 L during one cycle. This fatigue exposure is ten times larger than in our simulation. However, by extrapolating our simulation results, we found that the regime of the starting of the nucleation of NiO island is still to be considered at 15,000L, equivalent as at 1500L. A stable epitaxy growth needs a much longer time. Fig. III.16 corresponds to an oxidation process between nickel and oxygen. The horizontal axis is time and the vertical axis gives the number of oxygen atoms chemisorbed. That number increases very rapidly at the beginning, when the nickel surface is still clean. It then increases much less rapidly, and even slowly after 1 ns.

We can thus say that the condition of our simulations should be comparable with the ones of VHCF tests on the point of view of the oxygen exposure. Of course the time of exposure differs strongly between the MD simulations and experimental ones. That difference should affect more Ni and O diffusion processes than the adsorption ones.

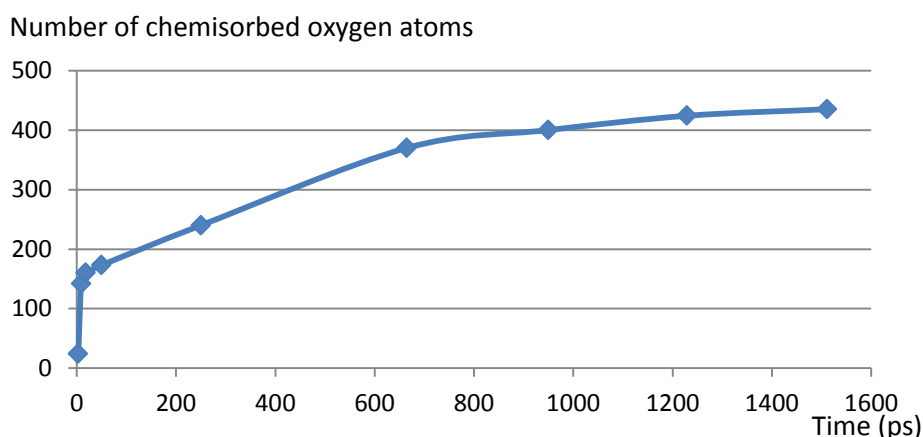


Fig. III.16 Number of chemisorbed oxygen atoms on a nickel (111) surface as a function of time, at 600K.

	pressure	time	Oxygen exposure
MD simulation	10^8 Pa	2 ns	1500L
One cycle of mechanical fatigue tests	Atm (10^5 Pa)	10^{-4} to 1 s	15000L – $1.5 \cdot 10^8$ L
Experimental studies of the first stages of oxidation	10^{-4} Pa	20 min	900L

Table. III.2. A comparison of oxygen exposures for an MD simulation, typical mechanical fatigue tests and typical experimental first stage oxidation studies. Fatigue tests are usually from 1 to 10,000Hz. The exposure time for each cycle is thus 10^{-4} to 1s. The values of experimental study of the first stages of oxidation are taken from [Wiame et al. 2007].

Surface step reconstruction is first tested in oxygen environment at five different temperatures, from 10K to 700K, see Fig. III.17. An initial configuration with a 2b large surface step is geometrically prepared. Snapshots are taken at each temperature after 30 ps. It is found that the surface step is reconstructed at all temperatures in oxygen environment, as in inert environment. The oxidation and surface reconstruction take place at the same time and the surface step reconstruction is even slightly accelerated, probably because oxygen atoms disturb nickel atoms positions, which facilitates the step reconstruction. From these snapshots, one also sees that oxygen penetrates deeper with the augmentation of oxygen gas temperature and pressure.

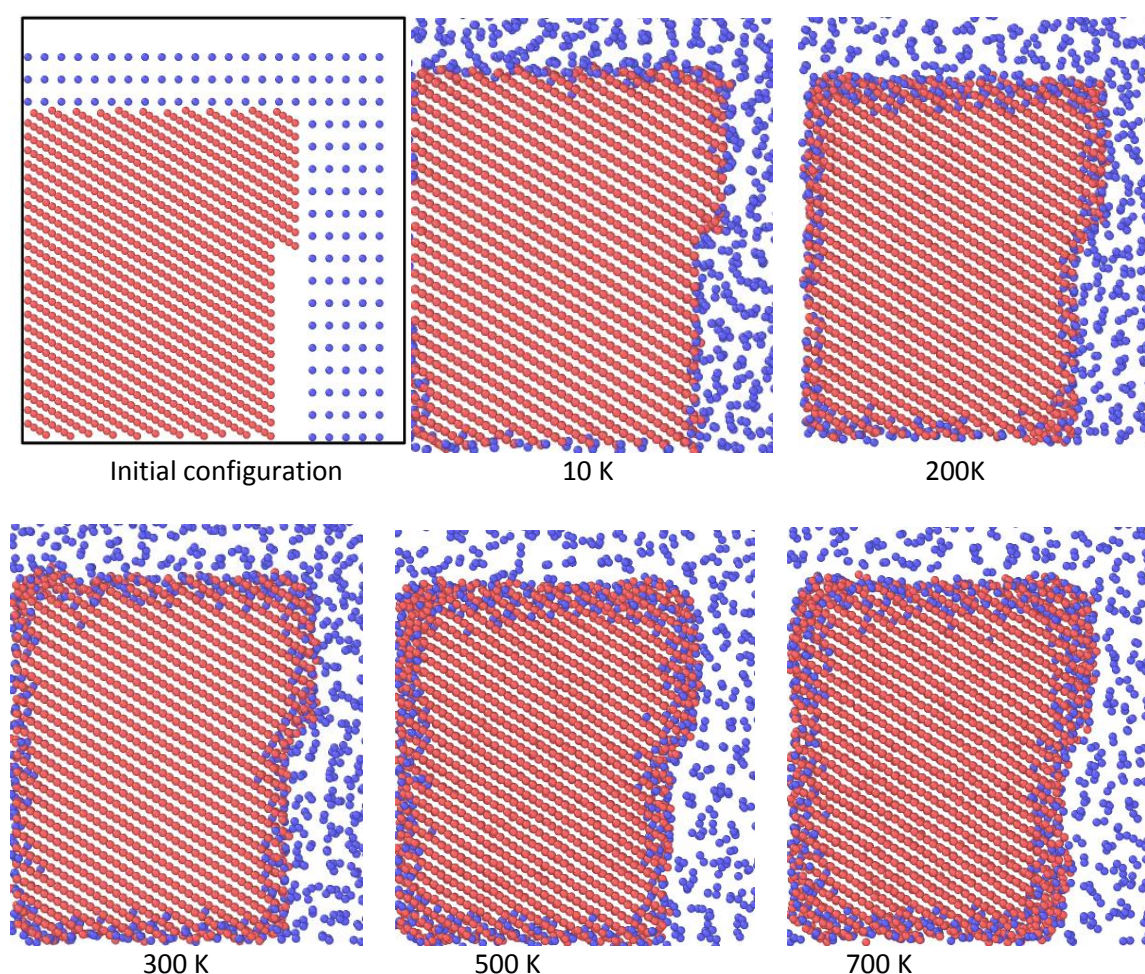


Fig. III.17 Surface step reconstruction at different temperature after 30 ps in nickel with oxygen.

These simulations have been carried out with geometrically prepared surface steps in order to ease the visualization of step reconstruction. In real fatigue condition, steps should be created by gliding of dislocations toward an already oxidized surface. In the following, I first

let surface oxidation occurs, and only then will dislocations be inserted in the bulk and glide to the oxidized surface.

The oxide layer formed at 600K after 2 ns is presented in Fig. III.18. Oxygen molecules are dissociatively chemisorbed on nickel (113) surface and the oxygen atoms penetrate through a thickness of nearly 6 Å. Some nickel atoms diffuse outwards, which induces an external growth. The distribution of nickel and oxygen atoms as a function of their position along X is presented in Fig. III.19. The numbers of Ni and O are nearly the same for the external layer, which suggests NiO nucleation. The (113) atomic planes are relatively sparse, (low atomic planar density) with very small distances between them ($a/\sqrt{11}$) (see chapter 2). This, together with thermal motion at 600K explains why the nickel red curve never goes to zero in the substrate in Fig. III.19. The max-min contrast will be larger at a lower temperature such as 300K: see Fig. III.23. The position of some nickel atoms at surface area are slightly disturbed by chemisorptions of oxygen atoms. By removing oxygen atoms (Fig. III.18, right picture), one can see more clearly the disturbed nickel surface. I note and insist that this perturbation is rather small and the nickel atoms still retain their fcc environment (this is at variance with what we will observe with COMB3 copper, see section 3.5)

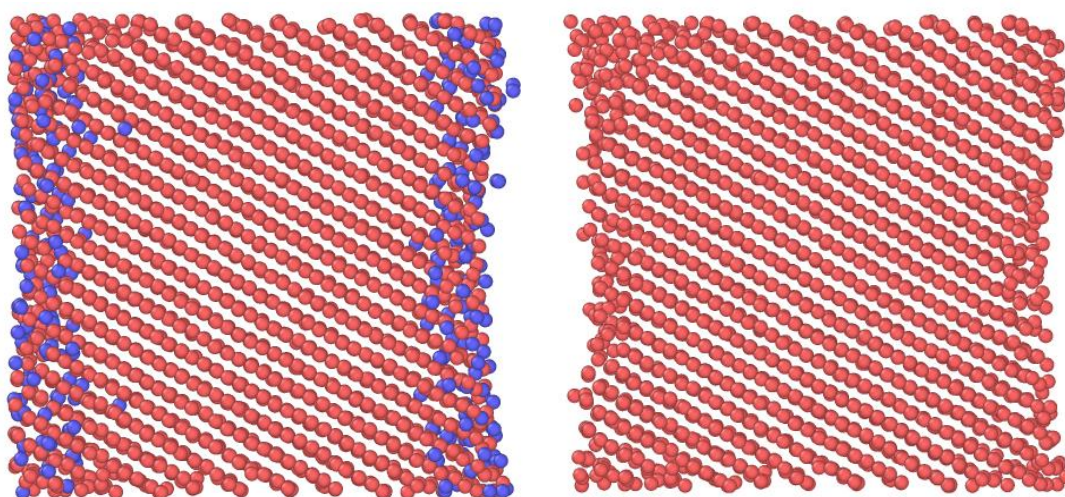


Fig. III.18 Nickel (113) surface oxide layer at 600K after 2ns (left), and the same configuration shown without oxygen atoms. Nickel atom positions at both (113) surface are slightly disturbed.

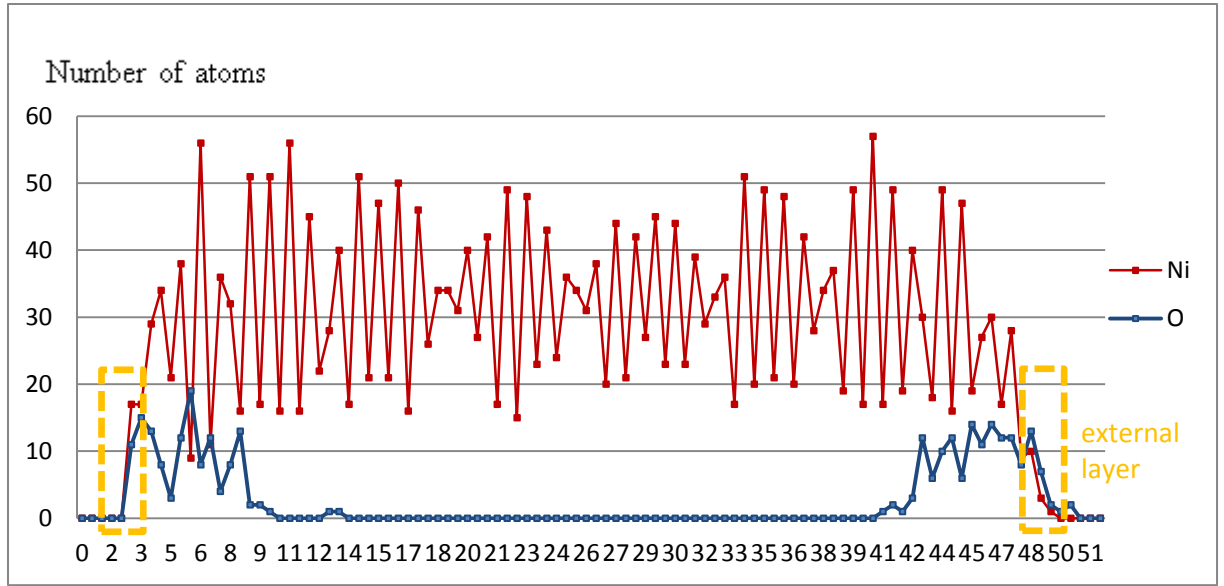


Fig. III.19. Distribution of nickel and oxygen atoms along the X [-131] direction at 600K after 2ns (see snapshot in Fig.III.18). There are 39 initial nickel planes in X direction, the slices are 0.2 Å thick (see Fig. III.11 caption).

Dislocations are then introduced in the bulk near the free surface as shown in Fig. III.20. For the simulations in inert environment, once a dislocation is introduced near a perfect pure nickel free surface, it is attracted to that surface (see chapters 1 and 2), and no extra loading is needed for the gliding of the dislocation towards the surface. In the present simulation with an oxidized nickel surface, dislocations are no longer attracted to the surface and an extra loading is needed to let the dislocations glide to the surface.

In order to check whether this behavioural change is directly, or indirectly due to the presence of the oxygen atoms, we re-use the same initial atomic configuration as in figure III.20, with an inserted dislocation, but removing the oxygen atoms and keeping the surface nickel atoms in their relatively disordered states. The dislocation is not spontaneously attracted by the surface. This sounds reasonable since the design of the surface image force requires elasticity applied on a perfect crystalline surface. Oxygen atoms are light, compared to the nickel atoms, and play no significant role on the physical interaction exerted or not exerted by the surface on the dislocation. The role of the oxygen atoms was chemical, to disorder the positions of the surface nickel atoms with which they chemically interacted. This, I believe, is a nice illustration of the difference between ‘physical’ interaction and ‘chemical’ interaction.

Although the surface image force is changed because of oxidation, dislocations can always glide to the surface under a small stress and disappear at the surface (Fig. III.20). A surface step can be created, and reconstruct afterwards, similar to the mechanism observed in

inert environment. To visualize nickel step reconstruction in “oxide” layer, some atoms at surface step appearance area are coloured in order to follow their movement (Fig. III.21). Some nickel atoms in plane A are coloured in pink and those in plane B are coloured in yellow. The dislocation core glides to the surface in plane B. We can see in Fig. III.21 that at the beginning of the reconstruction, some nickel atoms in plane A drop to B, and some atoms in plane B can drop to C. This movement will continue until a lower and stable surface energy is obtained, as for the case in inert environment. It is found that oxygen atoms also change their positions during the step reconstruction which means there should be chemical bond breaking and reforming between oxygen and nickel during surface step reconstruction.

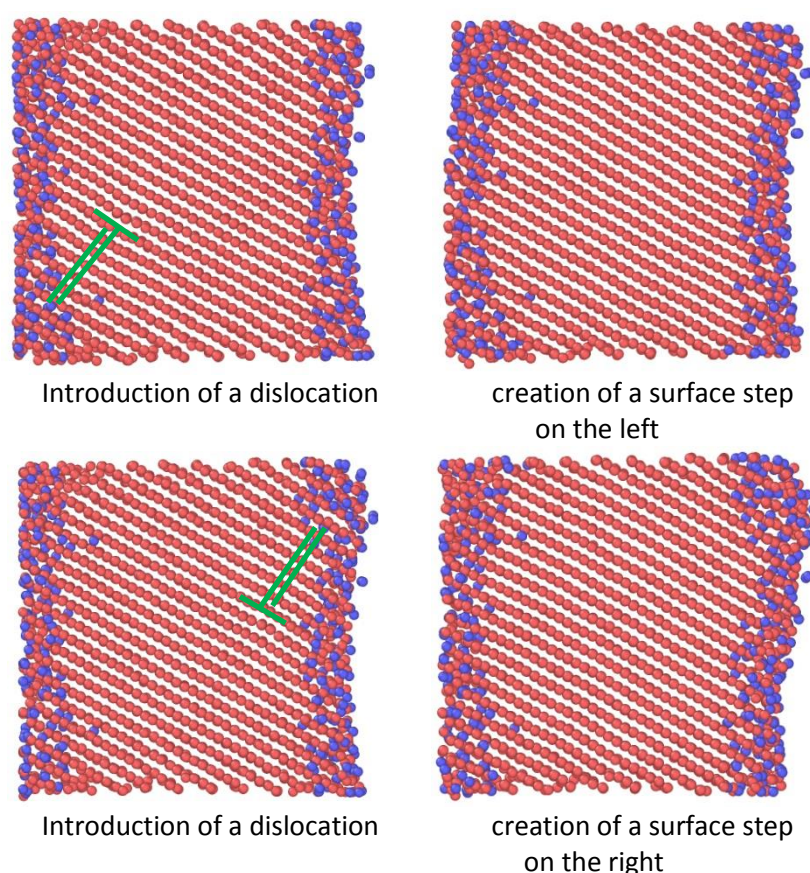


Fig.III.20. Gliding of dislocations under compression towards oxidized surface, creation and reconstruction of surface steps. The green lines represent dislocations. The dislocation in the lower configuration is inserted in front of a surface small NiO island.

One of the dislocations inserted (the lower one in Fig. III.20) is intentionally positioned in front of a surface small NiO island and the step will appear at the position of this island. The other one (the upper one in Fig. III.20) is positioned at a place where there is no small NiO island. No obvious difference on surface irreversibility is found between these two cases. Other simulations have been done by inserting dislocations at different places to investigate a

large number of configurations and ensure this observation. One can thus say that neither the oxide layer nor a nucleated small NiO island impede the appearance of surface steps and their reconstructions. I must stress that in these simulations, the nucleated NiO islands are extremely small, up to about one to two nanometres in size (see Fig.III.10).

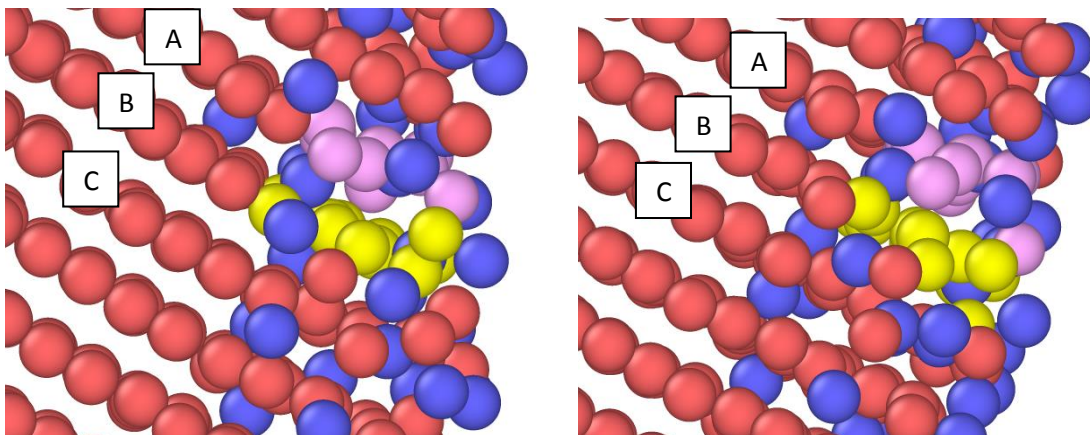


Fig. III.21. The beginning of nickel surface step reconstruction in oxide layer.

To simulate the small micro notch initiation, opposite sign dislocations are successively inserted in not direct neighbour planes, and glided to oxidized nickel surface at 300K. As can be seen in Fig. III.22, a small micro notch is initiated, as in inert environment. The oxide layer at 300K is thinner than the one obtained at 600K. Since oxide layers have no significant effect on surface step reconstruction and surface relief evolution, this simulation was carried out at 300K in order to be in more comparable conditions with experimental fatigue tests. The MD relaxation time after each insertion of a dislocation was about 1 ns. The oxygen and nickel distributions are plotted along the $[-131]$ direction at 300K after 1 ns (Fig. III.23). The plot is quite similar to the one obtained at 600K after 2 ns (Fig.III.19).

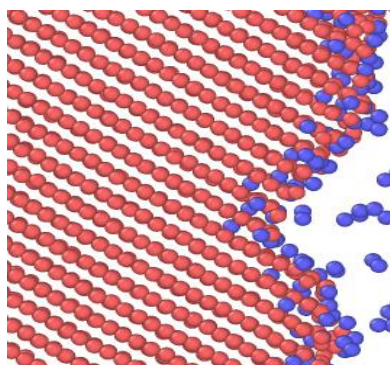


Fig.III.22. Nucleation of a surface micro notch at 300K in oxygen environment. Six opposite sign dislocations are inserted in the bulk in not direct neighbouring (111) planes for the initiation of this micro-notch.

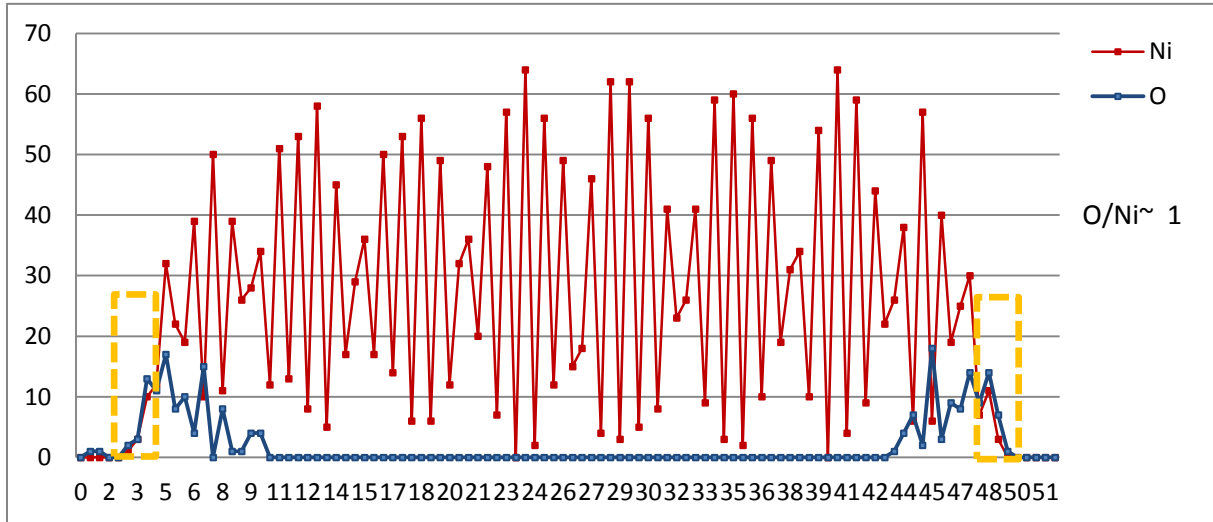


Fig.III.23. Distribution of nickel and oxygen atoms along the $[-131]$ direction for systems with (-131) surfaces, checked after a 1 ns MD simulation at 300K.

In short, what is observed about the ‘irreversibility of nickel surface steps in oxygen environment’ are the following ones:

- The step reconstruction, i.e. the disappearance of a geometrically built surface step, is slightly accelerated in presence of oxygen.
- A very thin oxidised layer does not attract a nearby dislocation, by contrast with what a pure crystalline surface does. Yet the oxidised layer does not prevent the dislocation to glide in response to loading or unloading. When the dislocation reaches the oxidised layer, it is very rapidly reconstructed.
- The surface roughness is not changed and the irreversibility factor is almost not affected by environment for the studied potentials and durations up to 2 ns. This, of course, only holds for surface relief evolution. It is in agreement with some experimental observations [Wang and Mughrabi 1984; Basinski et al. 1992] that the surface relief in PSBs is the same in inert environment as in air.
- It is also worth noting that the presence of oxygen environment does not prevent the nucleation of surface micro notches by the same mechanism we found during cyclic loading in inert environment in section 2.4.

3.5 Copper surface oxidation using both COMB3 and ReaxFF.

In the previous sections (3.3 & 3.4), my MD LAMMPS-ReaxFF simulations thus showed that nickel oxidation mechanisms (dissociative-chemisorption, NiO germ nucleation) are similar on {111} {100} and {113} surfaces, even if there are some differences on oxide superstructures, oxygen coverage, oxide layer thickness and epitaxial growth, due to the differences in surface crystallography. To avoid redundancy, only oxidation on copper (-131) surface is discussed in this section. The aim is to check the copper (-131) surface oxidation mechanisms as compared with those of nickel with the same surface and to similarly analyse the surface step irreversibility of copper in oxygen environment.

Two atomic models exist for copper with oxygen, viz. COMB3 and ReaxFF (see section 3.2). I will use both of them, at different temperatures. Results will be compared with experimental observations, ab-initio simulations and nickel oxidation. The simulation system is the same as for the nickel oxidation simulations.

3.5.1 Cu and Cu₂O physical properties

The cubic lattice parameters and elastic constants for Cu and Cu₂O (cuprous oxide) are gathered in Table III.3. Cupric oxide, CuO, is monoclinic. ReaxFF current descriptions Cu are restricted to a simple pair potential description which forces the Cauchy relation $c_{12}=c_{44}$. ReaxFF has been primarily developed to study superficial chemical reactions and not bulk properties. This ought to be improved in the future. COMB3 is more successful to describe copper. The two available sets of experimental stiffness constants for the cuprous oxide are more consistent than for nickel oxide but are not too well reproduced by COMB3 (and are difficult to estimate with ReaxFF). Yet, for Cu and Cu₂O, one can say that Cu is stiffer than Cu₂O. Although, we deal with neither bulk NiO nor bulk Cu₂O per se in this Ph.D. work, it is interesting to note that none of these two oxides are stiffer than their pure metal counterparts, the contrary being true for Cu₂O vs. Cu. The T_m values predicted by ReaxFF and COMB for copper are about 1450 K and 1300 K respectively, reasonable comparable with the experimental value 1358 K. As these potential dependent T_m values are not too far from the experimental T_m , we shall indicate our simulated temperatures T numerically in Kelvins rather than in reduced units (T/T_m).

		a	c_{11}	c_{12}	c_{44}	c'	B
Cu	ReaxFF	3.72	225.4	119.8	119.8	52,8	155
	COMB3	3.61	179.14	123.69	48.06	27.72	142.17
	Exptal 0K	3.61	176.2	124.9	81.8	43.1	142
	Exptal RT	3.615	168.4	121.4	75.4	46	137
Cu ₂ O	COMB3	4.49	34.31	21	39.24	6.65	25.43
	Exptal 0K	4.27	121±5	105±4	10.9±.3	8±5	110±2
	Exptal RT		126.1	108.6	13.6	9.05	114

Table III.3. Lattice parameter a (in Å) and stiffness elastic constants (in GPa) of Cu and Cu₂O. The two cubic shear elastic constants are c_{44} and c' with $c' = (c_{11}-c_{12})/2$. The isotropic incompressibility is measured by the bulk modulus $B = (c_{11}+2c_{12})/3$. ReaxFF and COMB3 values are calculated at 0 K. Experimental values are given as extrapolated at 0 K (Exptal 0K) and at 300 K, viz. room temperature (Exptal RT). Cu Exptal 0K and RT: [Simmons and Wang 1971], Cu₂O Exptal 0K: [Hallberg and Hanson 1970], Cu₂O Exptal RT: [Beg and Shapiro 1976].

3.5.2 Copper surface oxidation using COMB3 potential

There are three generations of COMB (Charge-Optimized-Many-Body) potentials, starting with Sinnott and Phillpot in 2007 [Yu et al. 2007]. One now consider COMB (COMB2) potentials, developed by [Shan et al. 2010] and COMB3 developed by [Liang et al. 2013] (see section 3.2). Several physical properties of metallic copper, molecular oxygen, cuprous oxide (Cu₂O), and cupric oxide (CuO) have been carefully verified with this potential [Devine et al. 2011]. Simulations in this section are mainly carried out with COMB3 potential because I found that COMB potential does not correctly predict oxygen chemisorption on copper surfaces: oxygen molecules all stay physisorbed on copper surface as O₂ molecules and at relatively large distances from the copper atoms, see Fig. III.24. Oxygen molecules are polarized in COMB (COMB2) potential; an oxygen molecule thus has a positive charge atom and a negative charge atom. With COMB3 potential, one has the choice to depolarized oxygen molecules. In this work, O₂ are depolarized for the simulations with COMB3 potential.

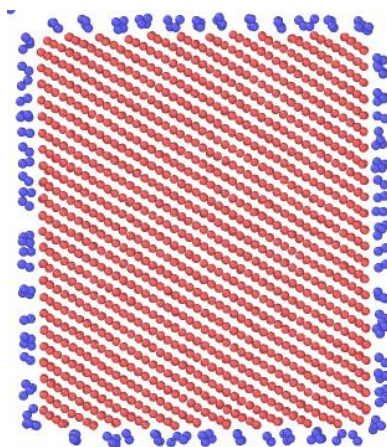


Fig. III.24. Physisorption of oxygen molecules on copper surface, at 300K, predicted by COMB (COMB2) potential.

Oxygen chemisorption is better predicted by COMB3 potential. Oxygen molecules are chemisorbed at a $\{113\}$ copper surface as shown in Fig. III.25. They do not dissociate but they disorder the surface copper atoms more intensely than in the case of nickel. It makes some copper atoms jump out from their initial position and migrate outwards. These movements induce an amorphous surface oxide layer which means that copper atoms are no longer close to their initial fcc positions. Oxygen molecules do not penetrate into the bulk during oxidation. Simulations at 300K and 600K provide the same results with no molecule dissociation being observed. Only relatively short 50 ps simulations are carried out here because the adsorption rate becomes much slower after 50 ps and will not change the final results.

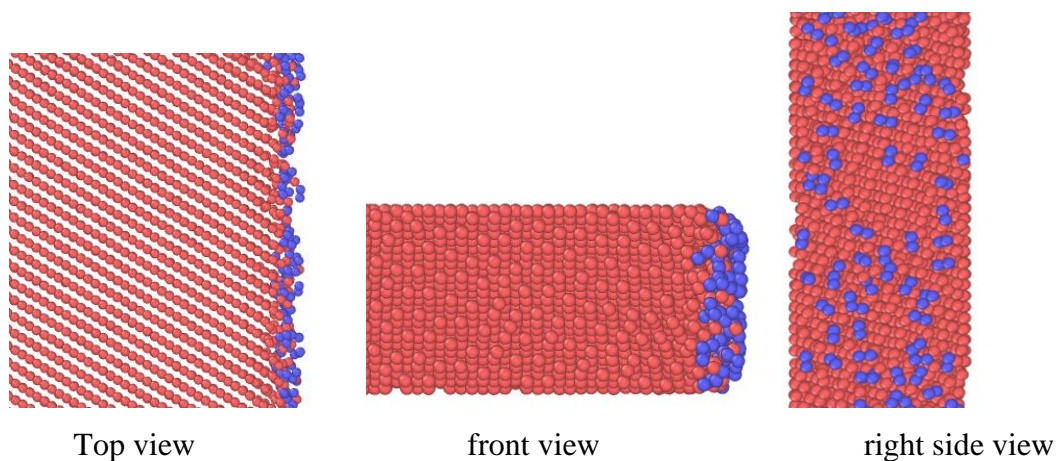


Fig. III.25: chemisorption of oxygen molecules at a (-131) copper surface at 300K after 50 ps with COMB3. No oxygen dissociation is observed. Simulations at 600K give similar results.

3.5.3 Copper surface oxidation using ReaxFF

Similar simulations have been carried out using the ReaxFF developed by Psofogiannakis and co-workers for copper [Psofogiannakis et al. 2015], at 300K and 600K. At 300K, oxygen is chemisorbed on the copper surface mainly as molecules but there are also several dissociations, see Fig. III.26. Adsorbed oxygen molecules do not disturb much the copper surface and are distributed quite homogeneously on the surface. Some dissociated oxygen atoms penetrate into the copper volume, albeit only slightly. At 600K, see Fig. III.27, oxygen is always adsorbed on metal surface mainly as molecules although more molecule dissociations occur than at 300K. The positions of copper surface atoms get slightly disturbed but these atoms still have an approximate fcc copper. Dissociated copper atoms can penetrate into the copper volume on a small thickness of nearly 2 Å.

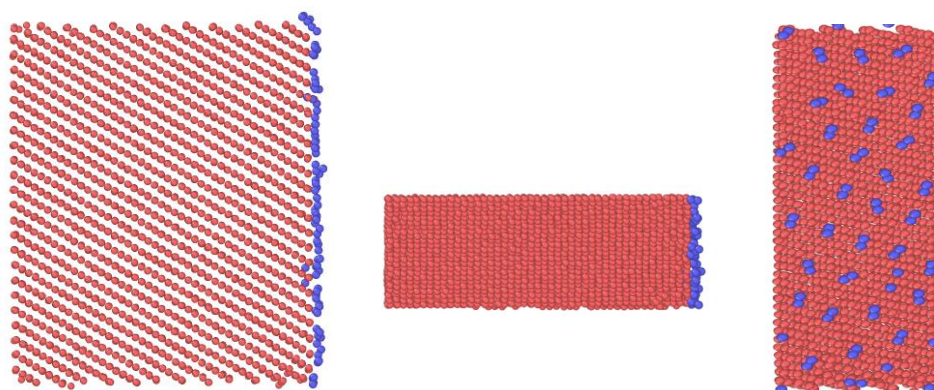


Fig. III.26. Chemisorption of oxygen molecules at a (-131) copper surface at 300K. Snapshot after 50 ps using ReaxFF. Dissociation of oxygen molecules is possible, yet rare.

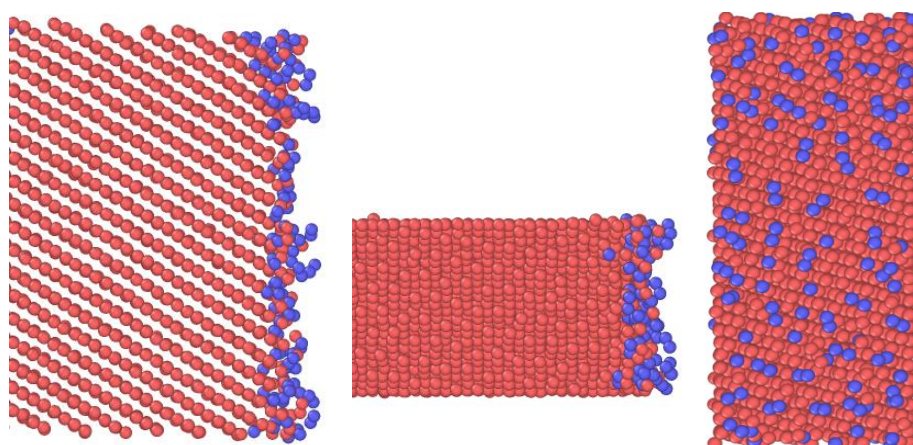


Fig. III.27. Chemisorption of oxygen molecules at a (-131) copper surface at 600K. Snapshot after 200 ps using ReaxFF. Several dissociations are observed and the copper surface is slightly disturbed.

3.5.4 Comparison between copper surface oxidation using COMB3 and ReaxFF

Both COMB3 and ReaxFF modellings predict the chemisorption of oxygen on copper at a (-131) surface mainly as molecules. COMB 3 gives no dissociation at both 300K and 600K. ReaxFF gives more oxygen dissociation, which seems more realistic as dissociations are widely observed experimentally at relatively low temperatures (see section 3.1). ReaxFF also predicts an acceleration of the oxidation rate with the increase of temperature from 300K to 600K.

With COMB3 potential, copper surface is disordered during oxidation. With ReaxFF, oxygen only slightly disturbs the copper surface. I found that this is probably because these two potentials give different prediction of adsorption sites of oxygen on copper, as shown in Fig. III.28. The two snapshots in the upper part present the oxidation of the (-131) copper surface predicted by M.D. simulations with COMB3 potential, after 30 ps and 50 ps. The snapshot in the lower part presents the oxidation as predicted with ReaxFF after 50 ps. Only one (-131) plane is presented for the sake of clarity and one can observe that it is made of well separated compact lines of atoms. Most oxygen molecule adsorption sites given by COMB3 are more or less the ‘bridge sites’ (double coordination, see Fig.III.28 and Fig.III.29) on these uppest lines of copper atoms. By contrast, the adsorption sites predicted by ReaxFF are mainly the ‘hollow sites’ (quadruple coordination, see Fig.III.28 and Fig.III.29) between these uppest copper lines. I believe this explains why ReaxFF oxygen has less effect on the surface atomic copper positions than the COMB3 oxygen system.

Neither CuO nor Cu₂O is nucleated in these simulations. It is because that only a few dissociated oxygen molecules are observed and further dissociation may need much longer time which cannot be reached in MD simulation. But there are reasons to believe that we are in similar situations as during fatigue tests, as explained in section 3.3.

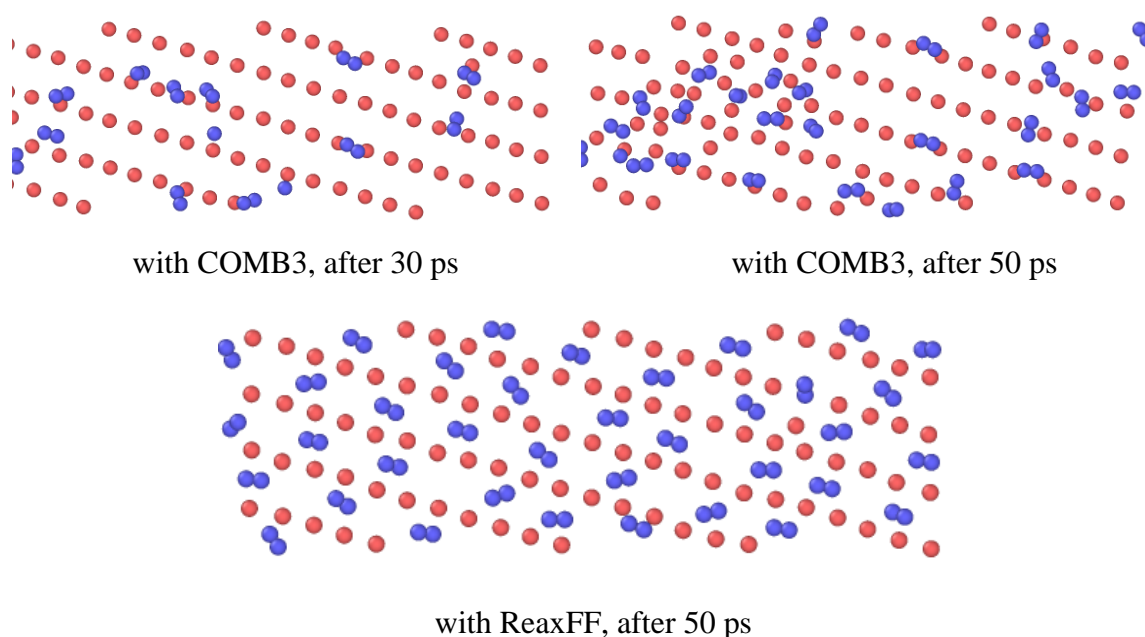


Fig. III.28. Oxygen molecules adsorption sites on a $\{113\}$ copper surface, as predicted by COMB3 and ReaxFF, at 300K. Oxygen molecules are absorbed on bridge sites with COMB3 and on hollow sites with ReaxFF.

3.5.5 Comparison between copper and nickel (-131) surface oxidation

By contrast with nickel oxidation, where oxygen molecule dissociation is almost immediate even at relatively low temperature (ambient), I mainly observed chemisorbed states of oxygen molecules on copper. This is in agreement with experimental and ab-initio studies. As described in the first section of this chapter (section 3.1), [Lou et al. 1994] found in an ab-initio (DFT) study the presence of two stable molecularly chemisorbed states of oxygen on copper (100) clusters, which do not exist for nickel and is consistent with experimental findings. This is also in agreement with [Devine et al. 2011] simulations with COMB3 potential, which found that if an O_2 is adsorbed in a ‘bridge site’ or a ‘hollow site’ between surface atoms, it remains as an O_2 molecule. Two such stable sites are shown in Fig. III.29. [Devine et al. 2011] also found that oxygen molecules only dissociate if they are on ‘top sites’ above a prominent copper atom of the surface. Both with COMB3 and ReaxFF, I found that oxygen molecules get chemisorbed at bridge or hollow sites between surface copper atoms. It seems that when an oxygen molecule gets close the copper surface, it tends to go to a bridge or hollow site rather than on the top of a prominent copper atom. This could be why dissociative chemisorption is very rare between oxygen and copper surfaces.

Chemisorbed oxygen molecules may also finally dissociate but it will presumably take a much longer time.

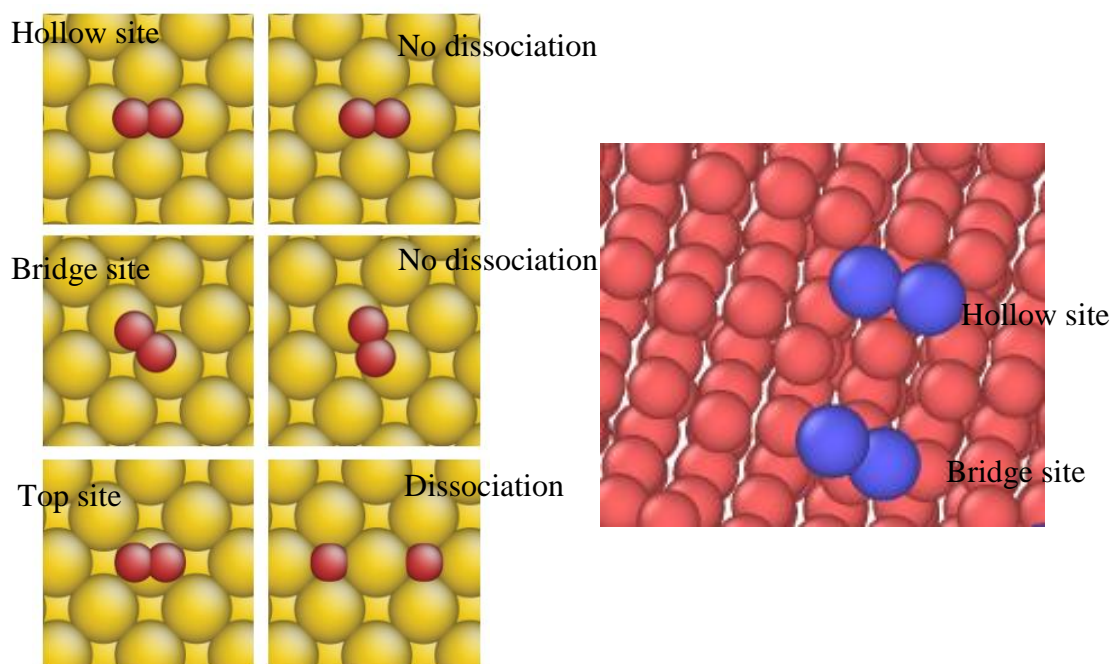


Fig. III.29: Adsorbed oxygen molecules on copper surfaces. Left part: two stable molecularly chemisorbed sites and a dissociative chemisorption site on a (100) surface, from [Devine et al. 2011]. Right part: an image from my simulation of a (-131) surface shows oxygen molecules absorbed in bridge and hollow sites.

3.6 Irreversibility of copper surface steps in oxygen environment.

3.6.1 Slip irreversibility and notch formation using the COMB3 potential

Dislocations are now inserted in the bulk of copper, with the usual geometry (see section 2.2), in order to analyse surface step irreversibility and notch formation in oxygen environment. Simulations are first carried out with COMB3 potential. Three dislocations are introduced successively and glide to the right disordered oxide layer, see Fig. III.30.

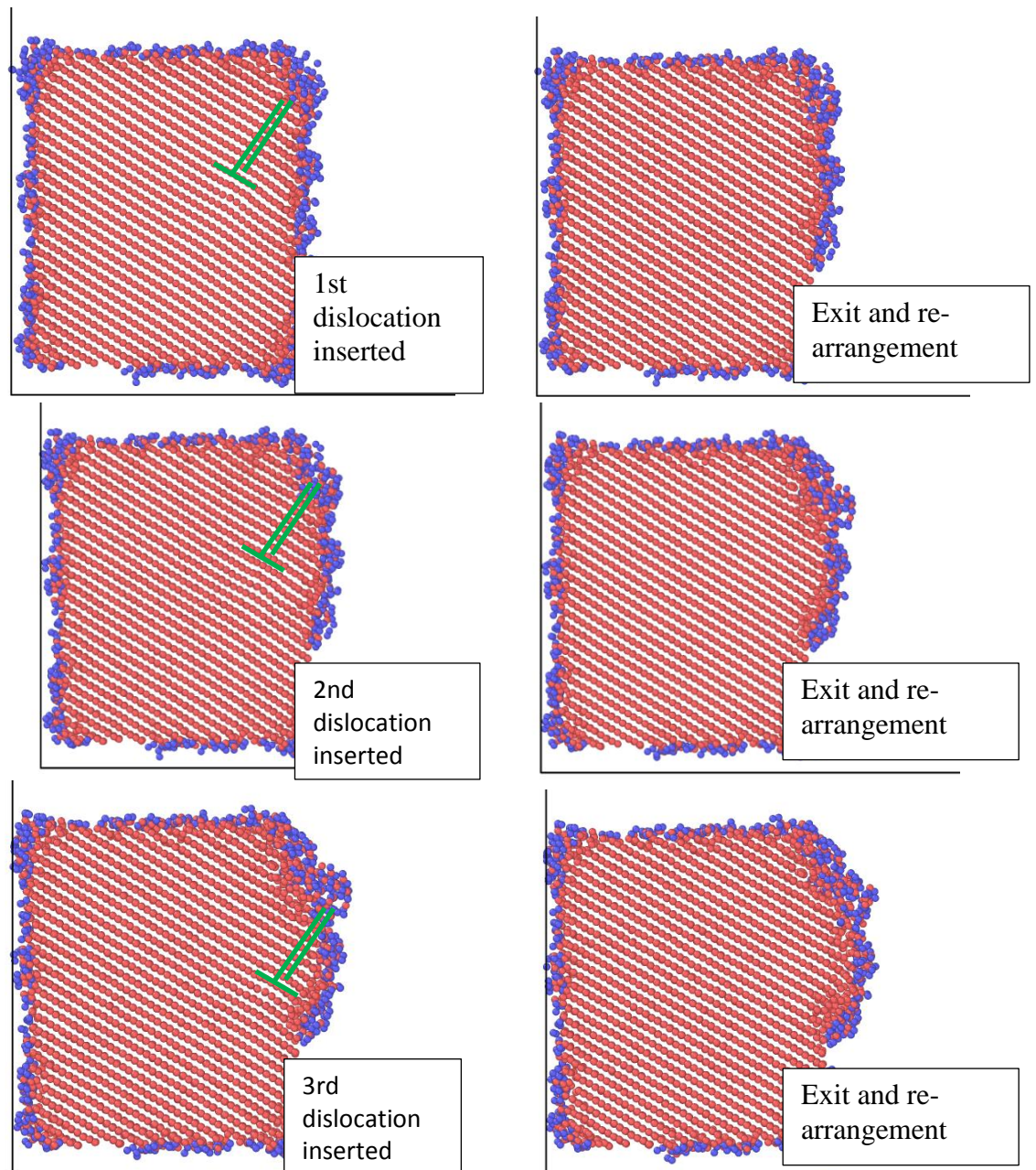


Fig. III.30. Gliding of dislocations towards a disordered surface oxide layer, in copper at 300K using COMB3 potential.

As already mentioned, there is a great disordering of the copper atoms in the oxide layer following the COMB3 predictions. Certainly as consequence, once a dislocation glides towards this amorphous oxide surface, a surface step cannot be created in the same way as in inert environment or in the case of Ni-O where nickel in the oxide layer essentially maintains a crystalline fcc structure. Let me try to propose the following interpretation. Although the concept of dislocation was developed by Vito Volterra in the context of polymers for continuous elastic media, a dislocation in a crystal is a localised defect defined as a defect with respect to some given atomic crystalline order (regular ordering of atoms). Hence, in our

case, when the edge $\langle 110 \rangle/2$ dislocation 'reaches' within the amorphous surface layer, the two extra atomic half planes which 'correspond' to that dislocation cease to transfer their 'extra' character (which was defined as a perfect crystalline order) and simply push outwards the atoms of the amorphous layer. The dislocation disappears inside the amorphous layer and creates a surface step whose extremity disorders and joins the amorphous layer. The amorphous layer gets thicker and thicker by absorbing more and more dislocations. This is what is observed in the copper-oxygen system in the set of pictures shown in Fig. III.30. As an obvious consequence, the disappeared dislocations cannot glide back under opposite loading and are thus fully irreversible.

Opposite sign dislocations are then inserted three planes apart from the previous dislocation and glide to the same surface. A small micro notch can be initiated as usual (Fig. III.31).

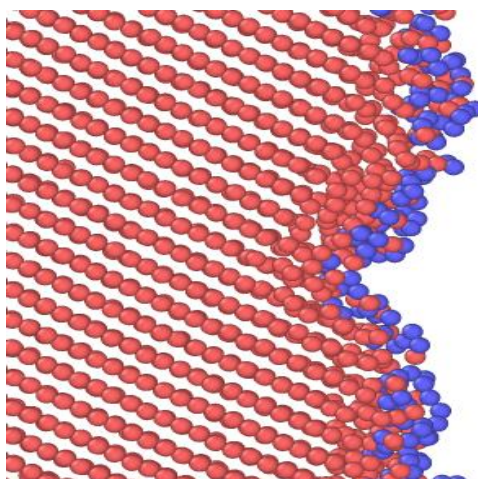


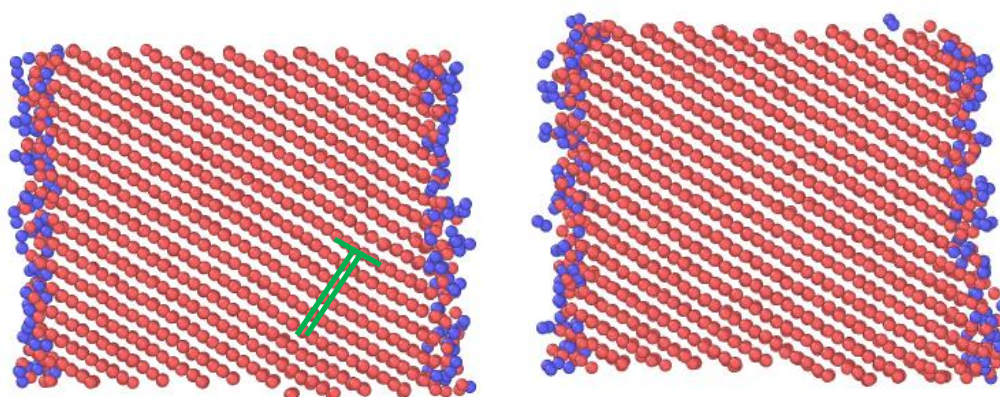
Fig. III.31. Nucleation of a surface micro notch at 300K with COMB3 potential.

The oxidation behaviour predicted by COMB3 potential may not be too reliable. Yet it still shows that even in this special case (creation of an amorphous layer which can be pushed outwards), surface steps can also be initiated by gliding of dislocations and are irreversible under opposite loading. A micro-notch can be created.

3.6.2 Slip irreversibility and notch formation using the ReaxFF potential

Surface step irreversibility and notch formation is also tested with ReaxFF potential. A surface oxide layer is created at 600K until 2 ns. Not as many oxygen molecules are chemisorbed as in the case of nickel. This is probably due to the existence of stable states for chemisorbed molecules which then dissociate very little during MD simulation, and saturate rapidly the surface oxidation sites. Neither Cu_2O nor CuO nucleation is observed during the time of my MD simulations. It could also be the case in rapid fatigue tests.

Inserted dislocations can get out of the surface oxide layer easily, because the surface copper atoms still retain more or less their fcc environment, which allows dislocations to transfer their character. This is similar with tests in inert environment (in chapter 2) and with tests with nickel and oxygen (in section 3.4). The surface step will reconstruct and thus get reversible under opposite loading, see Fig. III.32. If opposite sign dislocations are inserted continuously, a surface micro notch forms.



Configuration with a dislocation

creation of a surface step on the right

Fig. III.32. Creation of a surface step by dislocation gliding with the presence of oxygen, at 600K with ReaxFF.

3.7 Chapter conclusions and discussions

Nickel and copper surface step irreversibilities have been simulated in oxygen environment. Oxidation mechanisms were firstly investigated. Different mechanisms of early stage oxidation have been found in nickel and copper. These mechanisms found with MD simulations are in agreement with knowing experimental observations for both nickel and copper. MD simulations allow a more precise description and analysis of what happens at the atomistic level.

In nickel, oxygen molecules are dissociatively chemisorbed and penetrate into the bulk on a sub-nano thickness scale which depends on temperature and pressure. Nickel atoms can diffuse outwards and the nucleation of small NiO islands is observed. The oxygen structures on nickel surfaces can be different referring to different nickel surface crystallography. But the main mechanism remains the same. Surface nickel atom positions are disturbed by oxidation, yet nickel atoms are still in a more or less fcc crystalline structure.

In copper, oxygen is mainly chemisorbed as O₂ molecules because there are stable states of chemisorbed oxygen molecules on copper surfaces. The dissociation of O₂ molecules is possible but rare using ReaxFF at both 300K and 600K. This dissociation is easier with ReaxFF at 1000K. COMB3 does not show O₂ dissociation at 300K, 600K and 1000K. Neither Cu₂O nor CuO is observed in my simulations, probably because of the rare dissociations. COMB3 provides an amorphous oxide layer while the oxide layer predicted by ReaxFF is approximately crystalline.

However, whatever the oxidation mechanism and surface oxide structure, dislocations can always disappear on the surface and create irreversible surface steps, as in inert environment although the step structure can be different. A small micro-notch can form following the glide of opposite sign dislocations towards the free surface. The irreversibility is not changed. The estimations about the surface irreversibility factor carried out in inert environment should also be valid in oxygen environment.

With our MD simulations limited in time, we could only observe the formation of a sub-nanometer oxide film and the nucleation of NiO islands, and not the formation of a true crystalline oxide layer. This is because the simulation time (2ns) is too short to allow further atom diffusion which may lead to further epitaxy growth of a crystalline oxide. A thick crystalline oxide film may impede the production of surface steps, and cause dislocation pile-

ups under the oxide layer. Stress concentrations are expected which facilitates crack initiation, as suggested by [Shen et al. 1966] (see section 3.1.3).

Our simulations show that cyclic partial annihilation of surface step may increase the local oxygen atom penetration, but that has no influence on the slip irreversibility. Concerning the mechanism proposed by [Thompson et al. 1956] about the oxygen concentration induced crack initiation (see section 3.1.3), as there is no stress induced vacancies pre-existing in our simulation box, we cannot compare our simulation with this model. Further studies on this point will be an interesting work.

This work also shows that first stages of oxidation have no major effect on the surface step irreversibility and surface relief evolutions. This is in agreement with experimental observations that the development of PSB surface relief is the same for fatigue in inert environment as in air. Atmosphere may influence the crack propagation, but it probably does not influence the crack initiation. The M.D. simulations carried out in this chapter clarify at the atomic level why oxygen environment does not change surface evolution in the simulation conditions, which are moderate temperatures and high loading frequencies.

CHAPTER 4.

CRACK PROPAGATION IN INERT ENVIRONMENT

In this chapter, the propagation of nano-cracks will be simulated in order to first access the possible propagation mechanisms and try secondly to estimate a propagation rate. The work is mainly carried out in inert environment, using efficient EAM potentials, and will be compared to experimental observations and other atomistic simulations reported in literature.

Experimental studies on crack propagation in air and in high vacuum will first be reviewed in order to provide a general review about propagation mechanisms, propagation rates, effects of temperature and gas partial pressure... I mainly focus on studies on pure fcc metals such as copper and nickel. MD simulation results about crack propagation will be reviewed afterwards. Only nanoscale small cracks can be simulated due to the limited sizes of the simulation boxes one can achieve via atomistic simulations.

Experimental studies can be performed in high vacuum but not in perfect vacuum with no impurity. On the contrary, for MD simulations, vacuum tests are the easiest ones, and tests in oxygen environment are difficult to carry out due to the requirement of a fair and computationally efficient potential. That one should take into account at the same time different physical and chemical properties of the metal by itself and its interactions with oxygen molecules. A discussion about experimental and simulation studies will finally be proposed.

4.1 Literature review on experimental studies about crack propagation

4.1.1 General introduction of crack propagation in inert and in air environment

The oldest experimental studies about metal crack propagation were generally carried out in air environment. Since the 1960s, the cyclic fatigue life was found to be longer in high vacuum than in air for all metals except gold, see [Snowden 1964; Hordon 1966; Shen et al. 1966; Wadsworth and Hutchings 1958]. The effect of vacuum or inert environment on crack propagation has been extensively studied since then and compared to crack propagation in air. In this section, a short review about crack propagation will be presented in both air and vacuum (inert environment) in order to facilitate comparison. As only pure metals are considered in this work, I focus on experimental studies about pure metals, especially copper and nickel.

Compared to vacuum environment, air environment increases the fatigue crack growth rate. This has been confirmed experimentally for steels, aluminium, nickel, titanium and some other materials. [Laird and Smith 1963] observed a higher fatigue crack growth rate in air in pure Ni at room temperature, with a vacuum level of 6.65×10^{-3} Pa. [Wang and Mughrabi 1984] observed that cracks propagate more slowly in copper single crystals in vacuum than in air.

It also has been found that the atmospheric ‘active’ gases are oxygen for copper, nickel, Al alloys, brass, magnesium, lead etc. and water vapour for Al, Ti and some steels [Grinberg 1982]. [Duquette and Gell 1971] performed tests on nickel based alloy (Mar-M200 single crystal) at room temperature in dry, normal and humidified laboratory air, and they found that fatigue life time and fracture surface appearances are the same in the three environments. This implies that oxygen, rather than water vapour, is responsible for the higher fatigue crack growth rate observed for nickel based alloys.

In the following, crack propagation rates, propagation mechanisms, environment effects on the different stages of fatigue crack propagation, influence of temperature and pressure, crack closure and hysteresis loop will be discussed in vacuum and in air.

4.1.2 Crack growth rate and initial stage of crack propagation

It is generally agreed that there are two stages about the crack propagation. As presented in section 1.3, crack occurs initially along crystallographic slip planes at free surfaces, this stage is called stage I. The crack growth may subsequently undergo a transition to a second mode in which the plane of the crack is perpendicular to the tension-compression loading direction, this is stage II. [Kaplan and Laird 1967] suggested that stage I cracking is associated with a slip process characterized by coplanar motion of dislocations. The mechanisms of stage II crack propagation is usually considered as plastic blunting of the crack tip under tension and its re-sharpening under compression. The mechanism of crack tip blunting and re-sharpening is reviewed in section 4.1.3. Stage I slip is considered to be highly reversible, in contrast with stage II slip which is considered to be highly irreversible [Cheng and Laird 1983].

[Neumann et al. 1977] performed tests on a [100] oriented copper single crystal with a notch front along [011], they found that, in air, stage I crack growth could be obtained for any crack length, provided the load was maintained low enough to keep da/dN lower than 10nm/cycle. On the contrary, crack growth in vacuum (1.3 mPa) occurred always in stage II, for da/dN as low as 0.3 nm/cycle. These results are summarized in Fig. IV.1. [Neumann et al. 1977] demonstrated that re-welding occurred during compression, suppressing stage I crack advance completely and reducing stage II crack growth rates by an order of magnitude in vacuum. They concluded that this effect was responsible for the absence of stage II fatigue striations in vacuum.

However, different from Neumann, [Wang and Mughrabi 1984] observed that early crack growth in copper oriented for single slip at room temperature can occur in stage I along persistent slip bands both in air and in vacuum. They wrote that Neumann's specimen geometry favours symmetrical multiple slip at the crack tip and is therefore particularly suitable for promoting stage II crack growth and less suitable for stage I crack growth.

[Wang and Mughrabi, 1984] also showed that, irrespective of the environment, transitions from stage I to stage II crack growth, and backwards, could be induced at arbitrary crack lengths by appropriate increases, or reductions, in the amplitude. [Cheng and Laird 1983] postulated that in copper single crystals, the criterion for this transition is the attainment of the regular PSB formation stress on the secondary slip system at the crack tip. They also suggest that the factor which most affects the transition is the orientation of the crystal. The higher the

stress on the secondary system relative to that on the primary, the shorter is the length of the stage I crack when the transition to stage II occurs.

Fatigue crack propagation rate was measured by [Neumann et al. 1977] on the [100] oriented copper single crystal with a notch front along [011]. A very low crack propagation rate down to only several angstroms per cycle was observed in vacuum of 1.3mPa (Fig. IV.1). A similarly low propagation rate has been measured by other authors on different metals and alloys with a low fatigue intensity factor ΔK of a few $MPa\sqrt{m}$, see [Petit et al. 2003].

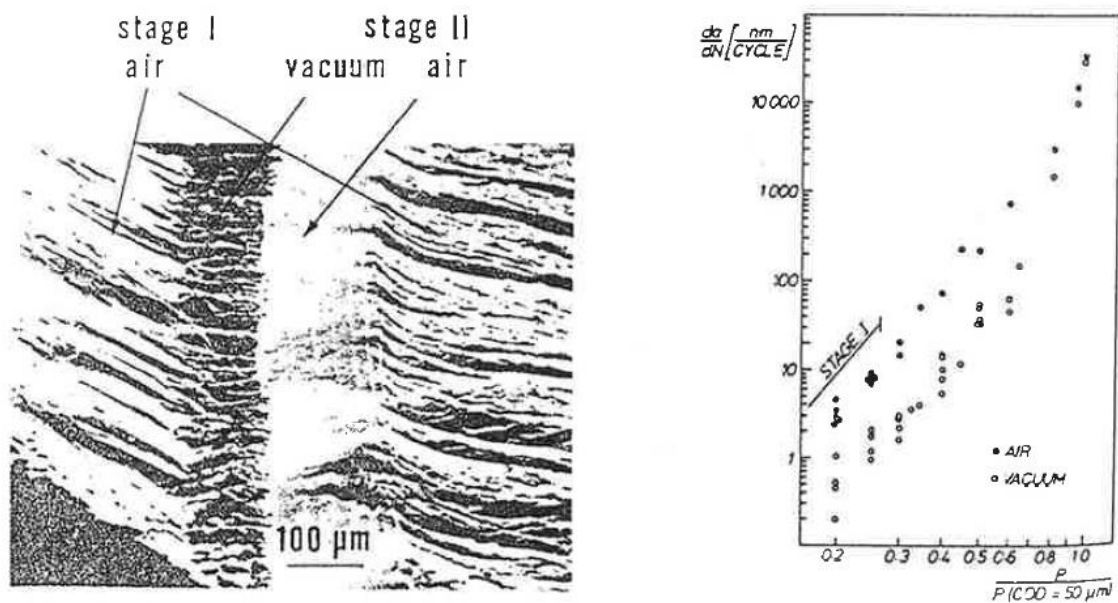


Fig. IV.1. Fatigue crack growth in [100] orientated copper crystals. Left: fatigue fracture surface with crack front along [011]. Crack propagation rates, from right to left : 3nm/cycle, 50 μm/cycle, 0.3nm/cycle, 3nm/cycle. Right: Crack growth rates da/dN versus load P , normalized with respect to load giving a crack opening displacement of 50 μm. Stage I is observed only in air. From [Mughrabi 1979]

[Wang et al. 1984] examined the role of environment on the formation of PSBs in Cu single crystals at a constant plastic resolved shear strain amplitude of 2×10^{-3} in high vacuum (about 1-10 mPa). They found that the fatigue life was nearly 1.3×10^5 cycles in air and 15-30 times longer in vacuum. Up to the number of cycles to failure in air (about 10^5), the cyclic deformation behaviours in air and in vacuum were similar in all investigated aspects. In particular no significant differences were observed with regard to the distribution, surface features and dislocation microstructures of the matrix and persistent slip bands (PSBs). They thus suggested that the reason of prolonged fatigue lifetime in vacuum is largely due to the strongly reduced rate of early crack growth in stage I and also possible in early stage II.

It is important to note that [Petit et al. 2003] write in their review that in inert environment, most of the dislocations put into motion are used to blunt the crack tip and to accommodate the strain around the crack tip, see Fig. IV.2. Therefore, only a limited number of dislocations would directly contribute to the propagation process, which would explain the observed very low crack propagation rate in inert environment.

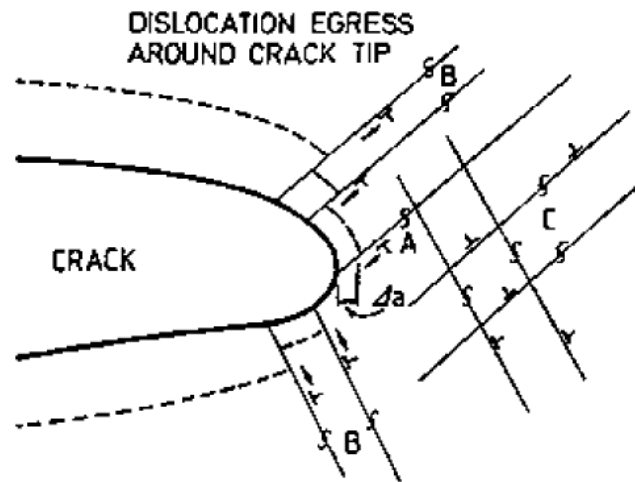


Fig. IV.2. Schematic diagrams illustrating dislocations near a crack tip. (A) exactly on planes intersecting crack tips produce an increment of crack advance, Δa , but dislocations emanating from sources. (B) and (C) produce only opening or contribute to the general strain ahead of cracks.

The crystallographic orientation play an important role on the crack propagation rate in air and in inert environment [Petit et al. 1994]. [Rieux et al. 1979] examined the crack propagation rate in function of crack plane orientation and crack propagation direction in single crystal fcc stainless steel (Fe-17 Cr-13 Ni) in air by three point bending ($R = 0.2$) at 50 Hz in a load controlled machine. They found that for this fcc alloy, crack propagation is sensitive to the crack plane orientation. For a given value of ΔK , crack propagates more rapidly in the (100) plane than in the (111) plane (see Fig. IV.3). A possible explanation is that there are more activated slip systems ahead of a crack in the (100) plane than ahead of a crack in the (111) plane.

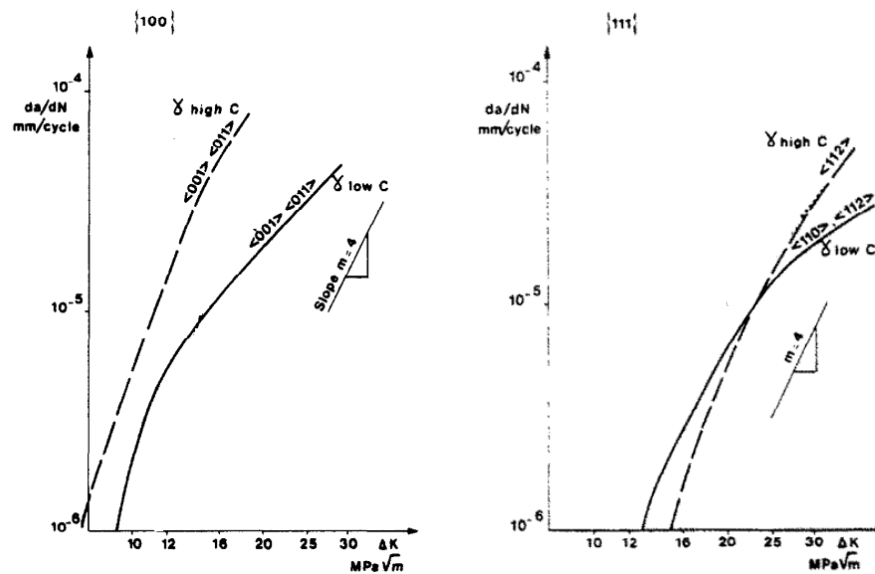


Fig. IV.3. Crack propagation rate in the (100) plane (left) and in the (111) plane (right) with different propagation directions in fcc austenitic steel in air. From [Rieux et al. 1979].

4.1.3 Crack propagation models

There are in general two models explaining metal crack propagation: the crack tip blunting and re-sharpening model, and the void absorption model.

a) Blunting and re-sharpening model

Crack tip blunting and re-sharpening is one of the basic mechanisms of fatigue crack growth in ductile metals and alloys. Blunting means crack tip opening under tension due to the activation of different slip systems. Re-sharpening means that during the reversed loading (compression), crack tip cannot be fully closed because of the irreversibility of some of the dislocation slips and/or the presence of gas molecules which leaves behind a sharp and narrow crack tip. An illustration is presented in Fig. IV.4. [Laird and Smith 1962] first proposed this model based on the direct observation of crack profiles. [Neumann 1974] performed push-pull tests with zero mean stress, on notched 99.999 per cent pure copper single crystals, in air at room temperature. His experimental observations clearly evidence the blunting and re-sharpening mechanism in air condition, see Fig. IV.5. White lines present slip lines. It is interesting to note that he observed a slip free area ahead of the crack tip. He also found that no slip occurred in front of the crack tip during compression, only the old tensile slips were reversed.

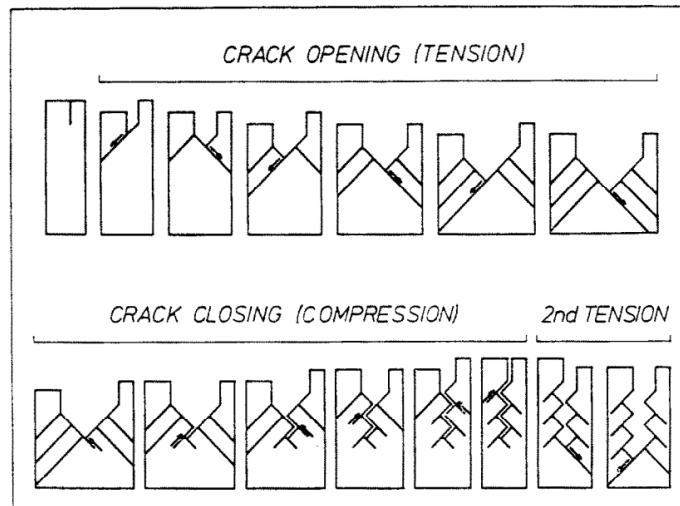


Fig. IV.4. Schematic illustration of crack tip blunting and re-sharpening during one loading cycle, with two slip systems. From [Neumann 1974].

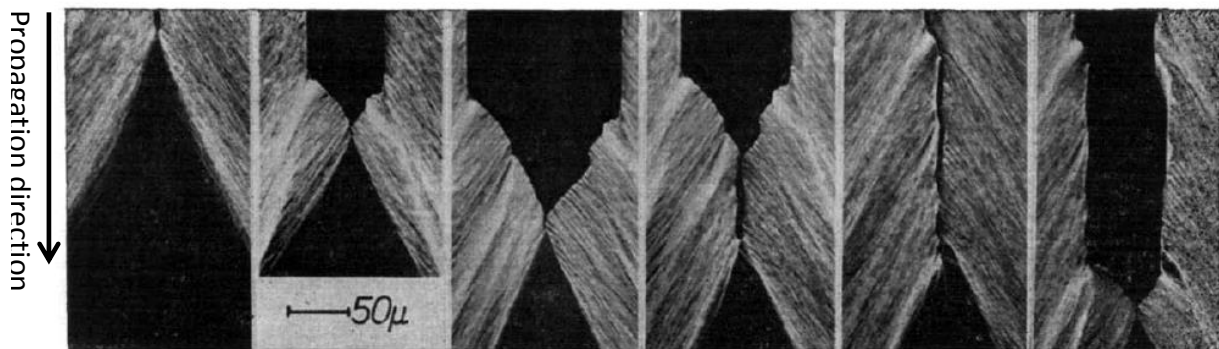


Fig. IV.5. Sequence of successive crack tip blunting and re-sharpening during one loading cycle, for copper in air at room temperature. The crack propagates from the top. Note that the black triangular area at the bottom ahead of the crack tip corresponds to a slip free area. From [Neumann 1974].

b) Void absorption model.

Void absorption model is another well-known model of metal fatigue crack propagation. This model involves the nucleation of voids ahead of the crack tip followed by void growth and coalescence driven by plastic deformation. As shown in Fig. IV.6, voids can be nucleated especially around impurities ahead of a crack tip; they then grow and join the crack tip. The nucleation of voids could be more difficult in pure metals due to the absence of impurities. Air molecules may help the voids nucleation by increasing the strain localization at the crack tip [Petit et al. 2003].

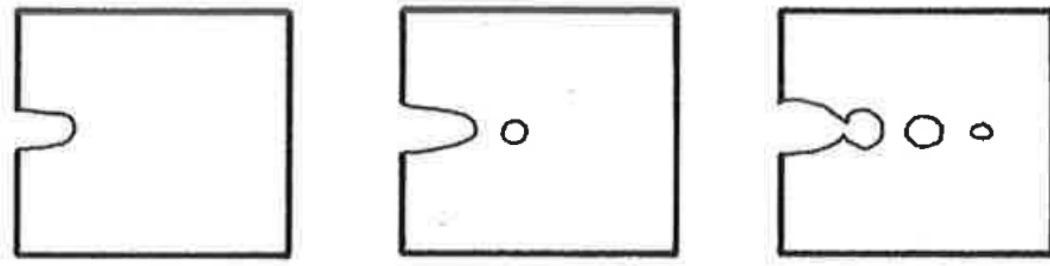


Fig. IV.6. Schematic diagrams illustrating crack propagation due to absorption of voids nucleated ahead of a crack. From [Meyers and Chawla 2009].

In a fatigue test, a crack can propagate due to both crack tip blunting and re-sharpening and to absorption of voids ahead of the crack. At lower temperature, cleavage and bond breaking are also possible mechanisms for crack propagation.

4.1.4 Role of gas partial pressure and temperature on fatigue life

Gas partial pressure and temperature affect fatigue life. The initial studies took place in the 1960s. [Ham and Reichenbach 1962] carried out tests on cold rolled strips of commercial Al fatigues in reverse bending at a frequency of 133Hz. They found that, with temperature increase, the fatigue life decreases in a narrow range of air pressure ($1-10^{-2}$ Pa) and then becomes stable. Similar results were reported by [Aubry and Bernardet 1968] on Al alloys and [Thompson et al. 1956] on Cu and brass. In all cases, the results are characterized by a transition-pressure zone where the fatigue life rapidly decreases as the pressure of air, oxygen, or water vapour is increased. An N_f -pressure diagram is presented in Fig. IV.7, showing a transition pressure and two plateaus in Pb. Oxygen is the major factor in reducing the fatigue life in Pb. One can see that below this transition pressure, there is no significant variation of the fatigue life with further decrease in air pressure (Fig.IV.7).

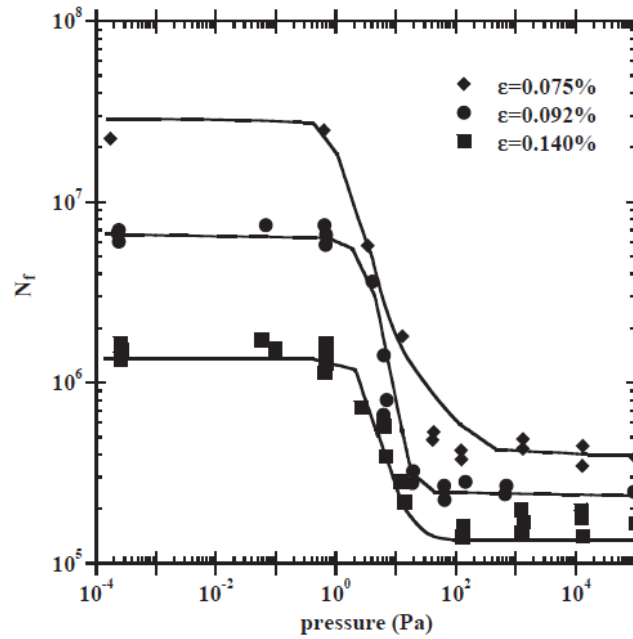


Fig.IV.7. Fatigue life variation as a function of air pressure for tests performed at various strain amplitude on Pb. Oxygen is the major factor in reducing the fatigue life in Pb. From [Snowden 1964].

Considering the temperature effect, at very low temperature cleavage may be favoured, cracks could propagate more rapidly. At room temperature and above, fatigue life could decrease with the increase of temperature. Environmental effect may be accelerated at elevated temperature due to accelerated oxidation reactions and diffusion processes. For further details, one should refer to [Petit et al. 2003].

Because of large increase in lifetime, some mechanisms may be observed only in inert environment, such as secondary hardening. Tests carried out on some austenitic steels show that when cycled in vacuum in the intermediate temperature range (300-500°C), they exhibit a considerable secondary hardening and a longer fatigue life than at room temperature or at 600K (see Fig.IV.8). Such an increase in fatigue life resistance at intermediate temperature in vacuum has been correlated to a secondary hardening associated with a typical dislocation structure called ‘corduroy structure’, consisting of a periodic array of dense dislocation walls, as shown in the right part of Fig.IV.8.

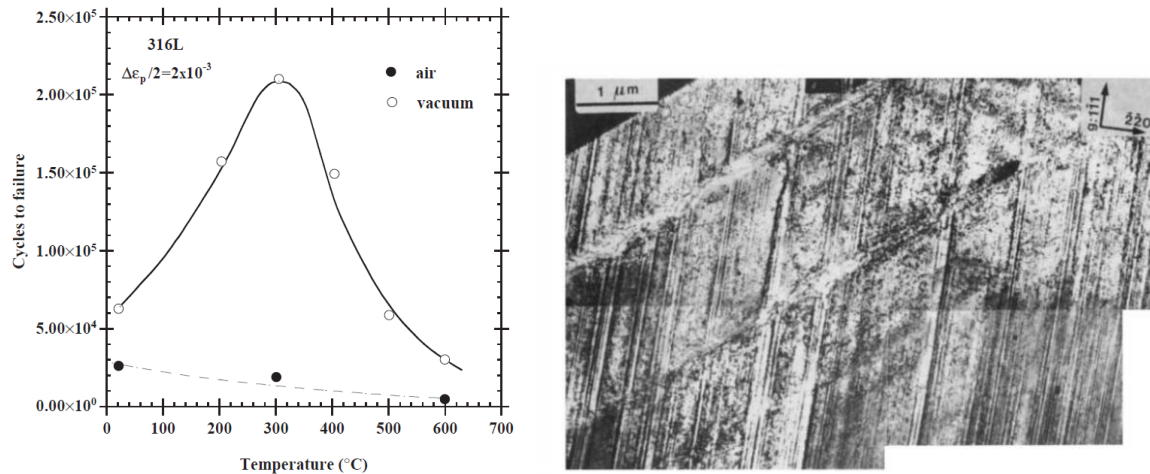


Fig.IV.8. Left: temperature influenced fatigue lifetime in austenitic steel, from [Alain et al. 1997] (see [Petit et al. 2003]). Right : corduroy structure after fatigue at 400°C in vacuum, $\Delta\epsilon_p/2=2\times 10^{-3}$, $N=135,000$ cycles, from [Gerland et al. 1993].

4.1.5 Fatigue crack closure

Crack closure is generally considered to arise from the fact that during the fatigue crack advance, the material is plastically strained at the crack tip and, due to the restraint of surrounding elastic material on this residual stretch, some closure of the crack surfaces occurs above the minimum applied load of the fatigue cycle. The crack then remains closed state even though some external tensile force acts on the material. During this process the crack opens only at stress above a particular stress. For the case there is no closure, $\Delta K = \Delta K_{\max} - \Delta K_{\min}$. When there is crack closure, $\Delta K_{\text{effective}} = \Delta K_{\max} - K_{\text{closure}}$, and $\Delta K_{\text{effective}} \leq \Delta K$.

There are different factors which could induce fatigue crack closure, such as:(cf. Fig. III.9)

- plasticity-induced closure results from compressive residual stresses;
- oxide induced crack closure which occurs where there is rapid corrosion during crack propagation which wedges a crack opening during fatigue loading;
- roughness induced crack closure due to heterogeneity in micro structure which induces some mismatch between the upper and lower crack faces.

Further details may be found in [Suresh and Ritchie 1982].

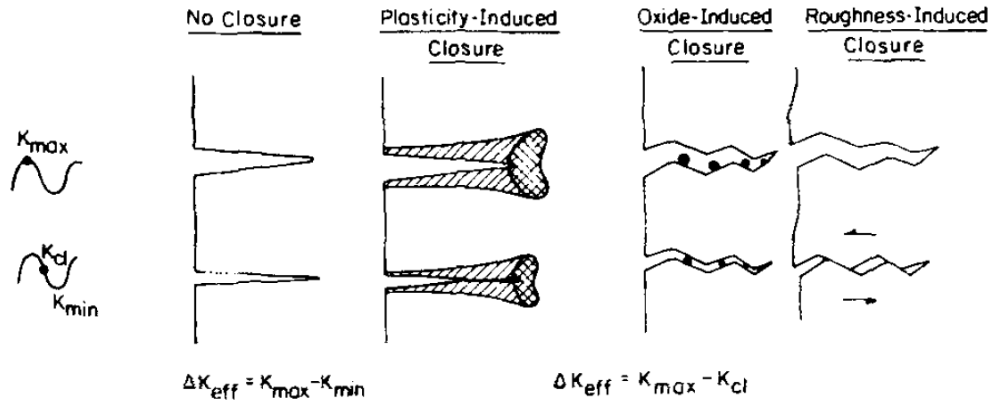


Fig.IV.9. Different mechanisms of fatigue crack closure, compared to no closure. From [Suresh and Ritchie 1982].

4.1.6 Hysteresis loop

Hysteresis, or memory dependence, is an important notion for complex systems. Since plastic deformation is normally accompanied by energy dissipation and is irreversible, the corresponding relation between stress and strain is not single-valued, and exhibits memory dependence, which is called hysteresis. A hysteresis loop is shown in Fig.IV.10. The plastic deformation is denoted as ϵ_p and the elastic deformation as ϵ_e .

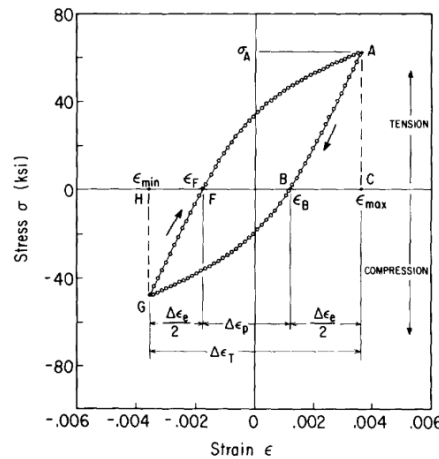


Fig.IV.10. Symmetric stress-strain hysteresis cycle.

Sustained hysteresis is related to the rate of damage accumulation. As shown in Fig.IV.11, at large strain range, plastic deformation is dominant, hysteresis loops are thick and failure occurs very rapidly. In contrary, at lower strain range, plastic deformation is less dominant, the hysteresis loop is thinner and one can get a longer fatigue life. During cyclic loadings, there is always a drifting which means progressive changes in the shape of the hysteresis loops. A detailed analysis of hysteresis and fatigue was carried out by [Erber et al. 1993].

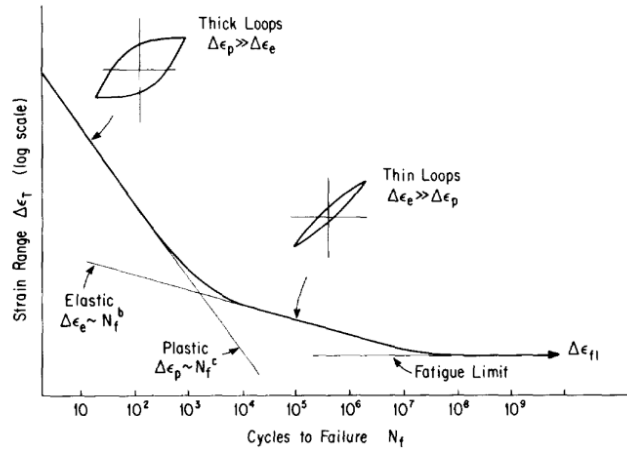


Fig.IV.11. General trend of the Manson-Coffin relation for low and high cycle fatigue.

4.1.7 Evaluation of the fatigue crack propagation rate

A well-known and widely applied model to predict fatigue crack growth rate da/dN is the Paris law (see section 1.3.2) using stress intensity factor ΔK (ΔK should be $\Delta K_{\text{effective}}$ in the case of crack closure, see 4.1.5). This model is based on the linear elastic fracture mechanics (LEFM) approach that assumes that the crack length is much larger than the crack tip plastic zone.

This assumption is not usually valid especially at high temperature or at ambient temperature when the material presents a very ductile behaviour. The crack can propagate with considerable plastic deformation and the plastic zone at a crack tip may have a size of the same order of magnitude as the crack size. In this case, the fatigue crack growth should be studied under elastic plastic fracture mechanics (EPFM) approach. The crack tip opening displacement range ($\Delta CTOD$) is considered as a fatigue crack growth rate (da/dN) criterion. There are a number of alternative definitions of CTOD. A very common definition of CTOD is the displacement at the original crack tip diameter considering $\pm 45^\circ$ intercept lines. This definition was suggested by Rice and is commonly used to infer CTOD in finite element measurements. This CTOD criterion is applied in a number of studies, for example [Ferrie and Sauzay 2009].

4.1.8 Discussions about experimental studies

Although Fatigue has been extensively studied experimentally during the last seventy years, the mechanisms of fatigue crack propagation, the reason of different fatigue life in air and in vacuum, the pressure, temperature and loading amplitude influences on fatigue life, and the fatigue life scattering are still not fully understood.

A lot of data have been obtained, but they are often on different metals and alloys, using different experimental procedures and considering different environment conditions.

For the fatigue tests in vacuum, [Laird and Duquette, 1972] have pointed out that, even in relatively good high vacuum (0.1 mPa), a monolayer oxygen coverage on newly generated surfaces can occur within seconds. [Duquette 1978] found that the divergence in S–N curves between air and vacuum can sometimes be more pronounced in the high-stress or strain, short-fatigue-life regime, and sometimes in the low-stress, long-fatigue-life regime, due to different testing materials, procedures, and environment. It is thus difficult to conclude about mechanisms in vacuum or inert environment, due to the still existing possibility of oxidation, and to the observed differences between results.

Another limitation of experimental tests is that atomistic details are difficult to access; a rigorous understanding of the crack propagation is thus not easy to get. With the development of computers and models, atomistic simulations may help to understand mechanisms at the atomic level. Later, a strong coupling between experimental observations and computer simulations may help to better understand fatigue mechanisms and better predict fatigue lives.

4.2 Literature review on computer simulations

During the last 20 years, atomistic simulations have been carried in the aim of improving the understanding of crack propagation mechanisms. Molecular dynamics is one of the most suitable methods. However, because such fatigue simulations are very CPU time and memory consuming; only few M.D. simulations have been carried out up to now. These recent advances in atomistic simulation on fatigue propagation are now presented. The cracks simulated in MD studies are nanoscale small cracks (NSC), again because of size and time limitations of MD simulations.

4.2.1 Crack propagation mechanisms

The two main mechanisms observed in atomistic simulations related to crack propagation are:

- 1) the void absorption mechanism for which the main crack coalesces with some voids nucleated ahead of the crack tip.
- 2) the bond breaking mechanism for which some atomic bonds are broken at the crack tip in the crack plane.

[Horstemeyer et al. 2010] reviewed the results of some MD simulations carried out at 300K in nickel and copper single crystals. They showed crack tip blunting due to intense localization of plastic slip; void nucleation due to an increased dislocation density in front of the crack tip and cleavage due to certain orientation of the crack tip. [Nishimura and Miyazaki 2004] carried out MD simulations at 300K on α -Fe with a system of one million atoms and found the crack propagates due to the coalescence of the crack and the vacancies caused by the emission of dislocations. They also found phase transition near the crack tip. [Farkas et al. 2005] performed MD simulations on nickel polycrystalline and found that the main atomistic mechanism of fatigue crack propagation is the formation of nano-voids ahead of the main crack. [Baker and Warner 2014] performed simulations at 0K on aluminium using a multi-scale coupled atomistic-discrete dislocation method (CADD software). They observed crack growth either on a low energy crystallographic plane by cleavage, or on the crack plane by individual bond breaking events at the crack surface resulting from dislocation nucleation. They also observed some small lattice defects, but no large voids. The cyclic blunting and re-sharpening propagation is not observed by any of these authors.

4.2.2 Nano-scale small crack propagation rate

[Horstemeyer et al. 2010] compared their simulation results about nanoscale small crack (NSC) propagation rate with measured crack growth rate for both small cracks (micron range) and long cracks (millimetre range) and concluded that the quantified NSC growth rate in copper single crystals were similar with those experimentally measured for small cracks and with those observed at stress-intensity-factor ranges lower than the threshold for long cracks, as shown in Fig.IV.12. At ΔK about $1 \text{ MPa}\sqrt{\text{m}}$, the crack propagation rate could be less than 1 \AA per cycle. [Farkas et al. 2005] also found a sub Angström propagation rate at low stress intensity amplitude (about $1 \text{ MPa}\sqrt{\text{m}}$). It should be noticed that there are still undeniable differences between the crack growth rates simulated by [Horstemeyer et al. 2010] and those experimentally measured. These tentative comparisons, however, may not be meaningful because of the largely different conditions in the experimental tests.

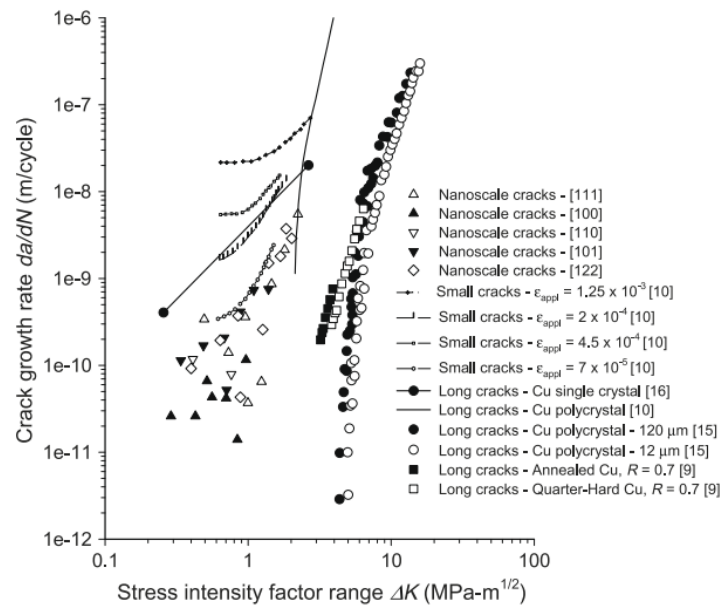


Fig.IV.12. Crack growth rates from the nanoscale atomistic simulations compared with small and long crack growth rates in Cu single and polycrystals. From [Horstemeyer et al. 2010], see their review paper for extended references.

[Horstemeyer et al. 2010] also found that the crystallographic orientation played an essential role in determining the crack propagation mechanisms and crack propagation rates. They performed tests on 5 different orientations. The different propagation rates are shown in Fig.IV.12. Concerning propagation mechanisms, they concluded that in the case of the activation of either single or double slip system(s) at the crack tip, a typical Mode I fatigue

crack arises along a slip band and then grows into a mixed Mode I+II crack growth mechanism. For crystal orientations characterized by multiple slip systems concomitantly active at the crack tip, the crack advance mechanism was characterized by nano-void nucleation ahead of the crack tip and by linkage with the main crack, leading to crack extension.

4.2.3 Limitations and advantages of computer simulations

a) Load application

Repetitive positive loadings are applied in most computer simulations, due to the small simulation systems and narrow distances between the two faces of cracks, in order to avoid crack closure. All the authors mentioned above in this review section applied positive load ratios with R equals to or higher than zero.

Concerning loading application, both [Horstemeyer et al. 2010] and [Nishimura and Miyazaki 2004] applied uniform displacement controlled loading. It corresponds to a uniform displacement field at the upper and lower boundaries where the load is applied. However, it is difficult to compare these loadings with experimental fatigue loadings, which can be strain controlled but the displacements are applied very far from the crack tip and the deduced displacement near the crack tip is not uniform. [Horstemeyer et al. 2010] calculated K with $= \sigma\sqrt{\pi a}$, with σ the volume average stress in the loading direction calculated from the dipole force tensor of all atoms in the model. But as there are plastic deformations in the model and the model is not loaded in the same way as in an experimental fatigue test, the comparison between the calculated K and the experimental K can only be rough. Finally the formula used for computing K is only valid in an infinite matrix whereas the considered simulation box is small with respect to the crack length.

[Farkas et al. 2005] and [Baker and Warner 2014] used displacement fields obtained from the linear elasticity fracture mechanisms (LEFM) for every given value of the cyclic stress. This seems to be a better way for load application. The comparison of the results obtained with $K_{\text{simulation}}$ and $K_{\text{experimental}}$ could be more convincing.

b) Periodic boundary conditions and effect of the thickness of the simulation box

Periodic boundary conditions are widely applied in MD simulations. [Horstemeyer et al. 2010] performed MD simulations with approximate dimensions of $36 \times 36 \times 1.4 \text{ nm}^3$ with periodic boundary conditions in both X and Z directions, with the crack oriented along the X direction. Only the loading direction Y is free from periodic boundary condition. They tested the effect of Z periodic thickness by doing simulations with thicknesses of 4, 8 and 12 times one unit cell length and found the results are converged when there are 4 unit cells in Z. [Nishimura and Miyazaki 2004] also used periodic boundary conditions through the thickness. However, an artefact in the use of a periodic boundary condition in Z is that it may impede certain oblique slip systems to be activated as they should be and trigger the production of non-standard dislocations. However, if one tries to simulate a 3D system without periodic boundary conditions, as the simulation box thickness is rather small, that may give rise to thin foil effects. This point will be discussed in detail later in this chapter.

c) Environmental effects

By contrast with experimental tests, where perfect vacuum conditions are difficult to reach, to simulate in oxygen environment is a challenge for MD simulations. All MD simulations discussed above were carried out without oxygen or water molecules.

The main difficulty of MD simulation in oxygen/water environment is the requirement of a powerful satisfying model which can consider both metal and oxygen and/or water, their interactions, and be fast enough on currently available computers (ab initio simulations are clearly ruled out). Some models like ReaxFF and COMB (see chapter 3 for details) have been recently developed, which enable metal/ O_2 / H_2O interactions. These potentials have been used to analyse chemical oxidation. They have not yet been largely used to simulate environmental metal fatigue. These potentials are CPU time and memory consuming. Fatigue simulations in air environment with one million atoms are still out of reach.

4.3 Simulation systems

The majority of simulations about crack propagation in this Ph.D. work were done with [Mishin et al. 2001] potential for copper. Some test simulations were carried out with [Jacobsen et al. 1987] potential for aluminium. All simulations were done with LAMMPS, and visualised with OVITO.

Two specimens with different orientations were employed to study fatigue crack growth in copper as shown in Fig.IV.13.

The first specimen is (x,y,z) orientated along [100], [010] and [001] with a horizontal crack in a [010] plane. We call it (100) box in the following. This orientation is chosen in order to compare with different experimental and simulation studies with the same orientation. The initial dimensions of the simulation box is about $72.3 \times 54.2 \times 2.17 \text{ nm}^3$ in the X×Y×Z directions. The initial lattice parameter for copper at 0K is 3.615 \AA given by Mishin's potential. Both simulations with and without periodic boundary conditions along the Z direction are carried out. The Z thickness for simulations without periodic boundary conditions is chosen to be 6.51 nm, three times larger than that with periodic boundary conditions. There are more than two millions atoms in the largest simulation box. The crack is about 36 nm long, and the distance between the two crack lips is 7.4 nm. The surfaces perpendicular to the X axis are free surfaces and tension-compression loading is applied along the Y direction on the upper and lower boundaries. This is similar to what has been done for other simulations in chapters 2 and 3. For this configuration, the crack is thus loaded under mode I. There are eight equivalent {111} oblique active slip systems for this orientation, with for each of them the same Schmid factor of 0.408.

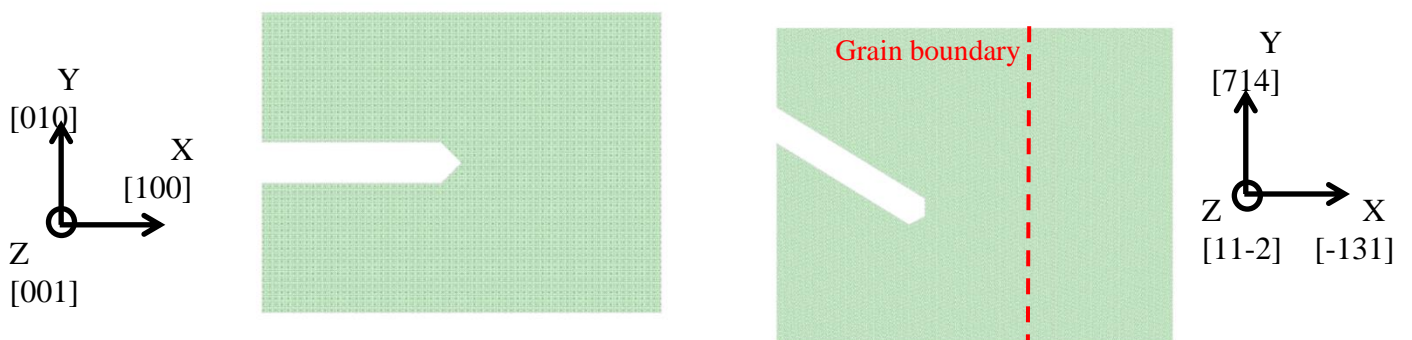


Fig.IV.13. The two differently oriented simulation boxes. The system on the right also has a grain boundary whose interface is indicated by the red dashed line.

The second specimen is oriented along $[-131]$, $[714]$ and $[11-2]$ with a crack along a (111) slip plane. We call it (714) box in the following. The angle between the crack and the x direction is 31.5° . A grain boundary is intentionally introduced into the system to test some grain boundary effects and avoid systematic surface effects. It is geometrically built by a 180° rotation around the X axis of the part of the box located right with respect to the plane indicated by the red dashed line in Fig.IV.13. This grain boundary is thus a hemitropic $\Sigma 11 \{113\}$ twist grain boundary, or equivalently, a $\Sigma 11 \{113\} \langle 112 \rangle$ symmetric tilt grain boundary. The initial dimensions of this simulation box are $120 \times 95.5 \times 1.77 \text{ nm}^3$ in the $x \times y \times z$ directions. The grain boundary is located 36 nm from the right surface. The length of the crack is nearly 65 nm with a distance of about 9 nm between the two lips. As with the first (100) box, simulations were carried out with both periodic and free surface boundary conditions along the Z axis. For simulations without periodic boundary conditions, the z thickness is multiplied by two. There are more than three million atoms in that later simulation box. The surfaces perpendicular to the X axis are free surfaces and tension-compression loading is applied along the Y direction on the upper and lower boundaries. The crack is loaded under mode I + mode II. There are two activated slip systems for this orientation. One is the $(111)[1-10]$ slip system with a Schmid factor of 0.445. The other one is the $(1-11)[110]$ slip system with a Schmid factor of 0.495. The first one is perpendicular to the x - y plane, easy to visualize. The second one is oblique with respect to the x - y plane. Other slip systems display much smaller Schmid factors and are only scarcely activated.

Different geometries of the crack tip, other than the triangle shape shown in Fig.IV.13, have been considered to assess the effect of the crack tip geometry (Fig.IV.14). It is observed that the change of the crack tip geometry change the stress field near the crack tip, thus the location of dislocation nucleation, but this has no influence on the irreversibility of dislocations and the crack propagation rate.

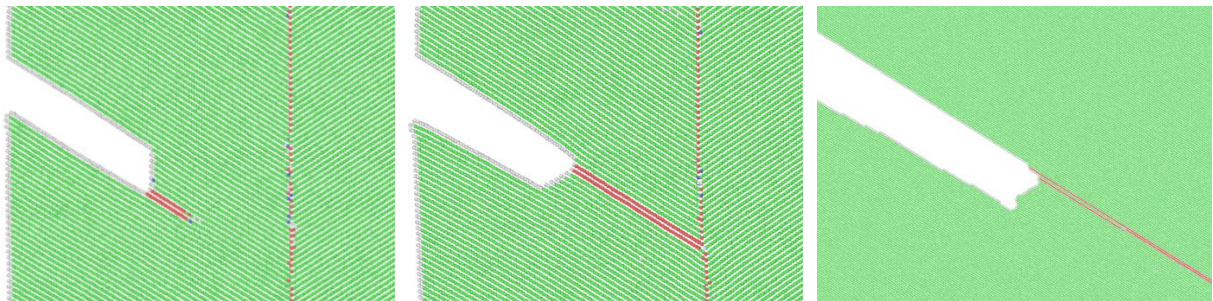


Fig.IV.14. Different tested geometries of the crack tip. Red lines correspond to the stacking fault behind a nucleated partial dislocation. Dislocations nucleated at different places due to the difference of the crack tip geometry. The first two tests were carried out with smaller simulation systems. Copper, 300K.

4.4 Force controlled loading and displacement controlled loading

A uniform displacement imposed loading is widely used in existing MD simulation works (see the literature review in section 4.2). In this work, both uniform displacement imposed loading and force imposed loading were applied to check the induced differences in the crack tip behaviour. For the displacement imposed loading, the upper and lower boundaries are loaded with a continuous sinusoidal displacement with $R_\epsilon=0$ or $R_\epsilon=-1$. Similarly, for the force imposed loading, the upper and lower boundaries are loaded with a continuous sinusoidal force. Both of these loadings have their own advantages and inconvenients.

For a displacement imposed loading, the specimen strain is controlled and repeated at each loading cycle. Same displacement is applied to all atoms located at the upper boundary at a given time. Opposite sign displacement is applied at the same time to atoms at the lower boundary. A schematic sketch of applied displacement and the induced stress is show in Fig.IV.15(b). Although this kind of loading is widely applied, it has the obvious shortcoming that it cannot reproduce the ‘curved’ displacement field around the crack as predicted by linear elasticity fracture mechanics (LEFM). In reality, and in agreement with the LEFM scale, the short crack in the MD box can be regarded as the end of a long crack (except if we were to consider nano-particles) and there should have a curved displacement field (similar as the displacement field in Fig.IV.15(c) around this crack tip.

A force controlled loading gives a better prediction of the specimen displacement field as shown in Fig.IV.15 (c and d). Yet, as the simulation box is rather small (nanometre scale), the plastic deformation zone near the crack tip occupies a large percentage of the total volume of the simulation box. It thus plays a very important role on the specimen deformation. Since dislocations are not always nucleated in a symmetrical way near the crack tip (because of the stochastic nature of thermal agitation at the atomistic level), the simulation box can deform in an unexpected asymmetrical way, as shown in Fig.IV.16. In consequence, no repeated deformation field could be observed under cyclic loading with such a box.

Another observed difference between force imposed and displacement imposed loadings is that under imposed force, dislocations rather stay in a volume close to the crack tip (see Fig.IV.15c, the plastic zone is encircled by a blue dotted line) and do not glide far away from the crack tip. By contrast, dislocations can glide rapidly to the free surfaces under imposed displacement (see Fig.IV.15a). This may be so because the stress is higher far away from the crack tip than close to the crack tip, as sketched in Fig.IV.15(b). Dislocations are no more

reversible once they glide out of a free surface (chapter 2) and this induce a higher irreversibility due to free surfaces.

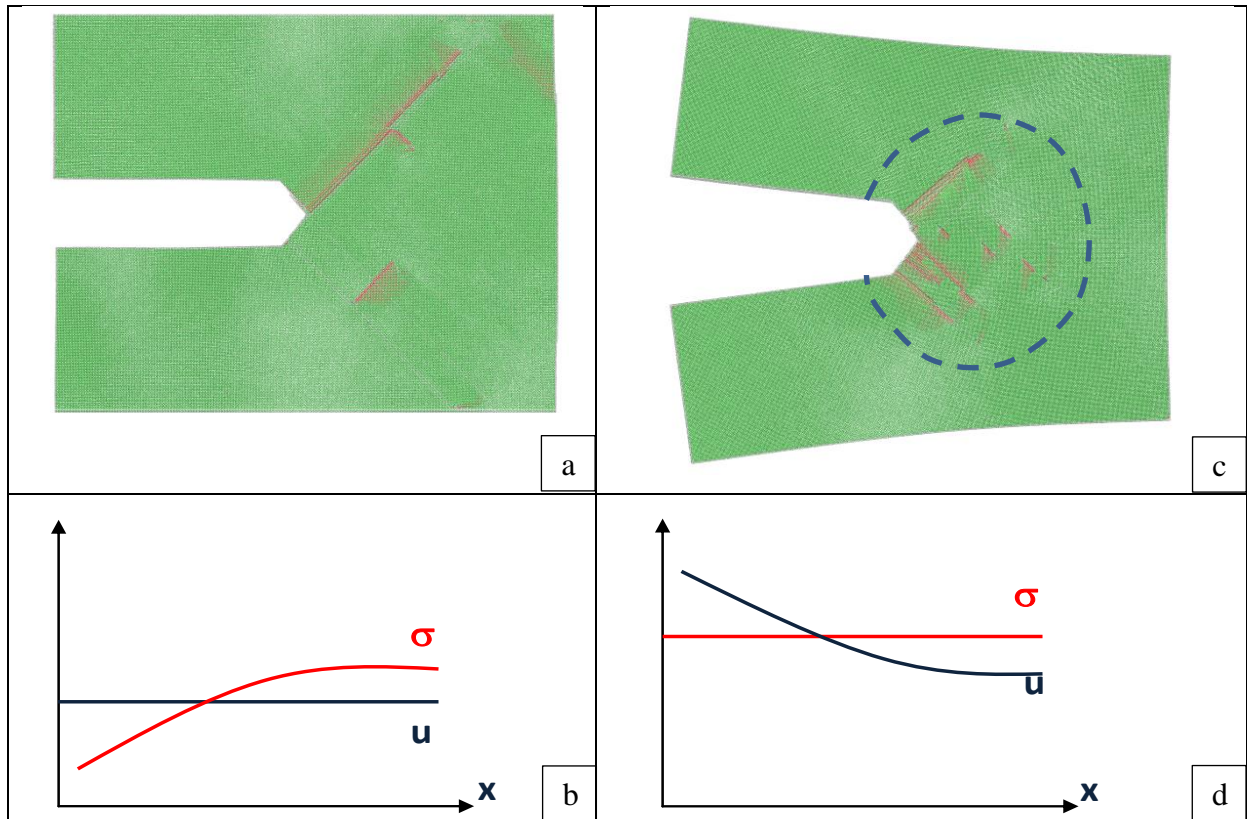


Fig.IV.15. Left: a simulation box under imposed displacement (a) and a sketch of the applied displacement (u) and its induced stress (σ). Right: a simulation box under imposed force (c) and a sketch of the applied stress (σ) and its induced displacement (u). Dislocations can easily glide to free surfaces under imposed displacement (left) but stay near the crack tip under imposed force (right). Red lines in (a) and (b) represent stacking fault behind emitted partial dislocations.

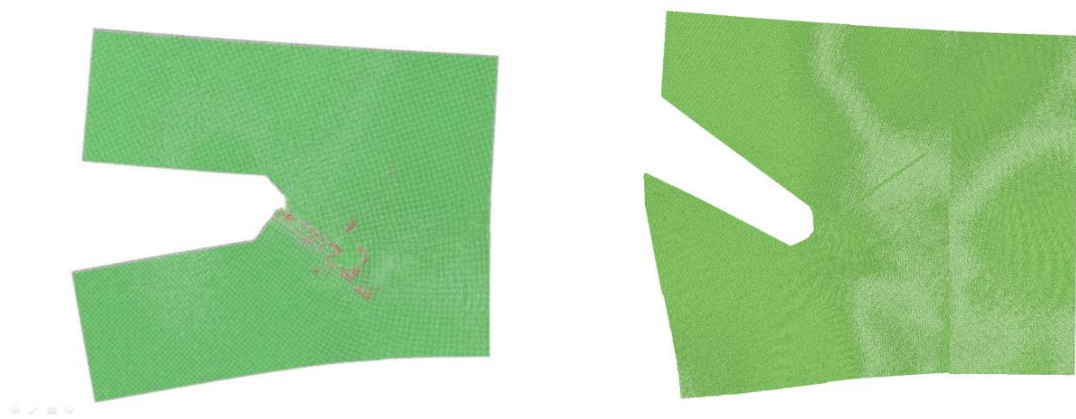


Fig.IV.16. Asymmetry of the specimen deformation under imposed stress due to the random asymmetrical nucleation of dislocations. For the (100) box (left) and the (714) box (right).

A better way to apply loading could be the application of a crack displacement field deduced from the LEFM (see section 4.1.7) on all boundaries of the simulation box, assuming that the plastic zone around the crack tip is small enough compared to the whole crack length. The crack length in the MD box could then be only the end of a long virtual crack. What we simulate in this case is a crack tip and a region near the crack tip. Another possible way is to apply a displacement field deduced from the EPFM (see section 4.1.7). Application of the LEFM and EPFM deduced displacement fields are perspectives of this work.

For each loading, there is a corresponding stress intensity factor range ΔK . One has $\Delta K = K_{max} - K_{min}$ with $K_{max} = F\sigma_{max}\sqrt{\pi a}$ and $K_{min} = F\sigma_{min}\sqrt{\pi a}$. The crack length is denoted as a and the stress y-component far from the crack is denoted as σ . The mode I and the mode II stress intensity factors ΔK_I and ΔK_{II} are characterised by F_I and F_{II} factors respectively, which depends on the geometry of the simulation box. F_I and F_{II} values can be obtained thanks to the curves given in the appendix (with $\theta=0$ and $a/W=0.5$). In our first simulation box, F_I turns out to be approximately equal to 2.7. In the second simulation box, F_I approximately equals 1.9 and F_{II} equals 0.55. For a repeated loading with $R=0$, the stress intensity factor range ΔK corresponds to the maximum stress intensity variation K_{max} . It should be noticed that the ΔK calculated in this work is reliable only when the applied loading is stress controlled. The ΔK of a displacement controlled test should be lower than for a stress controlled test, but we cannot compute it because we do not have appropriate formulae. The MD time step used in this chapter is 3 fs and a full cycle corresponds to 2 ns.

4.5 Specimen thickness effect and boundary conditions

Both periodic boundary condition and free surface boundary condition are applied along the Z direction, using different thicknesses. As shown later, different mechanisms are observed depending on the specimen thickness and the choice between periodic boundary condition and free surface boundary condition. It is important to be aware of these possible artefacts.

4.5.1 Thickness effect under periodic boundary conditions

Tests are first carried out with periodic boundary condition by changing the specimen thickness along the Z direction. The minimum thickness in Z corresponds to the thickness of a cell with the minimum crystalline periodicity in Z.

For the (100) box, tests are carried out on copper at 300K on a specimen with the minimum thickness and another specimen with six times the minimum thickness (see Fig.IV.17 upper images). Under a stress intensity factor of $0.6 \text{ MPa}\sqrt{\text{m}}$, cleavage occurs in the specimen with the minimum thickness but not in the thicker specimen. It might be because the minimum periodic boundary condition impedes the nucleation of oblique slip systems which should develop in the Z direction and cleavage occurs instead. On the contrary, some oblique dislocations can be nucleated within a much larger thickness layer. Tests were also carried out using even thicker specimens with 12 and 18 times the minimum thickness, with similar results found as in the case of 6 times the unit thickness.

Similar tests were carried out on the (714) box, with again a specimen with the minimum thickness along the Z direction and a specimen with a thickness of four times higher (Fig.IV.17 lower images). No cleavage was observed, on neither of these two specimens, with this (714) orientation. There exists a slip system perpendicular to the x-y plane, which seems to be sufficient for dislocation to develop, even with the minimal crystallographic thickness. As seen in Fig.IV.17, the shape of the crack tips differ slightly between the two specimens but this can be due to the random character of dislocation nucleation, rather than de difference of thickness. More tests would be required to precise this point.

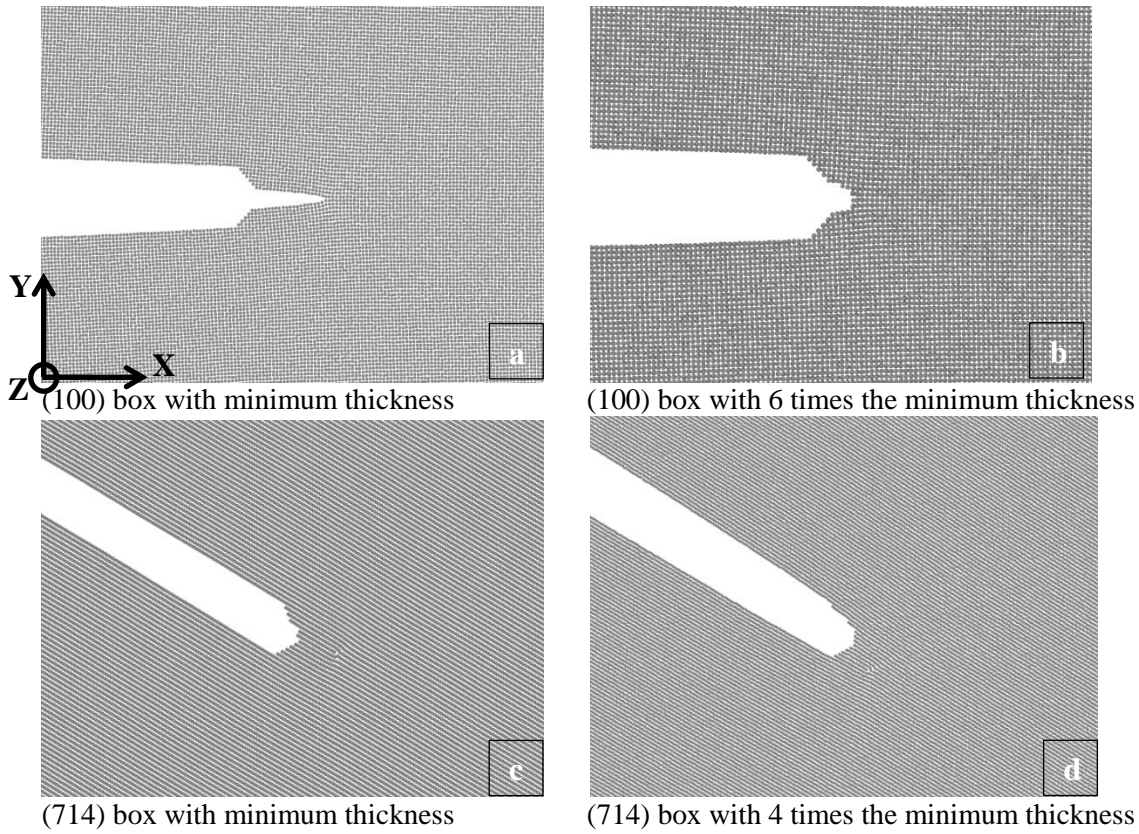


Fig.IV.17. Specimen thickness effect on the propagation mechanisms for the (100) box (a and b) and for the (714) box (c and d), at 300K in copper, tensile loading with a stress intensity factor of $0.6 \text{ MPa} \sqrt{\text{m}}$. Periodic boundary conditions along the Z axis.

From these simulations, one can say that periodic boundary condition impedes the nucleation of dislocations of oblique slip systems, and thus triggers crack cleavage. The increase in the specimen thickness can avoid this effect and results are saturated with respect to the thickness.

Another nuance of periodic boundary condition is that once a dislocation line is nucleated along an oblique slip plane, it might cut through the specimen and come through the other side of the box looking like a new dislocation. It is, however, just the same one because of the limitation of the periodic boundary condition.

4.5.2 Emission of non standard dislocations induced by periodic boundary conditions

‘Non standard’ dislocations are observed in differently oriented simulation boxes using periodic boundary conditions, as it was first noticed for the (714) box, with the x [-131], y [714] and z [11-2] directions and a notch along the (111) slip plane: Fig.IV.18 is a snapshot at 4K of a non standard dislocation which is not dissociated. The view is a little bit inclined in order to better observe the dislocation line and its core. The dislocation line does seem to be the z axis, [11-2]. The Burgers vector calculated from a Burgers’ circuit is $\frac{1}{2}[0-1-1]$. It visually looks like an edge dislocation (Fig.IV.18). The $b \cdot L$ product, however, is not equal to zero.

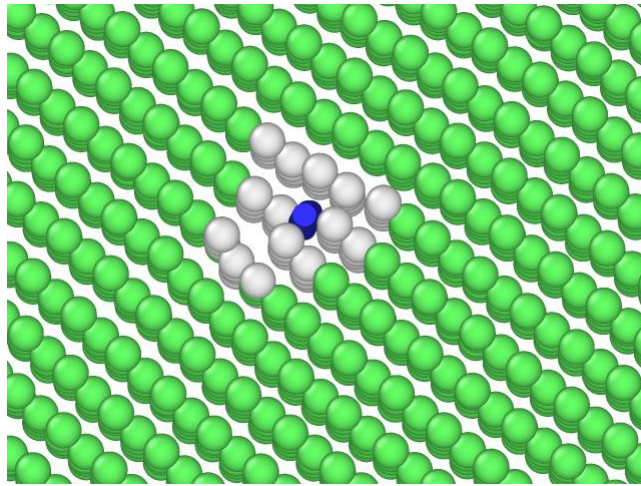


Fig.IV.18. A ‘non standard’ dislocation core observed with the (714) box at 4K. The image is a little bit inclined in order to see both dislocation core and dislocation line. The blue line is the dislocation line and it is perpendicular to the (x,y) plane.

In order to analyse this non standard dislocation by itself, I consider a ‘(111) box’, viz a x [-110], y [111], z [11-2] geometry, which is obtained by a rotation of the (714) geometry by 58.5° around the Z axis. This orientation is chosen because it generates non standard dislocations without generating too rapidly other types of standard dislocations. The (714) box generates at the same time non standard dislocations and usual edge dislocations. In this case, one cannot be sure if the non standard dislocation is influenced by the emission of usual edge dislocations or not. The crack in this (111) box is oriented along the (111) plane and the displacement is applied perpendicularly to it. A snapshot is shown in Fig.IV.19. The dislocation line seems to be once more the z axis: [11-2]. The Burgers vector is $\frac{1}{2}[-10-1]$ (analysis: $\frac{1}{12}[11-2] + \frac{1}{3}[-1-1-1] + 0.5 \cdot \frac{1}{2}[-110]$), and the observed slip plane is (-131)

($2[-110]+[111]=[-131]$). Again, it visually looks like an edge dislocation but the Burgers vector and the dislocation line are not perpendicular.

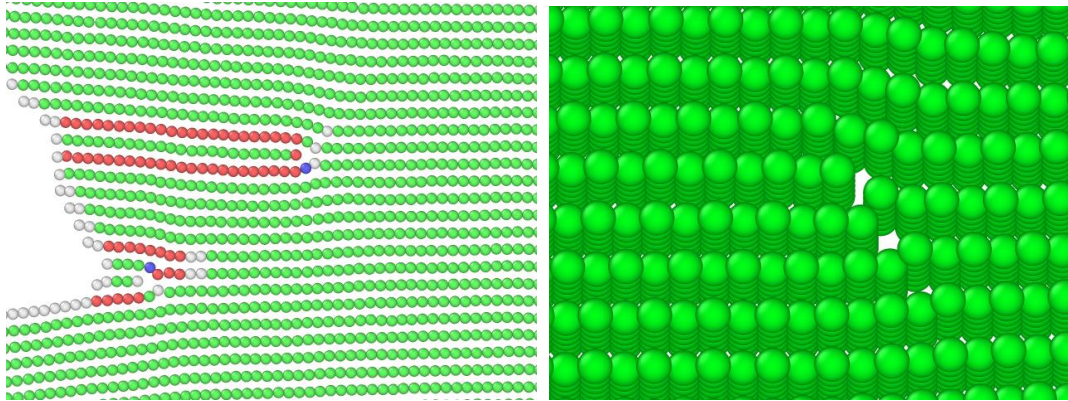


Fig.IV.19. Non standard dislocation observed with the (111) box at 4K. The image on the right is a little bit inclined in order to see dislocation core and dislocation line. Green atoms are in fcc environment and red atoms are in hcp environment (OVITO software).

The non standard dislocation observed in the (111) box at 4K has the same characteristics as the one observed in the (714) box at the same temperature. This shows that the non standard dislocation observed in the (714) box is not influenced by the emission of other dislocations.

Non standard dislocation can dissociate at temperatures higher than 200K. Its dislocation core is disturbed once dissociation occurs. Fig.IV.20 provides a clear presentation of non standard dislocations at 300K. Fig.IV.20(a) is a top view (along Z) of two dissociated non standard dislocations without colour, in order to show clearly the disturbed dislocation core. Fig.IV.20(b) is a coloured view showing the dislocation lines. Green atoms are fcc neighboured while white atoms are not. Green and blue lines more visible in parts (c) and (d) are dislocation lines, green lines present Shockley partial dislocations and blue lines present perfect dislocations. Fig.IV.20(c) is the same view as Fig.IV.20(b), removing all atoms. Fig.IV.20(d) is a rotated view to show more clearly the dislocation lines. It looks like the non standard dislocations try to dissociate into Shockley partials but end up into small dislocation loops. This might be due to the Z periodic boundary condition impeding the dissociation. A simulation with a double thickness specimen was performed and a similar result was observed. These non standard dislocations always dissociate into small dislocation loops. Long relaxation time is applied to make sure that these dislocations are completely dissociated.

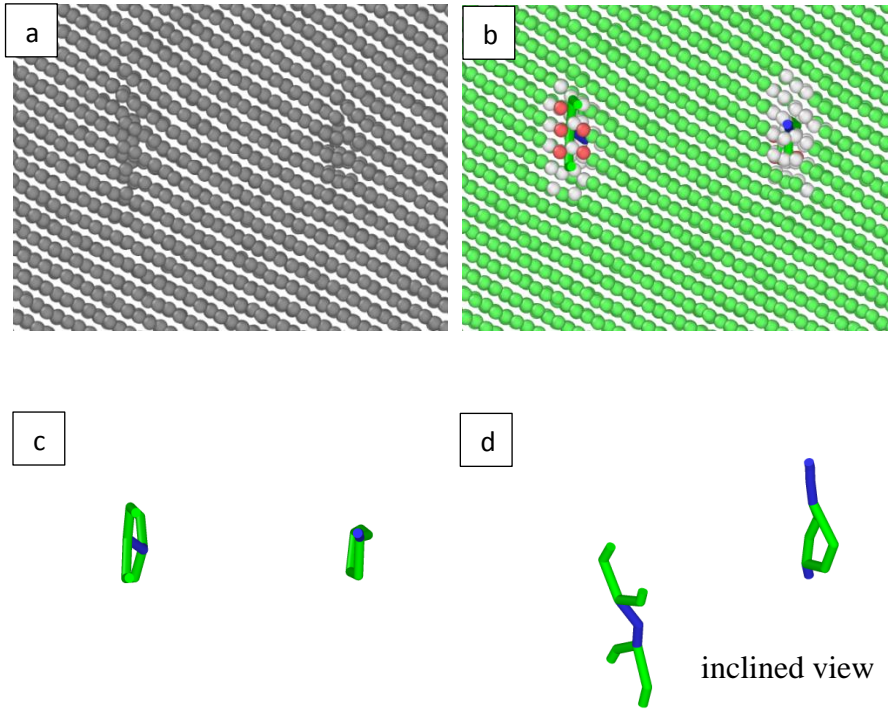


Fig.IV.20. Dissociation of non standard dislocations. (a) is a black and white top view. (b) is a coloured view with dislocations lines presented. (c) is the same view as (b) by removing all atoms and (d) is a inclined view to show more clearly dislocation loops. These are OVITO visualisations (many thanks again to its developer Alexander Stukowski).

Several different dissociations of these non standard dislocations have been observed. They can dissociate into Shockley and stair-rods partials, as shown in Fig.IV.21. One or several small dislocation loops in different planes may be nucleated during that dissociation. The dissociation is probably influenced by the external loading and/or interactions with other dislocations.

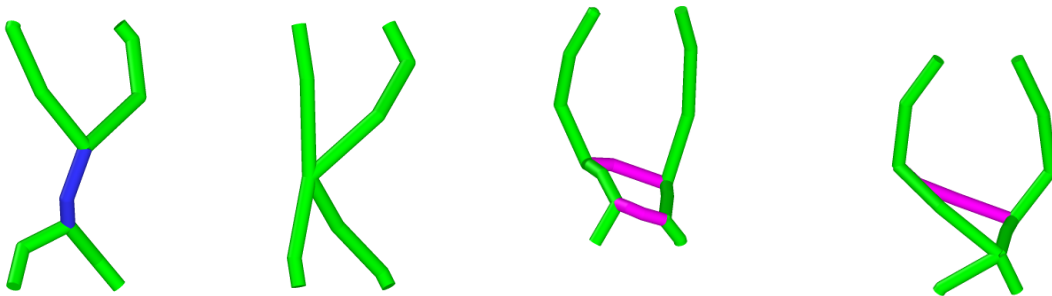


Fig.IV.21. Four of many possible dissociations of non standard dislocations. The colour code is the OVITO one, blue for perfect dislocation core, green for Shockley partials and pink for stair-rod partials. The non standard dislocations can dissociate into Shockley and stair-rod partials. There are two dislocation loops in different planes for the third and the fourth model.

These non standard dislocations are observed to glide in the material. The glide plane is about the plane of the major dislocation loop after dissociation (major: meaning the largest dislocation loop when there are several loops). Different slip planes associated with different dissociations are observed. Considering triplets of atoms in these loops, I estimated these planes to be $\sim(-8\ 16\ 1)$, $\sim(-11\ 23\ 1)$ and $\sim(13\ 1\ 1)$, which can be over-simplified as about (-120) and (100) . A sequence of slip on the $\sim(-8\ 16\ 1)$ plane is shown in Fig.IV.22, blue lines are slip planes, all atoms are removed for the sake of clarity.

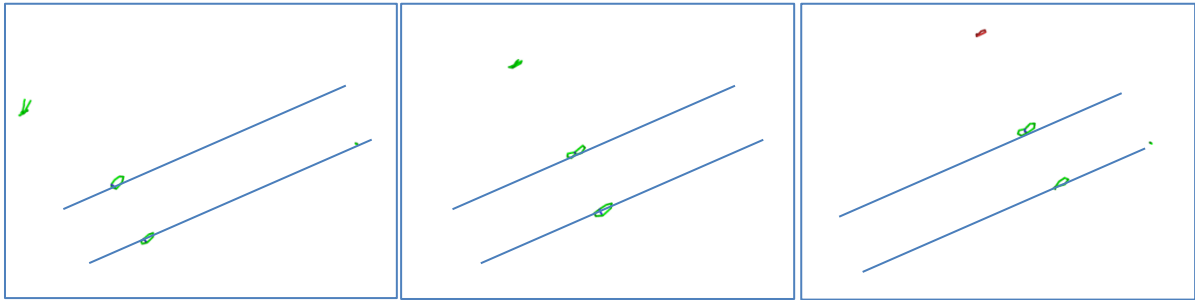


Fig.IV.22. Sequence of slip of two dissociated non standard dislocations.

Similar non standard dislocations are also observed in simulation boxes with a (100) orientation with periodic boundary condition. They dissociate at 300K in the same way as in the (714) and (111) boxes. In fact, only non standard dislocations were observed in this (100) box as all activated slip systems are oblique. Some observed non standard dislocations in a (100) box are shown in Fig.IV.23. They have similar dissociation and glide behaviours to the ones in the (714) and (111) boxes. Further details about their dissociations and slip planes will not be detailed here. An increase of the thickness along the Z direction does not change the nucleation of these non standard dislocations and their motions.

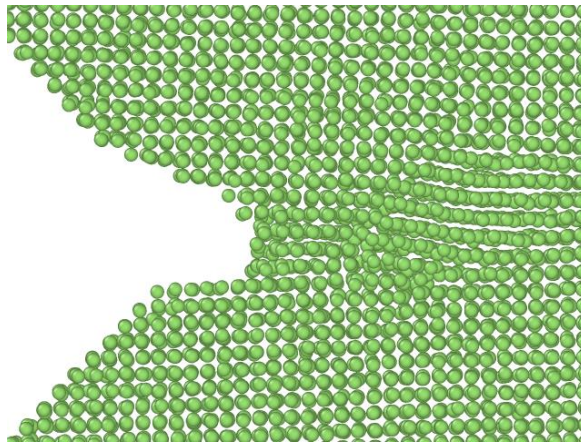


Fig.IV.23. Non standard dislocations observed in a (100) box.

The more we looked at these non standard dislocations and tried to analyze them, the more we become convinced that they are artefacts due to the Z periodic boundary condition (the help of Sylvie Lartigue, from CNRS-Thiais, is here duly acknowledged). The Z periodic boundary condition impedes the growth and dissociation of the standard dislocations of the oblique slip systems, and leads to the nucleation of the non standard dislocations. Removing the periodic boundary condition in Z, oblique standard dislocations nucleate and glide, whereas non standard dislocations are no more nucleated. This certainly also explains why only non standard dislocations were observed in the (100) box with periodic boundary condition: the eight activated slip systems are all oblique slip systems in the (100) box. They are all impeded by the periodic boundary condition, thus only non standard dislocations could be nucleated. The different observed slip planes for non standard dislocations correspond to different activated slip systems.

It is found that the only way to avoid this kind of non standard dislocation is to remove the periodic boundary condition. A simple increase of the specimen periodic thickness within reasonable computer limits does not help. For the considered orientations, one can thus say that simulations with periodic boundary conditions do not correspond to real physics because they impede the nucleation of oblique slip systems and lead to the nucleation of non standard dislocations. Simulations with Z boundary conditions are possibly reliable only if all activated slip planes are parallel to the Z direction.

4.5.3 Thinning effect without boundary conditions (Nano thin foil)

Simulations with free surface boundary conditions are now performed. This means that simulations are now made on nano-objects and effects due to their very thin thickness are expected.

Oblique slip systems can create surface steps in the Z direction, which could induce a local thinning in the Z direction under cycling, as shown in Fig.IV.24. This could facilitate the nucleation of some micro voids, as will be detailed in section 4.6.

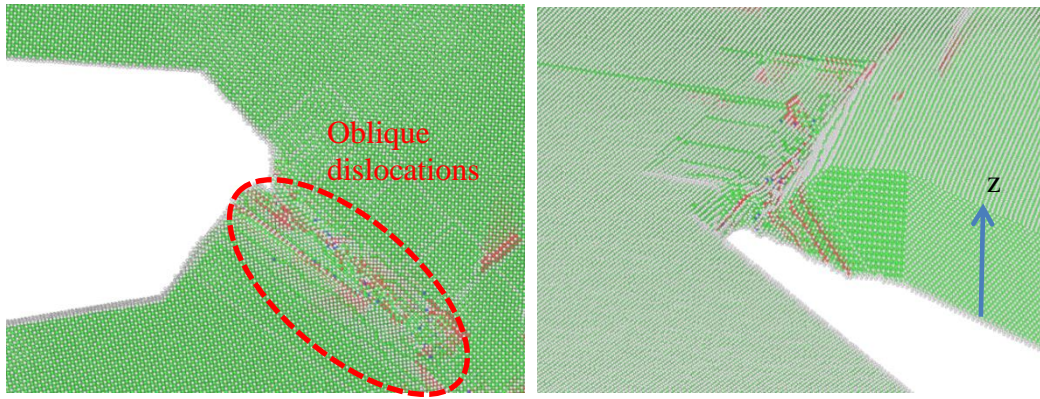


Fig.IV.24. Specimen thinning due to the free surface boundary condition in the Z direction, in a (100) box. Red lines present stacking faults behind a partial Shockley dislocation.

4.5.4 Section conclusions

Based on the simulations in this section, it is first found that for simulations under periodic boundary conditions, results are converged for thicknesses of four times of the minimum crystallographic thickness. Very small thickness could induce cleavage. The use of periodic boundary condition, however, impedes the nucleation of dislocations of oblique slip systems and causes the production of non standard dislocations which do not reflect real physics of bulk materials. Removing the periodic boundary condition avoids non standard dislocations but induces specimen local thinning.

The analysis of the non standard dislocations carried out in this section could be useful for cases when similar non standard dislocations are generated because of extreme stress conditions.

4.6 Crack propagation mechanisms

Crack propagation is now simulated in inert environment and propagation mechanisms are analysed. Tests are carried out for both '(100) box' and '(714) box', with and without periodic boundary conditions in Z.

4.6.1 Crack propagation in the '(100) box'

Simulations are first carried out using a '(100) box' without periodic boundary conditions, loaded in a force imposed way with $R_0=0$ and $\Delta K_I=2\text{MPa}\sqrt{\text{m}}$. Only three cycles are applied, with each cycle running over 2ns. During the first two cycles, nucleation of dislocations is observed along different slip systems during tension. Some of the slips of these dislocations are irreversible during unloading, which makes the crack tip propagate a little bit (nearly 1.5 \AA for these first two cycles). During the third cycle, due to the residual plasticity of the first two cycles and the newly nucleated dislocations, the irreversibility becomes more obvious.

The sequence of the third loading cycle is shown in Fig.IV.25. The first image corresponds to a stress intensity factor of nearly $1\text{MPa}\sqrt{\text{m}}$. The stress intensity factor is calculated using the geometry dependent formula given in the Appendix. One can observe that dislocations are nucleated asymmetrically. The second image corresponds to the maximum loading, at $2\text{MPa}\sqrt{\text{m}}$. A large number of dislocations are nucleated, which induces interactions between them. On the third image, the stress is relaxed to zero. Some dislocations glide back to the crack tip but some others are blocked by junctions created by the interactions between them, or by the elastic stress field. Lomer-Cottrell locks, Hirth locks and sessile Frank partial dislocations are observed. The crack propagates because of this irreversibility of dislocation slips just ahead of the crack tip. This simulation result shown in Fig.IV.25 (a) to (f) in copper at 300K is similar to Neumann's observation in copper in air at room temperature. A small crack increment is observed after each cycle. It should of course be noticed that both time and space scales differ strongly. The cause of irreversibility in Neumann's experiments is probably more complex.

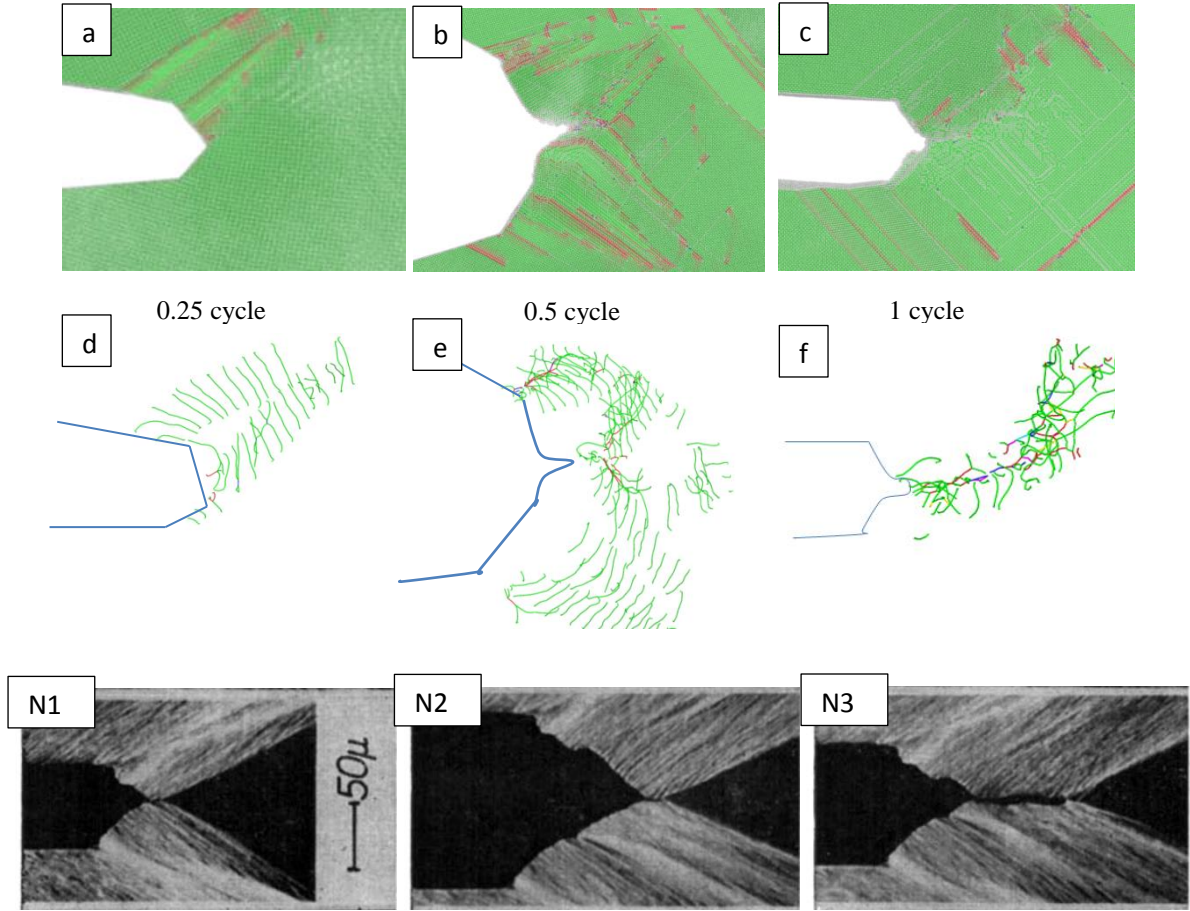


Fig.IV.25. Crack propagation due to the irreversibility of dislocation slips in copper at 300K. Red areas in images (a), (b) and (c) correspond to stacking faults. Atoms are removed in images (d), (e) and (f) in order to display dislocations lines and junctions between them. Green lines are Shockley partials, blue lines represent perfect dislocations, pink lines are Lomer-Cottrell locks, yellow lines are Hirth locks and blue lines correspond to Frack partial dislocations. No periodic boundary condition. Applied stress, $R_\sigma = 0$, $\Delta K = 2 \text{ MPa}\sqrt{\text{m}}$. Images (N1), (N2) and (N3) are Neumann's observations in copper at room temperature (see section 4.1.3). Even if the time and space scales differ, they can be compared with our simulations. The crack propagates from the left. Note that the black triangular area on the right ahead of the crack tip corresponds to a slip free area.

The crack in this simulation propagates along the (100) plane, perpendicularly to the loading. This is in agreement with the observation of [Neumann et al. 1977] who found that cracks can grow in stage II in inert environment, see section 4.1.2.

The crack grows nearly 3.9 \AA after the third cycle. This value is in the same order of magnitude as the crack propagation rate in copper in vacuum measured by [Neumann et al. 1977] at their lowest loading amplitude. [Horstemeyer et al. 2010] and [Farkas et al. 2005] also found sub-nanometer crack propagation rates in their simulations (see sections 4.1.2 and 4.2.1).

Similar tests have been carried out with displacement controlled loading. In this case, nucleated dislocations can reach free surfaces more rapidly and become irreversible (see section 4.4). As a result, there is a lack of dislocation interactions and junction productions. The crack propagates due to the irreversibility of the dislocations which have disappeared at the free surfaces. In these tests, however, free surfaces are not located very far away from the crack, as they are in real, non nanoscopic materials.

Simulations have also been carried out on the same system with Z-periodic boundary conditions, for comparative testing purpose. In that case, only non standard dislocations are generated. The crack also propagates, due to the irreversibility of these non standard dislocation slips.

4.6.2 Crack propagation in the '(714) box'

Simulations are then performed in a (714) box with imposed force, $R_0=0$, $\Delta K_I=2\text{MPa}\sqrt{\text{m}}$ and $\Delta K_{II}=0.6\text{MPa}\sqrt{\text{m}}$ (ΔK_I and ΔK_{II} are obtained using the geometry dependent formula in the Appendix), firstly without periodic boundary conditions. The thickness in the Z direction is eight times the minimum crystalline periodicity. The primary slip plane is perpendicular to the X-Y plane, together with an oblique slip plane corresponding to an activated slip system (see section 4.3).

Three cycles are applied and the crack tip blunting is observed under tension in each of these three loading cycles (see Fig.IV.26). Nucleated dislocations change the shape of the crack tip but no obvious crack propagation is observed. Contrary to what happened in the '(100) box', there is almost no production of irreversible junctions between dislocations and dislocation, slips are quite reversible on that point of view. This may be so because there are only two activated slip systems instead of eight equivalent slip systems for the '(100) box'.

Irreversibility slips in this '(714) box' are mainly due to the free surfaces. Some dislocations in the primary slip plane can go across the grain boundary and disappear on the right surface. Dislocations in the oblique slip plane can come out of the surfaces in the Z direction. However, these free surface induced irreversible slips are rare for the primary slips

and they do not lead to crack propagation in this ‘(714) box’, at least after 3 cycles. The crack length is not changed.

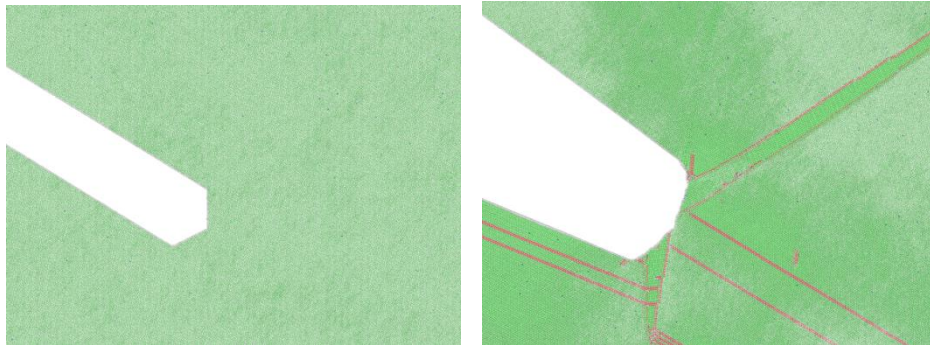


Fig.IV.26. Initial configuration (left) and crack tip blunting under tension with $K_I=2\text{MPa}\sqrt{\text{m}}$ (right).

The irreversibility of oblique slips in the thickness (Z direction) can induce local thinning, as presented in 4.5.3. When doing simulations on a box with lower thickness in Z (four times the minimum crystalline periodicity), a thin foil effect is observed with a nucleated nano-void. In such a box, a small area near the crack tip is observed to become thinner and thinner during cycling. This is due to the irreversibility of oblique dislocations, as indicated, in section 4.5.3. A nanometre scale void eventually nucleates ahead of the crack, grows and links back to the crack tip. The crack thus propagates by absorption of this nano-void, as shown in Fig.IV.27. This nano-void, however, is nucleated due to local thinning, which means that this mechanism is only valid for nano thin foils. This local thinning is also observed in thicker specimens. If further cycles are applied to a thicker specimen, similar-voids may probably also be nucleated.

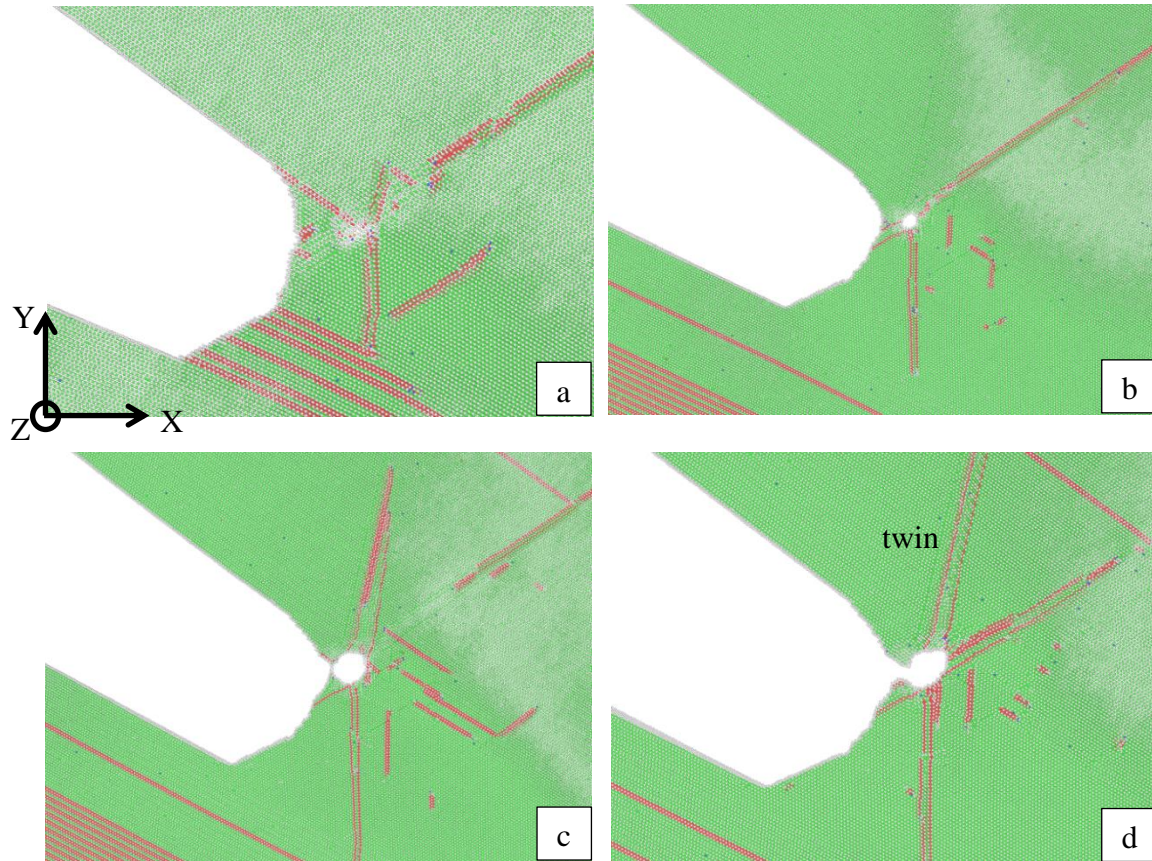


Fig.IV.27. Sequence of crack propagation by absorption of a nano-void in a nano-thin foil, in copper at 300K. Images (a), (b), and (c) present a nano-void nucleation and growth during the third loading cycle; the void is nucleated due to the local thinning in the Z direction. Image (d) is the beginning of the fourth cycle; the crack propagates due to the coalescence with the nano void. Some small twins are observed.

Similar simulations have also been performed with periodic boundary conditions in Z for test purposes, at the same temperature with the same loading. Dislocations of primary slip system and non standard dislocations are observed. At the end of the third cycle, no obvious crack propagation has occurred, see Fig.IV.28. There is only an evolution of the shape of the crack tip. It is possible that three cycles are not long enough to observe crack propagation for this orientation.

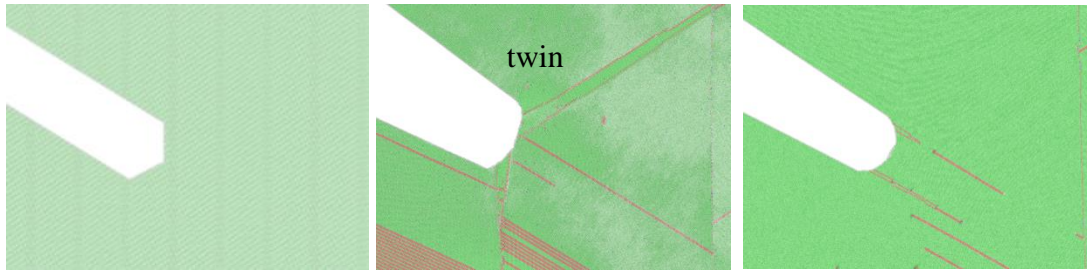


Fig.IV.28. Crack evolution after three cycles with periodic boundary conditions. No crack propagation is observed. The first image shows the initial geometry. The second image shows a snapshot at the middle of the third loading cycle with crack tip blunting. The third image corresponds to the end of the third loading cycle. Twinning is observed in the second image. It is reversible and not observed in the third image.

The $\Sigma 11 \{113\} \langle 112 \rangle$ symmetric tilt grain boundary in this ‘(714) box’ has some effects on the dislocation motion. During different simulations, it is observed that dislocations can temporarily stop at that grain boundary which may induce dislocation pile-ups. They then cross the grain boundary. And they may cross backwards under opposite loading and go back to the crack tip. New dislocations can also nucleate from the GB. Once a dislocation goes across the grain boundary, it leaves behind a residual dislocation which is along the vertical Y direction in our simulation. The decomposition of dislocations can induce GB disconnection and produce defects in the grain boundary, as shown in Fig.IV.29. In order to get more obvious phenomena near the grain boundary, some tests are performed by doubling the load. We note that twins are sometimes observed near the GB when the strain is maximum. More tests need to be done, also with other types of grain boundaries.

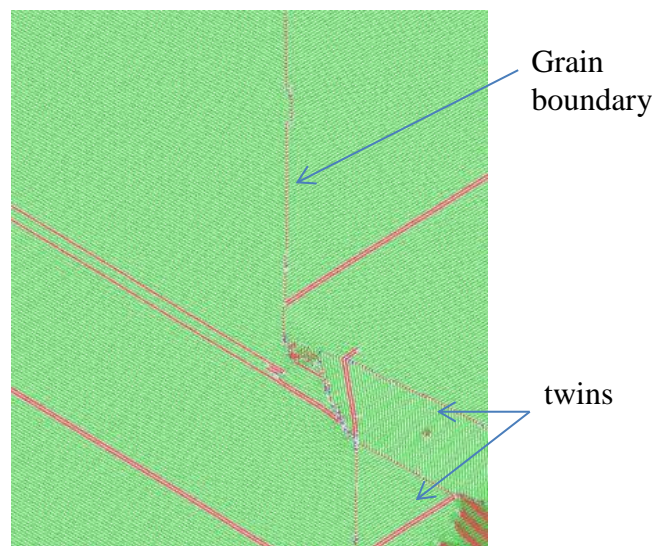


Fig.IV.29. Structural changes observed at a grain boundary in the loaded ‘(714) box’. The small blue points correspond to atoms whose local environment is far from fcc. Twins are observed near the grain boundary.

4.7 Temperature effect on the crack propagation

Tests have been performed on a '(100) box' at 300K and at 700K in order to investigate the temperature effect on crack propagation, without applying periodic boundary conditions. Fig.IV.30 shows two crack tips in copper for a stress intensity factor K of nearly $1\text{MPa}\sqrt{\text{m}}$, at 300K and at 700K. More dislocations are nucleated at 700K, with more complex dislocation interactions. One can also observe that the shape of the crack tip starts to change at 700K after 1ns but not yet at 300K, for the same loading amplitude.

One can thus say that a higher temperature triggers more dislocation nucleation and thus more interactions occur. A crack may propagate more rapidly at higher temperature, resulting in a shorter fatigue life. More loading cycles should be performed at these two different temperatures in order to predict the crack propagation rates and compare them together.

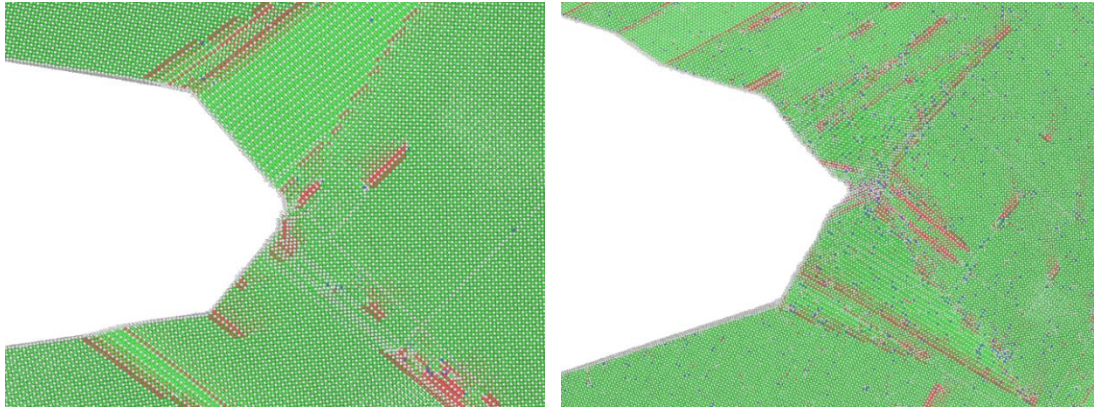


Fig.IV.30. Crack propagation in copper with a stress intensity factor of nearly $1\text{MPa}\sqrt{\text{m}}$ at 300K (left) and 700K (right). 0.25 cycle. Applied stress. Snapshots after 1 ns in both cases.

4.8 Comments about the influence of the crack plane orientation on the crack propagation rate

In our simulations, a crack propagation is observed in the '(100) box' where there are several activated slip systems. No crack propagation is observed in the '(714) box' where there are only two activated slip systems. It is of course quite possible that we did not perform enough loading cycles to observe crack propagation in the '(714) box'. Yet, our simulation results show at least that a crack whose plane is a (100) plane (stage II) grows more rapidly than a crack whose plane is a (111) plane (stage I).

This is in agreement with the review of [Petit et al. 1994] showing that the crystallographic orientation plays an important role on the crack propagation rate in air and in inert environment. [Rieux et al. 1979] also found that crack propagation is sensitive to the

crack plane orientation in fcc metals: for a given value of ΔK , cracks propagate more rapidly along the (100) plane than along the (111) plane (see section 4.1.2).

Based on our simulations, a possible reason could be that there are more activated slip systems ahead of a crack with a (100) plane than ahead of a crack with a (111) plane. When there is a large number of activated slip systems, dislocation glide could be more irreversible owing to the formation of ‘locks’ and sessile interactions between dislocation slips in different planes.

In order to check further the influence of the number of activated slip system on crack propagation, I carried out a small test on a ‘(111) box’ (see section 4.5.2) with an applied shear displacement on the upper and lower boundaries (cf. Fig.IV.31). With such a box, only one slip system is activated whose plane is the (111) plane. No crack propagation is observed in this box. What is observed after each loading cycle is just an evolution which looks like a material transport from the left side to the right side, then from the right side to the left side, as shown in Fig.IV.31. It is interesting to note that this observed material transport looks like the ‘float’ of PSBs observed by [Ma and Laird 1988] (Fig.IV.32) who comment that the deformation in the PSBs seems like a ‘float’ between matrix segments

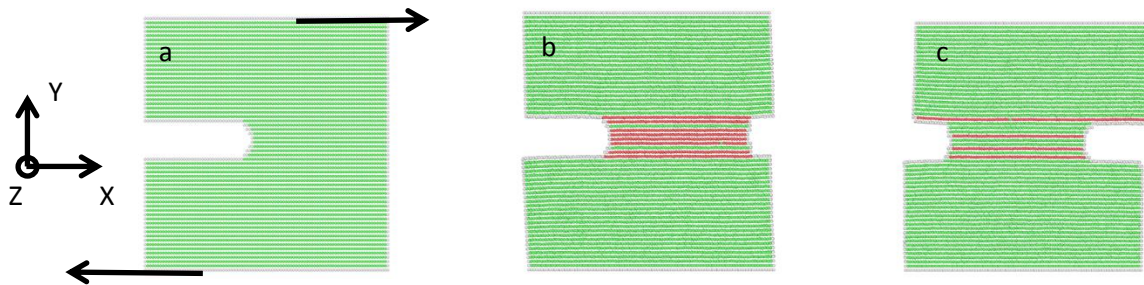


Fig.IV.32. ‘Material transport’ in the ‘(111) box’ under applied cyclic shear displacement. The shear displacement is applied on the upper and lower walls along X, presented by black arrows in (a).

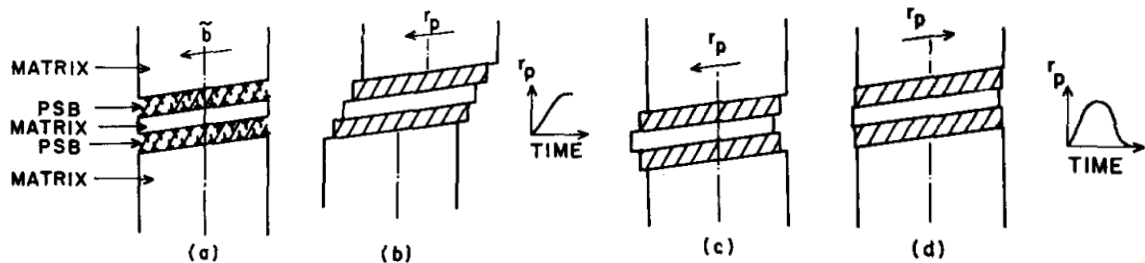


Fig.IV.32. Sketch of material drifting between PSBs and matrix during one loading cycle. From [Ma and Laird 1988].

4.9 Chapter conclusions and discussions

Atomistic simulations are carried out in this chapter to analyse crack propagation in vacuum environment. It is observed that in a (100) box, junction production due to dislocation interactions increases slip irreversibility. Cracks then propagate due to this slip irreversibility. It is also found that free surfaces can also increase irreversibility and favours crack propagation as it might be guessed from the results of chapter 2. No obvious crack propagation is observed in the (714) box. Yet a material transporting phenomenon is observed which seems like the ‘float’ described by [Ma and Laird 1988]. In thin nano-objects, nano-voids can be nucleated due to local cross section thinning ahead of a crack tip. Crack can then propagate by absorption of nano-voids. Crack tip blunting is observed for both (714) and (100) boxes under tension. The differences observed between the (100) box and the (714) box can be explained by the effect of the crack plane orientation and loading mode which directly affects the activation of the slip systems and thus plays a role in the crack propagation mechanism. Comparing the (100) box and the (714) box, there are more activated slip systems in the (100) box than in the (714) box. The higher slip irreversibility in the (100) box seems to be due to the large number of activated slip systems. Hysteresis effect is also observed during cycling due to the nucleated plasticity. Higher temperatures may accelerate dislocation nucleation, lead to more dislocation interactions and thus increase slip irreversibility. This may increase the crack propagation rates and thus decrease the metal fatigue life. Further simulations are ongoing to check the temperature influence on the crack growth rate.

Our simulation on the (100) box provides results comparable to Neumann’s observations in copper single crystal. It should be noticed that the irreversibility mechanisms in Neumann’s tests should be more complex because of air environment. A stage II crack propagation is observed in our (100) box, in agreement with [Neumann et al. 1977] observation that the crack grows in stage II in inert environment. The estimated propagation rate in our (100) specimen is nearly 1.8 \AA/cycle at 300K with $\Delta K=2\text{MPa}\sqrt{\text{m}}$, similar to [Neumann et al. 1977, 1979] observations in high vacuum at their lowest loading amplitude.

Contrary to some other simulation investigations reviewed in section 4.2 where the main observed propagation mechanism is void nucleation and absorption, in this work, it is found that the main propagation mechanism is due to irreversibility of dislocation glide. No nano-void was observed with periodic boundary conditions, at variance with what observed by [Horstemeyer et al. 2010]. And no crack propagation is observed due to absorption of

vacancies, again at variance with what [Nishimura and Miyazaki 2004] and [Farkas et al. 2005]. We note that only [Horstemeyer et al. 2010] observed nanoscale voids in their simulations. Other authors observed only small vacancies corresponding to the lack of several atoms. And I suggest that vacancies nucleated in [Farkas et al. 2005] simulation are mainly due to the presence of grain boundaries in the considered nano poly crystal. Vacancies are more difficult to nucleate in the bulk than at grain boundaries, particularly with nano-sized grains. A grain boundary is a two dimensional structural defect which may interact strongly with incoming dislocations.

Applying cyclic loading is a time consuming task for molecular dynamic simulations and that is a reason why simulations of only three cycles have been yet performed. Both force imposed and displacement imposed loadings are applied in this work. However, both of these loadings have their shortcomings. A better way to perform loading could be the application of a displacement field deduced from the LEFM or from the EPFM. This is one of the perspectives of this section, besides carrying out some simulations with other differently oriented systems and other types of grain boundaries.

Crack propagation under oxygen environment is another important perspective. In oxygen environment, mechanisms of crack propagation should be more complex. The presence of oxygen may trigger nucleation of dislocations, break atomic bonds, impede re-welding under compressive loading, stabilize junctions, etc. First tests have been carried out for copper in oxygen environment using the ReaxFF potential used in chapter 3.

One would need to be able to apply a large number of loading cycle with slower strain rates on larger systems of realistic metallic alloys already containing defects such as dislocations and grain boundaries in complex environments (hydrogen, oxygen, chlorides, sulfides, ...) : improvements in computer capacities and interatomic modelling are still welcome!

CHAPTER 5.

SUMMARY, CONCLUSIONS, AND PERSPECTIVES

In this work, mechanisms of surface step evolution and crack initiation are analysed in inert and oxygen environment. Nano crack propagation is also simulated in inert environment under cyclic loading.

Molecular dynamics simulations are carried out to follow at the atomistic level the evolution of the very first steps produced at a free surface until step accumulation, i.e. from the first cycle up to several cycles. Step irreversibility, crack initiation and propagation are analysed by explicitly taking into account surface steps and cracks. Different face centred cubic metals, viz. Al, Cu, Ni, and Ag, are considered. N-body embedded atom model (EAM) like potentials are used for simulations in vacuum. ReaxFF (reactive force field) and COMB (charge optimized many body) potentials are used for simulations in oxygen environment. All these potentials provide fairly correct estimations of different physical properties of the materials analysed.

Surface step irreversibility is first analysed in inert environment. Edge dislocations with a standard Burgers vector $b=a\langle 110 \rangle/2$ are inserted in the bulk. They either spontaneously glide towards free surfaces or a low stress is applied to let them glide. Their emergence at the free surface induces surface step production. A surface step reconstruction phenomenon is observed which minimizes the surface step energy and increases its irreversibility. Three different types of mechanisms can be identified for the reconstruction. The quasi-instantaneous reconstruction occurs at all temperatures, it takes only a few picoseconds and effectively decreases the step energy. The thermal vibration assisted reconstruction is another mechanism during which thermal vibrations are needed to let surface step atoms overcome local energy barriers and reach lower energy configurations. The third mechanism is a surface diffusion assisted reconstruction which takes place only at higher temperatures and requires the diffusion of superficial adatoms. A rough estimation coupling bulk estimations (Essmann-Gösele-Mughrabi model and the related Lépinoux-Kubin model) and our surface simulations gives an irreversibility fraction between 0.4 and 0.7. These values are larger than many estimations proposed in the past which only take into account bulk mechanisms [Essmann et

al. 1981; Lépinoux and Kubin 1986]. Our estimated values are closer to the value measured by atomic force microscopy (AFM), namely 0.8 [Weidner et al. 2011]. As surface steps are irreversible, a micro-notch initiation can be observed under cyclic loading.

Similar simulations are carried out in oxygen environment using ReaxFF and COMB3 potentials for nickel and copper, in order to assess the influence of oxygen environment on surface irreversibility. The predicted first stages of nickel and copper oxidation are observed to be different. They are both in general agreement with experimental observations.

Oxygen molecules adsorbed on the nickel surface dissociate into oxygen atoms which then penetrate into the metal over a small depth. Some nickel atoms diffuse outwards, which results in an external growth and initiation of small NiO islands.

Copper surface oxidation mechanisms are different from those of nickel. Oxygen is mainly chemisorbed as O₂ molecules which rarely dissociate even at high temperature. Neither cuprous oxide Cu₂O nor cupric oxide CuO is observed in the first stages of oxidation and there is only a very thin penetration in the bulk. It is worth noting that the COMB3 potential predicts the formation of an amorphous surface layer while the copper atoms essentially keep a copper fcc environment with ReaxFF.

For the very first oxidation stages at the temperatures we considered in our simulations of nickel and copper, oxygen alone never increases surface step irreversibility and the simulated surfaces evolve in the same way as in inert environment. It has no significant effect on the surface step reconstruction and does not impede the slip of dislocations towards the surface. These results agree with experimental observations made by several workers who noticed that the PSB surface relief is the same for fatigue in inert environment and in air [Basinski et al, 1992]. [Mughrabi and Wang 1981] observed that oxygen environment only acts on the crack propagation during stage I and the beginning of stage II but does not influence the initiation of cracks shorter than 1 μm . Based on our simulations, the irreversibility factor in oxygen environment should be the same as in inert environment. A nano-notch can still initiate under cyclic loading. At high temperature for which oxidation induces the formation of a deep oxide layer, the conclusions could be different.

Simulations are also carried out for crack propagation in inert environment. Dislocation interactions induce the formation of dislocation junctions and increase the slip irreversibility. In a $\{[100],[010],[001]\}$ box, or ‘(100) box’, a crack parallel to a (100) plane, which possesses several activated slip systems, propagates thanks to this junction-induced

irreversibility (stage II). In a $\{[-131],[714],[11-2]\}$ box, or '(714) box', no obvious propagation is observed on a crack orientated along a (111) plane with only two activated slip systems and under mixed mode (stage I). Crack tip blunting is observed in both '(714) box' and '(100) box' under tension. The differences observed between the (100) box and the (714) box can be explained as the effect of the crack plane orientation which directly affects the activated slip systems and thus plays a rôle in the crack propagation mechanism and crack propagation rate. It has also been experimentally observed that crack propagate more rapidly in the (100) plane than in the (111) plane in various austenitic steels by [Rieux et al. 1979].

In simulated nano-thin foils, cracks are also observed to propagate by coalescence between the crack tip and nano-voids nucleated ahead of it due to cross section thinning.

Force or displacement controlled loading, specimen thickness, application of periodic boundary conditions, specimen orientation and temperature affect the crack propagation mechanisms and crack propagation rates. The nanoscale crack propagation rate is estimated about 1.8 Å per cycle at 300K in the (100) box, similar to [Neumann et al. 1977, 1979] observations in high vacuum at their lowest loading amplitude. At variance with other simulation studies, we do not observe obvious crack propagation by absorption of vacancies or micro-voids with periodic boundary conditions.

More crystal orientations should be considered in order to compare different crack propagation mechanisms due to changes in the orientation. Crack propagation simulations should also be carried out in oxygen environment. An Fe-Ni-Cr O-H potential is being developed for austenitic stainless steels, such as the ones in service in nuclear power plants, thanks to a collaboration between CEA and Pennsylvania University. It will then be possible to simulate the fatigue behaviour of austenitic stainless steels in realistic environment. The final objective is a better prediction of macroscopic lifetime based on a deeper knowledge of microscopic mechanisms.

References

- ALAIN, R., VIOLAN, P., AND MENDEZ, J. 1997. Low cycle fatigue behavior in vacuum of a 316L type austenitic stainless steel between 20 and 600°C. Part I : fatigue resistance and cyclic behavior. *Materials science & engineering. A, Structural materials : properties, microstructure and processing* 229, 87–94.
- ASLANIDES, A. AND PONTIKIS, V. 1998. Atomistic study of dislocation cores in aluminium and copper. *Computational Materials Science* 10, 401–405.
- AUBRY, B. AND BERNARDET, H. 1968. *Proceedings of 4th International Vacuum Congress*, 787–790.
- BAKER, K.L. AND WARNER, D.H. 2014. An atomistic investigation into the nature of near threshold fatigue crack growth in aluminum alloys. *Engineering Fracture Mechanics* 115, 111–121.
- BASINSKI, S.J., BASINSKI, Z.S., AND HOWIE, A. 1969. Early stages of fatigue in copper single crystals. *Philosophical Magazine* 19, 161, 899–924.
- BASINSKI, Z.S. AND BASINSKI, S.J. 1989. Copper single crystal PSB morphology between 4.2 and 350 K. *Acta Metallurgica* 37, 12, 3263–3273.
- BASINSKI, Z.S. AND BASINSKI, S.J. 1992. Fundamental aspects of low amplitude cyclic deformation in face-centred cubic crystals. *Progress in Materials Science* 36, 89–148.
- BASINSKI, Z.S., PASCUAL, R., AND BASINSKI, S.J. 1983. Low amplitude fatigue of copper single crystals—I. The role of the surface in fatigue failure. *Acta Metallurgica* 31, 4, 591–602.
- BATHIAS, C. AND PARIS, P.C. 2005. *Gigacycle fatigue in mechanical practice*. Dekker, New York. NY.
- BEG, M.M. AND SHAPIRO, S.M. 1976. Study of phonon dispersion relations in cuprous oxide by inelastic neutron scattering. *Physical Review B* 13, 4, 1728–1734.
- BENNETT, V.P. AND McDOWELL, D.L. 2003. Crack tip displacements of microstructurally small surface cracks in single phase ductile polycrystals. *Engineering Fracture Mechanics* 70, 2, 185–207.
- BERNARD, M., VOGT, J.B., BUI-QUOC, T., AND DICKSON, J.I. 1987. Low-Cycle Fatigue Behaviour and Cumulative Damage Effect of 316 Stainless Steel at 20°, 427° and 650°C. *Fatigue* 84, EMAS.
- BERNSTEIN, N. AND TADMOR, E. 2004. Tight-binding calculations of stacking energies and twinnability in fcc metals. *Physical Review B* 69, 9.
- BROCHARD, S., HIREL, P., PIZZAGALLI, L., AND GODET, J. 2010. Elastic limit for surface step dislocation nucleation in face-centered cubic metals: Temperature and step height dependence. *Acta Materialia* 58, 12, 4182–4190.
- CATHCART, J.V., PETERSEN, G.F., AND SPARKS, C.J. 1969. The Structure of Thin Oxide Films Formed on Nickel Crystals. *Journal of The Electrochemical Society* 116, 5, 664–668.
- CHENG, A.S. AND LAIRD, C. 1981. FATIGUE LIFE BEHAVIOR OF COPPER SINGLE CRYSTALS. PART I: OBSERVATIONS OF CRACK NUCLEATION. *Fatigue & Fracture of Engineering Materials and Structures* 4, 4, 331–341.

- CHENG, A.S. AND LAIRD, C. 1983. The transition from stage I to stage II fatigue crack propagation in copper single crystals cycled at constant strain amplitudes. *Materials Science and Engineering* 60, 2, 177–183.
- CLEMENT, N. 1984. Influence de l'ordre à courte distance sur les mécanismes de déformation des solutions solides. In: F. Reynaud, N. Clément and J.I. Couderc, eds., *L'ordre et le désordre dans les matériaux*. Les éditions de physique, Les Ulis, 167–182.
- COTTERELL, B. 2010. *Fracture and life*. ICP, Imperial College Press, London.
- COTTRELL, A.H. 1964. *Theory of Crystal Dislocations*. Goldon and Breach, New York.
- COTTRELL, A.H. AND HULL, D. 1957. Extrusion and Intrusion by Cyclic Slip in Copper. *Proceedings of the Royal Society A: Mathematical, Physical and Engineering Sciences* 242, 1229, 211–213.
- DAVISSON, C. AND GERMER, L.H. 1927. Diffraction of Electrons by a Crystal of Nickel. *Physical Review* 30, 6, 705–740.
- DELCHAR, T.A., TOMPKINS, F.C., AND HAM, F.S. 1967. Chemisorption and Incorporation of Oxygen at a Nickel Surface. *Proceedings of the Royal Society of London A: Mathematical, Physical and Engineering Sciences* 300, 1461, 141–158.
- DEVINE, B., SHAN, T.-R., CHENG, Y.-T., ET AL. 2011. Atomistic simulations of copper oxidation and Cu/Cu₂O interfaces using charge-optimized many-body potentials. *Physical Review B* 84, 12, 125308.
- DIFFERT, K., ESMANN, U., AND MUGHRABI, H. 1986. A model of extrusions and intrusions in fatigued metals II. Surface roughening by random irreversible slip. *Philosophical Magazine A* 54, 2, 237–258.
- DU PLESSIS, P. DE V., TONDER, S.J. VAN, AND ALBERTS, L. 1971. Elastic constants of a NiO single crystal: I (Magnetic transitions). *Journal of Physics C: Solid State Physics* 4, 14, 1983.
- DUDAREV, S.L., BOTTON, G.A., SAVRASOV, S.Y., HUMPHREYS, C.J., AND SUTTON, A.P. 1998. Electron-energy-loss spectra and the structural stability of nickel oxide: An LSDA+U study. *Physical Review B* 57, 3, 1505–1509.
- DUQUETTE, D.J. 1978. *Environmental Effects on General Fatigue Resistance and Crack Nucleation in Metals and Alloys*.
- DUQUETTE, D.J. AND GELL, M. 1971. The effect of environment on the mechanism of Stage I fatigue fracture. *Metallurgical Transactions* 2, 5, 1325–1331.
- ERBER, T., GURALNICK, S.A., AND MICHELS, S.C. 1993. Hysteresis and Fatigue. *Annals of Physics* 224, 2, 157–192.
- ERTL, G. 1967. Untersuchung von oberflächenreaktionen mittels beugung langsamer elektronen (LEED). *Surface Science* 6, 2, 208–232.
- ESSMANN, U. 1982. Irreversibility of cyclic slip in persistent slip bands of fatigued pure f.c.c. metals. *Philosophical Magazine A* 45, 1, 171–190.

- ESSMANN, U., GÖSELE, U., AND MUGHRABI, H. 1981. A model of extrusions and intrusions in fatigued metals I. Point-defect production and the growth of extrusions. *Philosophical Magazine A* 44, 2, 405–426.
- ESSMANN, U. AND MUGHRABI, H. 1979. Annihilation of dislocations during tensile and cyclic deformation and limits of dislocation densities. *Philosophical Magazine A* 40, 6, 731–756.
- EWING, J.A. AND HUMFREY, J.C.W. 1903. The Fracture of Metals under Repeated Alternations of Stress. *Philosophical Transactions of the Royal Society A: Mathematical, Physical and Engineering Sciences* 200, 321–330, 241–250.
- FAN, Z., HARDOUIN DUPARC, O., AND SAUZAY, M. 2016. Molecular dynamics simulation of surface step reconstruction and irreversibility under cyclic loading. *Acta Materialia* 102, 149–161.
- FARKAS, D., WILLEMANN, M., AND HYDE, B. 2005. Atomistic Mechanisms of Fatigue in Nanocrystalline Metals. *Physical Review Letters* 94, 16, 165502.
- FEHLNER, F.P. AND MOTT, N.F. 1970. Low-temperature oxidation. *Oxidation of Metals* 2, 1, 59–99.
- FERRIE, E. AND SAUZAY, M. 2009. Influence of local crystallographic orientation on short crack propagation in high cycle fatigue of 316LN steel. *Journal of Nuclear Materials* 386–388, 666–669.
- FINNEY, J.M. AND LAIRD, C. 1975. Strain localization in cyclic deformation of copper single crystals. *Philosophical Magazine* 31, 2, 339–366.
- FINNEY, J.M. AND LAIRD, C. 1982. The development of slip offsets within persistent slip bands during a single fatigue cycle. *Materials Science and Engineering* 54, 1, 137–141.
- FISHER, J.C., JOHNSTON, W.G., AND THOMSON, R., EDS. 1957. *Dislocations And Mechanical Properties Of Crystals*. John Wiley And Sons Inc.
- FOILES, S.M., BASKES, M.I., AND DAW, M.S. 1986. Embedded-atom-method functions for the fcc metals Cu, Ag, Au, Ni, Pd, Pt, and their alloys. *Physical Review B* 33, 12, 7983–7991.
- FRANÇOIS, D., PINEAU, A., AND ZAOUÏ, A. 2013. *Mechanical Behaviour of Materials*. Springer Netherlands, Dordrecht.
- FRIEDEL, J. 1964. *Dislocations*. Oxford, Pergamon Press.
- GERLAND, M., MENDEZ, J., LÉPINOUX, J., AND VIOLAN, P. 1993. Dislocation structure and corduroy contrast in a 316L alloy fatigued at (0.3–0.5) Tm. *Materials Science and Engineering: A* 164, 1, 226–229.
- GREENFIELD, I.G. 1971. The effect of diffused surface layers and oxygen atmosphere on the development of fatigue striations and cracks in copper single crystals. *Acta Metallurgica* 19, 8, 857–869.
- GRINBERG, N.M. 1982. The effect of vacuum on fatigue crack growth. *International Journal of Fatigue* 4, 2, 83–95.

- GULBRANSEN, E.A. AND MCMILLAN, W.R. 1952. Electron Diffraction Studies on the Oxidation of Pure Copper and Pure Zinc Between 200° and 500°C. *Journal of The Electrochemical Society* 99, 10, 393–401.
- HALLBERG, J. AND HANSON, R.C. 1970. The elastic constants of cuprous oxide. *physica status solidi (b)* 42, 1, 305–310.
- HARDOUIN DUPARC, O., LARERE, A., LEZZAR, B., KHALFALLAH, O., AND PAIDAR, V. 2005. Comparison of the intergranular segregation for eight dilute binary metallic systems in the Σ 11' {332} tilt grain boundary. *Journal of Materials Science* 40, 12, 3169–3176.
- HIRTH, J.P. AND LOTHE, J. 1992. *Theory of Dislocations*. Krieger Pub Co, Malabar, FL.
- HOLLMANN, M., BRETSCHNEIDER, J., AND HOLSTE, C. 2000. Dislocation Structure and Strain Localisation in Nickel Single Crystals Cyclically Deformed at 77 K. *Crystal Research and Technology* 35, 4, 479–492.
- HOLLOWAY, P.H. 1981. Chemisorption and oxide formation on metals: Oxygen–nickel reaction. *Journal of Vacuum Science & Technology* 18, 2, 653–659.
- HOLLOWAY, P.H. AND HUDSON, J.B. 1974. Kinetics of the reaction of oxygen with clean nickel single crystal surfaces. *Surface Science* 43, 1, 123–140.
- HOLSTE, C. 2004. Cyclic plasticity of nickel, from single crystals to submicrocrystalline polycrystals. *Philosophical Magazine* 84, 3–5, 299–315.
- HORDON, M.J. 1966. Fatigue behavior of aluminum in vacuum. *Acta Metallurgica* 14, 10, 1173–1178.
- HORSTEMEYER, M.F., FARKAS, D., KIM, S., TANG, T., AND POTIRNICHE, G. 2010. Nanostructurally small cracks (NSC): A review on atomistic modeling of fatigue. *International Journal of Fatigue* 32, 9, 1473–1502.
- HULL, D. 1957. Surface structure of slip bands on copper fatigued at 293°, 90° 20° and 4.2° K. *Journal of the Institute of Metals*. 86, 425–427.
- HULL, D. AND BACON, D.J. 2011. *Introduction to dislocations*. Elsevier/Butterworth-Heinemann, Amsterdam.
- INDENBOM, V.L. 1992. *Elastic strain fields and dislocation mobility*. North-Holland.
- JACOBSEN, K.W., NORSKOV, J.K., AND PUSKA, M.J. 1987. Interatomic interactions in the effective-medium theory. *Physical Review B* 35, 14, 7423–7442.
- JOST, W. 1960. *Diffusion in solids, liquids, gases*. New York, Academic Press.
- KENNEDY, A.J. 1963. *Processes of Creep and Fatigue in Metals*. New York, Wiley.
- KITCHNER, H.O., KUBIN, L.P., AND PONTIKIS, V. 1995. *Computer Simulation in Materials Science*, NATO ASI series
- KRESSE, G. AND FURTHMÜLLER, J. 1996. Efficient iterative schemes for *ab initio* total-energy calculations using a plane-wave basis set. *Physical Review B* 54, 16, 11169–11186.

- KRUPP, U. 2007. *Fatigue crack propagation in metals and alloys: microstructural aspects and modelling concepts*. Wiley-VCH, Weinheim.
- LAIRD, C. 1976. *Mater. Sci. Eng.*, 231–36.
- LAIRD, C. AND SMITH, G.C. 1962. Crack propagation in high stress fatigue. *Philosophical Magazine* 7, 77, 847–857.
- LAIRD, C. AND SMITH, G.C. 1963. Initial stages of damage in high stress fatigue in some pure metals. *Philosophical Magazine* 8, 95, 1945–1963.
- LAWLESS, K.R. AND GWATHMEY, A.T. 1956. The structure of oxide films on different faces of a single crystal of copper. *Acta Metallurgica* 4, 2, 153–163.
- LÉPINOUX, J. AND KUBIN, L.P. 1985. In situ TEM observations of the cyclic dislocation behaviour in persistent slip bands of copper single crystals. *Philosophical Magazine A* 51, 5, 675–696.
- LÉPINOUX, J. AND KUBIN, L.P. 1986. Dislocation mechanisms and steady states in the cyclic deformation of facecentred cubic crystals. *Philosophical Magazine A* 54, 5, 631–649.
- LI, P., LI, S.X., WANG, Z.G., AND ZHANG, Z.F. 2011. Fundamental factors on formation mechanism of dislocation arrangements in cyclically deformed fcc single crystals. *Progress in Materials Science* 56, 3, 328–377.
- LIANG, T., SHAN, T.-R., CHENG, Y.-T., ET AL. 2013. Classical atomistic simulations of surfaces and heterogeneous interfaces with the charge-optimized many body (COMB) potentials. *Materials Science and Engineering: R: Reports* 74, 9, 255–279.
- LOU, L., NORDLANDER, P., AND HELLSING, B. 1994. Theoretical study of O₂ dissociation on copper and nickel clusters. *Surface Science* 320, 3, 320–330.
- LOURS, P. 2016. *Au coeur des matériaux cristallins*. Presses des Mines.
- LÜTH, H. 2014. *Solid Surfaces, Interfaces and Thin Films*. Springer.
- MARTIN, D.E. 1965. Plastic Strain Fatigue in Air and Vacuum. *Journal of Basic Engineering* 87, 4, 850–856.
- MARTIN, R.M. 2008. *Electronic Structure: Basic Theory and Practical Methods*. Cambridge University Press, Cambridge.
- MAY, A.N. 1960. A Model of Metal Fatigue. *Nature* 185, 303–304.
- MCEVILY, A.J. AND JOHNSTON, T.L. 1967. The role of cross-slip in brittle fracture and fatigue. *International Journal of Fracture Mechanics* 3, 1, 45–74.
- MCCAMMON, R.D. AND ROSENBERG, H.M. 1957. The Fatigue and Ultimate Tensile Strengths of Metals between 4° and 293 degrees K. *Proceedings of the Royal Society A: Mathematical, Physical and Engineering Sciences* 242, 1229, 203–211.
- MECKE, K. AND BLOCHWITZ, C. 1982. Saturation Dislocation Structures in Cyclically Deformed Nickel Single Crystals of Different Orientations. *Crystal Research and Technology* 17, 6, 743–758.

- MENZEL, E. 1949. Die Verwachsungen von Kupfer mit seinem Oxydul. *Annalen der Physik* 440, 3–5, 163–180.
- MEYERS, M.A. AND CHAWLA, K.K. 2009. *Mechanical Behavior of Materials*. Cambridge University Press.
- MISHIN, Y., MEHL, M.J., PAPACONSTANTOPOULOS, D.A., VOTER, A.F., AND KRESS, J.D. 2001. Structural stability and lattice defects in copper: *Ab initio*, tight-binding, and embedded-atom calculations. *Physical Review B* 63, 22.
- MOTT, N.. 1958. A theory of the origin of fatigue cracks. *Acta Metallurgica* 6, 3, 195–197.
- MUGHRABI, H. 1984. Dislocations and properties of real materials: proceedings of the conference to celebrate the fiftieth anniversary of the concept of dislocation in crystals, Institute of metals, 244–304.
- MUGHRABI, H. 1979. Plateaus in the cyclic stress-strain curves of single- and polycrystalline metals. *Scripta Metallurgica* 13, 6, 479–484.
- MUGHRABI, H. 1999. On the life-controlling microstructural fatigue mechanisms in ductile metals and alloys in the gigacycle regime. *Fatigue & Fracture of Engineering Materials & Structures* 22, 7, 633–641.
- MUGHRABI, H. 2006. Specific features and mechanisms of fatigue in the ultrahigh-cycle regime. *International Journal of Fatigue* 28, 11, 1501–1508.
- MUGHRABI, H. 2009. Cyclic Slip Irreversibilities and the Evolution of Fatigue Damage. *Metallurgical and Materials Transactions A* 40, 6, 1257–1279.
- MUGHRABI, H. 2010. Fatigue, an everlasting materials problem - still en vogue. *Procedia Engineering*, 3–26.
- MUGHRABI H, ACKERMANN F, HERZ K. Persistent slip bands in fatigued face-centered and body-centered cubic metals. In: Fong JT, editor. *Fatigue mechanisms*. ASTM STP 675. Philadelphia: ASTM; 1979. p. 69.
- MUGHRABI, H., BAYERLEIN, M., AND WANG, R. 1991. *9th Int Conf on the Strength of Metals and Alloys (ICSMA 9)*, 879–86.
- MUGHRABI, H. AND STANZL-TSCHEGG, S. 2007. *Proc. 4th Int. Conf. on Very High Cycle Fatigue (VHCF-4)*, J.E. Allison, J. Wayne-Jones, J.M. Larsen, and R.O. Ritchie, 75–82.
- MUÑOZ-MÁRQUEZ, M.A., TANNER, R.E., AND WOODRUFF, D.P. 2004. Surface and subsurface oxide formation on Ni(1 0 0) and Ni(1 1 1). *Surface Science* 565, 1, 1–13.
- MURAKAMI, Y., ED. 1987. *Stress intensity factors handbook*. Pergamon, Oxford [Oxfordshire] ; New York.
- MURR, L.E. 1975. *Interfacial Phenomena in Metals and Alloys*. Addison-Wesley Educational Publishers Inc, Reading, Mass.
- NABARRO, F. 1967. *Theory of crystal dislocations*. Oxford. Clarendon Press

- NEUMANN, P. 1974. New experiments concerning the slip processes at propagating fatigue cracks—I. *Acta Metallurgica* 22, 9, 1155–1165.
- NEUMANN, P., VEHOFF, H., AND FUHLROTT, H. 1977. On the mechanisms of fatigue crack growth. *Proc. 4th Int. Conf. on Fracture*, Pergamon, Oxford, 1313–1324.
- NISHIMURA, K. AND MIYAZAKI, N. 2004. Molecular dynamics simulation of crack growth under cyclic loading. *Computational Materials Science* 31, 3–4, 269–278.
- OED, W., LINDNER, H., STARKE, U., HEINZ, K., AND MÜLLER, K. 1989. Adsorbate-induced relaxation and reconstruction of $c(2 \times 2)O/Ni(100)$: A reinvestigation by LEED structure analysis. *Surface Science* 224, 1, 179–194.
- PARIS, P. AND ERDOGAN, F. 1963. A Critical Analysis of Crack Propagation Laws. *Journal of Basic Engineering* 85, 4, 528–533.
- PARIS, P.C., GOMEZ, M.P., AND ANDERSON, W.E. 1961. A Rational Analytic Theory of Fatigue - Documents. *The trend in engineering*, 9–14.
- PETIT, J., DE FOUQUET, J., AND HENAFF, G. 1994. Influence of ambient atmosphere on fatigue crack growth behaviour of metals A2 - Carpinteri, Andrea. In: *Handbook of Fatigue Crack Propagation in Metallic Structures*. Elsevier, Oxford, 1159–1203.
- PETIT, J., HENAFF, G., AND SARRAZIN-BAUDOUX, C. 2003. Environmentally assisted fatigue in the gaseous atmosphere. In: I. Milne, R.O. Ritchie and B.L. Karihaloo, eds., *Comprehensive Structural Integrity*. Newnes.
- PHILIBERT, J., VIGNES, A., BRECHET, Y., AND COMBRADE, P. 2013. *Métallurgie. Du minerai au matériau*. Dunod, Paris.
- PHUNG, N.L., FAVIER, V., RANC, N., VALÈS, F., AND MUGHRABI, H. 2014. Very high cycle fatigue of copper: Evolution, morphology and locations of surface slip markings. *International Journal of Fatigue* 63, 68–77.
- POLÁK, J. 1987. On the role of point defects in fatigue crack initiation. *Materials Science and Engineering* 92, 71–80.
- POLÁK, J. 2003. Cyclic deformation, crack initiation, and low-cycle fatigue. In: I. Milne, R.O. Ritchie and B. Karihaloo, eds., *Comprehensive structural integrity*. Elsevier, Amsterdam, 1–39.
- PSOFOGIANNAKIS, G.M., MCCLEEREY, J.F., JARAMILLO, E., AND VAN DUIN, A.C.T. 2015. ReaxFF Reactive Molecular Dynamics Simulation of the Hydration of Cu-SSZ-13 Zeolite and the Formation of Cu Dimers. *The Journal of Physical Chemistry C* 119, 12, 6678–6686.
- QUINN, C.M. AND ROBERTS, M.W. 1964. Chemisorption of oxygen and subsequent processes on metal films : work function measurements. *Transactions of the Faraday Society* 60, 899–912.
- READ, W.T. 1953. *Dislocations In Crystals*. McGraw Hill Book Company Inc.
- RIEUX, P., DRIVER, J., AND RIEU, J. 1979. Fatigue crack propagation in austenitic and ferritic stainless steel single crystals. *Acta Metallurgica* 27, 1, 145–153.

- SALANON, B., FABRE, LAPUJOLADE, J., AND SELKE, W. 1988. Roughening transition on Cu(113): A quantitative analysis of new experimental results. *Phys. Rev. B* 38, 11, 7385-7393.
- SAUZAY, M. AND LIU, J. 2014. Simulation of Surface Crack Initiation Induced by Slip Localization and Point Defect Kinetics. *Advanced Materials Research* 891–892, 542–548.
- SCHIJVE, J. 2009. Fatigue crack growth, physical understanding and practical application. *Fatigue & Fracture of Engineering Materials & Structures* 32, 11, 867–871.
- SEEGER, A. 1955. Stacking Faults in Close-Packed Lattices, in *Defects in Crystalline Solids* (Bristol July 1954) Londres, The Physical Society, 328-339.
- SEEGER, A. 1957. The Mechanism of Glide and Work Hardening in Face-Centered Cubic and Hexagonal Close-Packed Metals, in *Dislocation and Mechanical Properties of Crystals*, New-York, John Wiley & Sons, Inc., London, Chapman & Hall, Limited, 243-329.
- SENFTELE, T.P., HONG, S., ISLAM, M.M., ET AL. 2016. The ReaxFF reactive force-field: development, applications and future directions. *npj Computational Materials* 2, 15011.
- SHAN, T.-R., DEVINE, B.D., KEMPER, T.W., SINNOTT, S.B., AND PHILLPOT, S.R. 2010. Charge-optimized many-body potential for the hafnium/hafnium oxide system. *Physical Review B* 81, 12, 125328.
- SHEN, H., PODLASECK, S.E., AND KRAMER, I.R. 1966. Effect of vacuum on the fatigue life of aluminum. *Acta Metallurgica* 14, 3, 341–346.
- SHIN, I. AND CARTER, E.A. 2013. Possible origin of the discrepancy in Peierls stresses of fcc metals: First-principles simulations of dislocation mobility in aluminum. *Physical Review B* 88, 6.
- SIMMONS, G. AND WANG, H. 1971. *Single Crystal Elastic Constants and Calculated Aggregate Properties. A Handbook*. The MIT Press, Cambridge, Mass.
- SMEENK, R.G., TROMP, R.M., VAN DER VEEN, J.F., AND SARIS, F.W. 1980. A quantitative ion-scattering study of the Ni(110) surface during the early stages of oxidation. *Surface Science* 95, 1, 156–170.
- SMITH, A. 1990. The Versailles railway accident of 1842 and the first research into metal fatigue. *Proceedings Fatigue 90*, Materials and Component Publications Ltd., Birmingham, 2033–2041.
- SNOWDEN, K.U. 1964. The effect of atmosphere on the fatigue of lead. *Acta Metallurgica* 12, 3, 295–303.
- SPITZER, A. AND LÜTH, H. 1982. The adsorption of oxygen on copper surfaces. *Surface Science* 118, 1, 136–144.
- STANZL-TSCHEGG, S. AND SCHÖNBAUER, B. 2007. *Proc. 4th Int. Conf. on Very High Cycle Fatigue (VHCF-4)*, J.E. Allison, J. Wayne-Jones, J.M. Larsen, and R.O. Ritchie, 15–22.
- STANZL-TSCHEGG, S.E. AND SCHÖNBAUER, B. 2010. Mechanisms of strain localization, crack initiation and fracture of polycrystalline copper in the VHCF regime. *International Journal of Fatigue* 32, 6, 886–893.
- STOLTZE, P., NØRSKOV, J.K., AND LANDMAN, U. 1988. Disorder and Melting of Aluminum Surfaces. *Physical Review Letters* 61, 4, 440–443.

- SUEYOSHI, T., SASAKI, T., AND IWASAWA, Y. 1996. Molecular and atomic adsorption states of oxygen on Cu(111) at 100–300 K. *Surface Science* 365, 2, 310–318.
- SURESH, S. 1998. *Fatigue of materials*. Cambridge University Press, Cambridge; New York.
- SURESH, S. AND RITCHIE, R.O. 1982. A geometric model for fatigue crack closure induced by fracture surface roughness. *Metallurgical Transactions A* 13, 9, 1627–1631.
- THIJSEN, J. 2013. *Computational Physics*. Cambridge University Press, Cambridge.
- THIJSEN, J.M. 1999. *Computational Physics*. Cambridge University Press, Cambridge; New York.
- THOMPSON, N., WADSWORTH, N., AND LOUAT, N. 1956. Xi. The origin of fatigue fracture in copper. *Philosophical Magazine* 1, 2, 113–126.
- TOWLER, M.D., ALLAN, N.L., HARRISON, N.M., SAUNDERS, V.R., MACKRODT, W.C., AND APRÀ, E. 1994. Ab initio study of MnO and NiO. *Physical Review B* 50, 8, 5041–5054.
- UCHIDA, N. AND SAITO, S. 1972. Elastic Constants and Acoustic Absorption Coefficients in MnO, CoO, and NiO Single Crystals at Room Temperature. *The Journal of the Acoustical Society of America* 51, 5B, 1602–1605.
- VAN DER VEEN, J.F., SMEENK, R.G., TROMP, R.M., AND SARIS, F.W. 1979. The effect of oxygen coverage on surface relaxation of Ni(110) measured by medium energy ion scattering. *Surface Science* 79, 1, 212–218.
- WADSWORTH, N.J. AND HUTCHINGS, J. 1958. The effect of atmospheric corrosion on metal fatigue. *Philosophical Magazine* 3, 34, 1154–1166.
- WANG, R. AND MUGHRABI, H. 1984. Fatigue of copper single crystals in vacuum and in air II: Fatigue crack propagation. *Materials Science and Engineering* 65, 2, 235–243.
- WANG, R., MUGHRABI, H., MCGOVERN, S., AND RAPP, M. 1984. Fatigue of copper single crystals in vacuum and in air I: Persistent slip bands and dislocation microstructures. *Materials Science and Engineering* 65, 2, 219–233.
- WATT, D.P., EMBURY, J.D., AND HAM, R.K. 1968. The relation between surface and interior structures in low-amplitude fatigue. *Philosophical Magazine* 17, 145, 199–203.
- WEERTMAN, J. AND WEERTMAN, J.R. 1964. *Elastic Dislocation Theory*. MacMillan Washington, DC.
- WEIDNER, A., BEYER, R., BLOCHWITZ, C., HOLSTE, C., SCHWAB, A., AND TIRSCHLER, W. 2006. Slip activity of persistent slip bands in polycrystalline nickel. *Materials Science and Engineering: A* 435–436, 540–546.
- WEIDNER, A., MAN, J., TIRSCHLER, W., ET AL. 2008. Half-cycle slip activity of persistent slip bands at different stages of fatigue life of polycrystalline nickel. *Materials Science and Engineering: A* 492, 1–2, 118–127.
- WEIDNER, A., SAUZAY, M., AND SKROTZKI, W. 2011. Experimental Evaluation of the Cyclic Slip Irreversibility Factor. *Key Engineering Materials* 465, 223–226.

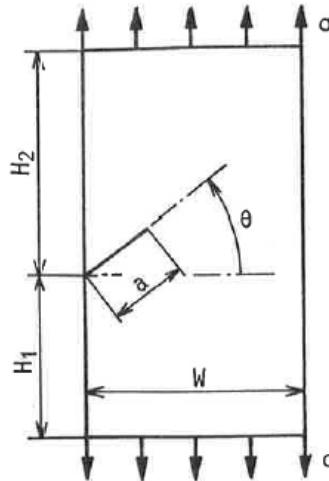
- WIAME, F., MAURICE, V., AND MARCUS, P. 2007. Initial stages of oxidation of Cu(1 1 1). *Surface Science* 601, 5, 1193–1204.
- WINTER, A.T. 1973. Etching studies of dislocation microstructures in crystals of copper fatigued at low constant plastic strain amplitude. *Philosophical Magazine* 28, 1, 57–64.
- WITMER, D.E., FARRINGTON, G.C., AND LAIRD, C. 1987. Changes in strain localization behavior induced by fatigue in inert environments. *Acta Metallurgica* 35, 7, 1895–1909.
- WOOD, E.A. 1964. *Vocabulary of Surface Crystallography*. Bell Telephone Laboratories.
- WOOD, W.A. 1958. Formation of fatigue cracks. *Philosophical Magazine* 3, 31, 692–699.
- WOODS, P.J. 1973. Low-amplitude fatigue of copper and copper-5 at. % aluminium single crystals. *Philosophical Magazine* 28, 1, 155–191.
- YU, J., SINNOTT, S.B., AND PHILLPOT, S.R. 2007. Charge optimized many-body potential for the Si/SiO₂ system. *Physical Review B* 75, 8, 85311.
- ZHU, T., LI, J., SAMANTA, A., LEACH, A., AND GALL, K. 2008. Temperature and Strain-Rate Dependence of Surface Dislocation Nucleation. *Physical Review Letters* 100, 2.

Appendix

Calculation of the stress intensity factor with a specific geometry

From [Fatigue intensity factor hand book]

10.4 EDGE SLANT CRACKED RECTANGULAR PLATE SUBJECTED TO UNIFORM UNIAXIAL TENSILE STRESS



[Reference] C. E. Freese[1]
[Method] Modified Mapping Collocation Method
[Accuracy] Undefined

[Reference] W. K. Wilson[2]
[Method] Boundary Collocation Method
[Accuracy] Undefined

$$K_I = F_I \sigma \sqrt{\pi a}$$

$$K_{II} = F_{II} \sigma \sqrt{\pi a}$$

References

- [1] O. L. Bowie, Solutions of Plane Crack Problems by Mapping Technique, Mechanics of Fracture (Ed. G. C. Sih), Vol. 1(1973), pp.1-55, Noordhoff.
- [2] W. K. Wilson, Research Report 69-1E7-FMECH-R1, Westinghouse Research Laboratories, Pittsburgh(1969).
- [3] Y. Murakami, A Simple Procedure for the Accurate Determination of Stress Intensity Factors by Finite Element Method, Trans. Japan Soc. Mech. Engrs., Vol. 42, No. 360(1976), pp.2305-2315.
- [4] Y. Murakami, A Simple Procedure for the Accurate Determination of Stress Intensity Factors by Finite Element Method, Engng. Frac. Mech., Vol. 8 (1976), pp.643-655.
- [5] Y. Murakami, Numerical Method for Stress Intensity Factors of a Crack in the Arbitrarily Shaped Plate, Trans. Japan Soc. Mech. Engrs., Vol. 43, No. 370(1977), pp.2022-2031.
- [6] Y. Murakami, Application of the Body Force Method to the Calculation of Stress Intensity Factors for a Crack in the Arbitrarily Shaped Plate, Engng. Frac. Mech., Vol. 10(1978), pp.497-513.

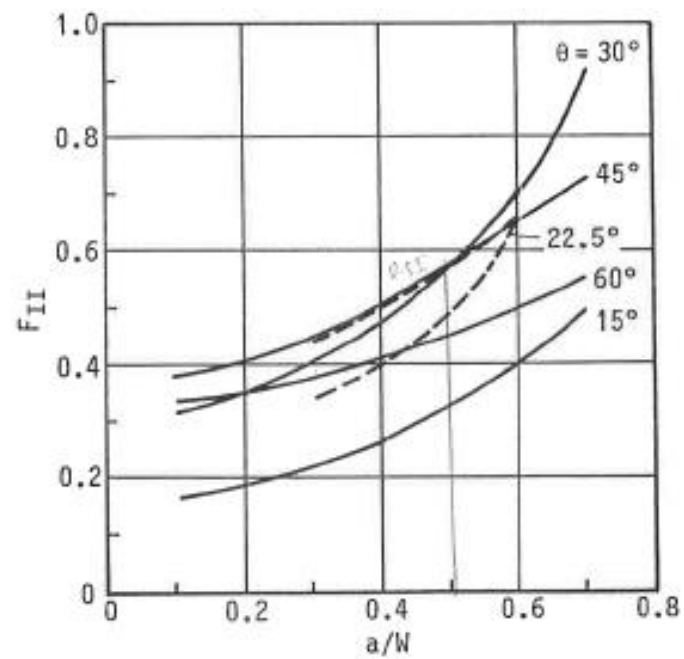
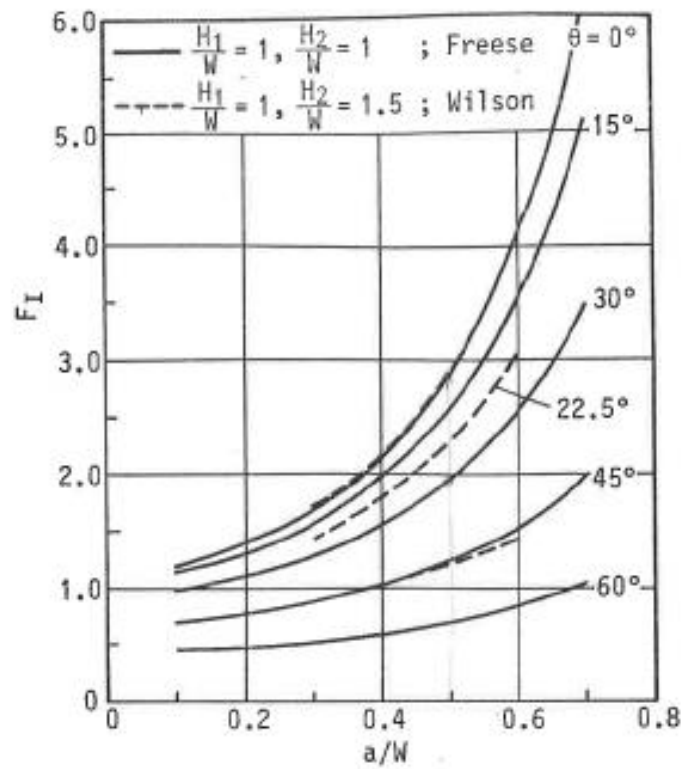


Fig. Stress intensity factors for edge slant cracked rectangular plate subjected to uniform uniaxial tensile stress as a function of crack angle θ and crack length a/W . [1] [2]

Publications

1 journal paper

Acta Materialia. doi:10.1016/j.actamat.2015.09.013

Zhengxuan FAN, Olivier HARDOUIN DUPARC, Maxime SAUZAY

Subject : Atomistic simulations of surface step reconstruction and fatigue crack formation and propagation in metals

1 conference paper

ICTAM 2016 (24th international congress of theoretical and applied mechanics)

Zhengxuan FAN, Olivier HARDOUIN DUPARC, Maxime SAUZAY, Boubakar DIAWARA

Subject : Atomistic simulation of surface cyclic slip irreversibility in fcc metals

Two other papers in preparation

Titre : Simulation atomistique de la fatigue dans les métaux cubiques à faces centrées

Mots clés : Fatigue, facteur d'irréversibilité, dynamique moléculaire, dislocations, effets de surface, effets environnementaux, initiation de fissures, propagation de fissures

Résumé : La fatigue induite par chargement cyclique est un mode d'endommagement majeur des métaux et alliages. Elle se caractérise par des effets environnementaux et de grandes dispersions de la durée de vie qui doivent être mieux compris. Les matériaux analysés sont de type cubique à faces centrées : aluminium, cuivre, nickel et argent. Le comportement de marches naturellement créées en surface par le glissement cyclique de dislocations est examiné grâce à des simulations en dynamique moléculaire sous vide pour tous ces métaux et sous environnement oxygène pour le cuivre et le nickel.

On observe pour les marches en surface un phénomène de reconstruction qui peut induire une forte irréversibilité. Trois mécanismes de reconstruction sont observés et décrits. L'irréversibilité de ces marches est ensuite analysée. Elles restent irréversibles pour toutes les amplitudes de chargement caractéristiques des essais expérimentaux, sauf en cas d'arrivée de dislocations de signe opposé sur un plan de glissement atomique directement voisin.

Avec l'arrivée de dislocations de signes opposés sur des plans non voisins, l'irréversibilité s'accumule cycle par cycle et il est possible de reproduire l'apparition en surface de nano entailles dont la profondeur

augmente peu à peu.

Un environnement oxygène modifie la surface dès le début d'oxydation mais pas l'irréversibilité du glissement en surface parce que ce début d'oxydation n'a pas d'influence majeure sur les différents mécanismes liés à l'évolution du relief induit par le glissement.

Une estimation simplifiée du facteur d'irréversibilité est proposée en couplant différents modèles purement volumiques et nos simulations en surface. On obtient des valeurs entre 0,4 et 0,7 pour le cuivre sous vide et sous environnement oxygène, soit des valeurs plus élevées que celles prédites par les modèles volumiques, en meilleur accord avec des mesures par microscopie à force atomique.

La propagation de fissures est simulée sous environnement inerte. Les effets de mode de chargement, d'orientation cristalline, d'épaisseur de l'échantillon, de température et de conditions de bords sont analysés. Les fissures peuvent se propager à cause de l'irréversibilité du glissement des dislocations générées, irréversibilité due à leurs interactions mutuelles allant jusqu'à la création de jonctions. Le clivage et la formation de nano-cavités sont peu observés dans nos simulations.

Title: Atomistic simulation of fatigue in face centred cubic metals

Keywords: Fatigue, irreversibility factor, molecular dynamics, dislocations, surface effects, environmental effects, crack initiation, crack propagation

Abstract: Fatigue induced by cyclic loading is one of the major damage mechanisms of metals and alloys. It is characterized by strong environmental effects and wide scattering in lifetime which must be better understood. Different face centred cubic metals, Al, Cu, Ni, and Ag are considered in this work. The mechanical behaviour of surface steps naturally produced by the glide of dislocations subjected to cyclic loading is examined using molecular dynamics simulations in vacuum for all these metals and in oxygen environment for Cu and Ni.

An atomistic reconstruction phenomenon is observed at these surface steps which can induce strong irreversibility. Three different reconstruction mechanisms are defined. Surface slip irreversibility is then analysed. All surface steps are intrinsically irreversible under characteristic fatigue laboratory loading amplitude except in the case of the arrival of opposite sign dislocations on a direct neighbouring atomic plane.

With the arrival of opposite sign dislocations on non-direct neighbour planes, irreversibility cumulates cycle by cycle and a nano-notch is produced whose depth

gradually increases.

Oxygen environment affects the surface but the first stages of oxidation do not lead to higher irreversibility because they have no major influence on the different mechanisms linked to the surface relief evolution.

A rough estimation of the slip irreversibility factor is proposed by coupling different bulk models and our simulations which describe surface effects. An irreversibility fraction between 0.4 and 0.7 is estimated in copper in vacuum and in air, higher than the values estimated by bulk models and in better agreement with AFM measurements.

Crack propagation mechanisms are simulated in inert environment. The effects of loading conditions, crystal orientation, box thickness, temperature and boundary conditions are analysed. Cracks can propagate owing to the irreversibility of the glide of some of the dislocations emitted from the crack tip because of their mutual interactions up to the formation of dislocation junctions. In our simulations, cleavage and void formation are scarcely observed.